Experimental and numerical analysis of multiphase flow within horizontal pipeline with variable cross-sectional area

Parham Babakhani Dehkordi (ID.no 818540)

POLITECNICO DI MILANO

A thesis submitted for the degree of

Doctor of Philosophy

April 2017

Tutor and Supervisor: Prof. Luigi P.M. Colombo

Coordinator: Prof. Carlo Enrico Bottani

Abstract

The main purpose of this thesis is to study the hydrodynamic behavior of high viscous oil-water flow within the ducts with variable cross-sectional area. Experimental investigation, theoretical modeling and CFD simulation approaches were conducted. Another part of this thesis is devoted to the high viscous oil-water-air mixture in a horizontal straight tube.

Experimental results on high viscous oil-water flow through sudden contraction and expansion were discussed, the main flow parameters such as distributed and concentrated pressure drop, flow pattern, and phase holdup were reported. Three pipe configurations for sudden expansion (21-30 mm, 30-40 mm, and 30-50 mm) and one case for sudden contraction (30-21 mm) were selected. The main flow patterns included core-annular and dispersed flows. It was concluded that for the largest cross-sectional area change (30-50 mm), the dominant flow pattern resulted dispersed flow, whereas core-annular flow was the major flow pattern in the other configurations. The presence of sudden expansion caused the oil-water flow to be more eccentric. A mechanistic model based on the Two-Fluid Model (TFM) for fully-developed Core-Annular flow of oil-water mixtures was developed. A new correlation to compute water holdup as a function of measured pressure gradient, superficial water velocity, rheological properties of water was developed.

Two differential pressure flow meters (VFM and NFM) have been developed to measure volumetric mixture flow rate. The mixture superficial velocity has been calculated by adoption of the theoretical approach of Bernoulli's equation and introducing the definition of discharge coefficient from calibration curve.

CFD simulation of very viscous oil-water flow through measurement devices (VFM and NFM) as well as sudden expansion was studied by means of commercial CFD code Fluent, most important aspects of flow such as oil holdup, pressure gradients and flow patterns were predicted. It was shown that, CFD simulation was able to predict the core eccentricity without oil contact at the pipe wall during core-annular flow. This is consistent with flow visualization observed experimentally. The concentrated pressure drop through the convergent section of the VFM and NFM computed by CFD showed a very good agreement with experimental data.

The results of an experimental campaign devoted to three-phase flow of very viscous oil-water-air mixtures in a straight horizontal pipe (40 mm i.d.) were reported. Slug body, elongated bubble and total slug unit lengths were experimentally measured by optical probes. It was concluded that superficial gas velocity has a considerable effect on slug body and bubble length, that is, the higher the superficial gas velocity, the higher the slug body and bubble length.

Acknowledgment

It is pleasant to express my sincere gratitude to all those who contributed to the completion of the current work. I am sincerely grateful to the following:

To Prof. Luigi P. M. Colombo, my supervisor, for initiating the study and providing support throughout the duration of this work; without him, this work could not have been started and finished to a success.

To Prof. Giorgio Sotgia, for his advice on the design of experimental campaign and fruitful discussions which have helped me immensely. I would also like to acknowledge Prof. Manfredo Gherardo Guilizzoni, who was always ready to discuss with me on the CFD simulation and gave me useful comments on the CFD part of the manuscripts. Special thanks are dedicated to Dr.Davide Arnone to help me develop the optical probes.

I would like to give special thanks to my parents, brother, sister, family, and all my friends whose spiritual support are greatly appreciated.

Table of Contents

List of Figures

List of Tables

List of Abbreviations

This section includes the list of abbreviations used in this thesis.

A	Annular
ANSI	American National Standard Institute
API	American Petroleum Institute
ASME	American Society of Mechanical Engineers
BD	Dispersed Bubbles
BE	Bubbles-Stratified
CAF	Core-annular Flow
CCA	Corrugated Core-annular Flow
CFD	Computational Fluid Dynamic
CICSAM	Compressive Interface Capturing Scheme for Arbitrary Scheme
CSF	Continuum Surface Force
D	Dispersed Flow
Do/w	Dispersed oil in water
Do/w & Dw/o	Dispersed oil in water and dispersed water in oil
Do/w & w	Dispersed oil in water & water
Dw	Downstream pipe
Dw/o	Dispersed water in oil
EA	Eccentric annular flow
EAD	Eccentric annular with big drops
ECA	Eccentric core-annular with oil entrainment
ECA-E	Eccentric core-annular without oil drop entrainment
ECT	Electrical Capacitance Tomography
ERT	Electrical Resistance Tomography
FS	Full scale
I	Intermittent

ID	Internal diameter
ISO	International organization for standardization
MAPE	Mean absolute percentage error
MPE	Mean percentage error
NFM	Nozzle flow meter
OC	Oil-continuous
OLP	Dispersed oil lumps in water
OP	Orifice plate
OPL	Oil plugs in water
OS	Optical sensor
PCAF	Perfect core-annular flow
PISO	Pressure implicit with splitting of operator
PRESTO	Pressure staggering option
QCV	Quick closing valve
RANS	Reynolds-average Navier Stokes
RKE	Realizable k-ε
RMS	Root mean square
SBIM	Single bubble identification method
SST	Shear stress transport
ST	Stratified flow
ST+M	Stratified plus mixing
TFM	Two-fluid model
UP	Upstream
VC	Video camera
VFM	Venturi flow meter
VOF	Volume of fluid
WCAF	Wavy core-annular flow

Nomenclatures

In this section the most commonly used notations in this thesis are presented. A few symbols denote more than one quantity.

A	Pipe cross-sectional area, m^2
A_o	Cross-sectional area occupied by oil, m^2
A_w	Cross-sectional area occupied by water, m^2
C and n	Coefficients of Blasius equation
C_μ	Variable coefficient to compute turbulent viscosity
C_0	Distribution parameter
$C_2, C_{1\varepsilon}$	Constant coefficients
C_d	Drift velocity, $m \cdot s^{-1}$
c_i^o	Coefficient presented by Ullmann and Brauner (2004)
C_w	Input volumetric water fraction according to Arney et al. (1993)
D	Pipe diameter, m
D_w	Annulus hydraulic diameter, m
f	Friction factor
F_a	Thermal expansion factor
F_i	Coefficient accounting for the waviness of inteface
Fs	Slug frequency, Hz
g	Acceleration due to gravity, $m \cdot s^{-2}$
H	Holdup
h_f	Frictional energy loss per unit mass, $J \cdot kg^{-1}$
h_L	Liquid height in film section, m
I	Turbulent intensity
J	Superficial velocity (Volumetric flux), $m \cdot s^{-1}$
k	Kinetic energy of turbulence, $m^2 \cdot s^{-2}$
k_1	Loss coefficient due to irreversibility
k_2	Loss coefficient due to changing cross-sectional area
ke	Expansion loss coefficient
k_{tot}	Total loss coefficient

L	Pipe length, m
L	Distance between two probes, m
L_b	Bubble length
L_s	Liquid slug length
L_u	Total slug unit length
P_{cal}	Calibration pressure of flow rate, bar
P_{eff}	Effective pressure measured by the manometer at the inlet, bar
P_{pipe}	Actual pressure within the duct, bar
Q	Mass flow rate, $kg \cdot s^{-1}$
Q_o	Oil volumetric flow rate, $m^3 \cdot s^{-1}$
Q_w	Water volumetric flow rate, $m^3 \cdot s^{-1}$
Re_A	Characteristic two-phase Reynolds number defined by Arney et al. (1993)
R_{eg}, R_{el}	Actual gas and liquid Reynolds number
Re_{so}, Re_{sw}, Re_{sg}	Superficial oil, water and gas Reynolds number
Re_w	Actual water Reynolds number
R_{LG}	Pressure reduction factor for three-phase flow
R_τ	Correlation function
S	Normalized signal
S	Slip ratio
S	Perimeter, m
SG	Specific gravity
T	Temperature, °C
U	Effective velocity, $m \cdot s^{-1}$
U_d	Drift velocity, $m \cdot s^{-1}$
U_{eb}	Elongated bubble velocity, $m \cdot s^{-1}$
U_f	Effective velocity of liquid in film section, $m \cdot s^{-1}$
U_h	Velocity of head of leading liquid slug, $m \cdot s^{-1}$
U_h'	Velocity of tail of trailing liquid slug, $m \cdot s^{-1}$
U_n	Velocity of tail of leading liquid slug or head of bubble, $m \cdot s^{-1}$
U_s	Slug velocity, $m \cdot s^{-1}$
$\dot{V}_{cal}$	Volumetric air flow rate read by the flow meter, $m^3 \cdot s^{-1}$

$\dot{V}_{pipe}$ Actual volumetric air flow rate within the duct, $m^3 \cdot s^{-1}$

X   Lockhart-Martinelli parameter

Y   Compressibility coefficient

Subscripts

1	Upstream pipe
2	Downstream pipe/Throat section
b	Bubble
c	Core
f	Liquid in film section
g	Gas
i	Interface
L	Liquid
ls	Liquid slug
m	Mixture
o	Oil
s	Slug
t	Total
w	Water/Wall

Greek letters

This section includes the most commonly used Greek letters in this thesis. A few letters denote more than one quantity.

α_o	Volume fraction of oil phase
β	Inclination angle, °
β	Cross-sectional area ratio of small to the larger pipe
ε	Input volumetric fraction
ε	Turbulence dissipation rate, $m^2 \cdot s^{-3}$
ε_{Lg}	Ratio between gas and liquid (oil+water) superficial velocity in three-phase flow
ε_{Lo}	Ratio between oil and liquid (oil+water) superficial velocity in three-phase flow
ζ	Diameter ratio
ζ	Distribution parameter
η	Ratio between core and pipe radius

θ_w	Wall contact angle, °
μ	Viscosity, Pa·s
μ_s	Average mixture viscosity in slug body, Pa·s
μ_t	Turbulent viscosity, Pa·s
ρ	Density, kg·m^{-3}
ρ_s	Average mixture density in slug body, kg·m^{-3}
σ	Surface tension, N·m^{-1}
σ_ε	Turbulent Prandtl number for turbulent dissipation rate
σ_k	Turbulent Prandtl number for turbulent kinetic energy
$\sigma_{o\text{-}w}$	Interfacial tension between oil and water, N·m^{-1}
τ_f	Liquid-wall shear stress, Pa
τ_g	Gas-wall shear stress, Pa
τ_i	Interfacial shear stress, Pa
τ_s	Mixture-wall shear stress in slug body, Pa
ϕ	Ratio between oil and water superficial velocity
ϕ_A	Dimensionless two-phase pressure gradient

1. Introduction

1.1 Background

As depletion of light oil reservoirs occurs, a tendency to produce hydrocarbon from heavy crude oil is becoming important. Deep understanding of multiphase flow behavior in pipeline for system design and production is vital. High viscous oil in reservoir does not flow easily specially after primary recovery (where oil produced as a result of natural energy of reservoir), even in high permeable reservoirs. Hence, enhanced oil recovery methods are required to force oil moving toward production wells. One of the mechanisms is to reduce oil viscosity by gas injection, thermal treatment, steam flooding, etc. After lifting of oil to wellhead surface, transportation facilities are needed to transport oil downstream. The presence of high viscous oil in pipeline would result in increasing distributed pressure gradient. Considerable savings in the pumping power can be obtained by introducing water in annulus where oil is surrounded by water. This method is so-called water-lubricated oil flow and associated flow regime is core-annular flow. Design of pipeline downstream of hydrocarbon wells is highly dependent upon topology of region where oil is flowing. Thus, frequent area change in pipeline systems such as expansion, contraction, existence of risers, valves, and elbows, etc is present. In the last decades (beginning with development of nuclear plants), there have been a large number of research studies on two-phase gas-liquid flows in the presence of singularities, e.g. sudden contraction and expansion, see for instance, Wadle (1989), Attou and Bolle (1997), Chen et al. (2007) and Chen et al. (2009). However, a limited number of research activities are dedicated to liquid-liquid flow through singularities, in spite of the relevance to petroleum industries. One may refer to the works carried out by Hwang and Pal (1997), Balakhrisna et al. (2010) and Colombo et al. (2015).

In order to reduce risk of operation for industrial application with respect to liquid-liquid flow through singularity, characteristics of oil-water flow, such as distributed and concentrated pressure gradient, spatial distribution of phases (Hold-up) and flow regimes must be well understood.

Another important aspect of multiphase flow design in pipelines is the ability of measuring appropriately the mass flow rate of phases. In the past a significant amount of efforts have been

conducted to design intrusive and non-intrusive devices. Almost all measuring devices are building such a way that they interfere with the flow path. Thus, multiphase measuring devices can be considered as a type of singularity. So, if multiphase behavior through abrupt change of cross-sectional area of pipe is understood, it would help characterize liquid-liquid or liquid-liquid-gas flow through multiphase flow devices.

Since the presence of gas together with oil and water is unavoidable, it would be necessary to investigate and predict the flow characteristics during multiphase production at different flow conditions. The most common flow pattern is slug flow, where a series of liquid slugs is separated by relatively large gas pockets. In spite of its importance, very limited information regarding such a three-phase flow is available in the literature. Hence, it is important to experimentally investigate the characteristics of three-phase slug flow because it significantly affects pressure gradients and phase holdup.

1.2 The Goals

The present work is divided into two main sections. In the first section, the focus is on the transport of high viscous oil-water through geometrical singularities, which included the experimental, theoretical, and CFD simulation analysis in sudden expansion, contraction, and measurement devices such as Venturi flow meter (VFM) and Nozzle flow meter (NFM). In the second section, identification of geometrical parameters of three-phase slug flow by means of optical techniques in a straight horizontal pipe with constant cross-sectional area has been studied.

The specific objectives of current PhD thesis are listed below:

- To determine the flow patterns, distributed pressure gradient, concentrated pressure drop, and phase holdup during two phase flow of very viscous oil-water flow in horizontal pipe configuration undergoing sudden contractions and sudden expansion.
- To compare the experimental results of pressure gradients and phase holdup with existing empirical correlations and mechanistic models in the literature.
- To develop a method of measurement of the concentrated pressure drop and volume flow rate by using Venturi Flow Meter (VFM) and Nozzle Flow Meter (NFM) for two phase flow of very viscous oil water mixtures in a horizontal pipe.

2

- To propose a new model for oil-water mixture through VFM and NFM to predict the total volumetric flow rate and the individual volume flow rate of oil and water.
- To simulate by using 3-D CFD modeling of very viscous oil-water flow through measurement devices (VFM and NFM) as well as in horizontal pipe configurations undergoing sudden expansion.
- To characterize the flow behavior of three phase flow of very viscous oil-water-air flow within a straight horizontal pipe.

1.3 Outline of the thesis

The present thesis is divided into 9 Chapters in which the introduction, the goals of the work, and objectives are described in Chapter 1.

Chapter 2 presents the literature review about liquid-liquid flow in horizontal pipes with/without changing cross-sectional area. Moreover, different types of multiphase flow meter are discussed, among all the multiphase flow meters, the structures of some differential pressure meters are explained and basic theory of application of such devices is presented. State of the art of three phase flow of oil-water-gas flow within horizontal ducts is also introduced in the last section of Chapter 2.

Chapter 3 deals with description of experimental facilities and procedure for multiphase two and three phase flow within horizontal pipes.

The experimental results for very viscous oil-water flow through sudden expansions and contractions, highlighting the most important features, are presented in Chapter 4.

Chapter 5 focuses on the modeling aspects of liquid-liquid flow in horizontal pipe. A comparison between experimental results and existing empirical correlation/mechanistic models is made. A new correlation to compute water holdup based on experimental pressure gradients is presented and validated.

Measurements of concentrated pressure drop during oil-water flow through VFM and NFM are presented in Chapter 6. Based on experimental singular and distributed pressure drops, a new model to compute total and individual volumetric flow rate is proposed.

Chapter 7 describes the CFD simulation setup and simulation results related to very viscous oil-water flow through sudden expansion and measurement devices are discussed.

Chapter 8 discusses very viscous oil-water-air flow within a straight horizontal pipe. The slug/bubble length, and bubble velocity are measured by means of optical techniques.

Chapter 9 gives the conclusion and recommendation for future work.

2. Literature review

In fluid mechanic, the term multiphase flow implies simultaneous flow of materials with different phases with different rheological properties. Multiphase flow can be classified as several combinations of state of different phases, e.g., gas-liquid flow, liquid-liquid flow, and gas-solid flow. From oil and gas industrial point of view, multiphase flow is often referred to simultaneous flow of oil, water and gas.

An oil zone in a reservoir is surrounded by two layers, including gas cap on the top and underlying water aquifer at the bottom. During the early time of oil reservoir (primary recovery), oil moves to the production wells due to the release of natural energy stored in the reservoir fluids and driving forces imposed by gas cap and water aquifer. As a result of oil production, gas cap and aquifer are expanded and the production from natural gas and saline water is increased. Moreover, by lifting natural gas from well bottom to surface facilities at wellhead, the dissolve gas in oil would be released (if pressure drops below the bubble point pressure) and the GOR (Gas oil ratio) increases as well. After average reservoir pressure declines, improved oil recovery methods such as waterflooding are needed to maintain reservoir pressure (secondary recovery). Two-phase flow of oil-water and three-phase flow of oil-water-gas are frequently occurred in petroleum industry.

As multiphase flows are lifted up to the surface from the reservoir, it must be transported to processing unit by pipelines. The direction of pipelines is classified as vertical and horizontal with or without the pipe inclination angle. Besides the direction of pipelines which is practically dependent upon topological situation of regions under production (whether on-shore or off-shore), different configuration of ducts is widely used such as sudden expansions, contractions, presence of elbows and valves, etc.

On the other hands, measurement and prediction of total and individual mass flow rates of phases is important. Many different solutions for this measurement were described throughout the literature and proposed for patents. A primary distinction is between devices that can monitor multiphase flow inline and meters that require flow spill and phase separation. The first ones can be simply mounted on the production facilities, and they are much cheaper alternatives to multiphase separators, also in terms of operational costs. Within the family of the inline

measurement tools, the most-used principle is the attenuation of single- or dual-energy γ-rays, with all the related issues and costs. Devices based on the electric permittivity of the mixture, on microwaves or ultrasounds, turbine and vortex flow- meters, and combination with the previous were also proposed (Falcone et al., 2009; NFOGM, 2005). Another type of metering devices is the one based on differential pressure measurements, including Venturi Flow Meters (VFM) and Nozzle Flow Meters (NFM). These can be of great practical interests for oil and gas industries because they have no moving part, thus greatly reducing (virtually to none) the need for maintenance (Atkinson et al., 2004), but an issue on the use of these meters is that they have to rely on models to link the measured pressure difference to the mass flow rates. Thus, it is necessary to characterize in detail multiphase flow across these devices.

In this chapter, heavy oil transportation methods and importance of water-lubricated heavy oil is briefly described in section 2.1. The previous experimental studies on liquid-liquid flow in horizontal straight ducts would be presented in section 2.2. Then, I will review previous experimental and modeling investigation of gas-liquid through sudden expansion and contraction in section 2.3. The previous study regarding liquid-liquid flow through singularity is outlined in section 2.4. In section 2.5, basic theories and methodologies on modeling of multiphase flow in computational fluid dynamic performed by CFD code Ansys Fluent is explained because it is used in the current investigation to characterize hydrodynamic behavior of very viscous oil-water flow. Typical multiphase measurement devices and techniques are introduced in section 2.6. Last but not least, previous experimental investigation on three phase flow of oil-water-gas is described in section 2.7.

2.1 Heavy oil transportation technologies

Oil hydrocarbon resources are divided into two main groups, conventional and unconventional resources. The former has a high value on the market but scarce in resources. Figure 2-1 shows forecast of world discovery of conventional oil per billions of barrels. Since 1970s, the total reserves of conventional reserves are dramatically reduced. Hence, there is a necessity to use unconventional resources (Santos et al., 2014).
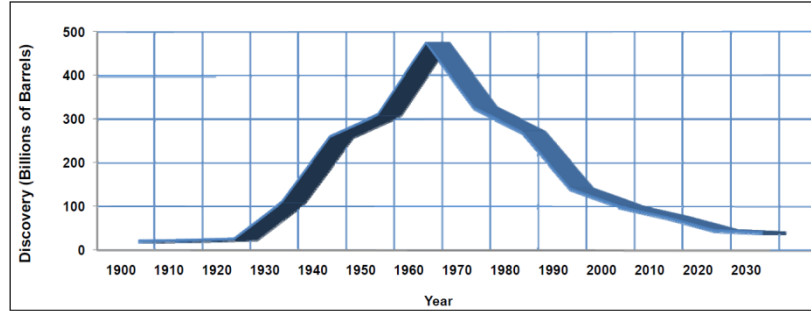
Figure 2-1. Conventional oil reserves per billions of barrels

According to Santos et al (2014), heavy oil, extra-heavy oil, tar sand oil, shales oil are all considered as unconventional oils. These are characterized by high viscosity and larger density than conventional oils. These types of crude oils do not flow easily. Thus, specific techniques and system designs are required for production, transportation, and refining of heavy oil. American Petroleum Institute defined a criterion for oil classification which is widely used and named as °API. Heavier oils are recognized by lower °API but oil classification has not been standardized.

The API degree is calculated as:

$$\text{API Gravity} = \frac{141.5}{\text{SG at } 60\ °\text{F } (15.56\ °\text{C})} - 131.5 \qquad (2.1)$$

Where SG is the specific gravity of the fluid, $SG = \rho_o / \rho_w$. According to American Petroleum Institute, heavy oil is characterized by API degree less than 23°. Although oil density is a crucial parameter for evaluating operating cost and resource value, the rheological property that most influence on producibility and recovery of oil is viscosity. It is worth noting that there is no standard relation between density and viscosity of oil. Conventional oil viscosity varies from 0.001 Pa·s [1 centipoise (cp)] to 0.01 Pa·s (10 cp), while viscosity of heavy and extra-heavy oil may range from 0.02 Pa·s (20 cp) to more than 1,000 Pa·s (1,000,000 cp), see Alboudwarej et al.(2006).

A review of most important technologies for heavy oil transportation is listed in the work by Hart (2014). To transport heavy oil, reduction of pressure drop along pipelines is vital because it can significantly reduce pump power to push oil over a long distance. A diagram of heavy oil transportation technique is shown in Figure 2-2. The methods to transport heavy oil are generally

divided into three main sub-sections as shown in Figure 2-2: a) viscosity reduction [e.g. preheating of heavy oil and subsequent heating of oil over a long distance, dilution and blending of heavy oil by means of light hydrocarbon or solvent, emulsification by formation of oil-in-water mixture and reduction of oil's pour point with pour point depressant (PPD)]; b) drag/friction reduction (e.g. lubricating process by core-annular flow and drag reducing additives) ; c) in-situ partial upgrading of heavy oil to provide a syncrude with modification of oil viscosity, density and reduction of heavy contents of oil such as asphaltenes, wax and sulfur. In the following section, each method is described and challenges would be addressed. According to previous works, see for instance Gateau et al. (2004), the lower the viscosity of the diluents, the lower is the viscosity of the blended mixture of heavy oil. The materials which are widely used for dilution are condensate from natural gas production, kerosene, lighter crude oils as well as organic solvents such as alcohol, etc. The main issue regarding to application of diluents is initial cost, and they are not relatively cheap. Another method to transport heavy oil and reduce viscosity is increasing temperature by installation of heating stations along pipelines. As a result of heating, flowability of heavy oil would be enhanced, and resistivity is considerably reduced. There are several issues associated with usage of such technology, including the significant amount of energy and cost, heat losses occurring along pipelines. The heat losses would be solved by using pipe insulation. However, most of the times due to presence of sudden expansion and contraction, it induces some problems. The situation is much more dramatic when crude oil must be transported from sub-sea wells. Emulsification of heavy oil by water is considered to be a new technology. In this method, heavy oil is emulsified by water and stabilized with the help of surfactant. The surfactant monolayer is placed on the oil-water interface to stop drop growth and phase separation into single oil and water phases. Transportation of crude oil by emulsification requires special treatment because O/W emulsion must be produced, transported, then the oil must be separated from water. To separate the oil-in-water emulsion, thermal demulsification, electro-demulsification and chemical demulsification is needed, which adds additional cost to heavy oil transportation. The last technology to reduce oil viscosity to improve flowability is pour point reduction. Heavy crude oils have been described as a colloidal suspension of solute asphaltenes and a liquid phase maltenes such as aromatics and resins. The oil viscosity and density can be increased by presence of asphaltenes macromolecules in the oil, resulting in higher resistivity to flow in pipelines. The rheological properties of oil can

8

be greatly improved by use of pour point depressant. The pour point of the oil is the lowest temperature at which it stops flowing. The second group of heavy oil transportation is friction reduction methods. Much of energy applied by the pump to heavy oil to transport is wasted due to high frictional loss as a result of high viscosity of crude oils. Hence, polymer additives are alternative to reduce drag near pipe walls. According to Toms (1948), about 30-40% of drag reduction can be achieved by injection of polymer drag-reducing components. Three common problems encountered by using such technology are the tendency of polymers to separate as stored, obstacles of dissolving polymers in heavy oil and shear degradation when dissolved in crude oil.
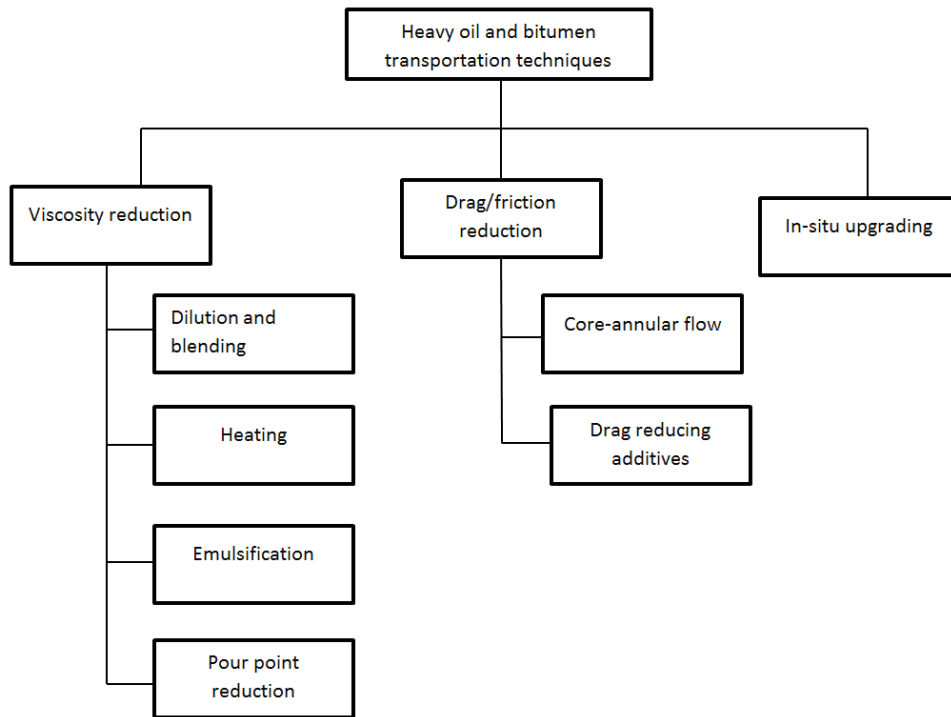
Figure 2-2. Transportation techniques for heavy oil and bitumen

Water-lubricated heavy oil transportation is considered as one of the effective ways of oil transportation due to low operating cost. The most ideal spatial distribution of water-lubricated heavy oil is so-called core-annular flow, where the oil core is surrounded by a film layer of water or solvent, which is placed near the pipe wall. The water acts as a lubricant which significantly reduces friction and pressure drop over a long distance in pipelines. The pump pressure is comparable to that required to pump the single-phase water. Hence, two-phase pressure drop of heavy oil-water is weakly dependents on viscosity of oil. The problem related to this method is the difficulty to maintain perfect core-annular, where oil moves to the center of pipe by density matching of oil and water, as well as oil fouling. Figure 2-3 compares two-phase pressure drop against total flow rate for different oil transportation technology. As it is evident, core-annular technology is the best option to reduce two-phase pressure drop for the whole range of volumetric flow rate.
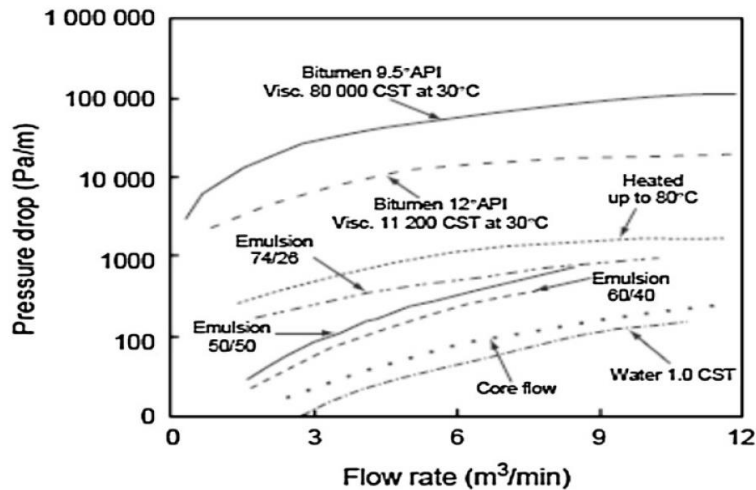
Figure 2-3. Two phase pressure drop as a function of flow rate for different heavy oil transportation technologies (Hart, 2014)

The focus of the present study is to understand flow behavior of core-annular flow in presence of sudden expansion, contraction, as well as Venturi and Nozzle flow meter. In the following section, a survey on the application of water-lubricated technology is presented.

2.2 Experimental investigation of water-lubricated flow in horizontal straight pipe

2.2.1 History of water-lubricated flow

One of the earliest works about core-annular flow dates back Clark and Shapiro (1950) who patented a process of pumping high viscous oil (μ_o=0.8-1 Pa·s) by introducing oil and demulsifying agents into heavy crude oil. They preferred to use the treated water in proportion of 8% to 15% of total mixture liquid velocity. They also suggested the possibility of higher portion of water flow rate but concluded that greater amount of water would not facilitate flow sufficiently to compensate for the additional load. They concluded that injection of 24% water would result in the reduced pressure drop up to a factor of 7.8-10.5% and optimum pressure reduction would be achieved when 8-10% water was introduced into heavy oil.

2.2.2 Governing parameters of oil-water flow

Before introducing previous works on oil-water flow, it is necessary to describe most important aspects of two-phase flow of oil-water characterized by flow regime, superficial phase velocity and hold-up. If other multiphase flow notations are required, it would be specified as needed in the further chapters.

1) Flow regime

When more than one phase flow through the pipeline, the interaction between phases would result in different spatial distribution at axial, radial and tangential direction, which is so-called flow regime or flow pattern. Several parameters affect the flow pattern, depending on input velocity of phases, viscosity ratio, density ratio, wetting properties, surface tension and pipe diameter. There are several techniques to monitor flow patterns within ducts. The simplest method is the visual observation of transparent pipe, which is the most common used method by today. Other techniques include local sampling, electrical resistance tomography (ERT), electrical capacitance tomography (ECT), and ultrasonic techniques. Different flow pattern names are assigned by different researchers in oil-water flows. The widely used terms for liquid-liquid flow patterns include dispersed flow, core-annular flow, stratified flow, and slug/plug flow.

11

2) Phase volumetric flux

Superficial velocity (volumetric flux) of each phase is defined as phase velocity as if the phase is flowing alone in the tube. If we consider immiscible liquid-liquid fluids flowing simultaneously through pipe with cross-section area A, with Q_o and Q_w as input flow rate of oil and water, respectively:

$$J_o = \frac{Q_o}{A} \qquad\qquad J_w = \frac{Q_w}{A} \qquad\qquad J_m = \frac{Q_w + Q_o}{A} \qquad (2.2)$$

Where J_o, J_w and J_m are superficial velocities of oil, water and mixture, respectively. The oil and water phases are distributed within the pipe in such a way that they occupy a smaller area than cross-sectional area of the pipe. Due to this fact effective velocity of phases, that is, in-situ phase velocity, is different from superficial velocity of phases. If the cross-sectional area occupied by oil and water is A_o and A_w, respectively, effective velocity of oil and water is given:

$$U_o = \frac{Q_o}{A_o} \qquad\qquad\qquad U_w = \frac{Q_w}{A_w} \qquad\qquad (2.3)$$

From equations (2.2) and (2.3), effective or in-situ area fraction (holdup) of oil and water is defined as:

$$H_o = \frac{J_o}{U_o} = \frac{A_o}{A} \qquad\qquad H_w = \frac{J_w}{U_w} = \frac{A_w}{A} \qquad\qquad (2.4)$$

Input volumetric oil and water are defined as superficial velocity of each phases divided by mixture superficial velocity, that is:

$$\varepsilon_o = \frac{J_o}{J_m} \qquad\qquad\qquad \varepsilon_w = \frac{J_w}{J_m} \qquad\qquad (2.5)$$

The slip ratio between two phases is defined as ratio of effective velocity of oil to water, which is yardstick of determining slippage between two phases:

$$S = \frac{U_o}{U_w} \qquad\qquad\qquad (2.6)$$

When slip ratio is greater than unity, it means that oil moves with higher than water and oil is an accumulating phase, while slip ratio less than unity means that water is an accumulating phase.

2.2.3 Previous studies on high viscous oil-water flow in horizontal straight pipe

1) Research council of Alberta, Canada

Russel and Charles (1959) analyzed two flow patterns of oil/water, with two different geometries, which included: 1) two layers between wide parallel plates, and 2) concentrically in a circular pipe. A theoretical analysis was performed to link the volumetric flow rate of two immiscible liquids to the pressure gradient, the geometry of the system and the liquid viscosities. They defined a parameter as a pressure reduction factor to evaluate how much two-phase pressure gradient was reduced as a result of injecting less viscous phase (water), without reducing the volumetric flow rate of more viscous phase. The results for oil viscosities between 0.8-1 Pa·s showed that maximum predicted pressure reduction factor up to 500 can be achieved for the case of concentric configuration. Much larger pressure reduction factor was achieved for the concentric case than the parallel plate system in which stratified flow occurs.

Charles et al. (1961) conducted a series of experiments on equal density oil-water flows. The horizontal pipe, with an internal diameter of 1 inch (D=26 mm) and 4.3 m long was considered. Three oil viscosities of 6.29, 16.8, and 65 cp (0.00629, 0.0168 and 0.065 Pa·s) were used in the experiments. The flow pattern, pressure drop and holdup measurements were performed for a range of superficial oil velocities from 0.05-3 ft/s (0.015-0.94 m/s), while superficial water velocities varied from 0.1-3.5 ft/s (0.03-1.06 m/s). Carbon tetrachloride was added to the oil to give the oil equal density as water. I used a much higher oil viscosity than Charles et al. (1961) without matching densities of phases. Hence, in addition to inertia, viscous, and interfacial stresses, gravitational forces can also act, resulting in an eccentric oil-water flow. Charles et al. (1961) have monitored flow regime by photographic recording. Five flow regimes were detected, which includes water drops in oil, oil in water concentric (Core-annular flow), oil slug in water, oil bubbles in water, and oil drops in water. Figure 2-4 shows sketches of oil-water flow pattern for the 16.8 cp oil viscosity for constant superficial water velocity of a) J_w=0.03 m/s , b) J_w=0.20 m/s, and c) J_w=0.62 m/s. Superficial velocity of oil decreased for fixed amount of water.
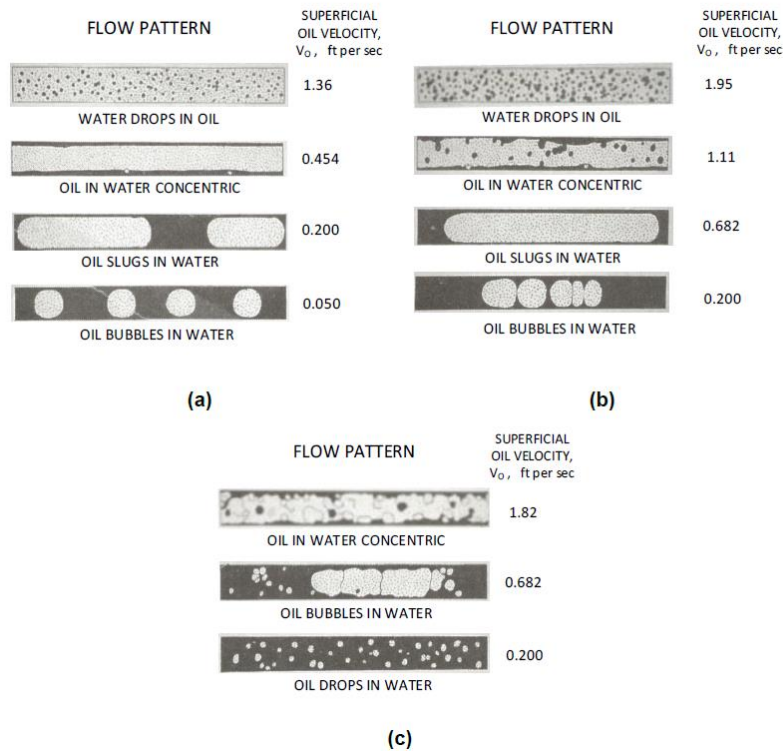
Figure 2-4. Schematic photographs of the oil-water flows with oil viscosity μ_o=0.016 Pa.s taken from Charles et al. (1961). a) J_w=0.03 m/s, b) J_w=0.20 m/s and c) J_w=0.62 m/s

At high superficial oil velocity and relatively low superficial velocity of water, the water drops in oil was observed. However, the transition from water drops-in-oil to core-annular flow was demonstrated as superficial oil velocity decreased. Further reduction of oil velocity caused flow becoming oil bubbles in water. Almost similar behavior has been seen in all cases. In addition to flow patterns, Charles et al. (1961) also investigated two-phase pressure drop as well as in-situ contents of phases. They measured phase holdup by means of quick action valves technique in which, two valves positioned in an axial distance, were closed simultaneously and trapped oil and water were measured. The measured holdup ratio of oil to water showed that almost in all experiments oil holdup is higher than water holdup.

(2) Laboratory of Aerodynamics and Hydrodynamics, Delft University of Technology, Netherland

Ooms et al. (1984) developed a theoretical analysis by means of the hydrodynamic lubrication theory for core-annular flow of very viscous oil core and water annulus. The focus of the study was to understand how the buoyancy force on the core, due to density difference of oil and water, was counterbalanced. According to the model, oil is considered to be solid due to very high viscosity, and there is a solid/liquid interface. They assumed that any flow inside the oil core is negligible and there is no variation of the profile at oil-water interface with time. The lubrication theory was validated against experimental data. The experimental tests were conducted for a 2 inch (ID=0.05 m) and 8 inch (ID=0.20 m) pipe. In 2 inches experimental tests, oil viscosity varied from 2.3-3.3 Pa·s, while they used oil viscosity of 1.2-2.2 Pa·s for 8-inch pipe. The difference between density of water and oil was 30 kg/m^3. Constant superficial oil velocity of 1 m/s and water superficial velocity, ranging from 0.01-0.25 m/s was considered for tests. They measured pressure drop and pressure reduction factor, concluded that when the amount of water is so small, the pressure reduction factor rarely changes with water fraction. They also emphasized that core-annular flow regime is less beneficial for larger diameter. From visual observation, they detected ripples in the core and concluded that the presence of ripples is essential for core-annular flow because in the absence of ripples, there is no force to balance the buoyance force, resulting in oil contact at the wall.

Oliemans et al. (1987) have performed experimental tests on core-annular water flow with test facilities similar to what Ooms et al. (1984) used in their tests, except oil viscosity, which was selected to be 3 Pa·s. The superficial oil and water velocities were ranged; J_o=0.5-2.5 m/s and J_w=0.03-0.6 m/s. They developed a semi-empirical correlation for the water holdup based upon experimental data. As a rule of thumb, they suggested that core-annular technique is suitable for the crude oils with higher viscosity than 0.5 Pa·s.

(3) University of Minnesota, Minneapolis, USA

Arney et al. (1993) carried out experiments on high viscous oil-water in a horizontal pipe. Two types of oil were used, which included waxy crude oil (stable water-in-oil emulsion, with viscosity ranging between 200 and 900 Pa·s after yielding) and No. 6 fuel oil (viscosity 2.7 Pa·s

and density 989 kg/m^3). Superficial oil velocity varies between 0.14-1.16 m/s for oil and 0.06-0.65 m/s for water. The test section was composed of a glass pipe with an internal diameter of 15.9 mm and length of 6.35 m. The original test section contained a pipe with PVC materials, however, No. 6 fuel oil tended to stick to the pipe wall, resulting in difficulties in cleaning the pipe by water. Hence, the PVC pipe section was replaced by a glass pipe due to its water-wet features. Flow patterns were observed by means of a high speed video camera. To reduce the lens effect regarding to pipe curvature, a rectangular box filled with glycerol (glycerol has an index of refraction, which closely matched with glass pipe) surrounding the outer part of glass pipe was used. They concluded that at low water flow rate, the risk of oil contact at the wall increased, which must be avoided. At higher water flow rates perfect core annular flow (PCAF), wavy core annular flow (WCAF), and oil slug in water were detected. In addition, water holdup was measured by means of a removable section, which included two pairs ball valves. Water holdup was always larger than input water fraction, meaning that oil tended to move with higher velocity. They developed a semi-empirical correlation based on large database. A formula was derived which was, in fact, the modification of Oliemans (1986) correlation. Figure 2-5 showed the result of measured water holdup versus water input fraction.
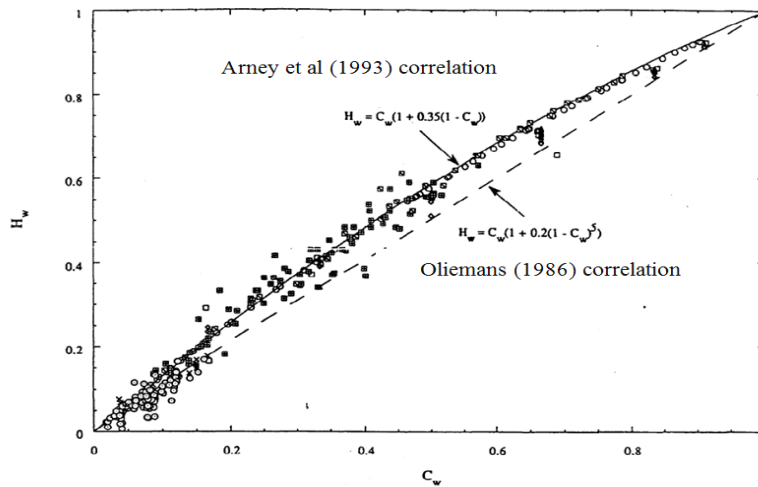
Figure 2-5 Measured water holdup (H$_w$) against input water fraction (C$_w$) for large data sources in the literature (Arney et al., 1993)

(4) University of Campinas, Brazil

Bannwart (2001) studied modeling aspect of core-annular flow in both horizontal and vertical tubes, and developed correlations for volume fraction and pressure drop for this flow regime. To ensure the possibility of forming core-annular flow regime, they emphasized that two immiscible liquids must have very different viscosity and relatively small density difference. Furthermore, interfacial tension plays an important role in favoring annular configuration. The proposed correlations were compared with data source in the literature survey, showing satisfactory results. Later, Bannwart et al. (2004) experimentally investigated flow patterns in heavy crude oil (initial viscosity and density 0.488 Pa·s and 925.5 kg/m^3 at $20\,°C$) and water flow within vertical and horizontal 28.4 mm i.d. pipes. The volumetric flux for oil and water varies between 0.007-2.5 m/s and 0.04-0.5 m/s, respectively. The flow patterns in the horizontal pipe were observed as stratified (E), bubbles-stratified (BE), dispersed bubbles at high flow rates (BD), annular (A).

(5) University of Brescia, Italy

Grassi et al. (2008) conducted experimental tests on high viscous oil-water in the horizontal and inclined pipe. Six transparent polycarbonate tubes of ID=21 mm were selected with total 9 m long pipe. The pipe stood up by means of a steel beam, which was hinged midway to a vertical 1.2 m high support. This configuration was arranged such a way that it allowed the maximum inclination angle up to $\pm15\,°$. To reduce optical distortion induced by pipe curvature, a glass box filled with water is positioned at the half way of the test section. For higher viscosity fluid, paraffin oil (viscosity 0.8 Pa·s at $20\,°C$ and density 886 kg/m^3) and for lower viscous fluid tap water were selected. Inlet nozzle was designed such a way that core-annular flow was formed, that is, oil and water were injected concentrically to the test section. They used a dimensionless Eötvös number defined by Brauner (2002), as the ratio between gravitational and interfacial forces, to interpret their results. They developed the flow pattern maps and realized that larger portions of flow pattern maps were devoted to core-annular flow and oil-in-water dispersion flow. Elongated oil-in-water flow pattern was also observed in a smaller portion of maps. However, smooth stratified flow pattern was never detected. It has been also concluded that the

effect of inclination angle, with the same experimental conditions, on flow patterns has not been considerable.

(6) Laboratory of Multiphase Thermo-Fluid Dynamics, Politecnico di Milano, Italy

Sotgia et al. (2008) experimentally investigated very viscous oil-water in horizontal pipes, with diameters ranging from 21 mm to 40 mm. Mineral oil (viscosity 0.9 Pa·s and density 889 kg/m^3) and tap water were used as test fluids. Tap water and mineral oil were injected to the test section co-axially and oil injector was positioned 25 °with respect to the horizontal axis. They used different designs for the inlet devices to evaluate the effect of inlet nozzle on flow pattern and pressure gradient. Visual observation confirmed that as gradual contraction exists after inlet nozzle, core-annular flow regime was favored, while the presence of sudden contraction after the inlet nozzle resulted in the much more perturbed flow regime, that is, dispersed flow regime. According to visual inspection, flow patterns were classified as dispersed flow, transition from dispersed to annular flow, perfect core-annular flow, wavy annular flow, corrugated annular flow, and wavy stratified flow. Figure 2-6 illustrates the typical example of different core-annular flow of oil-water in the 40 mm Pyrex tube.

a)   Annular (Jo=0.75m/s; Jw=0.75m/s)

b)   Wavy-Annular (Jo=0.75m/s; Jw=0.32m/s)

c)   Corrugated Annular (Jo=0.75m/s; Jw=0.05m/s)
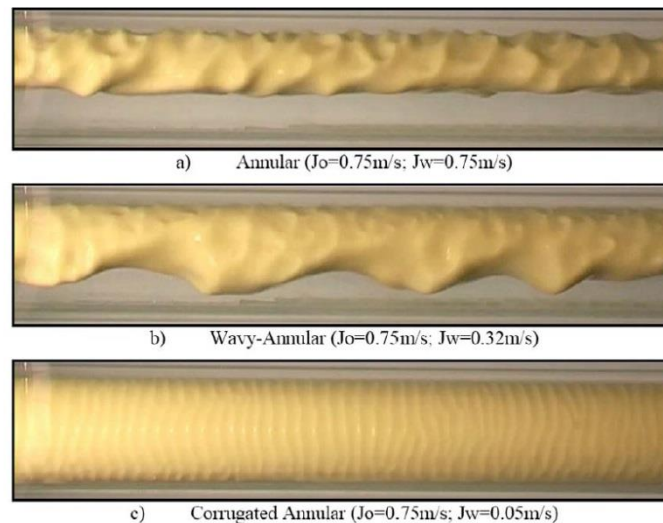
Figure 2-6 Photos of different core annular flow regimes in 40 mm Pyrex pipe for J_o=0.75 m/s taken from Sotgia et al (2008). a) Perfect core-annular flow, b) Wavy annular, c) Corrugated annular

A new criterion for the transition from annular to stratified flow was proposed based on an empirical law. The pressure gradients were experimentally measured, and results were compared to the models proposed by Arney et al. (1993) and Brauner (1991). The two models could predict pressure drop with good agreements. In the current study, the rheological properties of oil are the same as the oil used by Sotgia et al (2008).

(7) School of Energy, Environment and Agrifood Oil and Gas Engineering Centre, Cranfield University

Experiments on very viscous oil (oil viscosity ranged from 3.3 to 16.0 Pa·s) and water flows were conducted in a horizontal 25.4 mm i.d. pipe by Shi (2015). Superficial oil velocity was in range 0.04-0.54 m/s, while water superficial velocity was ranged between 0.01-1.8 m/s. They observed different flow patterns, which included oil-continuous (OC), inversion (Inv), core-annular flow (CAF), oil plugs in water (OPL), dispersed oil lumps in water (OLP). Figure 2-7 shows the flow patterns corresponding to the oil with viscosity of 3.3 Pa·s.
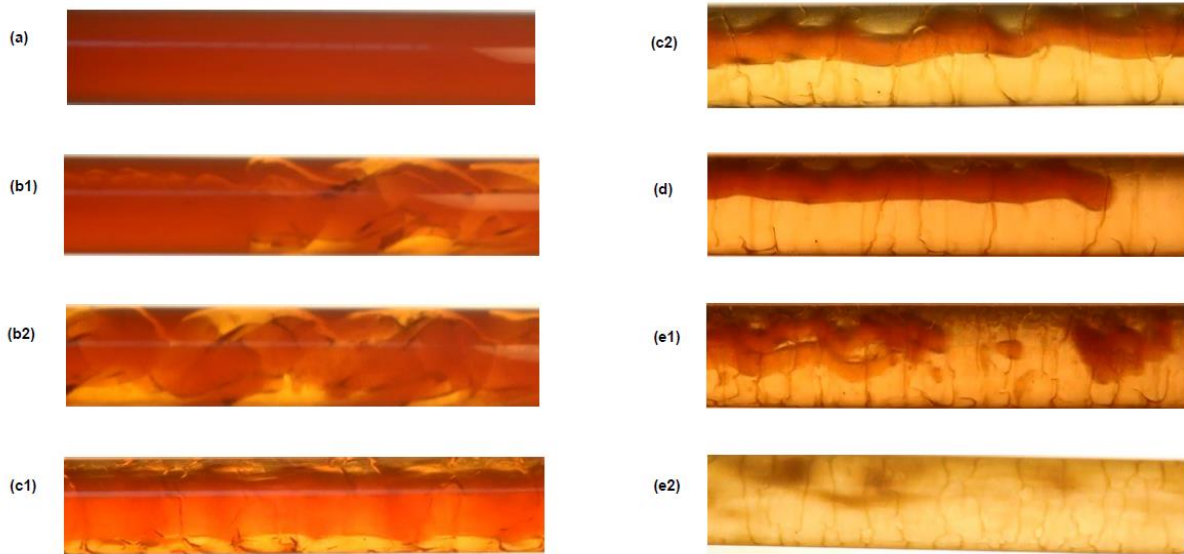
Figure 2-7 Visual inspection of different flow patterns for oil-water flow with oil viscosity of 3.3 Pa.s in a horizontal pipe with 25.4 mm internal diameter taken from Shi (2015). a) OC, b1 and b2) Inv, c1 and c2) CAF, d) OPL, e1 and e2 (OLP)

Pressure drop and holdup have been measured by means of sampling method. The results were compared to the theoretical models and empirical correlations in the literature survey. CFD analyses by using software Ansys Fluent were performed under different operating conditions, and pressure gradients, water holdup were extracted from simulation results. It is concluded that for high viscosity of oil-water, maximum relative errors between predicted pressure drop and measurements were observed to be 69%. Underestimation and overestimation of pressure drop predicted by CFD simulation were detected to be as a result of oil fouling at the pipe wall. When the pressure drop predicted by CFD is under predicted, little oil contact at the wall was observed in calculated configuration, while thin layer of oil has been seen in the experimental images. However, the water holdup calculated from CFD simulation showed satisfactory agreements with experimental QCV data.

(8) Department of Mechanical Engineering, National University Singapore

Recently, Loh and Premanadhan (2016) have published their work regarding oil-water flow in a horizontal 27.86 mm i.d. pipe. Light oil (viscosity 0.030 Pa·s) and heavy oil (viscosity 0.3 Pa·s) were used as test fluids. To study flow patterns of oil-water, high-resolution visualization techniques by means of a high speed camera was adopted. Pressure reduction factor as a function of oil input fraction was analyzed for both light and heavy oil. They realized that phase inversion phenomenon (replacing of one phase as continuous flow to another phase) for light oil can be achieved earlier than heavy oil. Moreover, heavy oils tended to remain dispersed in water with higher pressure reduction factor. As far as flow pattern is concerned, smooth stratified flow was not achieved for heavy oil-water flow in their experiments.

Brief reviews on core-annular flow of oil and water within horizontal and vertical pipe with constant diameter is provided by Ghosh et al. (2009). A summary of experimental studies on oil-water flows in horizontal pipe, with uniform cross-section area is listed in Table 2-1. The density of water is not reported because it is regarded as 998 kg/m^3.

Table 2-1 Summary of experimental studies on oil-water flows in horizontal pipe with uniform cross-sectional area

Author	Pipe I.D. (mm)	ρ_o (kg/m^3)	σ (N/m)	μ_o (Pa.s)	Velocity range (m/s)	Observed flow pattern [a]
Charles et al (1961)				0.00629-0.0168-0.065	J_o:0.015-0.94	CAF, I, D
	26	998	0.045		J_w:0.03-1.06	
Ooms et al (1984	50			2.3-3.3	J_o: ~1	CAF
	200	968	-	1.2-2.2	J_w:0.01-0.25	
Oliemans et al (1987)					J_o: 0.5-2.5	CAF
	50	968	-	3	J_w:0.03-0.6	
Arney et al (1993)				200-900	J_o: 0.14-1.16	CAF, I
	15.9	989	0.26	2.7	J_w:0.06-0.65	
Bannwart et al (2004)					J_o: 0.007-2.5	ST, CAF, I, D
	28.4	925.5	-	0.488	J_w:0.04-0.5	
Grassi et al (2008)					J_o: 0.03-0.7	ST, CAF, I, D
	21	886	0.05	0.8	J_w:0.2-2.5	
Sotgia et al (2008)					J_o: 0.1-1.0	ST, CAF, I, D
	21-40	889	0.02	0.9	J_w:0.1-2.51	
Shi (2015)		905			J_o: 0.04-0.54	OC, Inv, CAF, OPL,OLP
	25.4	910	0.02	3.3-16.0	J_w:0.01-1.8	
Loh and Premanadham (2016)	27.86	845	-	0.03	J_o: 0.05-2.0	ST, ST-wavy, Do/w & w, Do/w & Dw/o, ST+M, Do/w, Dw/o
		880-885		0.3	J_w:0.05-2.0	

a) Different nomenclatures were used by different researcher. The flow regimes included: ST (stratified flow), ST-wavy (stratified wavy), CAF (core-annular flow), I (intermittent flow such as slug/plug flows), D (dispersed flow of one phase in another phase), OC (oil continuous), Inv (inversion), OPL (oil plugs in water), OLP (dispersed oil lumps in water), Do/w & w (dispersed oil in water & water), Do/w & Dw/o (dispersed oil in water and dispersed water in oil), ST+M (stratified plus mixing), Do/w (dispersed oil in water), Dw/o (dispersed water in oil)

2.3 Previous studies on multiphase flow within horizontal pipe with variable cross-section area

2.3.1 Two-phase flow of gas-liquid through variable cross-section horizontal pipe

In the following section, a brief description of two-phase flow of gas-liquid within horizontal pipe, undergoing sudden expansion and contraction is presented. Delhaye (1981) developed a model to estimate the concentrated pressure drop for gas-liquid flow in the presence of sudden expansion, contraction, inserts and grids, tees and wyes, and manifolds, assuming steady-state flow. The momentum and mechanical energy equations were derived to take into account the effect of changing cross-sectional area, mass velocity, quality, and density of phases on the concentrated pressure drop. He concluded that the pressure increase computed by the momentum balance can fairly well predict experimental data in the presence of sudden expansion due to the fact that both reversible pressure increase (because of singularity) and irreversible pressure increase (because of viscous dissipation) have been considered. Wadle (1989) proposed a new equation for the pressure recovery in the presence of sudden expansion based on superficial velocities of two phases. The pressure recovery has been correlated to the difference in heads between downstream and upstream of singularity based on several assumptions, which included steady-state flow conditions, no pressure loss due to wall friction, incompressibility of fluids, no effect of gravity, constant mean quality, and pressure equilibrium between the phases. The developed model has been validated by means of experimental data of steam-water and air-water showing satisfactory agreements. Guglielmini et al. (1997) studied the structure of gas-liquid flow in both horizontal and vertical pipes in the presence of sudden contraction. The experimental concentrated pressure drop was collected from the literature survey and compared to the models and correlations in the previous studies. The concentrated pressure drop was obtained by extrapolation of the upstream and downstream axial pressure profiles. The results of

concentrated pressure drop are plotted against the gas volume fraction for the horizontal pipe showing two different behaviours: 1) monotonic behaviour in which the concentrated pressure drop increased by increasing gas volume fraction, and 2) anomalous behaviour in which the concentrated pressure drop went first through a maximum value and then through a minimum. They concluded that the maximum value of the concentrated pressure drop may refer to a transition from plug to slug flow. Abdelall et al. (2005) performed experimental tests using air and water flow in the horizontal tube, with the larger and smaller tube diameter of 1.6 mm and 0.84 mm, respectively. Concentrated pressure drop was measured in the presence of abrupt expansion and contraction. It is concluded that concentrated pressure drop was considerably lower than the prediction by homogeneous model, showing significant velocity slip at flow area change. Chen et al. (2007) conducted experiments on two-phase flow of gas-liquid, with horizontal tube made of transparent acrylic resin and expansion area ratio ranging from 0.26 to 0.39. The total mass flux was in range of 100-700 kg/m^2.s, while quality was varied from 0.001 to 0.8. The effects of area ratio, gas quality, and mass flow rate have been evaluated. Moreover, two-phase flow pattern upstream and downstream of sudden expansion were observed, showing a unique flow pattern 'liquid jet-like' flow pattern at very low quality. According to their findings, influence of this flow pattern avoids appreciable increase of pressure difference. The works by Ahmed et al. (2007) and Ahmed et al. (2008) may also be cited, considering oil-air flow in a 25.4 mm i.d. pipe, undergoing abrupt expansion with three area ratios, namely, 0.0625, 0.25 and 0.444. Superficial oil velocities ranged within the interval 0.02 $<J_o>$ 0.756 m·s^{-1}, while superficial gas velocities ranged within the interval 0.136 $<J_g>$ 3.75 ms^{-1}. The investigation included: pressure gradient upstream and downstream of singularity, flow patterns by means of high speed video camera, and measurement of cross-sectional void fraction by using double ring capacitance meter and a hot film anemometer.

2.3.2 A difficult journey from gas-liquid to liquid-liquid two-phase flow

Hewitt (1997) published a work on the main differences between gas-liquid and liquid-liquid flows in pipelines. Regarding flow patterns, the following general observations have been concluded:

- For both gas-liquid and liquid-liquid flows, stratified flow regime can be observed.

- Slug flow is a common flow regime in gas-liquid flows but rarely occurs in liquid-liquid flows.

- Complete dispersion of gas and liquid phase does not usually occur except under diabatic situations where hot channel walls prevent droplet contact to the wall. However, intedispersion of the liquid-liquid phase is possible over the whole range of phase fraction. Continuity of one phase depends mainly on a phenomenon so-called phase inversion in which maximum mixture viscosity can be achieved.

- Annular flow regimes often occurs in gas-liquid flows, especially at high void fraction but is rarely seen for liquid-liquid flow except for high viscosity and low density differences between the phases.

2.4 Previous experimental studies on liquid-liquid flows with variable cross-section area

Although variable cross-sectional area of pipelines is a common occurrence in cross-country transportation, a survey on the literature corresponding to oil-water flows reveals that most of the past investigations are related to the horizontal and vertical pipes with uniform cross-section. On the other hand, a few works dealt with gas-liquid flows across abrupt expansion and contraction. Regarding liquid-liquid flows through these pipe configurations, not much work is known, in spite of its importance in petroleum industry. In fact, we are able to find only four contributions, which are briefly explained in the following section.

One of the preliminary studies on oil-water mixture through sudden expansion and contraction was conducted by Hwang and Pal (1997). Mineral oil (μ_o=0.0027 Pa$^{.}$s and ρ_o=780 kg/m^3) and water is used as test fluids. The whole range of oil concentration (0-97.3 % volume oil) was tested. The emulsions were made of oil-in-water up to oil concentration of 64 vol.%, while above this concentration, the emulsions were water-in-oil type.

To form sudden expansion and contraction, two straight pipes of stainless steel, with an internal diameter of 20.37 and 41.24 mm were used. The pressure changes across sudden expansion and contraction were measured from extrapolating the distributed pressure profile downstream and

upstream of singular plane. They measured the frictional energy loss per unit mass as a function of concentrated pressure drop, mixture velocity, mixture density and area ratio as:

$$h_f = \frac{\Delta P}{\rho_m} \pm \frac{(\sigma^4 - 1) J_m^2}{2} = (k_1 \pm k_2).\frac{J_m^2}{2} \qquad (2\text{-}7)$$

Where h_f, ΔP, ρ_m, σ and J_m are frictional energy loss per unit mass, concentrated pressure drop, mixture density, diameter ratio, and mixture superficial velocity. The schematic of pressure profiles for sudden expansion and contraction is depicted in Figure 2-8. Figure 2-9 shows the results of loss coefficient ($k_e = k_1 \pm k_2$) as a function of oil concentration for expansion and contraction. The experimental values of loss coefficients were compared to Borda-Carnot (see Perry and Green, 1984), equation (2-8), and Wadle (1989), equation (2-9), for expansion, and McCabe et al. (1993) correlation, equation (2-10), for contraction. It is worth noting that these correlations have been originally developed for gas-liquid flows.

$$k_e = (1 - \beta)^2 \qquad (2\text{-}8)$$

$$k_e = 2\beta (1 - \beta) \qquad (2\text{-}9)$$

$$k_e = 0.4 (1 - \beta) \qquad (2\text{-}10)$$

Where, β is the cross-sectional area ratio of small pipe to the larger pipe.

a)   b)
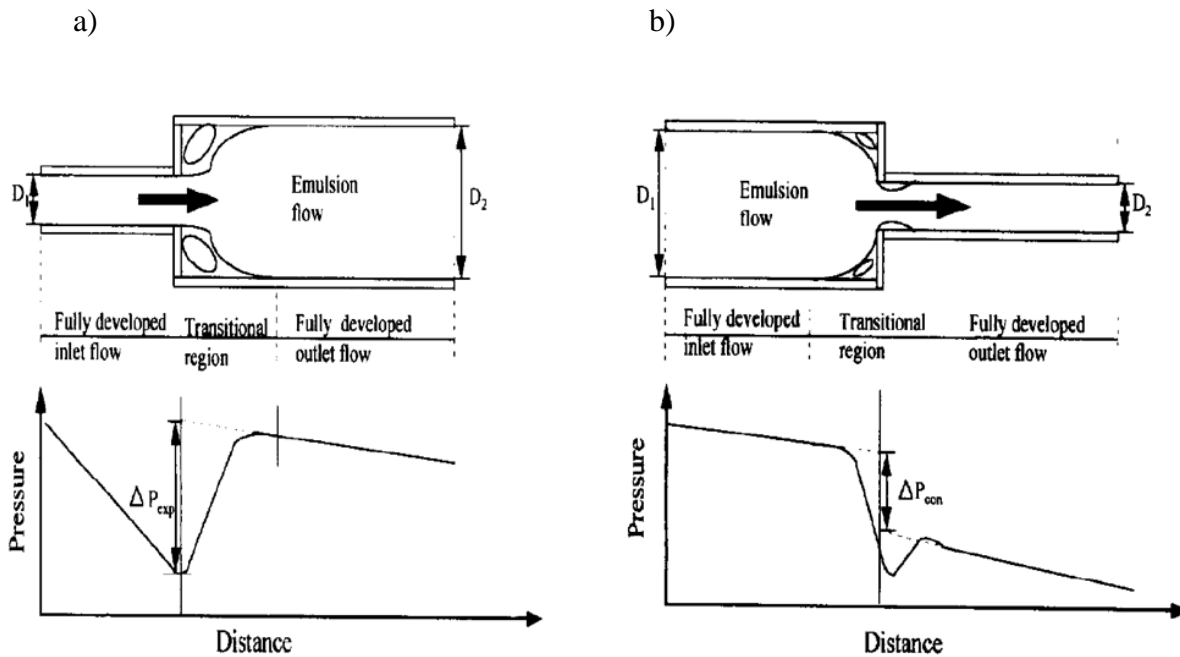
Figure 2.8 Schematic of pressure profiles taken from Hwang and Pal (1997) for a) sudden expansion and b) sudden contraction
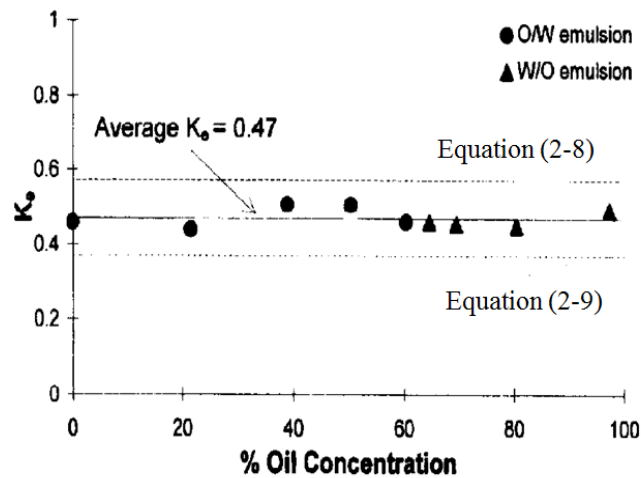
Figure 2-9. Expansion loss coefficient versus oil concentration taken from Hwang and Pal (1997)

Figure 2-9 shows that the expansion loss coefficient is independent on oil concentration, type of emulsion, and found to be 0.47 for expansion. The average contraction loss coefficient showed the same behavior and measured to be 0.54.

Balakhrisna et al. (2010) carried out experimental tests on oil-water in a 7 m horizontal tube. The experimental setup was composed of two test sections, namely T_1 and T_2. The ducts present sudden contraction from 0.025 m to 0.012 m (T_1) and a sudden expansion from 0.012 m to 0.025 m (T_2). Hence, for both cases the ratio of the cross-sectional areas of smaller to larger pipe was selected to be 0.23. Two types of oil have been selected, namely, lube oil (viscosity 0.2 Pa·s and density 960 kg/m^3) and kerosene (viscosity 0.0012 Pa·s and density of 787 kg/m^3). The focus of study was to investigate the influence of these changes in cross-sectional areas on phase distribution and pressure drop. Figure 2-10 and 2-11 illustrate the phase distribution of lube oil-water, undergoing abrupt contraction and expansion, respectively. The following conclusions can be drawn from flow patterns for expansion and contraction cases:

- The presence of sudden expansion causes thickening of oil core for lube oil at downstream pipe. This technique can increase the stability of core-annular flow. However, care must be taken while establishing core-annular flow because the risk of oil fouling increases at downstream pipe of sudden expansion.
- The thickness of oil core can be reduced in the presence of sudden contraction at downstream of singularity. Hence, the chances of oil fouling would be reduced.
- The flow patterns of oil and water both upstream and downstream of singularity is significantly influenced by rheological properties of oil phases. Higher viscous oil tends to form different types of core-annular flow, while kerosene, characterized by lower viscosity, has a tendency to exhibit a wider variety of distribution in water.
- Different types of core-annular flow patterns were observed for lube oil-water, which included thick and thin core, and sinuous core for both cases of expansion and contraction.
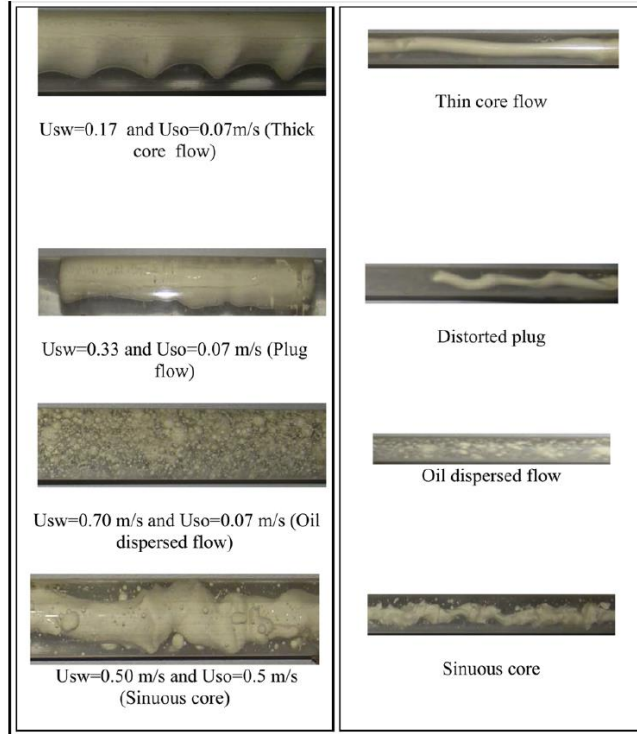
Figure 2-10 Images of flow patterns for lube oil in sudden contraction taken from Balakhrisna et al. (2010)
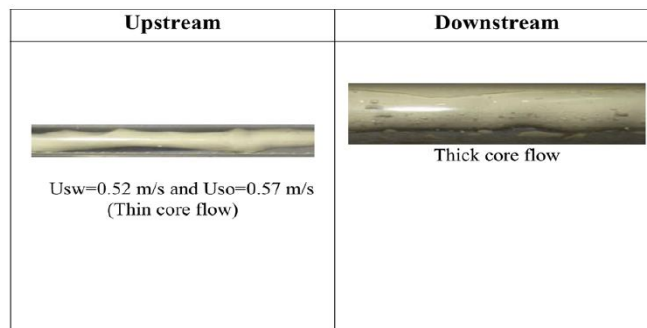
Figure 2-11 Images of flow pattern for lube oil in sudden expansion taken from Balakhrisna et al (2010)

The expansion and contraction loss coefficients were also measured, taking into account the same procedure as was performed by Hwang and Pal (1997). The result of loss coefficients as a function of mixture superficial velocity for a) contraction and b) expansion are presented in Figure 2-12.
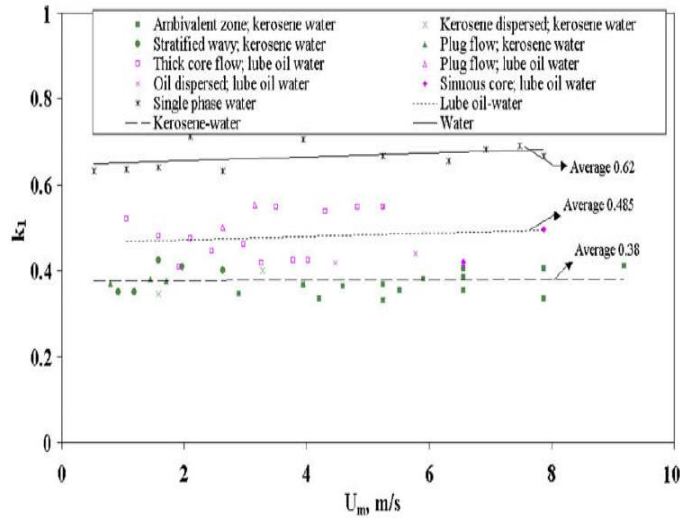
Figure 2-12 Contraction loss coefficients taken from Balakhrisna et al (2010)
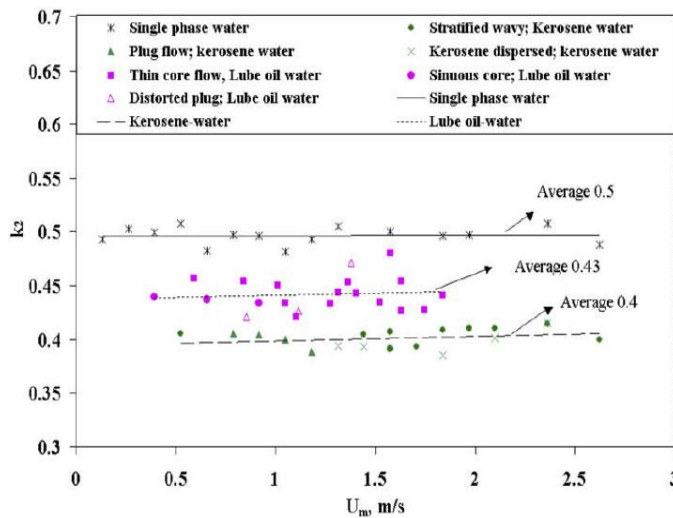
Figure 2-13 Expansion loss coefficients taken from Balakhrisna et al (2010)

By a close observation, one may realize that the loss coefficient for both types of oil is independent on flow regimes. Furthermore, the loss coefficient for oil-water was found to be lower than loss coefficient for only water flowing through the same test rig.

The only study conducted on very viscous oil-water in the presence of sudden contraction was performed by Colombo et al. (2015). The ducts underwent abrupt contractions from 50 mm to 40 mm i.d. and from 50 mm to 30 mm i.d., with contraction ratios of 0.64 and 0.36, respectively. The mineral oil (viscosity 0.838 Pa·s at $20\,^\circ C$; density:890 kg/m^3) and tap water were used as test

fluids. The in-situ oil fraction (holdup) was measured by means of quick closing valve technique downstream of singularity, and experimental data were compared with the prediction of Arney et al. (1993). The major flow regimes under investigation were dispersed and core-annular flow. Figure 2-14 depicts the measured oil holdup as a function of oil input volume fraction.

a)   b)
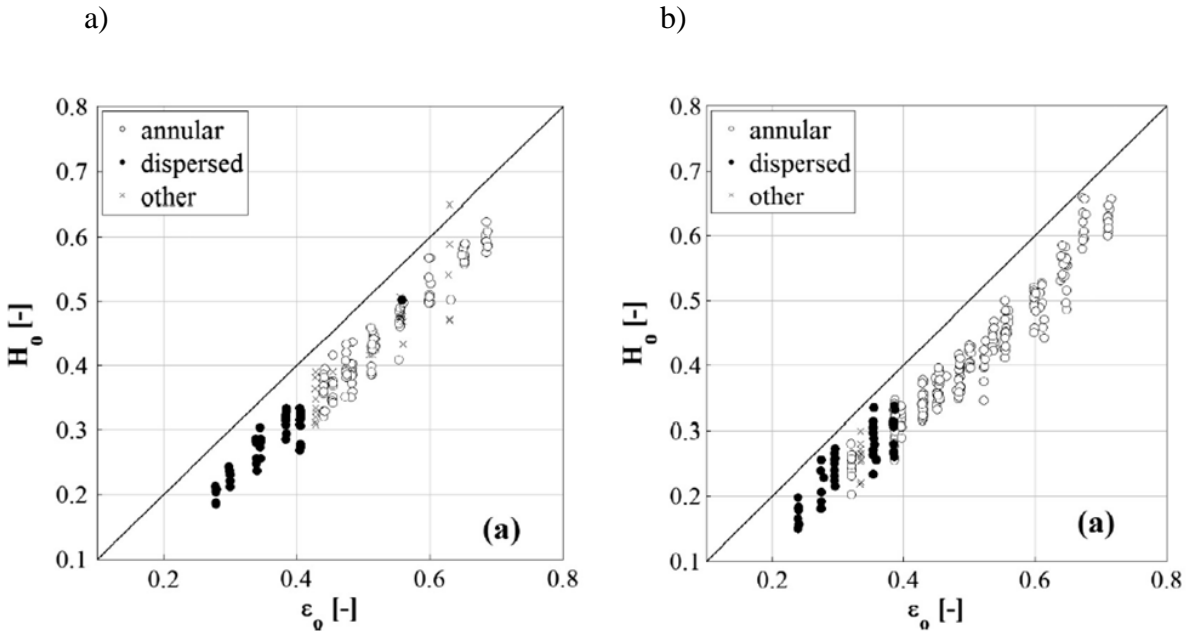
Figure 2-14 Measured oil holdup by quick closing valve technique as a function of oil input volume fraction for contraction area ratio taken from Colombo et al. (2015); a) β=0.64, b) β=0.36

As it is evident from Figure 2-14, two-phase flow of very viscous oil-water cannot be considered as pseudo-homogeneous flow because all data except one falls below bisector (homogeneous line). It is also shown that the oil holdup is lower than oil input volume fraction, suggesting that effective oil velocity is greater for oil than water or, in other words, slip ratio is larger than unity. Comparison of measured oil holdup and prediction by Arney et al (1993) correlation are shown in parity plot, Figure 2-15, for both cases of contraction ratios.

a)   b)
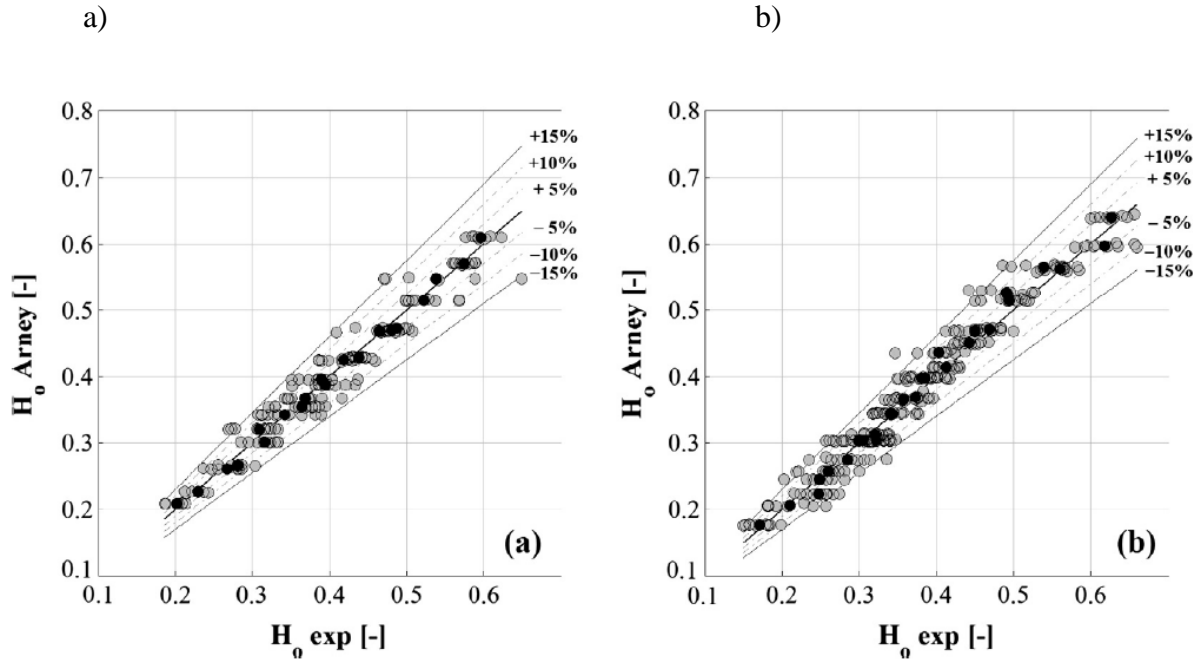
Figure 2-15 Comparison of measured oil holdup and correlation by Arney et al (1993) for contraction ratios of a) β=0.64, b) β=0.36. The data are taken from Colombo et al (2015)

According to Figure 2-15, the average relative error between holdup measurements and prediction by Arney et al (1993) correlation were found to be 5.15% for β=0.64 and 5.88% for β=0.36. They concluded that the higher deviation in the latter case may be due to vigorous influence of sudden contraction at downstream pipe. The summary of experimental studies on oil-water flows, undergoing sudden expansion and contraction is listed in Table 2-2.

Table 2-2 Summary of experimental investigations on oil-water flows through singularity

Author	Pipe configuration	β (-)	ρ_o (kg/m^3)	μ_o (Pa.s)	Velocity range (m/s)	Observed flow pattern	Experimental measurement
Hwang and Pal (1997)	Sudden expansion & contraction	0.24	780	0.0027	Not reported	Emulsion (w/o) and (o/w)	Concentrated pressure drop, loss coefficient
Balakhrisna et al. (2010)	Sudden expansion & contraction	0.23	787	0.0012	J_o & J_w	Thick, thin, sinuous core, oil dispersed, plug flow	Concentrated pressure drop, loss coefficient
			960	0.2	Up to 2.5		
Colombo et al. (2015)	Sudden contraction	0.36			J_o:0.43-1.48		
		0.64	890	0.838	J_w:0.34-2.37	D, EAD, EA, S	Holdup

a) The nomenclature used in the work by Colombo et al (2015) regarding flow patterns includes: D) dispersed flow, EAD) eccentric annular with big drops, EA) eccentric annular, S) stratified (oil contact at the wall)

Comparison of Table 2-1 and 2-2 clearly show that experimental data corresponding to liquid-liquid flows through sudden expansion and contraction is still lacking.

2.5 Multiphase flow measurements

Understanding the characteristic behavior of oil-water flows within horizontal pipes with variable cross-sectional area is essential to study such a phenomenon in multiphase flow devices, especially in all types of differential pressure measurement tools, where changing in cross-sectional area of pipe occurs. The objective of the two-phase flow measurement is to determine the volume flow rates of the phases within a duct. In addition to detection of flow rate, other fundamental parameters of flow, such as phase void fraction, interfacial area, etc are crucially

important. Finding a single instrument which is capable of measuring all characterization of flow is almost impossible. Several combinations of instruments can be made, which highly depends on whether or not the phases can be fully mixed (homogeneous behavior) upstream of instrument. If homogeneity of flow is assured, the number of instruments is reduced otherwise individual phase fraction and velocities of phases have to be measured. In the following section, multiphase flow instruments are classified based on the physical principle of each device and parameter that can be measured.

2.5.1 Instrument classification

Good reviews on the multiphase flow instrumentations have been written by Baker (2000), Falcone et al. (2009) and Bertani et al (2010). The following main categories for multiphase flow measurements can be considered:

- In-line measurement
- Separation phase measurement
    - Full two phase flow separation
    - Partial separation
    - Separation in sample line

In-line measurement meters do not require separation or sampling of fluids in the multiphase flow line. The volume flow rate of each phase can be estimated by multiplication of velocity of each phase and area fraction. Tables 2-3 and 2-4 show the classification of multiphase instruments based on their physical principles and measured flow parameters.

Table 2-3 classification of multiphase flow meter based on physical principle

Measurement physical principle
Mechanical
Hydraulic
Acoustic
Electrical
Gamma and X-ray
Neutrons
Microwave attenuation
Infrared spectroscopy

Table 2-4 classification of multiphase flow instrument based on measured flow parameters

Measurements of phase fraction	**Measurements of density**
Gamma-ray absorption	Gamma-ray absorption
Neutron interrogation	Neutron interrogation
Optical sensors	Hot film anemometer
Quick-closing valve	Ultrasonic flow meter
Capacitance/Conductance probes	Capacitance/Conductance probes

Table 2-4 (Continued)

Measurements of velocity	Measurements of mass flow
Pulsed-neutron activation	Differential pressure flow meters
Electromagnetic flow meter	True mass flow meter
Turbine flow meter	Vibrating tube
Gamma-ray cross correlation	Measurement of momentum flux
Neutron cross correlation	Drag disk
Acoustic cross correlation	
Capacitance/conductivity sensors cross correlation	
Lase Doppler velocimeter	

2.5.2 General selection factors for multiphase flow measurements

There are several selection factors that need to be taken into account when dealing with multiphase flow measurements. Different flow meters are designed for different operating conditions. Moreover, the response of meters is significantly dependent on the flow pattern, upstream configuration of pipe, and flow history. The parameters that need to be considered to include: process conditions, accuracy, fluid compatibility, pipe size/configuration and maintenance need. In high pressure application, a phenomenon so-called fluid hammer can considerably damage conventional flow meters. Fluid hammer is a pressure wave caused by kinetic energy of a fluid when it is forced to stop or change direction. Hence, flow meters should be able to respond immediately to this phenomenon. Accuracy of flow meters is crucial for situation where batching, sampling of fluids is required. To examine the accuracy of the measurement devices, the whole acquisition system should be considered, which includes: the information corresponding to the fluid, transformation of the information through sensor, and

conversion of the extracted information from analogical to digital electric signal. Care must be taken because at each step, a degree of distortion and noise is introduced, which must be minimized. The relative magnitude of instrumental length scale (pipe diameter for Venturi flow meter, probe plate area for impedance probe, etc.) compared to the length scale of low objects (drop or bubble diameter, film thickness, etc.) can significantly affect the information provided by each measurement devices. Fluid compatibility of measurement devices is also an important factor. Flow meter manufacturers have invested so much time and resources to develop devices with thermoplastic materials, which are capable of handling corrosive liquid and gas. Regarding pipe size and configuration, it is worth noting that almost all measurement flow meters need a sufficient straight tube upstream and downstream of devices to ensure fully developed flow. Furthermore, Elbows, reducers, injectors, valves can cause significant radial and tangential swirling effects, which result in reducing the accuracy and repeatability of devices. Generally, multiphase measurement devices with no moving parts are less problematic than complex devices and require less attention. Two major problems arise from measurement devices with moving parts, which include: problems regarding to lubrication, wearing and coating, and necessity to have clearance spaces. The latter often introduce additional slippage to the fluids.

Measurement devices can be either non-intrusive (external to the flow field), or intrusive (internal to the flow field which causes distortion to the flow geometry). The intrusive flow meters may significantly change the flow regime. By considering all the limits and drawbacks of flow meters, the only devices which are able to operate in different operating conditions are, see Monni (2013):

- Drag Disk
- Turbine Flow Meter
- Venturi Flow Meter
- Impedance Probes

Since one of the objectives of current work is to develop multiphase measurement devices for very viscous oil-water flows by means of differential pressure devices, we only focus on these types of tools. In the following section, configuration and theory of differential devices would be introduced.

2.5.3 Differential pressure meters

The measurement of fluid flow rate is detected by reading pressure loss across a tube restriction, and it is a widely used flow measurement technique for industrial applications. Different configuration for flow measurement devices can be considered, including Venturi Flow Meter (VFM), Nozzle Flow Meter (NFM), Orifice Plate (OP), etc. In this section, general characteristics and performance for VFM is reported.

The classical Herschel Venturi (Figure 2-16) is composed of three sections, which include two conics at the inlet and outlet joined with a horizontal tube so-called throat section (downstream). The throat section has the minimum cross-sectional area, minimum pressure and maximum velocity in the meter. The converging cone can be designed with 15° to 20° angle, while diverging cone has the angle from 5° to 7° which completes transition back to full tube diameter. The static pressure can be measured at upstream and throat section. The pressure taps are installed (1/4 to 1/2 pipe diameter upstream of converging cone and in the middle of throat section), giving an average pressure reading over the entire circumference of the elements.
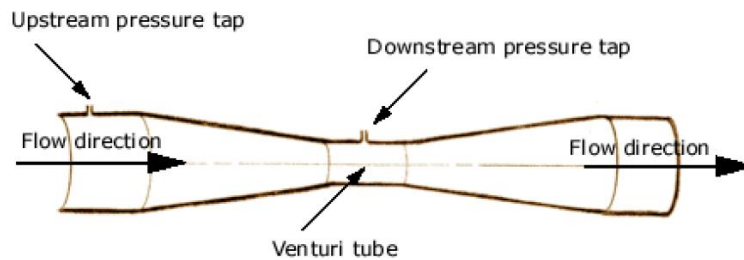
Figure 2-16 Schematic of classical Venturi Flow Meter (VFM)
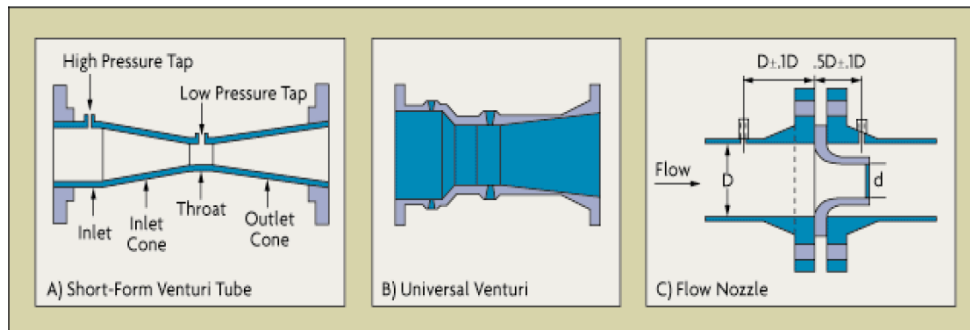
Figure 2-17 Schematic of different types of VFM and Nozzle Flow Meter (NFM)

In short-form Venturi meter, the entrance angle is increased, and the annular champers are replaced by pipe taps, see Figure 2-17-A. The short-form Venturi meter is superior over classical Venturi flow meter because of reduced initial cost, reduced weight, and shorter length. Another type of VFM is so-called universal Venturi, which provides better pressure recovery than classical Venturi flow meter, see Figure 2-17-B. They all have short lay length, normally varying between 2 to 4 pipe diameters. From economic point of view, they cost less than classical Venturi tube due to reduced length. Nozzle flow meters (Figure 2-17-C) have a similar configuration to Venturi flow meters. The only difference is that they encounter an abrupt expansion after throat section. As compared to VFM, they require lower investment and provide less pressure recovery. Due to gradual decrease and increase of cross-sectional area for the case of VFM, the frictional loss is quite small. Therefore, the value of discharge coefficient, C_d, for VFM is almost unity. Furthermore, VFMs are less sensitive to the influence of velocity profile and require less straight pipe run than Orifices. Typical discharge coefficient values for VFM range from 0.95 to 0.995 in single phase liquid flow. VFMs are available in sizes up to 1.8 m (72 inches), and provide 25% to 50% more flow than orifice at the same pressure drop, see Figure 2-18.
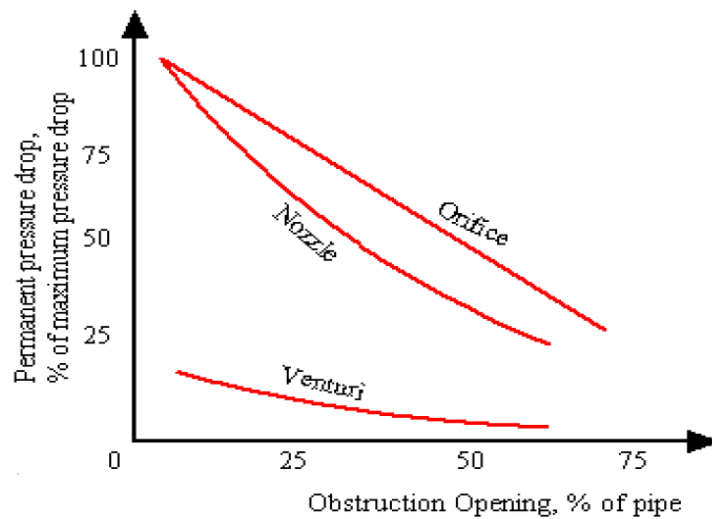
Figure 2-18 Permanent pressure drop for different flow meters, taken from Monni (2013)

2.5.4 Theory of differential pressure flow meters for single-phase flow

According to Bernoulli's equation, the static energy can be linked to kinetic energy in a flowing stream. For the general Differential Flow Meter, the equation can be written as:

$$Q = C_d A_2 \left(\frac{2\Delta p \rho}{(1-\zeta^4)} \right)^{0.5} \tag{2-11}$$

Where Q is mass flow rate, C_d discharge coefficient for the particular flow meter, Δp differential pressure between upstream tube (1) and throat section (2), the throat cross-sectional area is A_2, and ζ is the diameter ratio D_2/D_1.

If also compressibility and thermal expansion influences are included the equation becomes (Oliviera, 2009):

$$Q = C_d A_2 \left(\frac{2\Delta p \rho}{(1-\zeta^4)} \right)^{0.5} \cdot F_a \cdot Y \tag{2-12}$$

Where F_a and Y are thermal expansion factor and compressibility coefficients, respectively. Different numerical values for both coefficients can be achieved based upon experimental data for different flow measurement devices. These numerical values are tabulated in standard regulations, such as ISO, the American National Standard Institute (ANSI), the American Society of Mechanical Engineers (ASME), and the American Petroleum Institute (API). For liquids (incompressible fluids), F_a=1 and for gases (compressible fluids), $F_a > 1$. The discharge coefficient C_d correlates actual to ideal flow rates to account for the effects of turbulence and flow separation. Therefore it is usually related to the Reynolds number. The numerical values of discharge coefficients are tabulated in ISO5167-4 (2003). By using these published values, it is feasible to calculate accurate flow measurement with uncertainties, varying from 0.5% to 3% for single phase flow. The relationship between flow and pressure depends upon the velocity profile (whether the flow is laminar or turbulent), which ultimately relates to Reynolds Number (Re). When the Reynolds number is less than 2300, the flow is considered as laminar, while for Re>2300, the flow is turbulent. For sufficiently large Reynolds Number (Re>2$\times$ 10^5), discharge coefficient C_d tends to have the numerical value close to unity. On the other hand, discharge coefficient is significantly reduced as Reynolds number decreases.

Much attention is required to design a flow meter in operating conditions where high pressure and temperature occurs because changes in operating conditions can tremendously influence on density of a fluid, especially in single phase gas flow, which result in the erroneous flow measurement. In chapter 6, we would develop the required equations to be used in multiphase flow measurement devices based on theory of Bernoulli.

2.5.5 State of the art of two phase flow measurements

Both experimental and numerical studies about flows through measuring devices can be found in the literature, but the majority of them are related to gas-liquid flows, and particularly to the so-called "wet-gas", i.e. the flow of low-mass flow rate of liquid in gas main stream. As significant examples, the papers by Chisholm (1967), De Leeuw (1997) and Oliveira et al. (2009) can be cited. Chisholm (1967) developed a model to estimate concentrated pressure drop across orifices during incompressible two-phase flow mixtures. Concentrated pressure from the upstream tube to the throat section is correlated to the mass flow rate of mixture by a Lockhart-Martinelli parameter. The work by De Leeuw (1997) deals with two-phase flows of gas-liquid through a Venturi meter, developing an empirical correlation that shows dependence of the mass flow rate of mixture on the gas Froude number. The relative error to compute the mass flow rate of mixture between predictions by the correlation and experimental data is less than 2%. Oliveira et al. (2009) measured mass flow rates related to wet gas flows using a resistive void fraction meter and a Venturi/Orifice plate meter. Upward vertical and horizontal pipes were considered for this purpose, including bubbly, annular, churn and slug flow regimes. The duct inclination, and therefore, gravity, is found to exert a negligible influence on the frictional pressure, and a slip ratio lower than 1.1 is predicted for bubbly and slug flow regime. Additional references to works dealing with gas-liquid flows across a Venturi meter can be found in the paper by Jana et al. (2008).

Concerning liquid-liquid flows, which will be the subject of the present work through measuring devices, there are fewer papers and information is still partially lacking. The work by Pal (1993) deals with the application of the Venturi and Orifice flow meters to monitor the flow rate of water/oil emulsion in presence of surfactant.

Oil concentration varied over a wide range of 0-84.32 vol%. They developed an empirical correlation based on their experimental data for discharge coefficient of the Venturi and Orifice

flow meters. Skea and Hall (1999) evaluated oil-water flows in single-phase flow meters, considering water-in-oil and oil-in-water emulsions. Water with oil (kinematic viscosity = $1 \cdot 10^{-5}$ m^2/s at 50 °C) fraction up to 15% and oil with water fraction up to 15% have been considered. Different devices were tested including 50.8 mm (2-inch) and 101.6 mm (4-inch) positive displacement meters, turbine and Venturi meters. Single phase flow meters turned out to be suitable for oil-water emulsions, showing a maximum error within 1% of the reference total volume flow rate. Oddie and Pearson (2004) reviewed the most important techniques for gas-liquid, gas-solid, liquid-solid and liquid-liquid flows to measure mixture flow rates by means of combinations of multiphase flow devices for both horizontal and vertical pipes. They emphasized the importance of the flow regime to select an appropriate multiphase flow meter. The work by Li et al. (2009) deals with development of a hybrid flow meter for measurement of oil-water two-phase flow. Three Venturi meters and three oval gear flow meters were introduced for this purpose. Three pipe diameters equal to 15 mm, 25 mm and 40 mm were selected to measure the total flow rate ranging from 1.2 m^3h^{-1} to 5.5 m^3h^{-1}. Tap water and diesel oil with density 847.95 $kg \cdot m^{-3}$ were used. Different throat/inlet area ratios were tested, namely, 0.74 for the 15 mm i.d. tube, 0.68 for the 25 mm i.d. tube and 0.58 for the 40 mm i.d. tube. Mass flow rate is correlated to two-phase concentrated pressure drop (between upstream pipe and throat section) by a coefficient k, which is referred to the calibration coefficient of the Venturi meter. Thus, two calibration coefficients k_{water} and k_{oil} are defined, whose numerical values are obtained based on single phase flows. k_{water} is slightly different from k_{oil}, with the difference more significant for low volume flow rates. The conclusion is that when oil fraction is less than 40%, k_{water} must be used. On the contrary, in flow conditions associated with oil fraction higher than 60%, k_{oil} has to be considered. An average calibration coefficient is selected for oil fraction between 40% and 60%. It is worth noting that both oil fraction and selection of calibration coefficient have a considerable influence on the results. Tan and Dong (2010) proposed a new correlation to take into account the effect of oil viscosity of water-oil through a V-cone multiphase flow meter. Superficial oil and water velocities were varied in the ranges of 0-3.6 $m \cdot s^{-1}$ and 0.63-1.69 $m \cdot s^{-1}$, respectively. A low-viscosity oil was selected and the flow regimes were emulsion oil/water and emulsion water/oil. A comparison of experimental data to homogeneous and separated flow models were performed, evidencing that the total mass flow rate predicted by

the homogeneous model shows a lower root mean square (RMS) deviation as compared to the separated model, which seems consistent with the flow structures.

The above literature reveals that detailed information about core-annular flow of high viscous oil-water through VFM and NFM measuring devices is lacking.

The results of experimental and CFD analyses of two-phase flows of very viscous oil-water are reported in Chapter 6 and 7, respectively. Hence, the aim of this part of present research is double. The first aim is to investigate if two-phase CFD analysis, validated through a comparison to experimental data, can be a reliable tool to investigate VFMs and NFMs and offer significant insight about the behavior of high viscous oil-water flows in such devices. If so, CFD would be candidate as a valuable engineering tool for the design and use of these devices in all those situations, quite common in the oil and gas fields, where experiments may be too complex or time consuming. The second aim is to assess the performance of VFMs and NFMs in the prediction of the flow rates of high viscous oil-water mixture in core annular Flow.

2.6 Literature survey on three phase flows of gas-oil-water

Since very few experimental data have been presented in the literature, the last objective of the present study is to expand the data related to pressure drop measurements. Hydrodynamic behavior of high viscous oil-water-gas flow and slug characteristics in horizontal pipe is not well understood. Thus, there is still a room for improvement and three-phase flow of high viscous oil-water-gas is in order. First, we present previous studies on low viscosity oil-water-gas flows, then, I introduce some of the most important investigations regarding high viscous oil-water-gas flows. The results of experimental campaign on very viscous oil-water-air would be presented in Chapter 8.

2.6.1 Experimental investigations on low viscosity oil-water-gas flows

The presence of oil, water and gas frequently occurs during depletion of conventional oil reservoirs. Thus, understanding of three-phase flows of oil, water and gas is crucially important for production and transportation systems.

As an example of three-phase flows, the work by Acikgoz et al. (1992) can be cited, which deals with the identification of low viscosity oil/water and gas flow patterns in horizontal pipe with the diameter 19 mm. They used low oil viscosity μ_o=0.116 Pa·s and density of 864 kg/m^3. Very low

superficial oil velocity (J_o=0.24 m/s), superficial water velocity (J_w=0.66 m/s), and high superficial gas velocity (up to 50 m/s) were used. Many different flow patterns were classified depending on the fact that flow is water-based (water is continuous) or oil-based (oil is continuous). Series of research activities have been conducted at the test facilities (WASP) at Imperial College, London. The work by Pan et al. (1995) deals with oil/water/gas three-phase flowing in a 76.2 mm i.d and 38.0 m long horizontal pipe. The tests were performed at 0.5 MPa test facilities, and operating conditions were similar to Acikgoz et al. (1992). Hewitt (2005) conducted three-phase flow tests with oil viscosity of 0.04 Pa·s and high flash point oil. The pressure drop and liquid phase holdups by means of a dual-energy gamma densitometer were measured. Two different behaviors were observed from the analysis of pressure drop measurement depending on gas flow rates. At high gas flow rate, a peak at the pressure drop was detected showing the inversion phenomenon in which continuous liquid phase changes from water to oil and effective viscosity is so high that it increases pressure drop, see also the works by Hall (1992) and Odozi (2000) . On the other hand, at low gas velocity, the peak of pressure drop was not observed. Keskin et al. (2007) suggested a two-step classification technique. Twelve individual flow patterns were identified in horizontal pipe, considering very low oil viscosity. Malinowsky (1975) tested slug flow experiments with very low viscosity (μ_o=4-5 mPa·s), internal diameter of 38.1 mm, and operating pressure of 2 bar. Superficial velocity of water, oil and gas ranged, respectively, within the intervals as follows: 0.19<J_w<2.08 m/s, 0.26<J_o<1.36 m/s, and 1.5<J_g<4.3 m/s. The major flow pattern under investigation was slug flow, with a few tests corresponding to high gas flow rates in which misty annular and slug were observed. He compared pressure drop measurement to classical correlation of Beggs and Brill (1973), which is widely used in oil industry, assuming that oil-water mixture had a viscosity following linear interpolation. Finally, He concluded that linear approximation for mixture viscosity of oil-water is a poor representation due to the fact that pressure drop predictions are highly under predicted his measurements by up to 50%. Stapelberg and Mewes (1994) measured pressure drop and slug frequency using a laser, with oil viscosity and density of 0.031 Pa·s and 886 kg/m^3, respectively. The tests were investigated in two different pipe diameters as 23.8 and 59 mm. Flow patterns were also detected, and flow maps developed.

2.6.2 Experimental investigations on high viscosity oil-water-gas flows

Multiphase flows of high viscous oil/water/gas behave completely different from flows of low viscous oil/water/gas. The main reason arises from the rheological property of oil phase, and special care must be taken to model the former fluid flow. In spite of importance of high viscous oil/water/ gas flows in oil industry, a few studies have been conducted in horizontal pipe.

Poesio et al. (2009) studied the flow of gas, water, and oil with two viscosities of 0.9 and 1.2 Pa.s at room temperature. Different pipe diameters were tested, including 21 mm, 28 mm and 40 mm i.d. Flow pattern under investigation was air bubble. Oil, water and air superficial velocities are in the ranges of J_o=0.46-1.08 m/s, J_w=0.04-0.67 m/s, and J_g=0.06-4 m/s. The pressure drop was measured 6 m downstream of injector. They developed a hybrid model which computes overall pressure drop based on Lockhart-Martinelli model and the results of comparisons between pressure drop predictions and measurements showed fairly good agreements. The work by Bannwart (2009) may also be cited, considering very viscous oil-air-water flows (μ_o=3.4 Pa.s and ρ_o=970 kg/m^3 at 20 ℃) in a 28.4 mm i.d. pipe (Laboratory scale) and a 77 mm i.d. pipe (full-scale facility). The tests were performed both in horizontal and upward vertical pipes, and the influence of inclination angle on three-phase flow pattern was investigated. Nine flow patterns were identified in horizontal pipe which are Bubble gas-Bubble oil (B_g, B_o), Bubble gas-Annular oil (B_g,A_o), Bubble gas-Intermittent oil (B_g,I_o), Bubble gas-Stratified oil (B_g,S_o), Intermittent gas-Bubble oil (I_g,B_o), Intermittent gas-Annular oil (I_g,A_o), Intermittent gas-Intermittent oil (I_g,I_o), Stratified gas-Bubble oil (S_g,B_o), Stratified gas-Stratified oil (S_g,S_o).

Oil, water and gas superficial velocities were in the ranges of J_o=0.01-2.5 m/s, J_w=0.04-0.5 m/s, and J_g=0.03-10 m/s. They measured pressure drop data and concluded that presence of gas phase has positive effect on increasing frictional pressure loss. Pressure drop was found to be highly dependent on superficial velocity of phases. The pressure drop increase caused by gas injection can be damped by increase of water, promoting the lubrication process and help preventing oil from sticking to the pipe wall. Wang et al. (2013) carried out oil-water-gas experiments with much lower oil viscosity (μ_o=0.15-0.57 Pa.s at 37.8-15.6℃). The internal pipe diameter is 52.5 mm, superficial water and oil velocities varied from 0.1-1 m/s, and gas superficial velocity ranged 1-5 m/s. The flow patterns were observed and images recorded by means of a high speed

video camera. The experimental pressure drop were compared to the model developed by Zhang and Sarica (2006), showing unsatisfactory agreements.

3. Experimental Setup and Procedure

3.1 Introduction

Experimental tests on multiphase flow of liquid-liquid and gas-liquid-liquid flows have been conducted in Multiphase Flow Laboratory at department of Energy in the Department of Energy, at Politecnico di Milano.

This chapter first describes the whole experimental facilities introduced in section 3.2, followed by experimental procedures for both liquid-liquid and liquid-liquid-gas in section 3.3. Experimental operating conditions are presented in section 3.4.

3.2 Experimental setup

The experimental facility is illustrated in Figure 3-1. The experimental setup is designed to be used for different pipe configurations and different combinations of fluid flows, which includes oil-water, oil-air, water-air, oil-water-air. Single phase water, oil and air pass through a coaxial mixture, before being introduced into a horizontal test line.

Figure 3-1. Snapshot of the experimental setup

In Figure 3-1, fluids flow from the right to the left direction, then, they are collected in a separation tank. Here the fluids are separated by gravity, owing to their density difference. Then, the two fluids are pumped back to their respective tanks. Figure 3-2 shows the schematic representation of experimental loop.
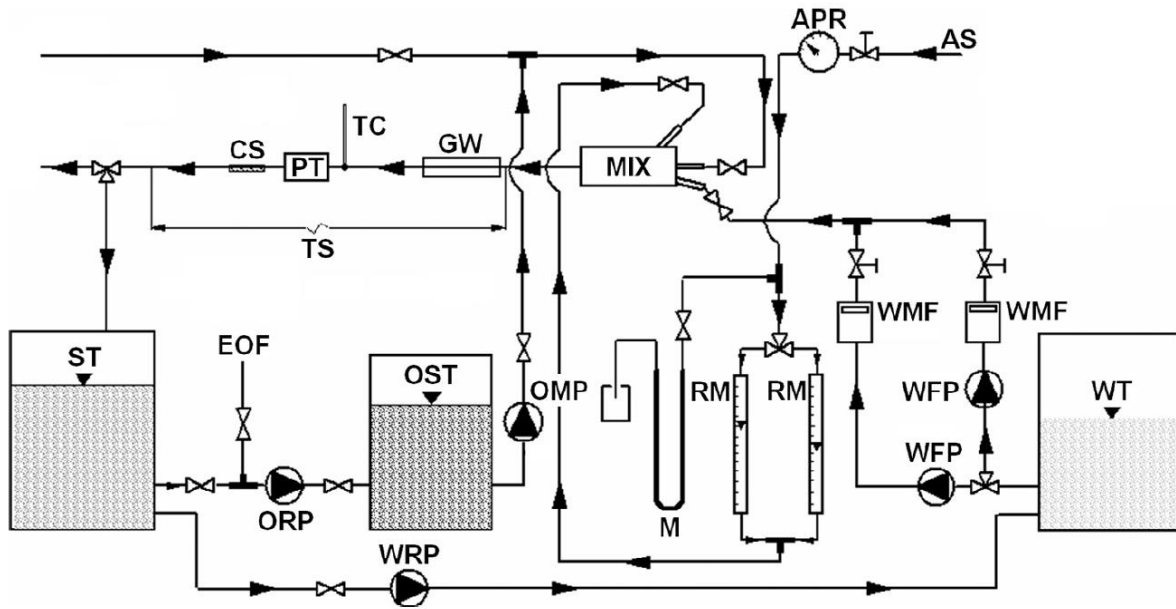
Figure 3-2. Schematic representation of the experimental multiphase loop

The abbreviations mean respectively:

- ➤ APR = Air Pressure Regulation
- ➤ AS = Air Supplying line
- ➤ CS = Capacitance Sensor
- ➤ EOF = External Oil Feeding
- ➤ GW = Glass Window
- ➤ M = Manometer
- ➤ MIX = phase inlet Mixer
- ➤ OMP = Oil Metering Pump
- ➤ ORP = Oil Recovering Pump
- ➤ OST = Oil Supply Tank (0.5 m^3)
- ➤ PT = Pressure Transducer
- ➤ RM = Variable area flow meter
- ➤ ST = phase collector/separator tank (1.0 m^3)
- ➤ TC = thermocouple (K-type)
- ➤ TS = Test Section
- ➤ WFP = Water Feeding Pump

47

- ➢ WMF = Water Magnetic Flow meter
- ➢ WRP = Water Recovering Pump
- ➢ WT = Water supplying Tank (5.0 m^3)

(1) Water loop

Water is stored in a tank (WT), with maximum capacity of 5 m^3, made of plastic material. The water is conducted to the multiphase flow line by using a water feeding pump (WFP), which is a type of centrifugal pump. The water flow rate is measured using a magnetic flow meter (Endress Hauser's Promag 30 FT15E), with a measureable range of 0.5-6.0 m^3/h and accuracy ±0.5 % of the reading (see Figure 3-3). The water flow rate is measured based on principle of the Faraday's law of induction, where passing of water as a conductive fluid would result in generating a magnetic field in flow meter, which is in turn related to the water flow rate if cross-sectional area and fluid properties are available.
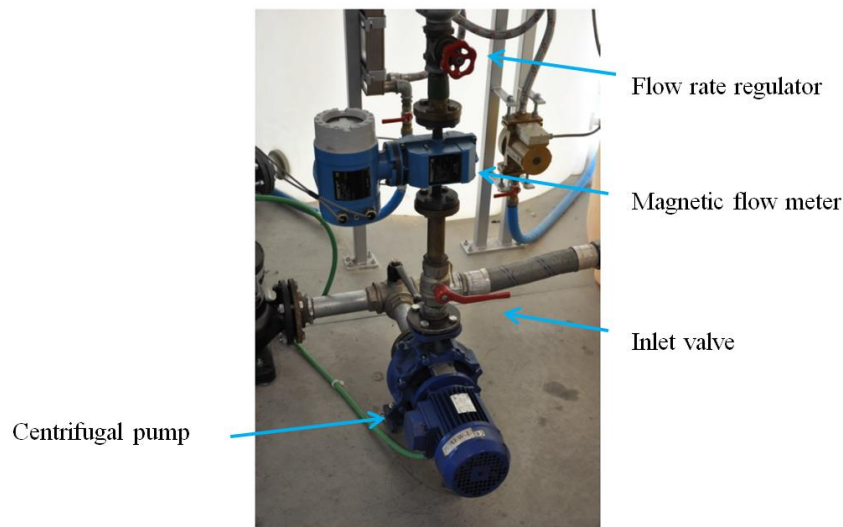
Figure 3-3 Snapshot of water system

(2) Oil loop

Oil is stored in a tank with a capacity of 0.5 m^3, which is made of plastic material. Oil is pumped to the multiphase flow test by using a metering gear pump provided by Pompe Cucchi, Opera,

Milano, see Figure 3-4. Gear type pumps are classified as positive displacement pumps such that a fixed amount of fluid is pushed at each revolution. They are suitable for very viscous fluids.

The oil flow rate is measured by setting an adjustable scale. To measure oil flow rate, a calibration is needed. Oil flow rate can be measured by the Hagen-Poiseuille law (Equation 3-1), providing laminar and fully developed flow in the test section:

$$Q_o = \frac{\Delta p \, \pi \, D_i^4}{128 \, \mu_o L} \qquad\qquad (3\text{-}1)$$

where:

- Q_o = Oil flow rate (m³/s);
- Δp = pressure drop (Pa);
- D_i = inner diameter of the pipe where Δp is being measured (m);
- μ_o = dynamic viscosity of the oil (Pa·s);
- L = pipe length (m)

The calibration was then performed by pumping single phase oil flow in the pipeline. The summary of the results of calibration reported as the relation between superficial oil velocity and adjustable scale is shown in Table 3-1.
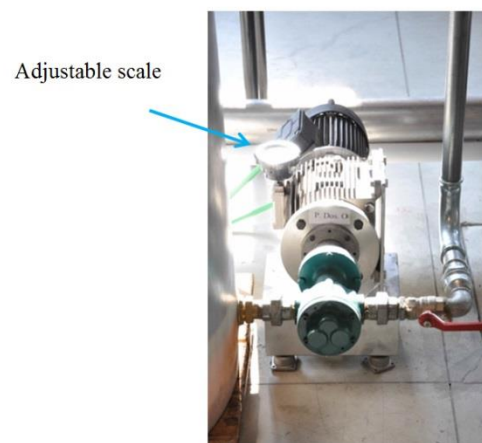
Figure 3-4 Snapshot of metering gear pump, with an adjustable scale

Table 3-1 Summary of calibration between adjustable scale and superficial oil velocity

Adjustable scale	J_o (m/s) for D=21mm	J_o (m/s) for D=30 mm	J_o (m/s) for D=40 mm	J_o (m/s) for D=50 mm
0.5	0.41	0.20	0.11	0.07
1.0	0.55	0.27	0.15	0.10
1.5	0.83	0.41	0.23	0.15
2	1.11	0.54	0.31	0.20
2.5	1.39	0.68	0.38	0.25
3.0	1.67	0.82	0.46	0.29
3.5	1.95	0.96	0.54	0.34
4.0	2.23	1.09	0.62	0.39
4.5	2.51	1.23	0.69	0.44
5.0	2.80	1.37	0.77	0.49
5.5	3.08	1.51	0.85	0.54
6.0	3.36	1.64	0.93	0.59

(3) Separation system

At the end of flow test lines, the mixture fluids falls in a separation tank of 1 m^3 capacity. The separator has a cylindrical shape, made of plastic material, allowing the possibility of monitoring the liquid level and separation process. To complete separation of oil and water, a residence time of around 30-45 minutes is needed. In the case of three phase flow, air is discharged out of the separation tank almost immediately. To start a new experimental test, first water is pumped back

to the water tank, then oil is pumped to the oil tank. Since during oil recovery some small amount of water can be entrained by the pump, a discharge valve is installed between separation and oil tank to easily remove such unwanted water from the oil tank.

(4) Fluid properties

Since rheological properties of fluids have a considerable influence on both the flow patterns and the pressure drop, they are periodically verified in dedicated laboratories. The test fluids used in the current study are tap water, Milpar 220 oil and air. Table 3-2 shows the rheological properties of test fluids considered for experimental runs at 20°C. Oil surface tension, water surface tension and interfacial tension between oil and water were measured at the Chemistry, Material and Chemical Engineering Department "Giulio Natta", Politecnico di Milano, by means of a LAUDA tensiometer. Dynamic viscosity and density were measured by the laboratory "INNOVHUB-Divisione Stazione Sperimentale per le industrie degli Oli e Grassi (SSOG)", Milan, Italy, according to the ASTM standard D 445/2010.

Table 3-2 Rheological properties of the fluids under investigation

Test fluids	ρ (kg/m^3)	μ (Pa·s)	σ (N/m)	σ_{o-w} (N/m)
Oil Milpar 220	890	838e-3	0.035	0.02
Tap water	999	1.02e-3	0.073	
Air	1.2	1.98e-5	-	

According to the ASTM standard D 445 (2010) standard regulation, the oil dynamic viscosity, μ_o (Pa·s), can be related to the temperature, T (°C), through an exponential regression:

$$\mu_o = 4.757 e^{-0.0694 \cdot T} \qquad \text{(3-2)}$$

Due to significant impact of temperature on the oil dynamic viscosity, the temperature must be measured at each experimental run. Two K-type thermocouples (10 % Cr-6 % Al) are used to

51

measure both ambient and flow temperature: the former is located outside the pipe and the later is positioned at almost half distance of the total pipe length. The thermocouples were calibrated by the calibration service of the Department of Energy, Politecnico di Milano, with an uncertainty of 0.2 °C. Figure 3-5 shows the behavior of the dynamic viscosity of the oil phase with the temperature in a typical range of operating conditions. The most common temperature range in the Laboratory lies within 20 and 25 °C.
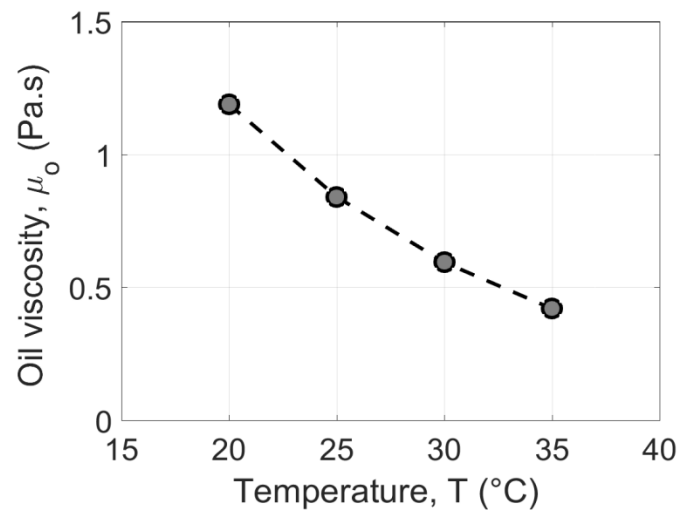
Figure 3-5. Oil dynamic viscosity versus temperature

(5) Multiphase flow loop

As already mentioned, the multiphase flow test line is composed of pipes joint together to form a 12 m pipeline. The pipe material is polymethyl methacrylate (PMMA), also known as acrylic glass which is commercially knows as Plexiglas®. It is a practical alternative to common glass allowing visual inspection of the flow regime. The multiphase flow test line measurements include:

- Pressure drop
- Holdup
- Gas phase velocity

(5-1) Inlet mixing device

The choice of mixing device is significantly important, since it was observed that suitable introduction of the phases helps formation of core-annular flow regime would help form core-annular flow downstream of inlet device and ensures its stability (Brauner (1998). Grassi et al (2006) studied the effect of inlet conditions on flow pattern of oil-water by using four different configurations of injectors for the same experimental conditions. The inlet injector used in the current study was also considered in their work. They reported that dramatic changes in flow patterns would occur for the same experimental conditions with different inlet devices. To promote the onset of core-annular flow regime, it is highly recommended that oil is axially introduced to the pipe, while water is injected in the annulus as it occurs in the current work.

The most important phenomenon to be avoided during the introduction of oil and water is pipe fouling by the more viscous phase, i.e. oil. If fouling occurs in the initial part of the pipe, major fouling will occur along the pipe, thus hindering onset and stability of annular flows

The specially designed mixing-device adopted in this work is shown in Figure 3-6. Water is injected peripherally by using a pipe, positioned with inclination angle of 25° with respect to the horizontal axis. Figure 3-7 illustrates the complete view of the mixing device including the air injector, positioned downstream.

.

Figure 3-6. Schematic of oil-water inlet injector

Figure 3-7. Complete view of inlet injector

A manometer is used to measure the volumetric flow rate of air. The actual air volumetric flow rate is the effective volumetric flow rate measured by the manometer multiplied by a pressure ratio correction factor:

$$\dot{V}_{pipe} = \dot{V}_{cal} \sqrt{\frac{P_{cal} \cdot P_{eff}}{P_{pipe}^2}} \qquad (3-3)$$

Where:

- $\dot{V}_{pipe}$: Actual volumetric air flow rate within the duct (m³/s)
- $\dot{V}_{cal}$: Volumetric air flow rate read by the flow meter (m³/s)
- P_{cal}: Calibration pressure of the flow meter (bar)
- P_{pipe}: Actual pressure within the duct (bar)
- P_{eff}: Effective pressure measured by the manometer at the inlet (bar)

Furthermore, since the end of the pipe is open to atmosphere and the overall pressure drop across the full length is in the order of dozen kPa in the "worst case" operating condition, it is assured that calibration pressure and actual pressure within the duct are approximately equal, that is, $P_{cal} \approx P_{pipe} \approx 1$ bar.

(5-2) Pressure drop measurement section

Downstream of inlet injector devices, pressure taps are installed at regular distances to measure the pressure drops. The pipes composing the test section are connected by flanges, and pressure taps are connected through small holes drilled in the pipe wall (i.d. 2-3 mm). The pressure taps are linked to a special collector by small Nylon tubes, which enable to connect each pressure tap to a differential pressure transducer (see Figure 3-8). Figure 3-9 shows an example of pressure taps.
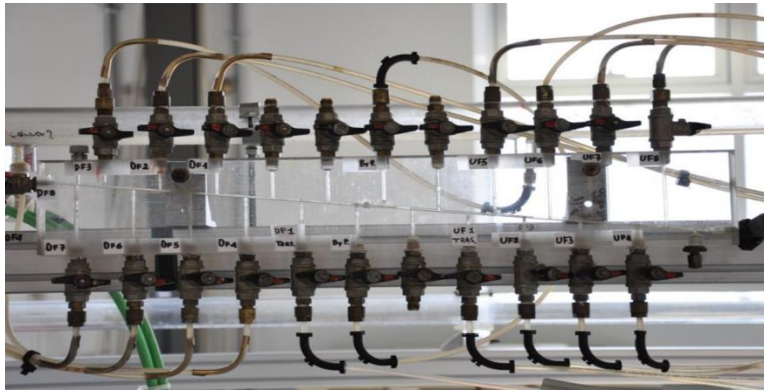
Figure 3-8. Sketch of pressure taps commutator
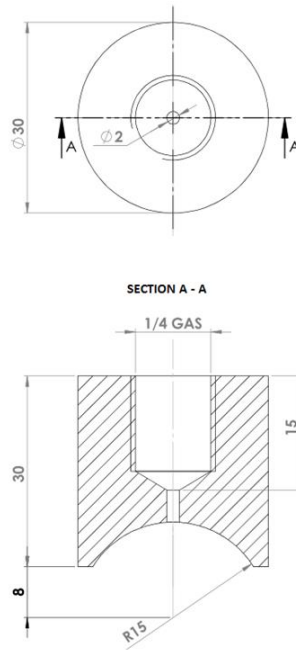
Figure 3-9. Sketch of a typical pressure tap

As it can be seen from Figure 3-8, the pressure tap tubes are attached to switching valves. Two ports are reserved for the pressure transducer. The schematic of pressure taps upstream and downstream of singularity for the investigated pipe configurations are depicted in Figures 3-10, 3-11, 3-12 and 3-13. These positions of pressure taps are required to calculate the concentrated pressure drop based on the pressure gradient method. In the case of sudden expansion 30-50 mm, a larger number of pressure taps has been inserted downstream in order to characterize the hydrodynamic development, which is particularly noticeable owing to the significant area ratio: in particular, in Figure 3-12, the blue pressure taps downstream of singularity are used to measure development length, while black pressure taps are used to measure pressure gradient in the fully developed region.
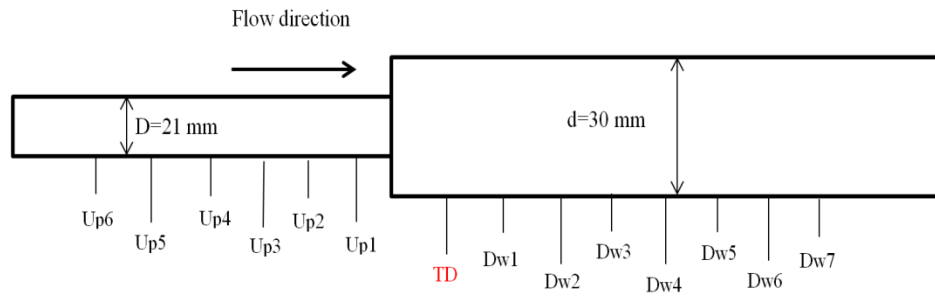
Figure 3-10 Schematic of tap positions for sudden expansion 21-30 mm. The flow direction is from left to right. The positions of pressure transducer and taps from singularity (in mm) are: TD (Pressure transducer)/955; Dw1/1395; Dw2/1885; Dw3/2385; Dw4/2905; Dw5/3385; Dw6/3875; Dw7/4595; Up1/230; Up2/730; Up3/1230; Up4/1730; Up5/2230; Up6/2730
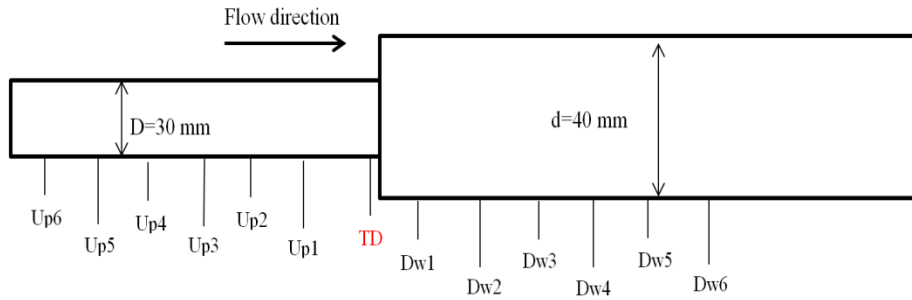
Figure 3-11 Schematic of tap positions for sudden expansion 30-40 mm. The flow direction is from left to right. The positions of pressure transducer and taps from singularity (in mm) are: TD (pressure transducer)/150; Dw1/500; Dw2/1050; Dw3/1640; Dw4/2135; Dw5/2630; Dw6/3130; Up1/500; Up2/1000; Up3/1500; Up4/2020; Up5/2500; Up6/2980
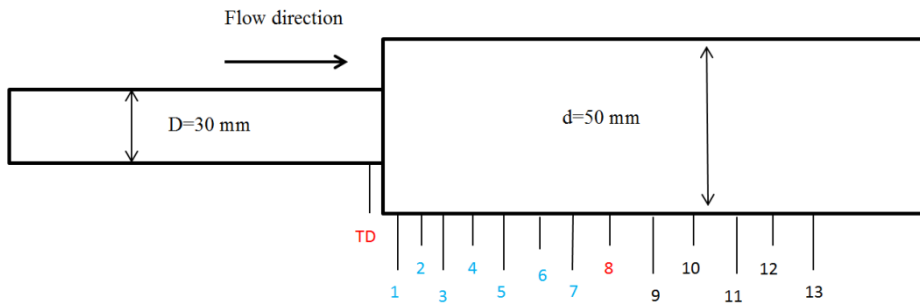
Figure 3-12 Schematic of tap positions for sudden expansion 30-50 mm. The flow direction is from left to right. The positions of pressure transducer and taps from singularity (in mm) are: TD (pressure transducer)/150; Dw1/50; Dw2/135; Dw3/240; Dw4/390; Dw5/540; Dw6/690; Dw7/900; Dw8/1380; Dw9/1880; Dw10/2370; Dw11/2860; Dw12/3540; Dw13/3840.
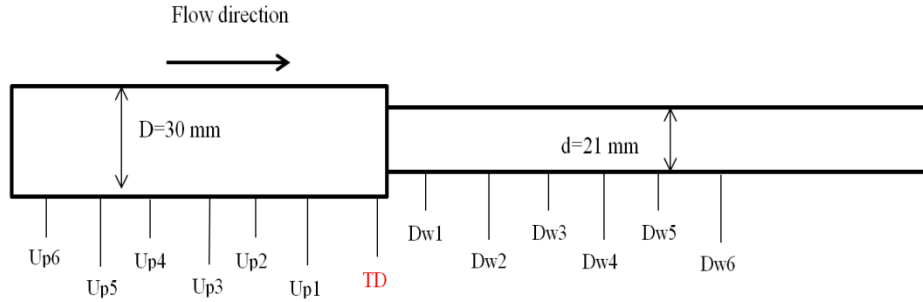
Figure 3-13 Schematic of tap positions for sudden contraction 30-21 mm. The flow direction is from left to right. The positions of pressure transducer and taps from singularity (in mm) are: TD (pressure transducer)/150; Dw1/500; Dw2/990; Dw3/1480; Dw4/1980; Dw5/2600; Dw6/3100; Up1/500; Up2/1000; Up3/1500; Up4/2020; Up5/2500; Up6/2980

(5-3) Flow visualization

Transparent pipes allow visualization of flows wherever along the test section and, in particular, upstream and downstream of geometrical singularities if present.

Basically, a digital HD video camera recorder (Nikon model D90) with AFS (Autofocus-Silent) 60 mm F2.8 Macro lens is used. In the present study, the videos are used to qualitatively examine flow regimes. In some cases a box filled with water is used to reduce the light distortion. Furthermore, in some other cases it was possible to install two mirrors with 45° angle with respect to horizontal axis to have additional views of the flow.

(5-4) Pressure transducers

Different combinations of flow rates and pipe diameters determine a rather wide range of pressure drop. Hence, two transducers have been used:

- Setra® Model 230 differential pressure transducer, full scale (FS): 1 psi = 6.89 kPa and FS accuracy: ±0.25%.
- Setra® Model 230 differential pressure transducer, full scale (FS): 10 psi = 68.9 kPa and FS accuracy ±0.25%.

To ensure higher accuracy, the transducers have been calibrated in the Turbomachinery Laboratory of the Department of Energy. Figure 3-14-a and 3-14-b show the calibration curves.

a)   b)
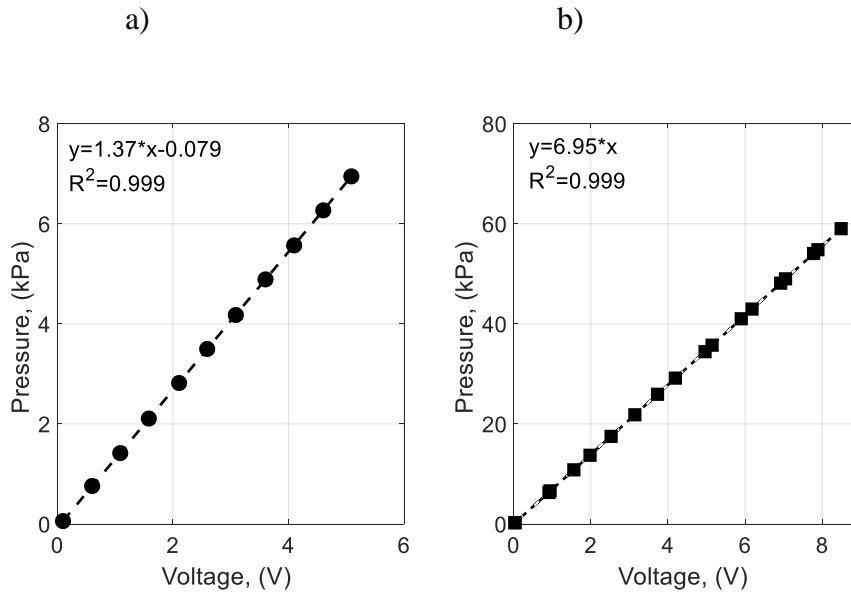
Figure 3-14 Calibration curves of the pressure transducers. The pressure (kPa) as a function of Voltage (V) is shown. a) Setra® Model 230, full scale 6.89 kPa, b) Setra® Model 230, full scale 68.9 kPa

Clearly, the lower full scale pressure transducer is applied for the configurations with 40 mm and 50 mm i.d. pipes, while the higher full scale pressure transducer for 30 mm and 21 mm i.d. pipes.

(5-5) Data acquisition system

Raw data acquired from online instrumentations, including water flow rate by the magnetic flow meter, pressure drop by the differential pressure transducer, the flow and ambient temperatures by K-type thermocouples. They are saved to a desktop computer by using a National Instrument Labview® data acquisition system. Figure 3-15 shows the complete chain of the data acquisition system.
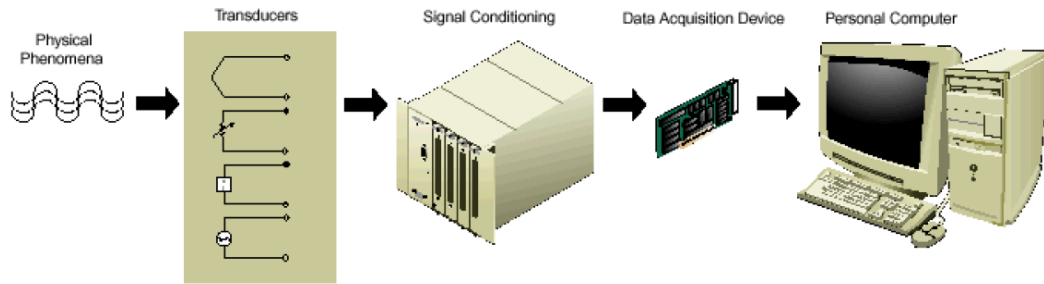
Figure 3-15 Schematic view of the complete chain of the data acquisition system

The signals are digitalized by means of a LAB-PC-1200 acquisition board. With the help of LabVIEW® Graphical User Interface (GUI), all the measured data are real-time monitored. For each experimental test, the acquisition interval can be set by GUI. The average value of raw data is taken for the measured quantity to reduce the influence of signal disturbances.

3-3 Experimental procedure

The aim of the experimental tests described in this work is to study the flow characteristics of oil-water and oil-water-air mixtures. Three major aspects of flow, including flow pattern, pressure gradient, and phase holdup have been investigated. The experimental procedures for two-phase flows and three-phase flows are described separately.

3-3-1 Experimental procedure for oil-water tests

Based on the long experience achieved at the Multiphase Flow Laboratory, the optimized procedure for oil-water tests is summarized as follows.

Before starting experimental tests, oil and water in the separation tank are pumped back into their respective tanks from the separation tank. Then:

1. The adjustable scale of the oil is set to the desired value.
2. The water valve between the water feeding pump and inlet test section is opened and the water feeding centrifugal pump is started.
3. The connection of the pressure taps are flushed (if needed) to eliminate air bubbles.
4. The oil pump is turned on and oil is injected into the test line at the set flow rate. The water flow rate can be adjusted manually at the desired value. Based on the above procedure, the duct is initially filled with water, then oil is injected: if both the superficial

60

velocities are such that annular flow regime is expected, by this procedure it is obtained from the injection point without appreciable disturbances.

5. When stabilized flow regime is obtained, the data from online instrumentation are collected in particular each pressure tap is scanned acting on the commutator previously described. According to the flow conditions, each acquisition lasts from 10 to 20 s at sampling frequency of 1 kHz.

6. At the same time that pressure drop and flow rates measurement are performed, it is possible to observe flow regimes and record video images at the selected positions along the pipe.

7. At the end of each test, the two phases are collected in the ST tank. Time interval between two tests is at least 30 min because of the gravitational separation of the phases.

3-3-2 Experimental procedure for oil-water-air tests

Almost the same procedure is used for experimental tests regarding three phase oil-water-air flows. The only difference is that after setting water and oil volume flow rates, air is introduced to the test section. The air volume flow rate is adjustable by a valve, while keeping constant the inlet pressure by a pressure regulator.

3-4 Experimental operating conditions

Tables 3-3 and 3-4 show the operating conditions considered in this study for oil-water and oil-water-air tests, respectively.

Table 3-3 Summary of experimental runs for oil-water tests

D (mm)	J_o (m/s)	J_w (m/s)	Re_{so} (m/s)	Re_{sw} (m/s)
21	1.67	0.49-0.74	37	10269-15509
	2.23	0.49-0.74	49	10269-15509
	2.79	0.36-0.63	62	7545-13203
	3.35	0.32-0.59	75	6706-12365
30	0.81	1.18-2.34	26	35329-70060
	1.09	1.18-2.34	35	35329-70060
	1.37	1.18-2.34	44	35329-70060
	1.64	1.18-2.34	52	35329-70060
40	0.46	0.67-1.34	19	26746-53493
	0.53	0.67-1.34	22	26746-53493
	0.61	0.67-1.34	25	26746-53493
	0.69	0.67-1.34	29	26746-53493
	0.77	0.67-1.34	33	26746-53493
	0.84	0.67-1.34	36	26746-53493
	0.92	0.67-1.34	39	26746-53493
50	0.29	0.42-0.85	15	20958-42415
	0.39	0.42-0.85	21	20958-42415
	0.49	0.42-0.85	26	20958-42415
	0.59	0.42-0.85	31	20958-42415

Table 3-4. Summary of the experimental runs for oil-water-gas tests

D (mm)	J_o (m/s)	J_w (m/s)	J_g (m/s)	Re_{so} (-)	Re_{sw} (-)	Re_{sg} (-)
40	0.36	0.66-1.32	0.38-2.10	15	26347-52694	921-5091
	0.48	0.66-1.32	0.38-2.10	20	26347-52694	921-5091
	0.60	0.66-1.32	0.38-2.10	28	26347-52694	921-5091
	0.71	0.66-1.32	0.38-2.10	30	26347-52694	921-5091

The superficial Reynolds number for each phase is defined as:

$$Re_{so} = \frac{J_o \rho_o D}{\mu_o} \qquad Re_{sw} = \frac{J_w \rho_w D}{\mu_w} \qquad Re_{sg} = \frac{J_g \rho_g D}{\mu_g} \qquad (3\text{-}4)$$

Subscripts o, w and g denote oil, water and gas phases, respectively. Though it is well-known that such a Reynolds number is not related to the actual flow regime of each phase, it is a useful parameter in one-dimensional models based on the momentum equation. It is then reported in Tables 3-3 and 3-4.

3-5 Repeatability of the experimental tests

To check repeatability, some experimental runs with the same flow conditions were performed several times. Generally, repeatability of pressure drop measurements is excellent and more details are reported in the sections dedicated to the discussion of the results. Generally, it is not easy to have exactly the same flow conditions, particularly for water flow rate because it can be controlled manually and some small degree of uncertainty is always present.

4 Experimental Results

4.1 Introduction

Experimental results for oil-water tests in the presence of sudden expansions and contractions are presented in this chapter. The discussion is divided into three main sections, which includes: flow patterns, two-phase pressure gradient, concentrated pressure drop and the phase holdup. Regarding flow patterns, stratified flow regime was not considered because the focus of the study was to investigate characterization of core-annular flow.

4.2 Flow patterns

4.2.1 Observed flow patterns in experiments

Visual observation is useful to evaluate the effect of flow disturbances in the downstream pipe caused by the sudden change in cross-sectional area. The photographs of typical flow patterns for different sudden expansion cases in downstream pipe are depicted in Tables 4-1, 4-2 and 4-3. The observed flow patterns include: 1) Dispersed oil-in-water flow, 2) Corrugated Core-Annular flow, 3) Eccentric Core-Annular with/without drop entrainment.

In Tables 4-1, 4-2 and 4-3, the frames are taken at a location less than 10D to the singularity to evaluate the influence of cross-sectional area change on flow patterns for different pipe configuration. Some degree of disturbances is introduced by the presence of singularity, showing itself as high entrainment rate at the oil-water interface. The following flow patterns can be classified:

Table 4-1 Photographs of the observed flow patterns for downstream of sudden expansion 21-30 mm. a) , b) Dispersed oil-in-water flow (D), c) Eccentric core-annular with oil entrainment (ECA-E), d) Corrugated Core-Annular (CCA)

a) Dispersed flow at low superficial oil velocity (D)

b) Dispersed flow at high superficial oil velocity (D)

c) Eccentric core-annular with oil entrainment (ECA-E)

d) Corrugated core-annular (CCA)

Table 4-2 Photographs of the observed flow patterns for downstream of sudden expansion 30-40 mm, a) Eccentric core-annular with oil entrainment (ECA-E), b) Dispersed oil-in-water flow (D), c) Eccentric core-annular without oil drop entrainment (ECA)

a) Eccentric core-annular with oil entrainment (ECA-E)   b) Dispersed oil-in-water flow (D)

c) Eccentric core-annular without oil drop entrainment (ECA)

Table 4-3 Photographs of the observed flow patterns for downstream of sudden expansion 30-50 mm. (a) , (b) and (d) Eccentric core-annular with oil entrainment (ECA-E), c) Dispersed oil-in-water flow
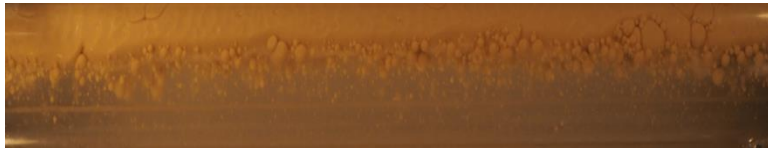
a)   Eccentric core-annular with oil entrainment (ECA-E)
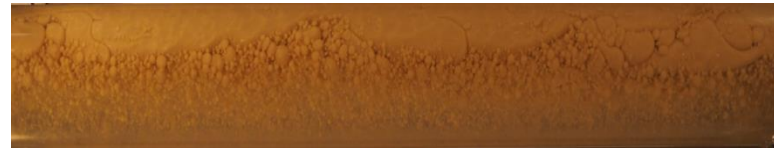
b) Eccentric core-annular with oil entrainment (ECA-E)

c) Dispersed oil-in-water flow (D)
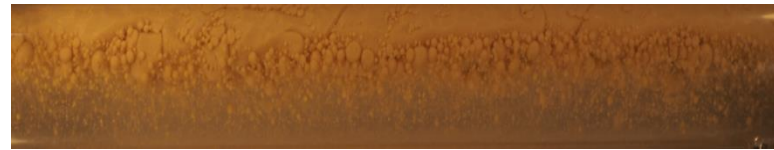
d) Eccentric core-annular with oil entrainment (ECA-E)

Dispersed oil-in-water flow (D): At sufficiently high superficial velocity of water, dispersion of oil drops within continuous water flow occurs. The degree of dispersion is highly dependent on the oil flow rate. At the higher oil flow rates oil drops tend to collide together. On the other hand, increasing water superficial velocity would result in breaking oil drops into smaller ones, which is inferred to be due to increased turbulent shear stress.

Core-Annular Flow (CAF): Core-Annular flow regime is a dominant flow regime in very viscous oil-water flows. It is the most frequent flow regime in the current study. The lower bound for flow regime can be reached by reducing the oil flow rate at constant water flow rate and vice versa. A particular type of CAF is the so-called Concentric CAF, where the oil core is nearly symmetric about the pipe axis.

Eccentric Core-Annular (ECA): Eccentric Core-Annular is a type of Core-Annular flow where oil core tends to migrate to the upper part of pipe due to the effect of buoyancy. In the present study, two variations have been observed: a) Eccentric Core-Annular with oil drop entrainment (ECA-E) where many oil drops are present at the interface of oil and water (the flow regimes downstream of the singularity are the same type as for the straight pipe according to the previous observations but they show in some cases a tendency to dispersion), and b) Eccentric Core-Annular without oil drop entrainment (ECA) where no oil entrainment is observed at the oil-water interface. Tables 4-1 (c), 4-2 (a), 4-3 (a), (b), (d) are examples of eccentric flow regimes with oil entrainment, while Table 4-2 (c) shows eccentric core-annular flow without oil drop entrainment.

Corrugated Core-Annular flow (CCA): The Corrugated Core-Annular flow is a type of core-annular, which forms in a limited range of operating condition. It is characterized by very thin water layer adjoining the wall and an almost concentric oil core. This flow regime is interesting because the pressure drop shows the lowest values (see Sotgia et al, 2008). Table 4-1 (d) illustrates an example of corrugated core-annular flow.

The photographic images of flow behavior downstream of sudden expansion for the minimum and maximum J_o and J_w are depicted in Figures 4-1, 4-2, 4-3, 4-4, 4-5, and 4-6 to show the flow evolution. Three views are available by using two mirrors, 45° inclined with respect to the horizontal axis. The upper, front and bottom views are shown at the top, middle and bottom

images in Figure 4-1 to 4-6, respectively. The dominant flow regime is core-annular flow, mainly eccentric. As water superficial velocity increases, the flow patterns are gradually evolving to disperse patterns of oil drops particularly at the oil water interface due to the increasing interfacial shear stress. The oil core tends to form a concentric flow in the case 21-30 mm, while eccentricity of the downstream flow patterns is increased in the cases 30-40 mm and 30-50 mm.

Figure 4-1 Flow pattern for downstream sudden expansion 21-30 mm for J_o=2.23 m/s, a) Jw=2.40, b) 2.80 m/s

Figure 4-2 Flow pattern for downstream sudden expansion 21-30 mm for J_o=3.35 m/s, a) Jw=2.40, b) 2.80 m/s

Figure 4-3 Flow pattern for downstream sudden expansion 30-40 mm for J_o=1.09 m/s, a) Jw=1.17, b) 1.37 m/s

Figure 4-4 Flow pattern for downstream sudden expansion 30-40 mm for J_o=1.64 m/s, a) Jw=1.17, b) 1.37 m/s
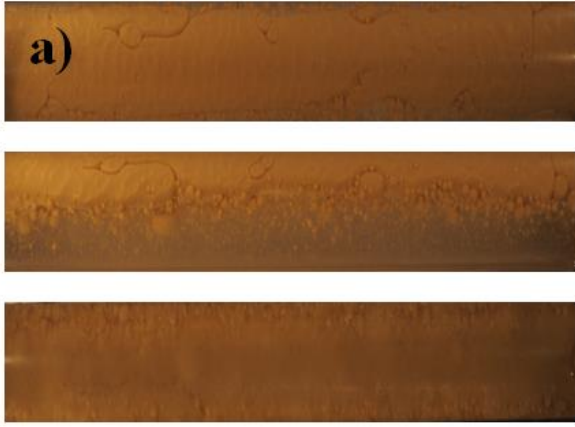
Figure 4-5 Flow pattern for downstream sudden expansion 30-50 mm for J_o=1.09 m/s, a) Jw=1.17, b) 1.37 m/s

Figure 4-6 Flow pattern for downstream sudden expansion 30-50 mm for J_o=1.64 m/s, a) Jw=1.17, b) 1.37 m/s

4.2.2 Flow pattern maps

Quantitative considerations from the flow pattern visualization can be drawn by drawing maps. Flow pattern maps relative to the flow downstream of sudden expansions 21-30 mm (Figure 4-7-a), 30-40 mm (Figure 4-7-b), 30-50 mm (Figure 4-7-c) are presented. Boundaries between different flow regimes are indicated. In particular, the transition between stratified and dispersed flow is observed only for the case 30-50 mm (Figure 4-7-c). In the other cases only transition between CAF and D is observed. Moreover, for 21-30 mm and 30-40 mm, the dominant flow pattern is CAF, while for sudden expansion 30-50 mm, where cross-sectional area ratio is lower (area ratio=0.36), the main flow pattern is dispersed flow. Regarding the type of CAF flow regime, it is evident that Concentric CAF is only present in the case 21-30 mm, however, eccentricity plays an important role in the other ones. According to operating conditions under investigations, CCA is only observed in the case of abrupt expansion from 30-40 mm.
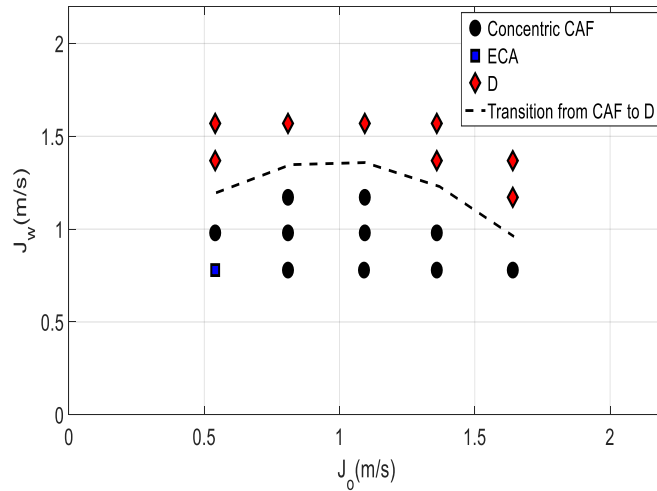
(a)
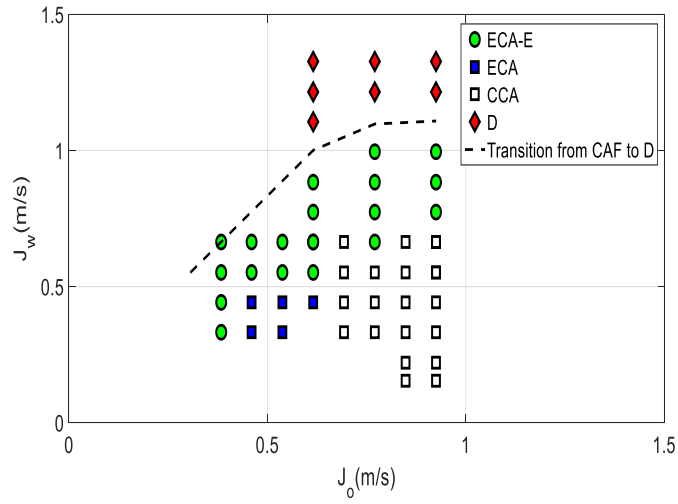
(b)
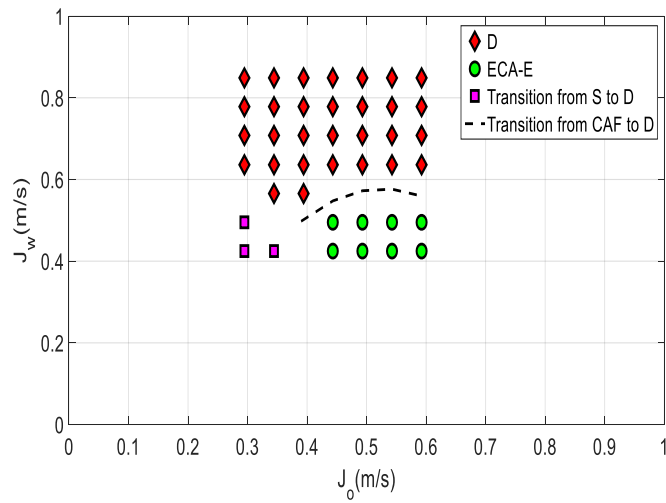
(c)

Figure 4-7. Flow regime maps for three cases of downstream sudden expansion. a) 21-30 mm, b) 30-40 mm, c) 30-50 mm

It is interesting to notice that, according to the flow pattern map reported for constant diameter (D=40 mm) pipe (Colombo et al. 2012), and shown in Figure 4-8, the transition boundary between CAF and D is shifted toward lower values of the superficial water velocity. This fact suggests that the flow disturbance induced by the sudden enlargement of the cross-section mainly results in a more accentuated tendency to dispersions.
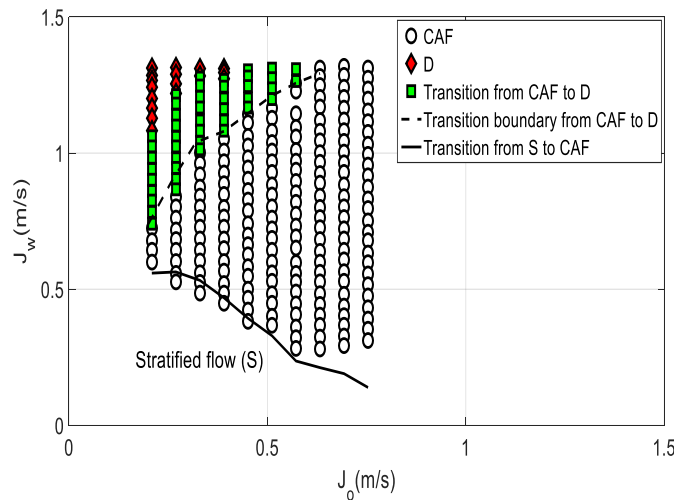
Figure 4-8 Flow pattern map for Pyrex® 40 mm i.d. straight pipe

4.2.3 Comparison of flow pattern map with literature data bank

Among many works performed on liquid-liquid flow, Sotgia et al (2008) reported flow pattern maps for very viscous oil-water flow, with oil viscosity 0.8 Pa·s, i.e. the same as the present work. The transition boundary lines between different flow patterns were investigated in their paper. Sotgia (2008) realized that there is a region between CAF and fully dispersed flow with transitional characteristics. A summary of the data used for flow map comparison is tabulated in Table 4-4. The pipe diameters that Sotgia et al (2008) used to develop flow pattern maps were 26 mm. Hence, the data regarding to the sudden expansion 21-30 mm can be reasonably compared in order to understand the variation flow pattern caused by the sudden expansion.

Table 4-4 Summary of data bank for straight pipe used to compare flow pattern maps

Author	Pipe I.D. (mm)	μ_o (Pa.s)	ρ_o (kg/m3)	σ_{o-w} (N/m)	J_w (m/s)	J_o (m/s)
Sotgia et al (2008)	26	0.8	889	0.02	0.066-2.38	0.20-0.97

Figure 4-9 (a) and 4-9 (b) shows a comparison of flow pattern maps developed in the current study regarding 30 mm i.d. pipe downstream of 21-30 mm and that produced by Sotgia et al (2008) in a straight pipe, with 26 mm i.d. pipe, represented in J_o, J_w, and ε_w, J_m coordinates. For the sake of the comparison, these two representations are equivalent. Two flow regimes are observed downstream of the sudden expansion 21-30 mm pipe, which includes CAF and dispersed flow. Furthermore, the transition boundary lines from CAF to D flow is illustrated by the dashed line in the presence of sudden expansion. The flow regimes in the work of Sotgia et al (2008) included wavy stratified, wavy annular, slug, transition from CAF to D, and dispersed flow. It is evident that CAF flow in the current study is overlapped in the CAF region developed by Sotgia et al (2008). In both cases, a transition from CAF to D flow regime occurs principally by increasing of water superficial velocity. The major difference between the two flow pattern maps is that the area of CAF region is reduced in the presence of singularity and the area of dispersed region is increased, very likely due to the disturbances caused by the area change. The dispersed data corresponding to sudden expansion (shown in red marker) in our maps is related to fully dispersed flow and it can be easily seen how far the transition line from CAF to D is placed with respect to the same transition boundary observed by Sotgia et al (2008). For the straight pipe it is more difficult to compare trends of CAF to D transition boundary because the lack of data with $J_o > 0.97$ m·s^{-1} in Sotgia et al. (2008). In any case, in the range $0.6 < J_o < 1$ m·s^{-1} it is observed a similar behavior with increasing with J_o.
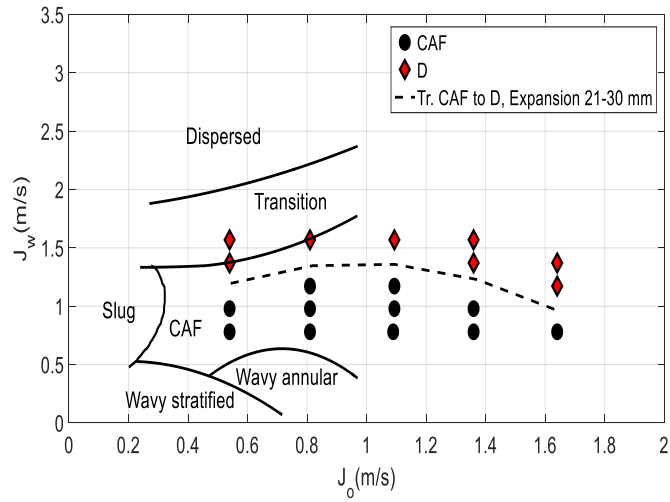
(a)
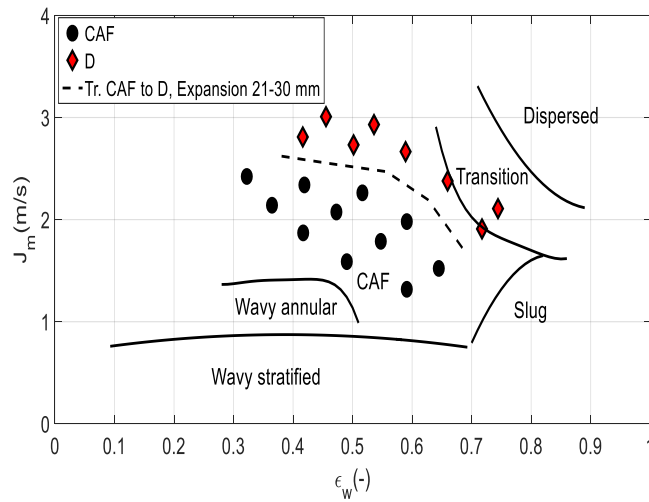
(b)

Figure 4-9 Comparison of flow pattern map of downstream the sudden expansion 21-30 mm and Sotgia et al (2008) with D=26 mm. Flow regimes regarding 30 mm downstream of sudden expansion are shown in markers. Solid lines are transition lines between different flow regimes in Sotgia et (2008). Dashed lines represent transition from CAF to D in 30 mm i.d. pipe downstream of sudden expansion 21-30 mm. (a) J_o and J_w as coordinates; (b) ε_w and J_m as coordinates.

4.3 Analysis of pressure gradient for very viscous oil-water flow

As water lubricated flow is the most effective method to transport heavy oil, it is also important to assess the influence of geometrical singularities which are likely to be present in a pipeline. A key point is to understand if the disturbance introduced by the pipe element can significantly alter the flow pattern and the pressure drop. In the following section, the results of two-phase pressure gradients for different pipe configurations are presented first because pressure gradients are required later to compute singular pressure drop as well as two-phase loss coefficient.

4.3.1 Distributed pressure gradient

It is interesting to try to relate the pressure gradient to the flow patterns, as seen in Figure 4-10. Three cases of sudden expansion, e.g. 21-30 mm, 30-40 mm, and 30-50 mm is considered. Apart from pipe configuration, core-annular flow regime provides the lower pressure gradient as compared to dispersed flow regime. Moreover, by comparison of sudden expansion 21-30 mm and 30-50 mm, one may find out that pressure gradient is significantly reduced in the latter case which suggest a simple technique to establish a core-annular flow regime.
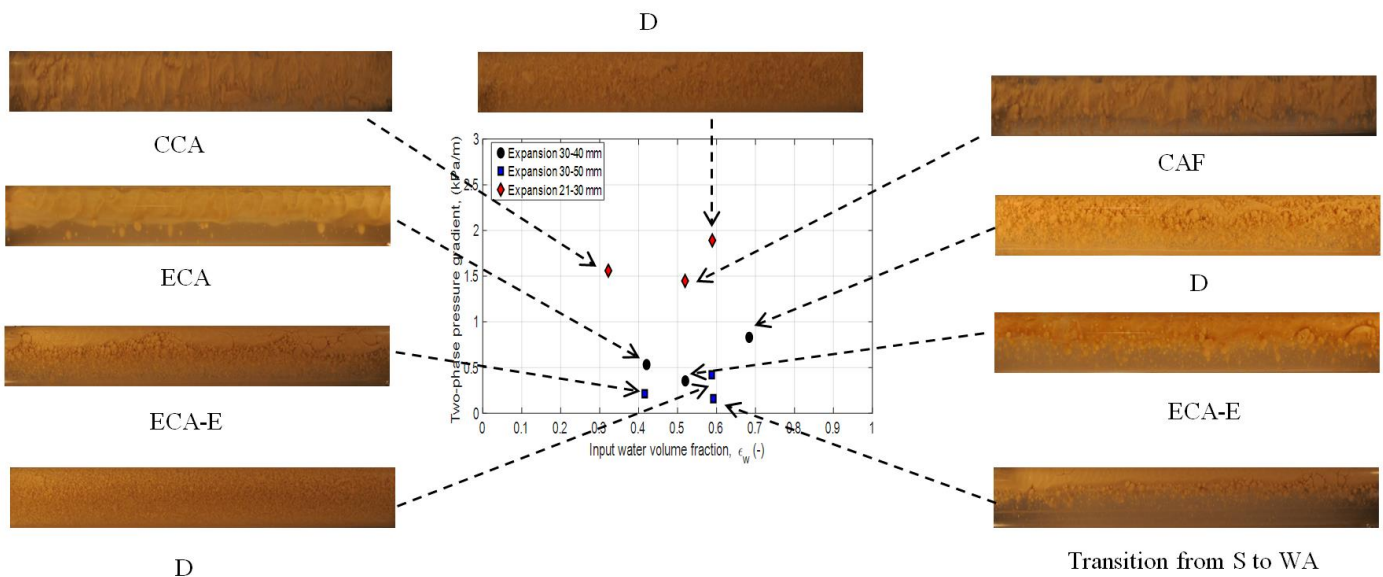
Figure 4-10. Typical pressure gradient versus input water volume fraction and corresponding flow pattern for all cases of expansion

The parametric investigation is conducted making use of the pressure gradient trend as a function of water input volume fraction because it is the basis of further analysis regarding physical mechanisms as reported in Chapter 5. One case of sudden contraction (TS1: 30-21 mm) and three cases of sudden expansion (TS2: 21-30 mm, TS3: 30-40 mm, and TS4: 30-50 mm) are considered in the analysis of pressure measurements. The typical trends of distributed pressure gradient with input water volume fraction (ε_w), parameterized by superficial oil velocity (J_o) are depicted in Figure 4-11 and Figure 4-12. Figure 4-11 shows the results of pressure gradient measurement in case of sudden contraction both upstream and downstream, while Figure 4-12 shows the pressure gradient measurement for the three cases of sudden expansion. For the pipe downstream of the sudden expansion, the corresponding flow patterns are also shown in Figure 4-12 (a-c). Since the inversion phenomenon occurs at low input water volume fraction, in all cases water always remains as a continuous phase. Shi (2015) proved that for very viscous oil-water flow, the transition from water-continuous to oil-continuous (phase inversion) occurs for input water volume fraction lower than 40%, depending on oil superficial velocity. It is also indicated that the stable water-lubricated flow can be developed at a lower ε_w with increase of oil superficial velocity. The investigated operating conditions correspond to a stable water-lubricated flow and are favorable for transport of heavy oil. Figure 4-11 shows the same trend of pressure gradient as a function of input water fraction both upstream and downstream of sudden contraction, that is, pressure gradient increases as input water fraction increases for fixed amount of oil. This is not surprising because increasing water superficial velocity would contribute to increase wall shear stress and finally pressure gradient. The magnitude of pressure gradient is higher downstream than upstream because of the higher magnitude of superficial velocity in the downstream pipe.
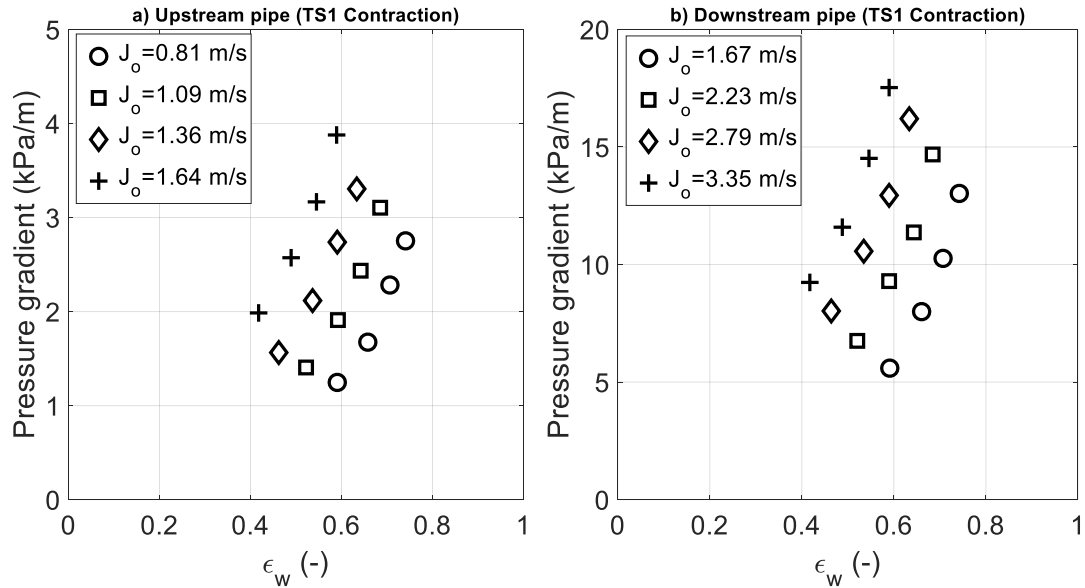
Figure 4-11 The trend of pressure gradient measurement as a function of input water volume fraction; a) upstream pipe (TS1, contraction), b) downstream pipe (TS1, contraction)

Almost the same trend of pressure gradient but different magnitude as a function of the water input volume fraction is observed for the all cases of sudden expansion. In Figure 4-12 (a-c), different symbols indicate different observed flow regimes, while different colors represent different oil superficial velocities. From the analysis, it is evident that core-annular flow is obtained at the lower values of input water volume fraction, while increasing water flow rate would result in transition from core-annular to dispersed flow. It can be noted also that no considerable deviation is observed for different sudden expansion configurations. Almost the same qualitative trend of pressure gradient as a function input water volume fraction is observed downstream of singularity. Core-annular flow always shows the lowest pressure gradient downstream of sudden expansion. The further physical analysis regarding pressure gradient is discussed in Chapter 5.
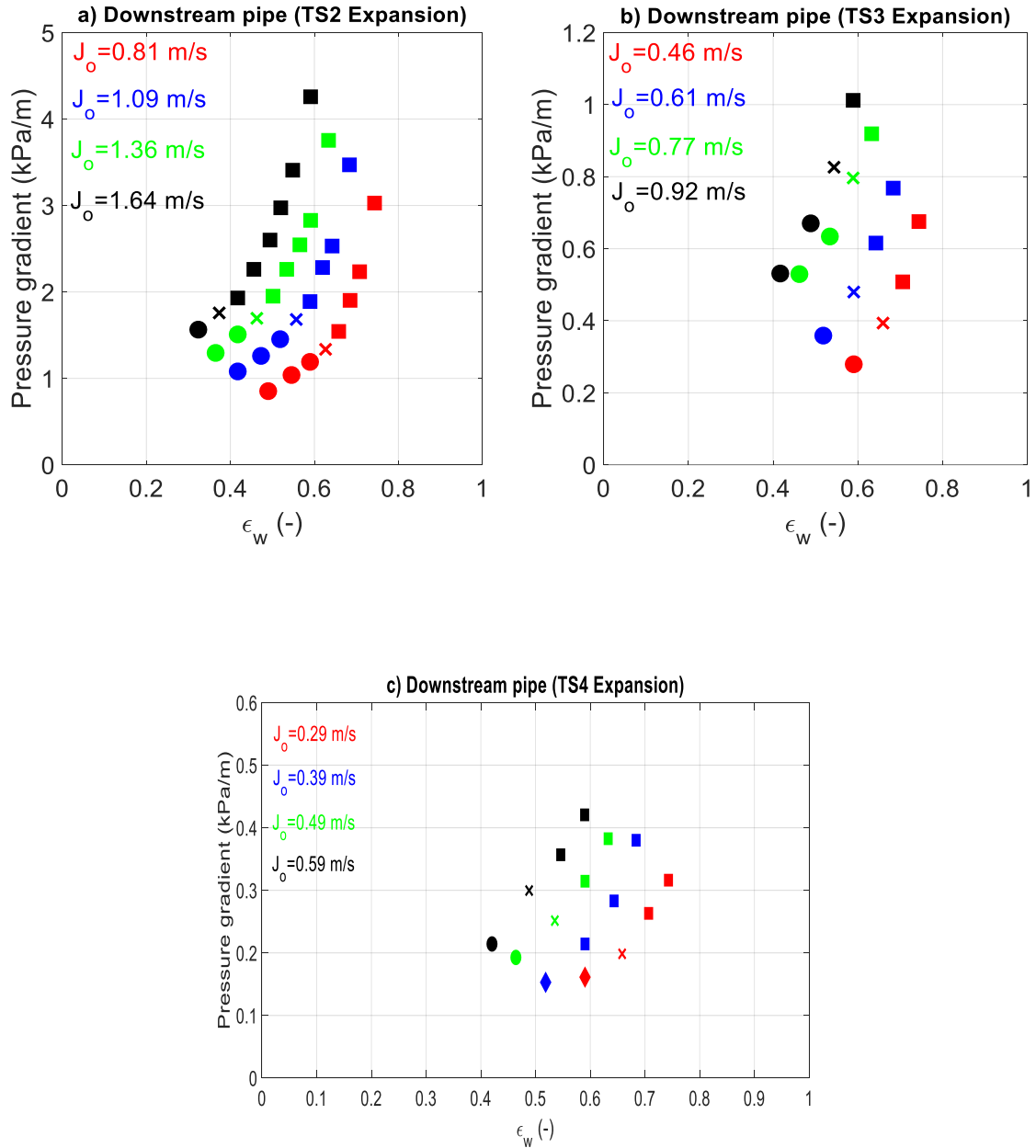
Figure 4-12 The trend of pressure gradient measurement as a function of input water volume fraction; a) downstream pipe (TS2, expansion), b) downstream pipe (TS3, expansion), c) downstream pipe (TS4, expansion). o:CAF, x:transition from CAF to D, □: D, ◊: transition from S to CAF.

81

4.3.2 Pressure reduction factor for very viscous oil-water flow

Two-phase multipliers are widely used to describe the characteristics of two-phase flows since their initial introduction by Lockhart and Martinelli (1949). For oil-water flows, in particular, the ratio of the two-phase pressure gradient to the "only oil" pressure gradient is physically significant, since for annular flows it is lower than unity. In this case, it is called "Pressure gradient reduction factor" (ϕ) and defined as the ratio of oil-water pressure gradient to single oil flow at the same oil flow rate. The pressure gradient regarding single oil flow can be calculated from Hagen-Poiseuille law for laminar flow. The pressure reduction factor has been already used by several researchers, namely, Russel and Charles (1959), Arney et al (1993), Sotgia et al (2008).

$$\phi = \frac{-\left(\frac{dp}{dx}\right)_{ow}}{-\left(\frac{dp}{dx}\right)_{o}} \qquad (4\text{-}1)$$

$$-\left(\frac{dp}{dx}\right)_{o} = \frac{32 \cdot \rho_O \cdot \mu_O}{D^2} \qquad (4\text{-}2)$$

Where:

ϕ: Pressure gradient reduction factor [-]

$-\left(\frac{dp}{dx}\right)_{ow}$: Pressure gradient along the pipe for oil for oil-water flow [kPa/m]

$-\left(\frac{dp}{dx}\right)_{o}$: Pressure gradient along the pipe for single oil flow [kPa/m]

ρ_o: oil density [kg/m^3]

μ_o: oil viscosity [Pa˙s]

D: pipe diameter [m]

The results of pressure gradient reduction factor both upstream and downstream of TS1 as a function of input water volume fraction, with superficial oil velocity as a parameter, are reported in Figure 4-13. It is worth noting that the values of two phase pressure gradient refer to fully developed flow in both the upstream and downstream pipes. Of course, for pumping purposes, the lower value of pressure reduction factor is preferable at constant oil flow rate. However, from

practical point of view, it is most desirable to transport as much oil as possible with the lower input water volume fraction. By a close observation, one may understand that there is slight change in the pressure reduction factor at the same water and oil flow rate switching from upstream to downstream pipe in the presence of abrupt contraction. Actually, it is observed that the pressure reduction factor is lower for the upstream pipe than for the downstream pipe, suggesting that oil core eccentricity might play a relevant role. In fact, in the downstream pipe, the annular flow pattern is more concentric. The minimum and maximum achievable pressure gradient reduction factor ranges between 0.047-0.12 for upstream pipe, whereas it varies between 0.050-0.14 for downstream pipe of TS1.
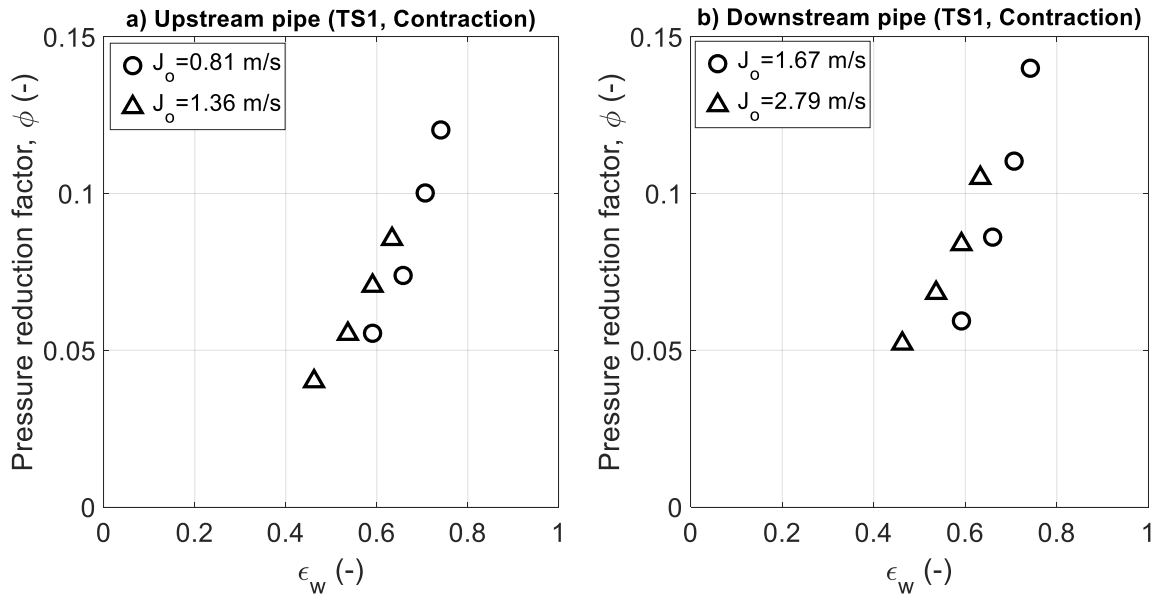
Figure 4-13 Pressure gradient reduction factor (ϕ) with input water volume fraction (ε_w) at various superficial oil velocity; a) upstream pipe (TS1, contraction), b) downstream pipe (TS1, contraction)
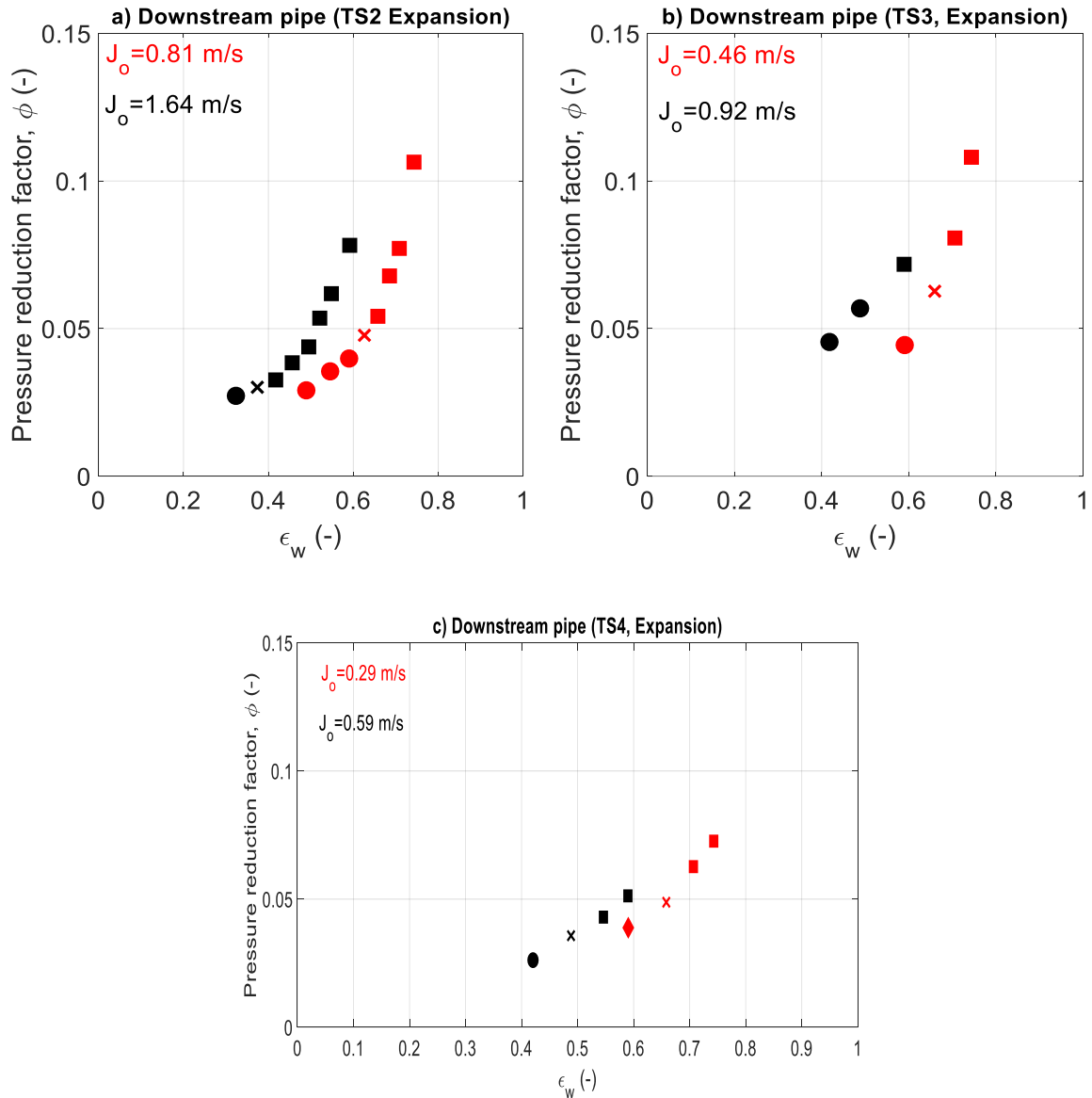
Figure 4-14 Pressure gradient reduction factor (ϕ) with input water volume fraction (ε_w) at various superficial oil velocity; a) downstream pipe (TS2, expansion), b) downstream pipe (TS3, expansion), c) downstream pipe (TS4, expansion). o:CAF, x:transition from CAF to D, ⊓: D, ◊: transition from S to CAF.

In Figure 4-14, the results of pressure reduction factor versus input water volume fraction for three cases of sudden expansion in downstream pipes, that is, TS2, TS3 and TS4 are shown. Each plot is parameterized by maximum and minimum possible superficial oil velocity. The flow pattern for each operating condition downstream of TS2, TS3, and TS4 are also indicated. For

fixed oil flow rate, the decrease of water flow rate results in lower pressure reduction factor and more effective lubrication influence. Therefore, oil transport with the lowest possible water amount is preferable. Downstream of the abrupt expansion, both the lubrication effect and eccentricity should contribute to the lower pressure drop. By comparison of Figure 4-14 (a), (b) and (c), it is evident that pressure reduction factor lowers in the latter case over the entire range of input water volume fraction, as a consequence of a stronger area ratio. The summary of minimum and maximum achievable pressure reduction factors for sudden contraction and expansion for both upstream and downstream pipes are reported in Table 4-5.

Table 4-5 Summary of minimum and maximum achievable pressure reduction factors for different pipe configurations

Pipe configuration	Minimum ϕ	Maximum ϕ	J_o and J_w (m/s)
upstream pipe (TS1)	0.047	0.12	J_o:0.81-1.64
			J_w:1.17-2.36
downstream pipe (TS1)	0.050	0.14	J_o:1.67-3.35
			J_w:2.41-4.81
upstream pipe (TS2)	0.034	0.12	J_o:1.67-3.35
			J_w:1.61-4.81
downstream pipe (TS2)	0.027	0.10	J_o:0.81-1.64
			J_w:0.78-2.36
downstream pipe (TS3)	0.044	0.10	J_o:0.46-0.92
			J_w:0.66-1.32
downstream pipe (TS4)	0.026	0.072	J_o:0.29-0.59
			J_w:0.42-0.85

4.4 Pressure distribution

Pressure profiles along the pipe are represented in Figure 4-15 (a-d). Figure 4-15-a shows the results of pressure profiles for contraction TS1, whereas Figure 4-15 (b-d) presents pressure profiles for three case of sudden expansion, e.g. TS2, TS3 and TS4, respectively. In all figures the measured two-phase pressure drop (ΔP_{ow}) are plotted as a function of tap distance (L) from the plane of singularity, normalized by pipe diameter (L/D). The lowest and highest mixture superficial velocities (J_m) are considered for the sake of comparison. Regarding the flow through contraction TS1, the pressure gradient increases both upstream and downstream of the plane of area change, with steeper slope downstream of singularity, which is due to the higher mixture superficial velocity. In fact, from the point of contraction, both frictional loss and sudden area change contribute to the steeper pressure gradient downstream of TS1. In the upstream pipe of TS1, pressure profiles are almost independent of mixture superficial velocity and water input volume fraction. The same trend is observed for three cases of expansion TS2, TS3, and TS4. The pressure profiles upstream of expansion have steeper slopes than the downstream pipe due to the larger volumetric flux in the former case. In all expansion cases, the two-phase pressure drop increases along the length of the pipes. The behavior of pressure profiles downstream of expansion is of complex interpretation. Actually, pressure gradients for TS2 and TS3 are highly dependent on mixture superficial velocity and input water volume fraction, while this is not observed for TS4. The trends of pressure profiles shown in Figure 4-15 (a-d) are in agreement with the reported results of Hwang and Pal (1997) and Balakhrisna et al (2010) who used much lower oil viscosity. It showed be noted that there is no information regarding pressure profiles for a very viscous oil-water flow through singularity in the previous studies to compare our results.
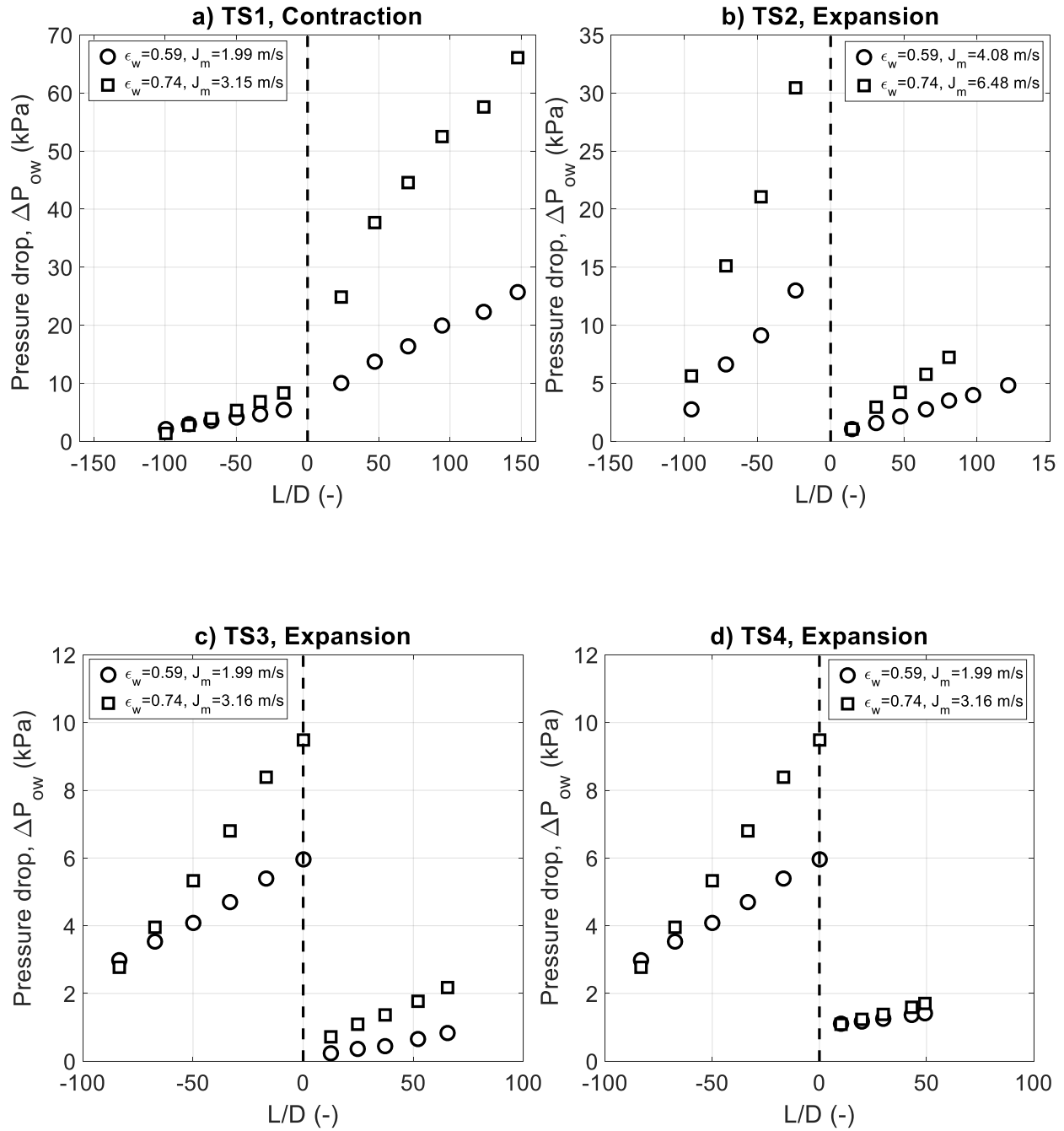
Figure 4-15 Pressure profiles along the pipe, a) sudden contraction TS1, b) sudden expansion TS2, c) sudden expansion TS3, d) sudden expansion TS4.

4.5 Method for concentrated pressure drop evaluation

In order to deeply understand the behavior of oil-water flow through singularity, the influence of changing of pipe cross-section on flow characteristics must be addressed. This is done by evaluating concentrated pressure drop across the singularity. By using the pressure gradient technique, it is possible to calculate concentrated pressure drop, without direct measurement of it across singularity. As explained in Chapter 2, the concentrated pressure drop can be measured by extrapolation of the pressure gradients relative to the fully developed region of upstream and downstream pipe up to the plane of the singularity. The schematic is depicted in Figure 4-16 for case of expansion. However, the same procedure for the contraction can be adopted. The calculation procedure is explained as follows.
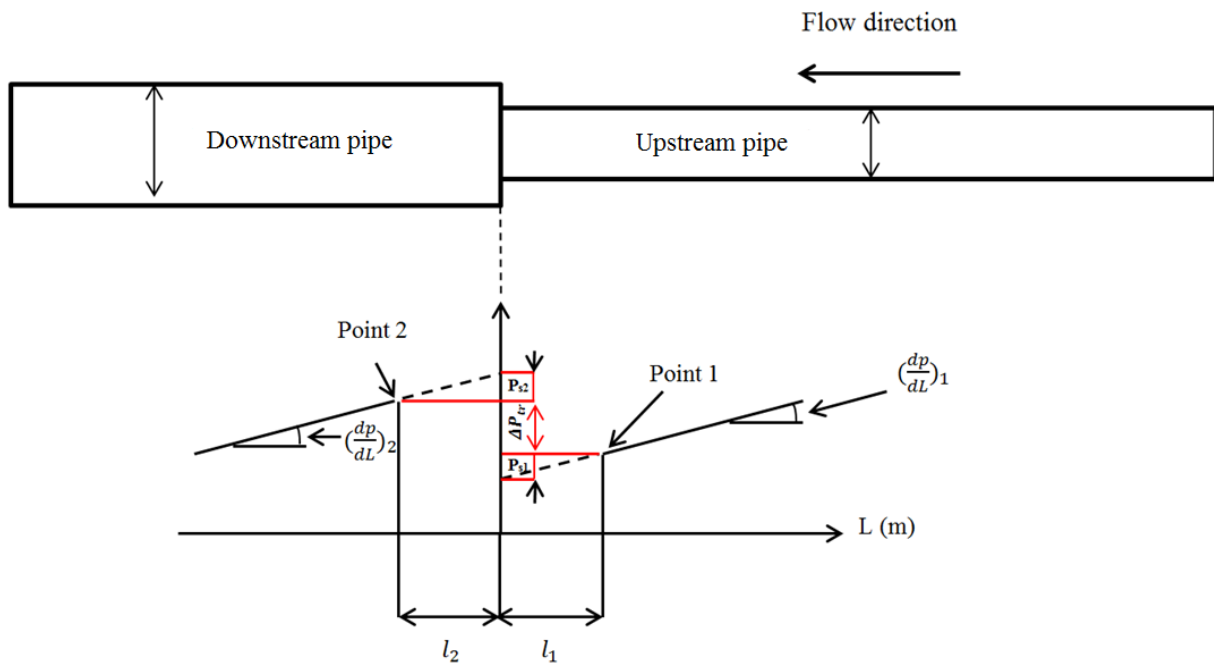
Figure 4-16 Schematic of pressure gradient method for sudden expansion

▪ Two points 1 and 2 are considered which corresponds to the nearest locations of pressure taps to the singularity. Point 1 and 2 refer to the pressure measured upstream and downstream, respectively.

▪ The pressure distribution for fully developed flow is represented by two straight lines, $\left(\frac{dp}{dL}\right)_1$ and $\left(\frac{dp}{dL}\right)_2$ for upstream and downstream pipes, respectively.

- The distances between points 1, 2 and the singularity plane are represented by l_1 and l_2, respectively.

- Δp_{tr} is the pressure drop across point 1 and 2 as measured by the transducer. by transducer between two arbitrary points 1 and 2.

- $P_{s,1}$ is a contribution to the value of the concentrated pressure drop ΔP_s given by $P_{s,1} = \left|\frac{dP}{dL}\right|_1 \cdot l_1$.

- $P_{s,2}$ is another contribution to the value of ΔP_s given by $P_{s,2} = \left|\frac{dP}{dL}\right|_2 \cdot l_2$.

- Therefore, the concentrated pressure gradient across the singularity plane can be calculated as:

$$\Delta P_s = P_2 + (\frac{dP}{dL})_2 \cdot l_2 - P_1 + \left(\frac{dP}{dL}\right)_1 \cdot l_1 = \Delta P_{tr} + P_{s,2} + P_{s,1} \qquad (4\text{-}3)$$

The resulting concentrated pressure drop (ΔP_s) is reported as a function of input water volume fraction (ε_w) in Figure 4-17-a (TS1) and 4-17-b-c (TS2 and TS4), at constant oil superficial velocity. It is evident that concentrated pressure drop increases with input water volume fraction for constant J_o, and also increases at constant ε_w with J_o.
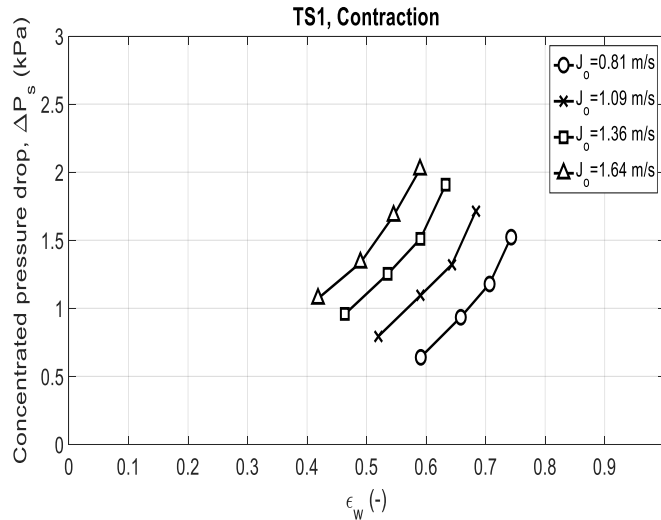
(a)
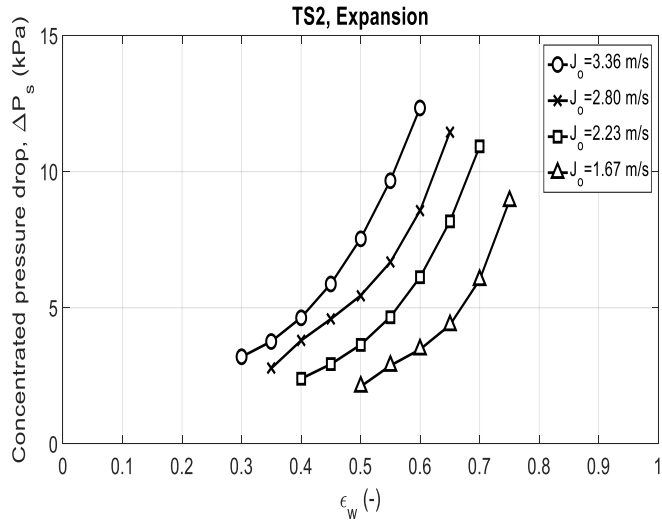
(b)
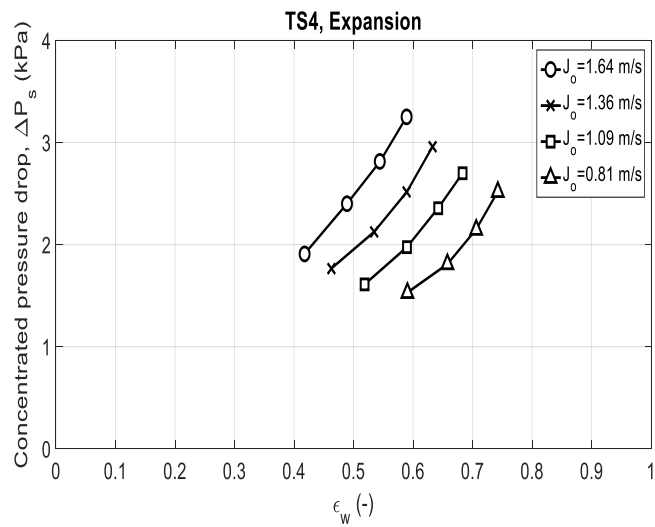
(c)

Figure 4-17 The concentrated pressure drop (ΔP_s) versus input water volume (ε_w) in different oil superficial velocity for a) TS1, b) TS2, and c) TS4

4.6 Determination of the loss coefficient

From a theoretical point of view, the concentrated pressure drop can be linked to the mechanical energy equation. Let us consider the generalized Bernoulli equation:

$$\frac{P_1}{\rho_m} + \frac{J_{m-1}^2}{2} + gh_1 = \frac{P_2}{\rho_m} + \frac{J_{m-2}^2}{2} + gh_2 + h_f \quad [\frac{J}{kg}] \tag{4-4}$$

Where, h_f, represents the energy loss due to friction, g is the acceleration due to gravity, h and P are the elevation and the pressure, respectively, and ρ_m is density. Since Equation 4-4 is widely used for single phase flow, it is needed to define a proper mixture density to account for two-phase flow. Under the assumption of homogeneous flow:

$$\rho_m = \varepsilon_w \rho_w + \varepsilon_o \rho_o \tag{4-5}$$

Considering upstream and downstream pipes at the same elevation, Equation 4-4 is rewritten as:

$$h_f = \frac{(P_1 - P_2)}{\rho_m} + \frac{J_{m-1}^2 - J_{m-2}^2}{2} \tag{4-6}$$

It is worth noting that subscripts 1 and 2 denote upstream and downstream pipes, respectively.

Assuming constant mixture density the mass conservation equation is simply given by:

$$J_{m-1} = J_{m-2}\frac{A_2}{A_1} \tag{4-7}$$

By substitution of Equation 4-7 in Equation 4-6 we have:

$$h_f = \frac{(P_1 - P_2)}{\rho_m} + \left(1 - \frac{J_{m-2}^2}{J_{m-1}^2}\right)\frac{J_{m-1}^2}{2} = \frac{(P_1 - P_2)}{\rho_m} + \left(1 - \frac{A_1^2}{A_2^2}\right)\frac{J_{m-1}^2}{2} = \frac{(P_1 - P_2)}{\rho_m} + \left(1 - \frac{D_1^4}{D_2^4}\right)\frac{J_{m-1}^2}{2} \tag{4-8}$$

For expansion $P_1 - P_2 = -\Delta P_{sing}$ and for contraction $P_1 - P_2 = \Delta P_{sing}$. By substitution of the measured concentrated pressure gradient into Equation (4-8), the final version of energy loss coefficient for abrupt expansion can be given by:

$$h_f = -\frac{\Delta P_{sing}}{\rho_m \frac{J_{m-1}^2}{2}}\frac{J_{m-1}^2}{2} + \left[1 - \left(\frac{D_1}{D_2}\right)^4\right]\frac{J_{m-1}^2}{2} = (-k_1 + k_2)\frac{J_{m-1}^2}{2} = k_{tot}\frac{J_{m-1}^2}{2}, \tag{4-9}$$

Where,

$$k_1 = \frac{\Delta P_{sing}}{\rho_m \frac{J^2_{m-1}}{2}} \qquad (4\text{-}10)$$

$$k_2 = \left[1 - \left(\frac{D_1}{D_2}\right)^4 \right] \qquad (4\text{-}11)$$

$$k_{tot} = k_2 - k_1 \qquad (4\text{-}12)$$

k_1 is the loss coefficient due to irreversibility, i.e. mechanical energy degradation. k_2 however only takes into account the geometrical configuration of the sudden change of cross-sectional area. The stronger change of cross-sectional area would result in more robust effect of k_2 on the total loss coefficient. For sudden contraction, Equation (4-9) holds provided that the signs of both terms on the right side are reversed. Since the value of k_2 is constant for a fixed geometrical configuration, only the results for k_1 will be presented and discussed. It has to be stressed that the definition of k_{tot} is merely conventional and related to the assumption of homogeneous flow, which is not generally verified. Hence, k_{tot} is simply an empirical parameter, useful to calculate ΔP_{sing} in a simple way.

4.7 Localized loss coefficient in liquid-liquid flow

Figure 4-18 (a-c) represents the respective variation of the localized loss coefficient (k_1) versus mixture superficial velocity. In all figures, different marker colors correspond to different superficial oil velocities. For TS1 and TS2, a single, best-fit line provides a proper correlation. A close observation of Figure 4-18 (a) and Figure 4-18 (b) reveals that the localized loss coefficient for TS1 is less that the case of abrupt expansion, e.g. TS2. Surprisingly, the results of the localized loss coefficient show a significantly decreasing trend for TS4 (which represents the stronger cross-sectional area ratio) by increasing mixture superficial velocity. It is worthwhile mentioning that all data crowd up quite well into the same line, irrespective of the superficial oil velocity.
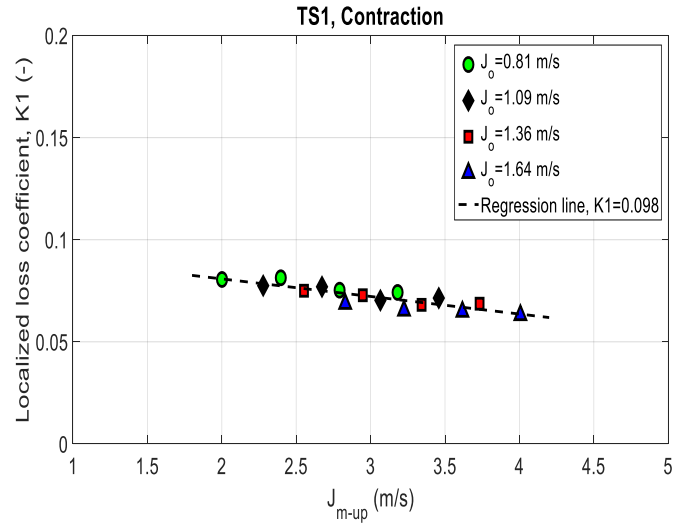
(a)
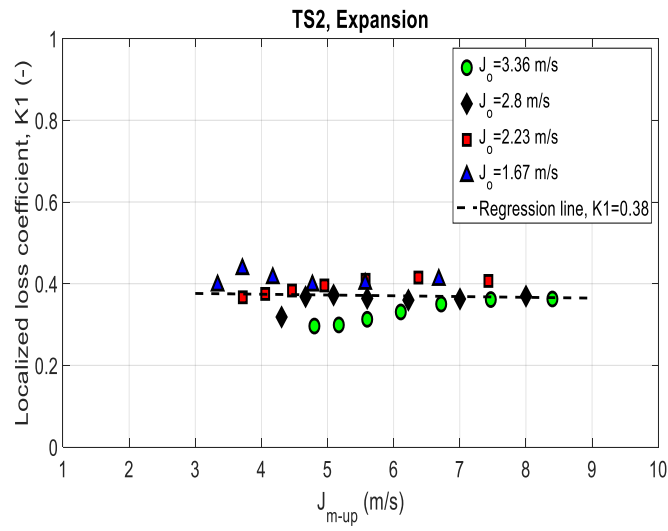
(b)
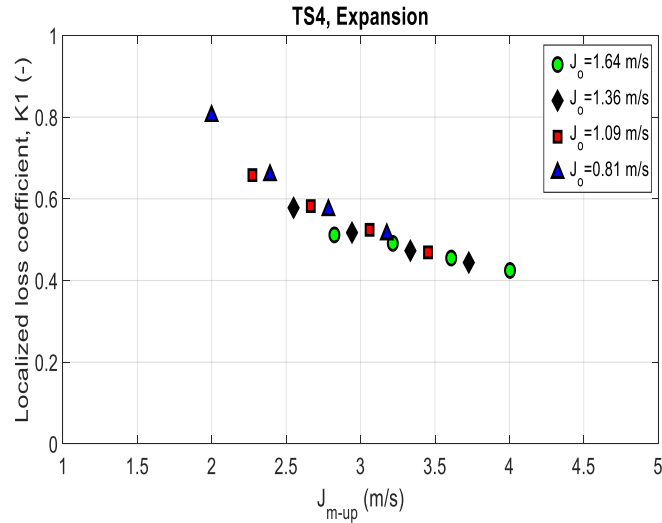
(c)

Figure 4-18 The localized loss coefficient (k_1) as a function of mixture volumetric flux upstream of singularity for a) TS1, b) TS2, and c) TS4

Another attempt was made to compare the total loss coefficient values (k_{tot}) with the reported values in the literature survey. Several researchers proposed empirical correlations to compute the loss coefficients for single-phase flow through abrupt contraction and expansion. Some of them are reported in Chapter 2. However, there are only two experimental works which reported the total loss coefficients in liquid-liquid flows. Hwang and Pal (1997) used very low viscosity oil and the main flow regimes was reported as oil-in-water and water-in-oil emulsion. Balakhrisna et al (2010) used two types of oils, which included lube oil (μ_o=0.2 Pa·s and ρ_o=960 kg/m^3) and kerosene (μ_o=0.0012 Pa·s and ρ_o=787 kg/m^3). Tables 4-6-a and 4-6-b listed the results of the total loss coefficients through contraction and expansion in the present experiment as well as the comparison with previous experimental data and empirical correlations. It is evident that in the literature models the effect of fluid properties has not been taken into account because the total loss coefficient is only presented as a function of diameter ratios. Table 4-6-a shows the wide range of the loss coefficient for sudden contractions varying from 0.20 by McCabe et al (1993) to 0.68 by Chishlom (1983). On the other hand, k_{tot} in the present experimental data is quite similar to the one measured by Balakhrisna et al (2010).

94

In Table 4-6-b dealing with the sudden expansion it is seen a better agreement with most of the experimental data, apart from the work by Hwang and Pal (1997). However, the latter deals with emulsions obtained from water and low-viscosity oil, i.e. a system strongly different from the one considered in the present work. Eventually, available models largely fail in predicting the loss coefficient.

Table 4-6-a Total loss coefficient for sudden contraction TS1

From experiment	Reported in the literature by				
	Chisholm (1983)	McCabe et al. (1993)	Hwang and Pal (1997)	Balakhrisna et al. (2010) Kerosene-water	Balakhrisna et al. (2010) Lube oil-water
	$k_{tot} = \dfrac{1}{[0.639\,(1-\sigma^2)^{0.5} + 1]}$	$k_{tot} = 0.4\,(1-\sigma^2)$			
0.45	0.68	0.20	0.54	0.38	0.48

Table 4-6-b Total loss coefficient for sudden expansion TS2

From experiment	Reported in the literature by				
	Borda-Carnot	Wadle (1989)	Hwang and Pal (1997)	Balakhrisna et al. (2010) Kerosene-water	Balakhrisna et al. (2010) Lube oil-water
	$k_{tot} = (1-\sigma^2)^2$	$k_{tot} = 2\sigma^2\,(1-\sigma^2)$			
0.37	0.26	0.49	0.47	0.4	0.43

4.8 Consideration about the holdup

The results of the measured oil holdup (H_o) versus input oil volume fraction (ε_o), collected from the work of Colombo et al (2015), under various superficial velocities are summarized in Figure 4-19 (a-d) and Figure 4-20 (a-b) for the ducts with sudden contraction from 50 mm to 30 mm, and from 50 mm to 40 mm, respectively. All the holdup data were measured downstream of the contraction. Considering Figure 4-19 (a-d), the value of H_o is always lower than ε_o, showing that oil moves faster than water. The dashed lines in Figure 4-19 and 4-20 present homogeneous flow conditions, where H_o is equal to input oil volume fraction (ε_o), i.e. the two phases have the same average velocity. The result is consistent with close observation of the flow patterns: for annular and eccentric annular flow prevail. In particular, eccentricity of oil core usually occurs at the lower oil flow rate (e.g. J_o=0.74 m/s in Figure 4-19-a), while at higher oil flow rate, the oil core is less eccentric (e.g. J_o=1.30 m/s in Figure 4-19-d). From the measured oil holdup, the oil-water slip ratio can be computed, see Equation 2-6 in Chapter 2. Figure 4-21 (a) and 4-21-b represent the slip ratio as a function of input water volume fraction for various superficial oil. For pipe contraction 50-30 mm, the oil-water slip ratio ranges from 1.26-1.62, while for the pipe contraction 50-40 mm it varies from 1.23-1.53. In all cases, the effective average velocity for oil is greater than for water since oil forms a core whereas water adjoins the pipe wall. The slip ratio parameter is also discussed in the CFD simulation analysis in Chapter 7.
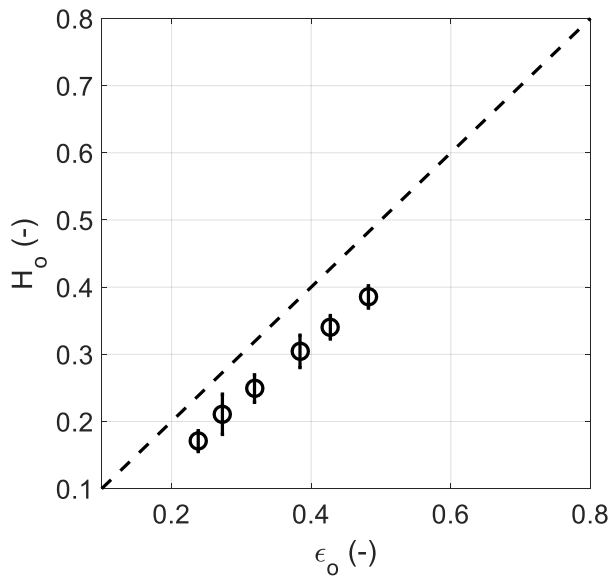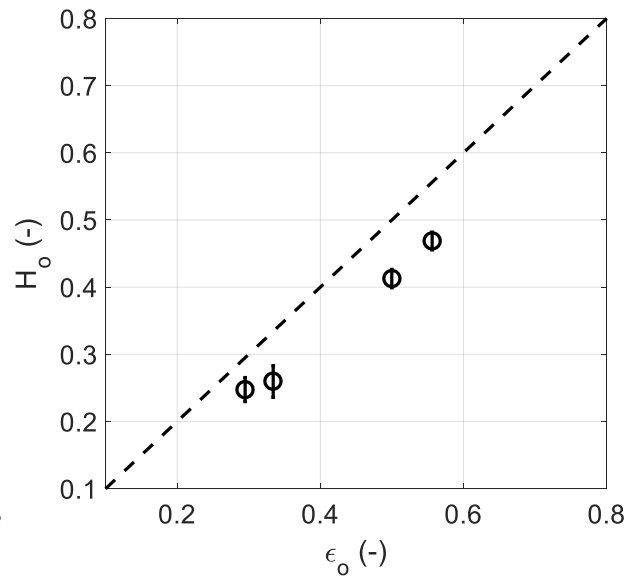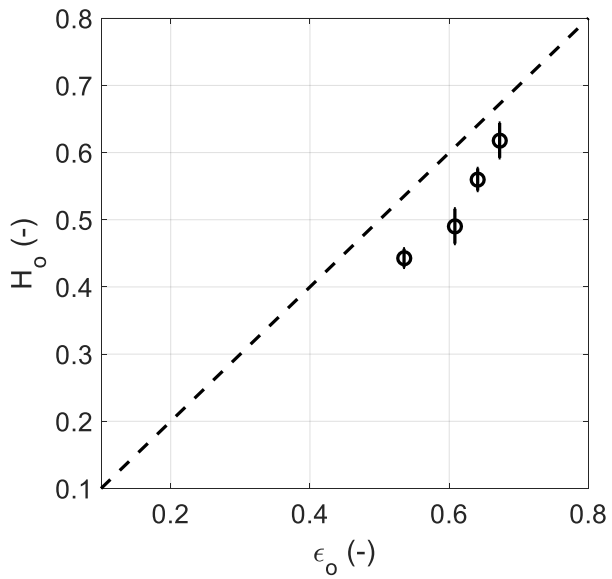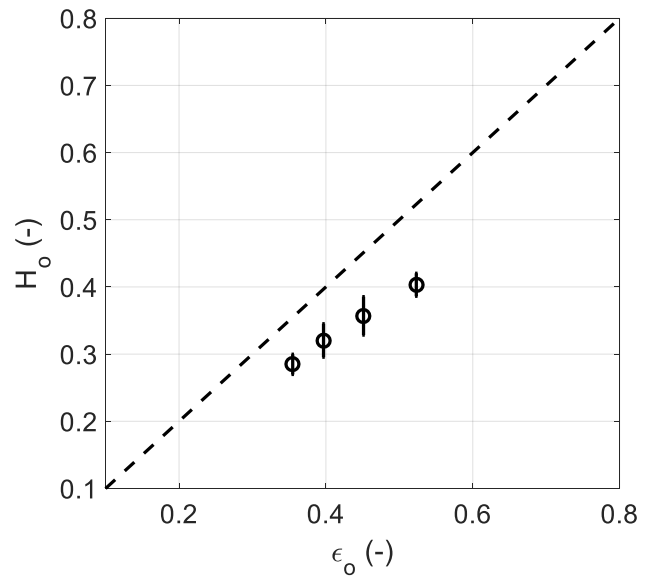
Figure 4-19 Oil holdup (H_o) versus input oil volume fraction (ε_o) for contraction 50-30 mm i.d. pipe at different oil superficial velocity; (a) J_o=0.74 m/s, (b) J_o=0.99 m/s, J_o=1.23 m/s, and J_o=1.30 m/s.
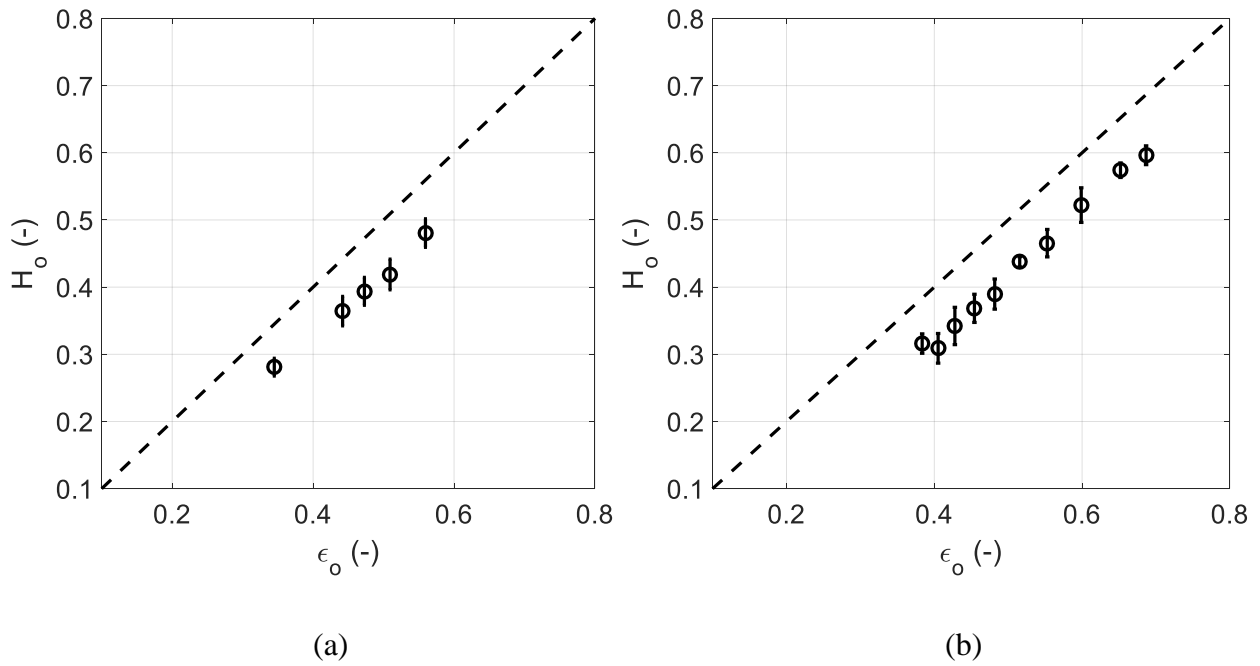
Figure 4-20 Oil holdup (H_o) versus input oil volume fraction (ε_o) for contraction 50-40 mm i.d. pipe at different oil superficial velocity; (a) J_o=0.70 m/s, (b) J_o=0.82 m/s.

(a)
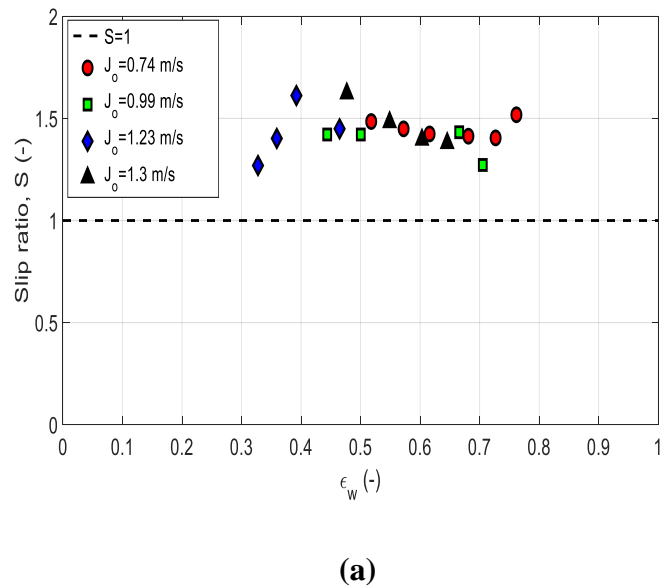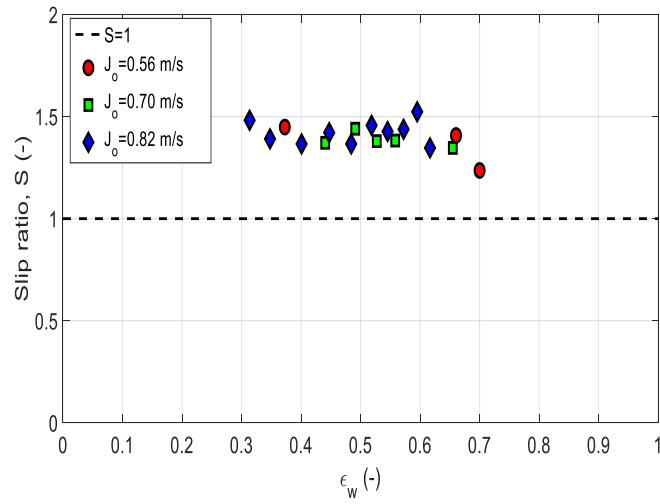
(b)

Figure 4-21 Oil-water slip ratio (S) as a function of water input volume fraction (ε_w) for various J_o for pipe configuration a) Contraction 40-30 mm i.d pipe, and b) Contraction 50-40 mm i.d. pipe

5 Theoretical modeling of viscous oil-water flow

5.1 Introduction

Flow characteristics of viscous oil-water through sudden expansion and contraction were investigated in Chapter 4. To understand the flow behavior within straight tube and the ducts undergoing sudden expansion and contraction, evaluation of previous empirical correlations and mechanistic models are reported in this Chapter. Furthermore, an attempt is made to predict the holdup and pressure drop based on the Two-Fluid model.

5.2 Water holdup and pressure gradient of viscous oil-water flow

From practical point of view, accurate estimation of the holdup and pressure gradient in viscous oil-water flow is crucially important. Simple empirical correlations and mechanistic 1-D models require few information but their applicability can be very restricted. On the other hand, CFD simulation tools can give much more detail since 3-D flow fields are obtained. However, the latter is not computationally cheap as compared to the former, which often provides suitable (though limited) information for industrial applications. There are major differences between empirical and mechanistic models to predict water holdup and pressure gradients. A unique mixture fluid is generally assumed for oil-water flow in the empirical models whereas rheological properties of fluids and friction factors are calculated based on empirical correlations. However, mechanistic models treat two fluids separately with two sets of transport equations. They are often so-called two-fluid models. Such models need closure relationships for frictional terms to solve the equations for pressure gradient and phase holdup. A review on existing models in the literature will be presented in the following section in chronological order.

5.3 Reviews on models of oil-water flow

(1) Oliemans (1986)

An empirical correlation was developed by Oliemans (1986) in which water holdup measured by photographs was correlated to input water volume fraction as:

$$H_w = \varepsilon_w[1 + 0.2(1 - \varepsilon_w)^5] \qquad (5\text{-}1)$$

This correlation was developed, considering a very viscous oil (μ_o=3.0 Pa·s) in a duct of 51 mm i.d.

(2) Arney et al. (1993)

A simple empirical correlation to predict water holdup was proposed by Arney et al. (1993).

$$H_w = \varepsilon_w[1 + 0.35\,(1 - \varepsilon_w)] \qquad (5\text{-}2)$$

The water holdup is expressed in terms of input water volume fraction and it is similar to the correlation developed by Oliemans (1986). They used broader experimental data base to predict water holdup. Furthermore, Arney et al. (1993) considered perfect liquid-liquid core-annular flow and applied the Navier-Stokes equation to relate pressure gradient to total flow rate. A two-phase flow characteristic Reynolds number was defined for core-annular flow as a function of rheological properties of phases, pipe diameter, water-holdup, and mixture superficial velocity, such as:

$$Re_A = \frac{\rho_c D\, J_m}{\mu_w}\left[1 + \eta^4\left(\frac{\mu_w}{\mu_o} - 1\right)\right] \qquad (5\text{-}3)$$

$$\eta = \sqrt{1 - H_w} \qquad (5\text{-}4)$$

$$\rho_c = (1 - H_w)\rho_o + H_w\rho_w \qquad (5\text{-}5)$$

To compute the characteristic two-phase Reynolds number from Equation (5-3), information of water holdup is required, which is calculated from Equation (5-2).

Arney et al. (1993) predicted the pressure gradient following the Darcy-Weisbach equation as:

$$-\frac{dp}{dx} = \frac{f}{D}\frac{\rho_c J_m^2}{2}$$
(5-6)

Where, f is the friction factor for the perfect core-annular flow and is expressed for laminar flow as:

$$f = \frac{64}{Re_A}$$
(5-7)

For turbulent flow, the Blasius formulation was used, therefore:

$$f = 0.316 \, Re_A^{-0.25}$$
(5-8)

Notice that equation (5-7) and (5-8) are the conventional expressions of the friction factor as used for single-phase flow, owing to the special definition of Re_A.

(3) Brauner (1998)

Brauner (1998) developed a mechanistic model based on the two-fluid approach for two immiscible fluids, denoted in the following with subscripts w and o, in a horizontal, slightly inclined duct. The schematic of CAF configuration is illustrated in Figure (5-1). By assuming fully developed flow, the integral forms of the momentum equations for the water (w) in the annular domain and oil (o) in the core can be written as:
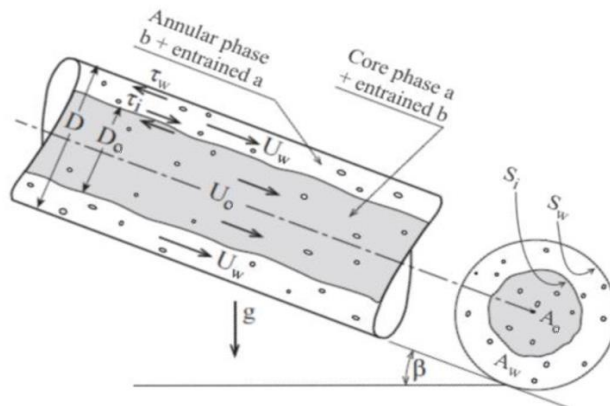
Figure 5-1. Schematic of CAF configuration (Brauner, 1998)

$$-A_w \frac{dp}{dx} - \tau_w S_w + \tau_i S_i + \rho_w A_w \, g \, \sin\beta = 0 \qquad\qquad (5\text{-}9)$$

$$-A_o \frac{dp}{dx} - \tau_i S_i + \rho_o A_o \, g \, \sin\beta = 0 \qquad\qquad (5\text{-}10)$$

In the above equations, A_w, and A_o are the actual areas occupied by water and oil, respectively. Here, pure oil phase and pure water phase, without entrainment of one phase into another are assumed. Eliminating the pressure gradient terms, it yields:

$$-\tau_w \frac{S_w}{A_w} \pm \tau_i S_i \left(\frac{1}{A_o} + \frac{1}{A_w}\right) + (\rho_w - \rho_o) \, g \, \sin\beta = 0 \qquad\qquad (5\text{-}11)$$

It is worth noting that the last term in Equation (5-11) vanishes in the case of horizontal pipe. As conventionally used in mechanistic two-fluid models, the wall shear stress (τ_w) is correlated to the corresponding friction factor f_w through the annulus hydraulic diameter D_w and effective water Reynolds number:

$$\tau_w = f_w \frac{f_w U_w^2}{2}; \qquad f_w = C_w \left(\frac{\rho_w U_w D_w}{\mu_w}\right)^{-n_w}; \qquad D_w = \frac{4 A_w}{S_w} \qquad\qquad (5\text{-}12)$$

Where U_w and S_w are the effective water velocity in the annulus and the perimeter of the wall, respectively.

The interfacial shear stress between water and oil, τ_i, can be obtained as:

$$\tau_i = f_i \frac{\rho_o (U_o - U_w)^2}{2}; \qquad f_i = F_i C_c \left(\frac{\rho_o U_o D_o}{\mu_o}\right)^{-n_o} \qquad\qquad (5\text{-}13)$$

The coefficients C_c, C_w, n_w, and n_o are selected based on the flow regime. Several combinations can be considered, which includes laminar-laminar (L-L), laminar-turbulent (L-T), turbulent-laminar (T-L), and turbulent-turbulent (T-T) regimes. For laminar flow C=16 and n=1, whereas C=0.046 and n=0.2 is set for turbulent flow conditions. F_i is a coefficient accounting for the waviness of the interface. In the case of long smooth waves as observed for liquid-liquid flows, it is assumed F_i=1.

Brauner (1998) used the following to correlate the two-phase pressure drop to the single phase one.

$$X^2 = \frac{\left(\frac{4C_w}{D}\right)\left(\frac{\rho_w J_w D}{\mu_w}\right)^{n_w}\left(\frac{\rho_w J_w^2}{2}\right)}{\left(\frac{4C_c}{D}\right)\left(\frac{\rho_o J_o D}{\mu_o}\right)^{n_c}\left(\frac{\rho_o J_o^2}{2}\right)} = \frac{\Delta p_w/L}{\Delta p_o/L} \qquad (5\text{-}14)$$

$$Y = \frac{(\rho_w - \rho_o)\, g\, \sin\beta}{\left(\frac{4C_c}{D}\right)\left(\frac{\rho_o J_o D}{\mu_o}\right)^{n_c}\left(\frac{\rho_o J_o^2}{2}\right)} \qquad (5\text{-}15)$$

For horizontal flows, Y=0. The parameter X^2 is the classical Lockhart-Martinelli parameter. The dimensionless two-phase pressure gradient is defined as:

$$\phi_A = \frac{-\left(\frac{dp}{dx}\right)}{\left(\frac{4C_c}{D}\right)\left(\frac{\rho_o J_o D}{\mu_o}\right)^{n_c}\left(\frac{\rho_o J_o^2}{2}\right)} \qquad (5\text{-}16)$$

The term in the denominator is equivalent to the pressure gradient occurring when the oil flows alone in the duct (i.e. with its superficial velocity). Brauner (1998) provided the simple explicit solutions for the in-situ holdup and dimensionless pressure gradient for the case of laminar oil (with laminar or turbulent annular water flow). Since in the present work water always have superficial velocities corresponding to turbulent flow regime, only expressions regarding the case of laminar oil-turbulent water are reported in Table 5-1. In more recent work, Ullmann and Brauner (2004) provided an analytical solution of the two-fluid model, suggesting an improved correlation for the interfacial shear stress. The equation provided by Ullmann and Brauner (2004) is also presented in Table 5-1, with the parameter c_i^0=1.17, as proposed by Grassi et al. (2008) for viscous oil-water flow.

Table 5-1 Water holdup and pressure gradient for Laminar oil-Turbulent annular flow

Author	Model	Additional information
Brauner (1998)	$$H_w = 1 - \left(\frac{\phi}{(\phi X) + \phi + 1}\right)$$ $$\phi_A = \frac{K_1}{\phi}\left[\frac{(K_1\phi)^{0.5} + \phi + 1}{(K_1\phi)^{0.5} + 1}\right]^2$$	$\phi = J_o/J_w$ $$K_1 = \frac{0.046}{16}\frac{\mu_w}{\mu_o}Re_{ws}^{0.8}$$
Ullmann and Brauner (2004)	$$H_w = \frac{c_i^0/2 - X^2\,\phi/F_i + \frac{c_i^0}{2}\left[1 + 4X^2\left(\frac{\phi}{c_i^0}\right)^2\right]^{0.5}}{c_i^0 + \phi - X^2\,\phi/F_i}$$	$c_i^0 = 1.17$ $$X^2 = \frac{0.046}{16}\frac{\mu_w}{\mu_o}\frac{1}{\phi}Re_{ws}^{0.8}$$

5.4 Mechanistic model for water-lubricated flow

In the current study, an attempt was made to predict the holdup and pressure drop based on the Two-Fluid model. The holdup value has been directly determined from the measured pressure drop. The advantage of this method relies on the fact that it is much simpler to measure pressure drop rather than holdup, and in many industrial applications, the latter cannot be measured at all. The holdup has been correlated to the input volume fraction and compared with the available models.

5.4.1 Theoretical approach

The Two-Fluid Model (TFM) for horizontal pipes, assuming fully developed flow, writes

$$\begin{cases} -A_o \dfrac{dp}{dx} - \tau_i S_i = 0 \\[2mm] -A_w \dfrac{dp}{dx} - \tau_w S_w + \tau_i S_i = 0 \end{cases} \tag{5-17}$$

where "*o*" denotes the core phase (oil) and "*w*" the phase in contact with the wall (water), *S* the wetted perimeter and A the cross-sectional area of the single phase, as indicated in Figure 5-2.
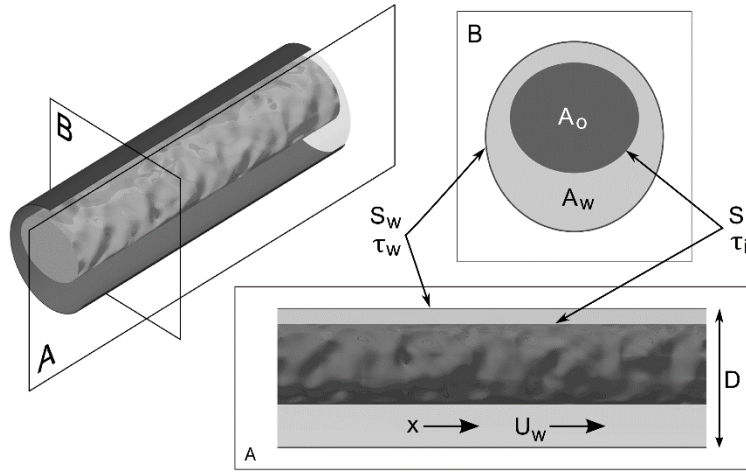
Figure 5-2. Schematic of core-annular flow

Eliminating the interfacial shear stress, and denoting the overall cross-sectional area $A = A_o + A_w$, it follows

$$-A \frac{dp}{dx} - \tau_w S_w = 0 \tag{5-18}$$

The wall shear stress can be replaced making use of the friction factor as

$$\tau_w = f_w \frac{\rho_w U_w^2}{2} \tag{5-19}$$

where the friction factor depends on the water Reynolds number. Introducing the water holdup as the ratio of the superficial velocity J_w to the actual one U_w

$$H_w = \frac{J_w}{U_w} \tag{5-20}$$

and the hydraulic diameter for the water phase (adjoining the pipe wall, see Figure 5-2)

$$D_w = \frac{4A_w}{S_w} = H_w D \tag{5-21}$$

the Reynolds number is then

$$\mathrm{Re}_w = \frac{D_w U_w}{\nu_w} = \frac{DJ_w}{\nu_w} \tag{5-22}$$

so that

$$f_w = C_w \mathrm{Re}_w^{-n_w} \tag{5-23}$$

For the laminar flow regime $C_w = 16$ and $n_w = 1$, whereas for developed turbulent flows, the Blasius formulation is often used; accordingly, $C_w = 0.079$ and $n_w = 0.25$ for Re < 50000. $C_w = 0.046$ and $n_w = 0.2$ for Re > 50000.

Replacing equation (5-19) to (5-23) in (5-18), the water holdup as a function of the superficial velocity and the measured pressure drop per unit length results

$$H_w = \left[\frac{C_w \left(\frac{\rho_w J_w D}{\mu_w} \right)^{-n_w} \rho_w J_w^2}{\left(-\frac{dp}{dx} \right) \frac{D}{2}} \right]^{0.5} \tag{5-24}$$

5.5 Model validation

Understanding the application ranges of the above models is crucially important, the accuracy of the empirical and mechanistic models can be evaluated by comparing experimental data and predicted counterpart. In the following sections, the holdup and pressure drop prediction are compared with experimental data for very viscous oil-water flow.

5.5.1 Holdup estimation

Different experimental campaigns were run to analyse test section configurations including pipes with uniform diameter or upstream/downstream of sudden variations in the cross-sectional area. In all the cases, the Reynolds number of water, Equation (5-22), resulted within about 17000 and 102000 (turbulent range) and the qualitative behaviour of the pressure drop data showed quite similar characteristics. Thus, in the following, reference is made to pipes with D = 30 mm, for which data can be compared in all the tested configurations.

Starting with the straight tube, the pressure gradient is reported as a function of the water input fraction, ε_w, for the different oil superficial velocities, J_o, in Figure 5-3. As expected, the pressure gradient increases with J_o, at constant ε_w. On the other hand, the data points at constant J_o show that the pressure gradient increases with the water content. This confirms that for core-annular flows the pressure drop lowers by reducing the water content and hence thinning the water annulus, see Charles and Redberger (1962). Incidentally, parabolic fitting seems to reproduce very well the behaviour with a regression coefficient always higher than 0.99. Moreover, it has been observed that interface instability may determine a sudden transition to stratified-wavy flow, if the mixture velocity, J_{mix}, lowers below a critical value (Colombo et al, 2012). This would cause an abrupt increase in the pressure drop. It is customary to define the inverse of pressure reduction factor, R, as introduced in Chapter 4 (section 4-3-2), as the inverse of the ratio between the two-phase pressure drop and the pressure drop of the oil-only flow with the same superficial velocity.
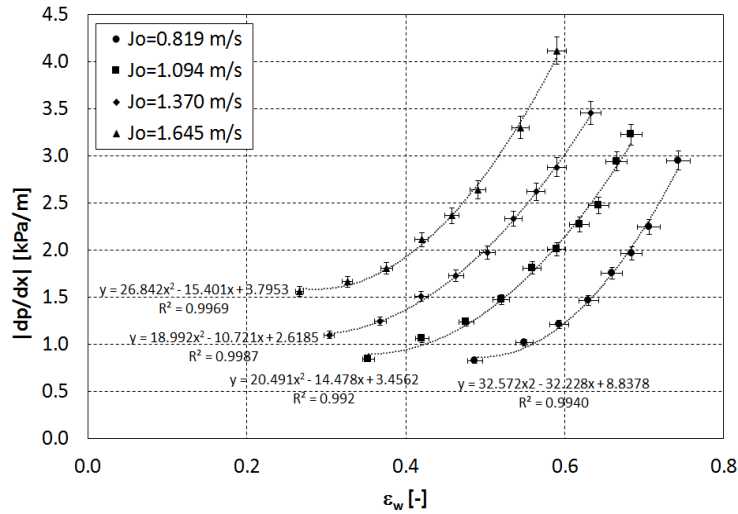
Figure 5-3. Pressure gradient versus water input fraction at constant oil superficial velocity (straight tube, D = 30 mm)

Figure 5-4 shows the inverse of pressure reduction factor (R) as a function of the water input fraction, ε_w, for the different oil superficial velocities, J_o. The monotonic behaviour shows that all the operating conditions correspond to stable core-annular flow regimes. A straight line fits properly the data and the slope seems to lower by increasing J_o. It is worth noting that the same pressure reduction factor is achieved at a reduced water input fraction as the oil superficial velocity increases.

Quite similar characteristics have been found for the flow upstream and downstream of an abrupt change in the cross-sectional area. Figure 5-5 compares the pressure gradient as a function of the water input fraction, ε_w, for the different oil superficial velocities, J_o, for all the configurations. Evidently, the plot reproduces the behaviour of Figure 5-3 with a slightly higher dispersion of data points. This seems to arise from the perturbation caused by the sudden contraction: though the flow regime remains annular, it has been observed that the oil-water interface becomes more irregular and shows a tendency to form small drops, see Balakhrisna et al (2010) and Colombo et al. (2015).

110
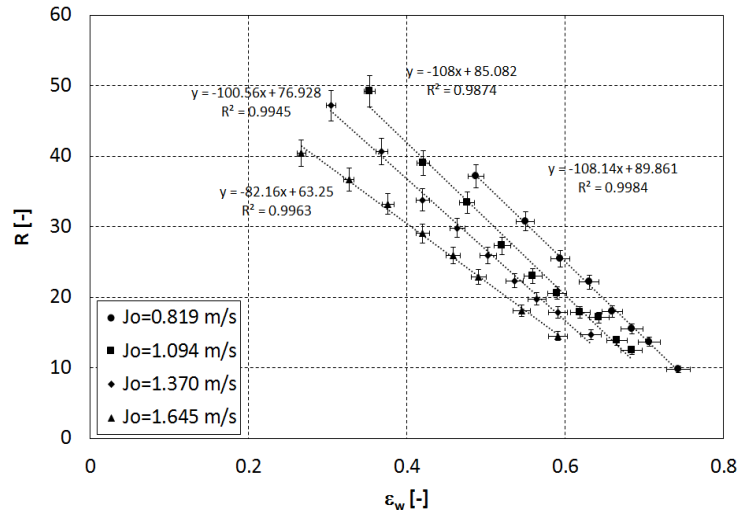
Figure 5-4. The inverse of pressure reduction factor (R) versus water input fraction (ε_w) at constant oil superficial velocity (straight tube, D = 30 mm)
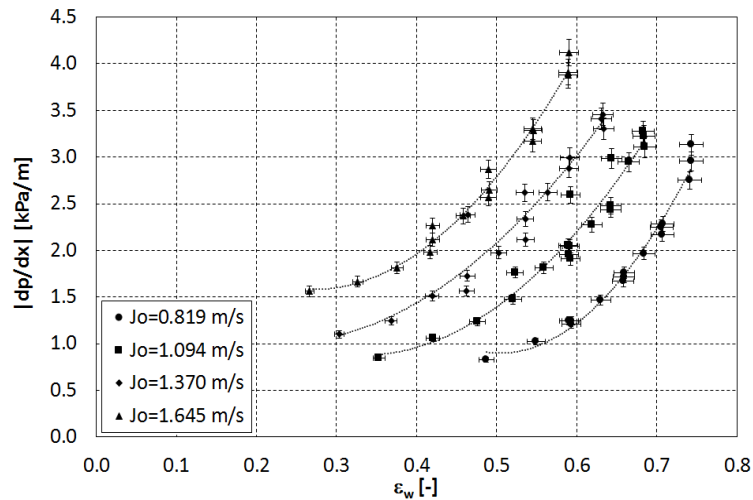
Figure 5-5. Pressure gradient versus water input fraction at constant oil superficial velocity (all data, D = 30 mm)

The water holdup is calculated from the measured pressure gradient according to Equation (5-24). It is reported in Figure 5-6 together with the experimental data collected by means of the quick closing valves technique for pipes of 30 mm and 40 mm i.d., respectively, see Colombo et al (2015). Substantial agreement is found between the measured and the calculated values.
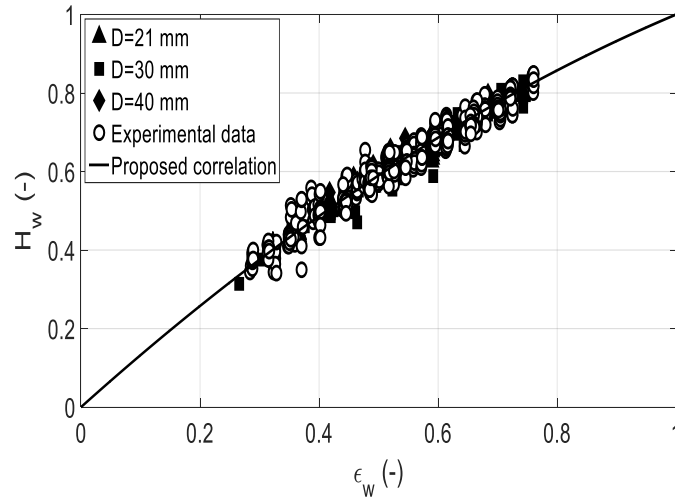
Figure 5-6. Water holdup versus water input fraction. Comparison between quick-closing valves data and TFM prediction

As previously mentioned, according to Arney et al. (1993), the water holdup as a function of the water input fraction can be expressed by a parabolic fitting

$$H_w = \varepsilon_w \left[1 + C(1 - \varepsilon_w) \right] \tag{5-25}$$

Least square fitting gives $C = 0.356$ with regression parameter $R^2 = 0.98$ for the calculated holdup, $C = 0.358$ with regression parameter $R^2 = 0.95$ for the measured holdup, and $C = 0.357$ with regression parameter $R^2 = 0.95$ for both calculated and measured holdup. Hence, a unique value of 0.36 is assumed without significant differences (solid line in Figure 5-6).

Mean Percentage Error (MPE) and Mean Absolute Percentage Error (MAPE) are defined as:

$$MPE = \frac{100\%}{N} \sum_{i=1}^{N} \frac{a_i - f_i}{a_i} \tag{5-26}$$

$$MAPE = \frac{100\%}{N} \sum_{i=1}^{N} \left| \frac{a_i - f_i}{a_i} \right| \tag{5-27}$$

where a_i is the actual value of the quantity being forecast, f_i is the forecast, and N is the population of the sample.

Accordingly, Equation (5-25) predicts the holdup data with $MPE = 0.1\%$ and $MAPE = 2.9\%$.

These findings are in very good agreement with Arney et al. (1993) that deals with holdup measurements for core-annular flows of waxy crude oil and No. 6 fuel oil, leading to $C = 0.35$ (see section 5-3). Figure 5-7 reports the comparison of Equation (5-25) and all the available experimental data from Charles et al (1961), Oliemans (1986), Sinclair (1970), and Bai et al (1992). *MPE* is 0.2% and *MAPE* is 3.8%. *MAPE* values indicate a very satisfactory accuracy of the prediction, whereas the very small *MPE* indicates that the forecast by Equation (5-25) is not significantly biased.
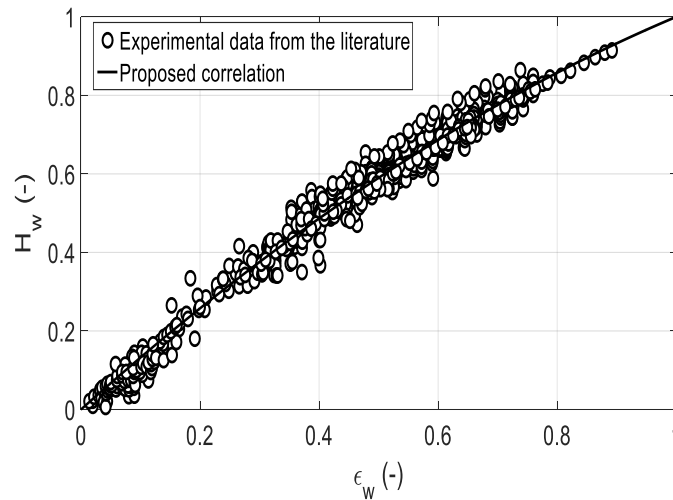
Figure 5-7. Water holdup versus input water volume fraction, Comparison between the proposed correlation and all the available data from the literature

On the other hand, Figure 5-8 reports the comparison between Equation (5-25) and the other models available in the literature for core-annular flow of liquid-liquid mixtures, listed in section 5-3 (Arney et al. correlation (1993) is not reported since, being in the same form as Equation (5-25), with $C = 0.35$ instead of 0.36, it cannot be distinguished).

The model by Oliemans (1986) always underestimates the water holdup with $MPE = -13\%$ and $MAPE = 16\%$. The model by Ullmann and Brauner (2004), which generalizes a former result from Brauner (1998), results slightly underestimating with $MPE = -0.5\%$ and $MAPE = 8.4\%$.
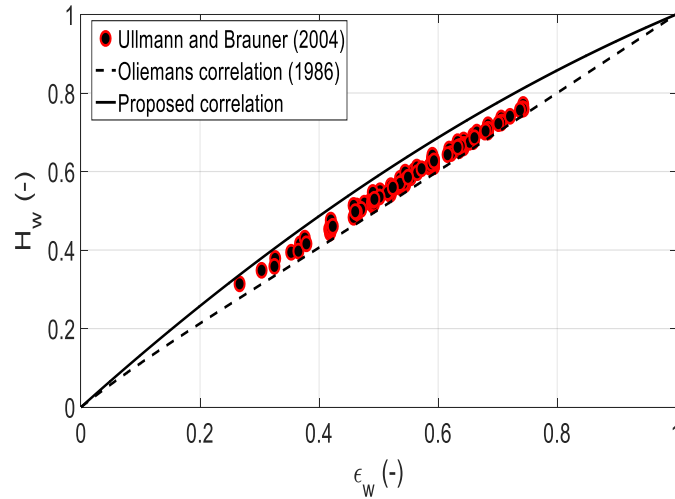
Figure 5-8 Water holdup versus input water volume fraction, comparison between the proposed model and available models in the literature

5.5.2 Pressure drop estimation

Once a suitable expression for the holdup is found, the proposed formulation of two-fluid model, equation (5-24) can be rearranged to equation (5-28) to predict the pressure drop.

$$-\frac{dp}{dx} = 2C_w \left(\frac{\rho_w J_w D}{\mu_w}\right)^{-n_w} \frac{\rho_w J_w^2}{D H_w^2} \qquad (5\text{-}28)$$

Prediction of pressure gradients by Arney et al. (1993), Brauner (1998), and the proposed model are compared with experimental data, shown in Figures 5-9 (a-d) to 5-11 (a-d), respectively. In each Figure, the prediction of pressure gradient is compared with measured counterpart, considering ducts with internal pipe diameters: (a) D=21 mm, b) D=30 mm, c) D=40 mm, and d) D=50 mm. The models by Arney et al. (1993) and Brauner (1998) give a quite similar prediction of pressure gradients. It is seen that both models overestimate the measured pressure gradients for pipe diameters 21 mm, 30 mm, and 40 mm. However, they underestimate the measured pressure gradients for D=50 mm. Both models gave satisfactory prediction of pressure gradients, with 80% and 87% of data falling within ±30 % relative error for Brauner (1998) and Arney et al. (1993), respectively. Comparing of the two models, it can be seen that the model by Arney et

al. (1993) shows slightly better performance than Brauner (1998) in the whole range of flow conditions under investigation.

(a)

(b)

(c)

(d)
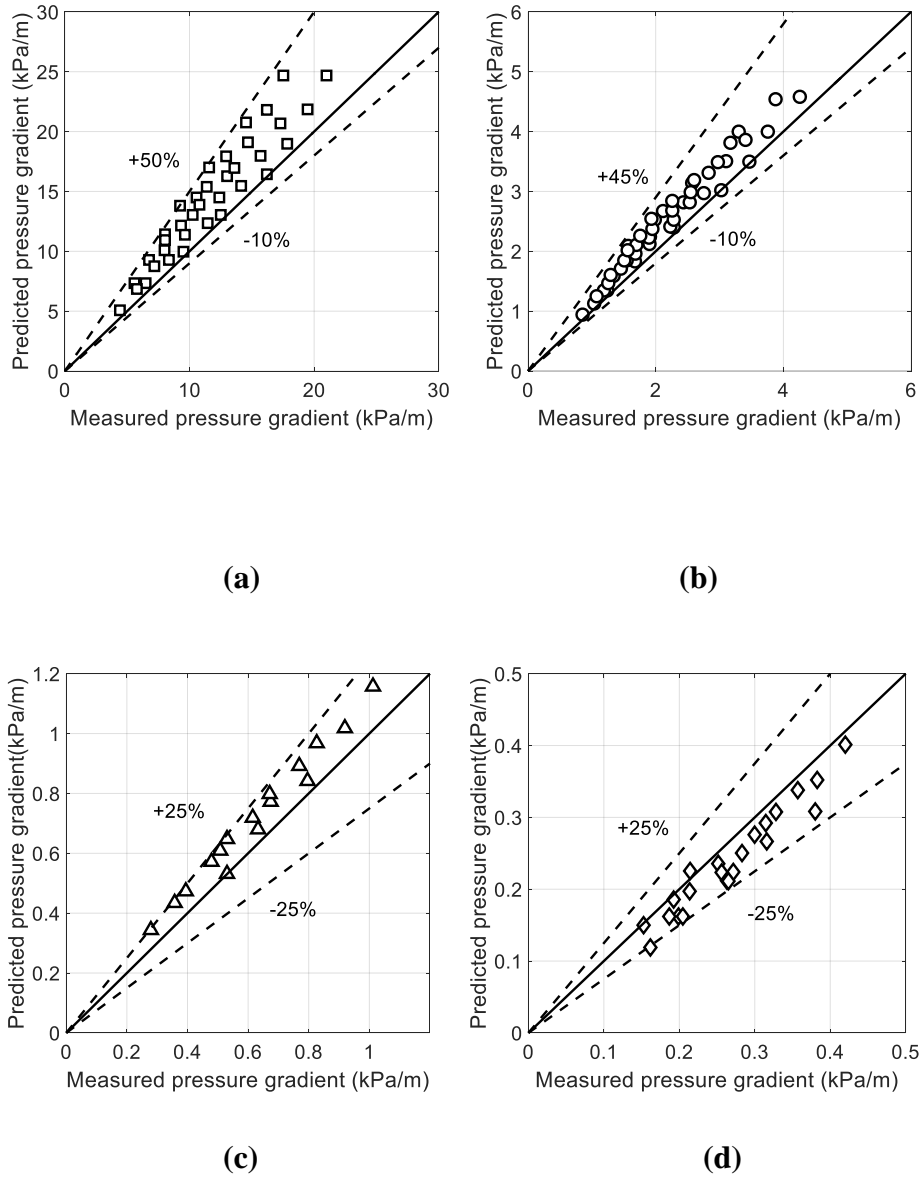
Figure 5-9 Comparison between measured pressure gradients and prediction from Arney et al. (1993) for a) D=21 mm, b) D=30 mm, c) D=40 mm, and d) D=50 mm
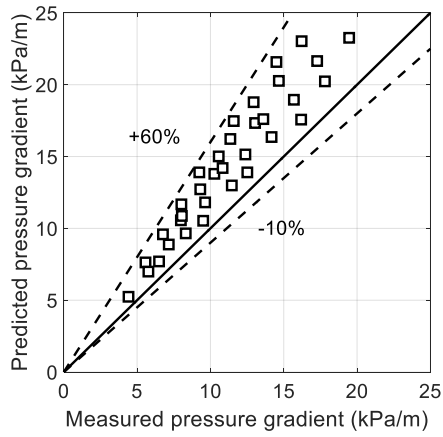
(a)
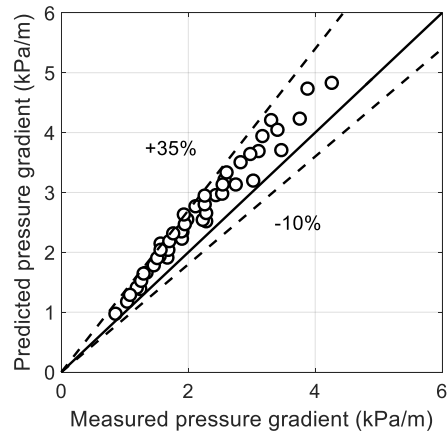
(b)
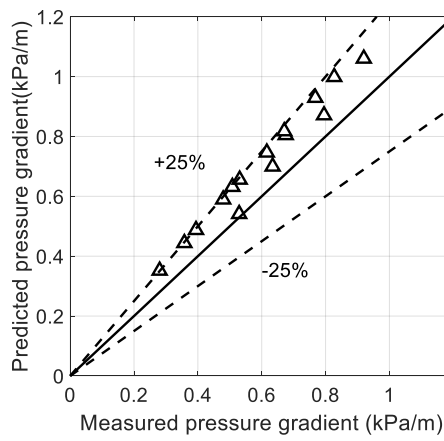
(c)
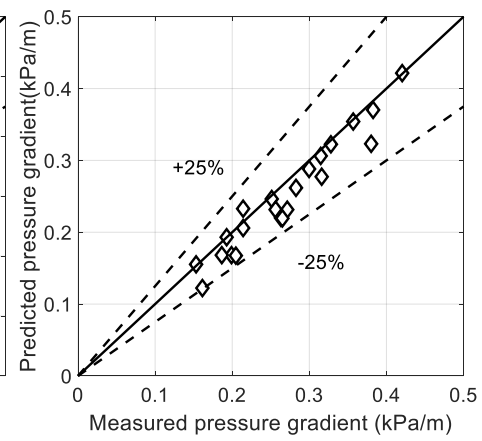
(d)

Figure 5-10 Comparison between measured pressure gradients and prediction from Brauner (1998) for a) D=21 mm, b) D=30 mm, c) D=40 mm, and d) D=50 mm

A comparison between the measured pressure gradient and the prediction from the model proposed in the current study is depicted in Figure 5-11 (a-d). Overall, 85 % and 98 % of the data fall within ±20 % and ±30 % of relative error, respectively. The improvement in the prediction is related to the fact that an empirical expression of the water holdup has been adopted instead of a model for the interfacial shear stress as a closure relationship for the Two-Fluid model. Table 5-2 shows in summary the statistical analysis of the performance for the selected models.

Comparison between the predicted pressure reduction factors from the model proposed and experimental data is illustrated in Figure 5-12. The dashed lines show the upper and lower limits of +35 % and -35 %, respectively. Almost 99% of the data are predicted within a percentage error of ±30 %.

(a)   **(b)**

(c)   (d)
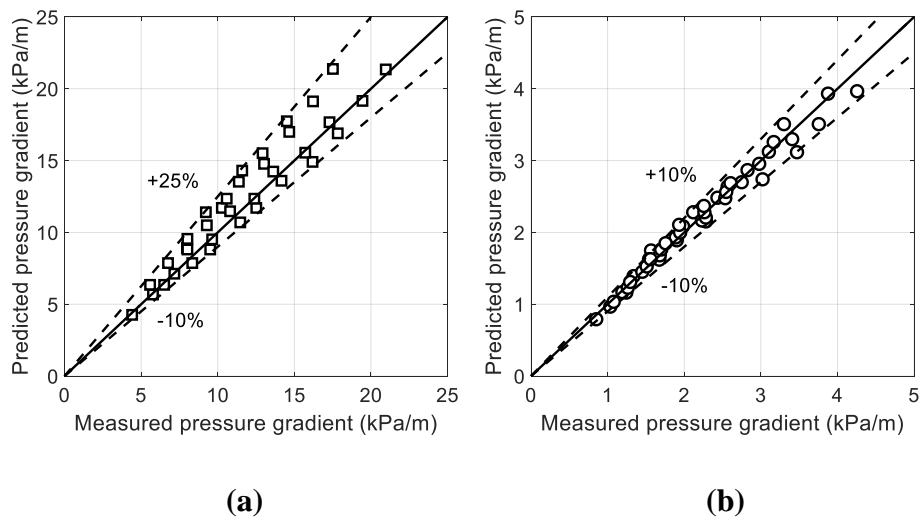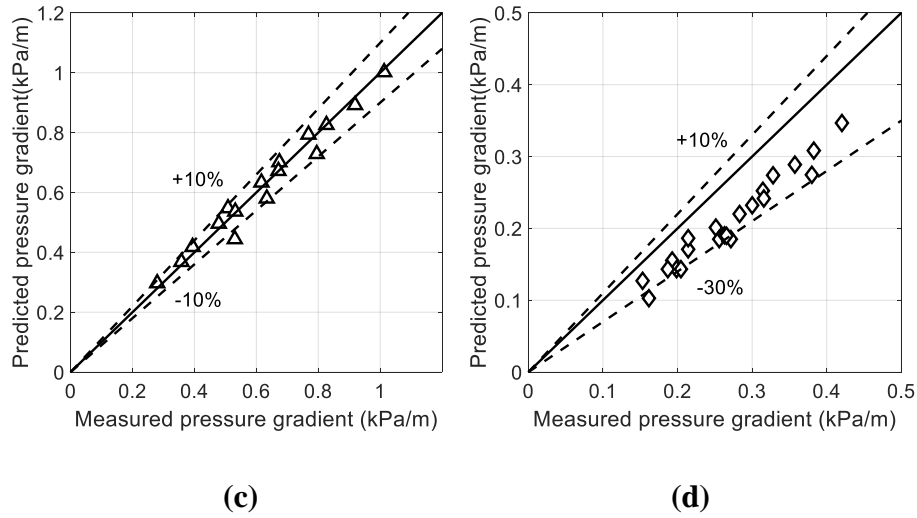
Figure 5-11 Comparison between measured pressure gradients and prediction from the model proposed in the current study for a) D=21 mm, b) D=30 mm, c) D=40 mm, and d) D=50 mm

Table 5-2 Statistical analysis of the performance of available pressure gradient models for viscous oil-water flow

Model	Average relative error (%)	Maximum relative error (%)	Minimum relative error (%)	MAPE (%)
Arney et al. (1993)	13.7	49.5	-26.5	17.9
Brauner (1998)	18.3	50	-24.1	21.3
Proposed	-2.1	23.5	-36.4	9.3
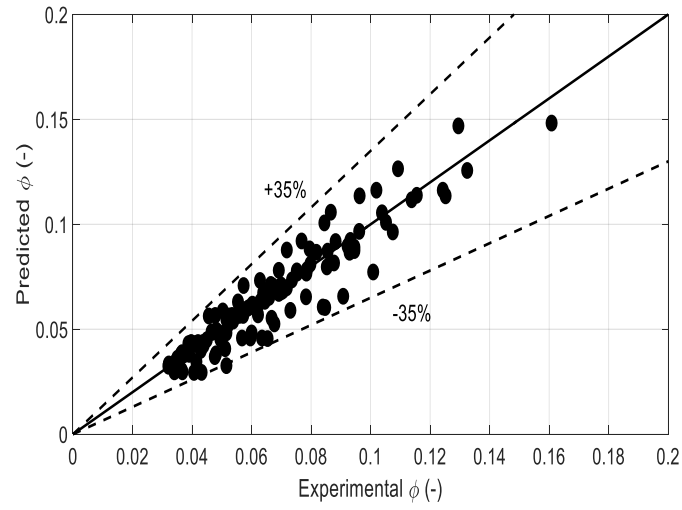
Figure 5-12 Comparison between measured pressure reduction factor and prediction from the model proposed in the current study

6. Experimental and mathematical modeling of multiphase flow through Venturi and Nozzle flow meters

6.1 Introduction

Information of phase holdup, pressure gradient and flow pattern is fundamental to properly characterize the flow behavior through differential pressure devices. From industrial point of view, the reduced number of instruments to measure the total volumetric and individual phase flow rate is important both from economical aspects and space requirements. If the phase holdup and flow pattern of multiphase flow is correctly determined, the application of multiphase differential pressure flow meters would result in estimation of the volumetric flow rate with a reasonable accuracy.

This Chapter reports on experimental and modeling activities on two differential pressure flow meters, namely, Venturi Flow Meter (VFM) and Nozzle Flow Meter (NFM) that have been realized in Plexiglass to allow flow visualization inside the instrument. The concentrated pressure drop across VFM and NFM were measured and plotted as a function of superficial velocity of phases for both oil-water two-phase and oil-water-gas three phase flow. Furthermore, distributed pressure drop upstream and downstream to the devices have been measured and analyzed because this information is required for modeling purposes. A new model was developed to compute the total and individual volumetric flow rate of phases in oil-water flow. The model correlates the total volumetric flow rate based on calibration curve between total volumetric flux and concentrated pressure drop. The experimental results have been evaluated as a function of superficial velocity of phases.

6.2 Test section

The experimental facility is described in more details in Chapter 3. In the following, only the details pertaining to the flow meters under investigation are reported. The test section is composed of 12 m long transparent Plexiglass tube, placed horizontally with the VFM and NFM installed near at the half of the test section length. Both upstream and downstream pipes have an internal diameter of D=40 mm. The VFM and NFM were manufactured according to the indications of the ISO standard (ISO, 5167-4, 2003), with a throat diameter of d=30 mm. A

differential pressure transducer (SETRA model 230, with full scale 6.89 kPa (1 psi), accuracy ± 0.5% of the full scale) and a K type thermocouple were used to measure pressure drop and mixture temperature, respectively. The high pressure tap is installed in the upstream tube, 5 mm before the beginning of the convergent section, while the low pressure tab is mounted at the throat section. The distance between the upstream and throat pressure taps is 30 mm. The instrument signals (concentrated pressure drop, distributed pressure drop, and temperature in the test section) are acquired as usual by means of National Instrument Labview® software.

6.3 Experimental flow condition

The experimental tests have been conducted by setting the volumetric flow rate of oil, water, and air at the inlet of the test section. For two phase flow, the superficial water velocity ranged between 0.44 and 1.33 m/s, while oil superficial velocity ranged between 0.25 and 0.71 m/s. For three phase flow, the same flow conditions are considered for water and oil, with superficial air velocity ranged between 0.38 and 1.14 m/s. The experimental investigation of three phase flow is only conducted through NFM. The summary of operating conditions is listed in Table 6-1 and 6-2 for two-phases and three-phase flow, respectively. These conditions correspond to either eccentric-annular or dispersed flows. More detailed considerations about the flow regimes are given in section 6.6.

Table 6-1 Summary of experimental flow conditions for very viscous oil-water flow through VFM and NFM

Flow meter device	J_o	J_w	Re_{os}	Re_{ws}
	(m/s)	(m/s)	(-)	(-)
VFM	0.25-0.75	0.44-1.33	11-32	17,565-53,094
NFM	0.36-0.71	0.44-1.33	16-31	17,565-53,094

Table 6-2 Summary of experimental flow conditions for very viscous oil-water-air flow through NFM

Flow meter device	J_o (m/s)	J_w (m/s)	Jg (m/s)	Re_{gs} (-)	Re_{os} (-)	Re_{ws} (-)
NFM	0.36-0.71	0.44-1.33	0.38-1.14	921-2764	16-31	17,565-53,094

6.4 Geometrical configurations of VFM and NFM

Both devices show a convergent angle of 7.5˚. Unlike the VFM, the NFM undergoes a sudden change of cross-sectional area after the throat section. Upstream and downstream pipes have the length of 7 m and 5 m, respectively to ensure flow development. A gradual increase of cross-sectional area after the throat section is designed for VFM to reduce the irreversible pressure drop, due to flow separation. The geometrical characteristics of VFM and NFM are listed in Table 6-3, while the devices are shown in Figure 6-1 (a-b). The concentrated pressure drop between inlet and throat section (ΔP_{Th}) is also shown in Figure 6-1 (a-b).

Table 6-3 Characteristics of VFM and NFM

D (mm)	40
d (mm)	30
$\theta_{convergent}$ (°)	7.5
L_{VFM} (mm)	150
L_{NFM} (mm)	50
$L_{upstream}$ (m)	7
$L_{downstream}$ (m)	5
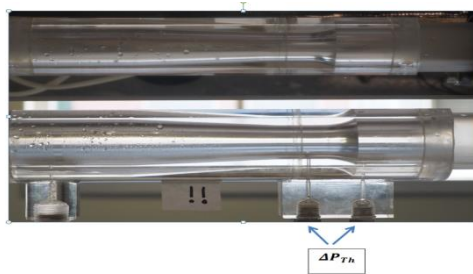
(a)
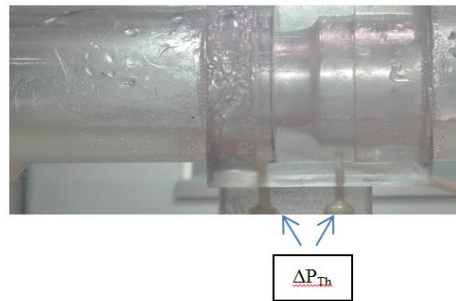
(b)

Figure 6-1 a) VFM, b) NFM

Application of Bernoulli's equation to flow meter for single-phase flow has been described in Chapter 2. We recall the formulation 2-12 as:

$$Q = C_d A_2 \left(\frac{2 \Delta p \rho}{(1-\zeta^4)} \right)^{0.5} \cdot F_a \cdot Y \tag{6-1}$$

The discharge coefficient C_d can be obtained by using the experimental values of volumetric flow rate and concentrated pressure drop for single-phase water flow, by adopting F_a and Y equal to unity. The calibration curve of concentrated pressure drop as a function of water superficial

velocity and the discharge coefficient of single-phase water flow versus water Reynolds number are depicted in Figure 6-2 and 6-3, respectively.

The discharge coefficient of single-phase water flow is dependent on the superficial Reynolds number through an exponential fitting line:

$$C_d = a \cdot (Re_{ws})^b \qquad\qquad (6\text{-}2)$$

Where, a and b can be obtained from the experimental data as a=1.08 and b=-0.009.

$$Re_{ws} = \frac{\rho_w J_w D}{\mu_w} \qquad\qquad (6\text{-}3)$$

Since the discharge coefficient is almost constant by increasing the superficial Reynolds number, an average value of C_d=0.99 can be considered for single-phase water flow through VFM. The discharge coefficient of single-phase water flow for NFM follows the same procedure as VFM, with the average C_d=0.92.
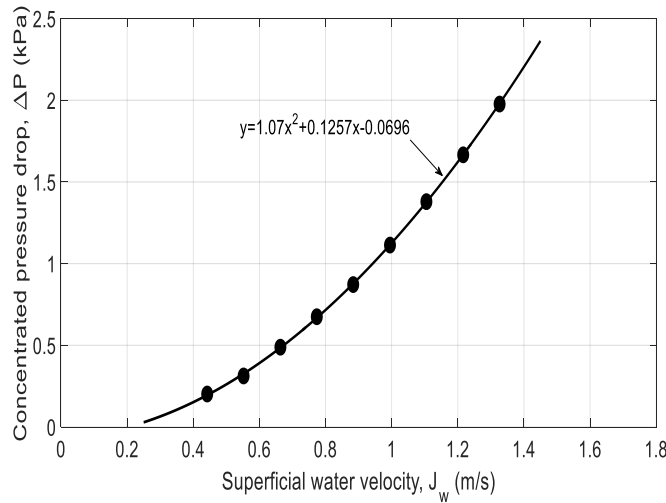
Figure 6-2 Calibration curve of single-phase water flow for VFM
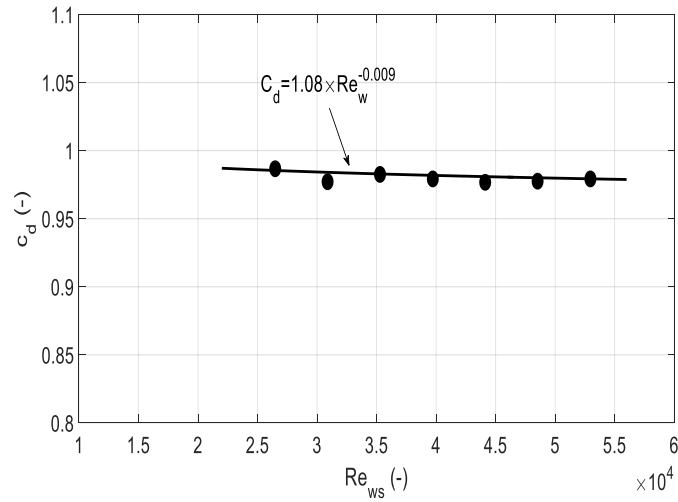
Figure 6-3 Discharge coefficient for single-phase water flow

6.5 VFM and NFM for very-viscous oil-water flow

In Chapter 2, theory of differential pressure for single-phase flow was presented. The total volumetric flow rate is correlated to the concentrated pressure drop, mixture density, and discharge coefficient. The Bernoulli's equation can be used to develop a model for the instruments to estimate the total volumetric flow rate by using the definition of discharge coefficient.

6.5.1 Application of Bernoulli's equation to flow meter for oil-water flow

The presence of the second phase in the response of VFM or NFM may significantly affect the discharge coefficient and estimation of the total volumetric flow rate. In order to accurately predict the total volumetric flow rate according to Bernoulli's equation, see equation 6-1, a proper model of the mixture density is required. In the current study, homogenous definition of the mixture density is assumed for sake of simplicity and it will be discussed in view of the experimental results.

$$\rho_m = \rho_w \varepsilon_w + \rho_o (1 - \varepsilon_w) \tag{6-4}$$

In our experiments ε_w is known but in a practical application of the flow meter it is not. Hence, a model based on an iterative procedure it needed to determine the flow rate from the measured pressure drop unless a calibration curve is provided. These aspects are described in section 6.8.

6.6 Experimental results

In figure 6-4, the experimental concentrated pressure drop between upstream pipe and throat section is plotted as a function of the water superficial velocity for a) VFM and b) NFM. In both figures, oil superficial velocity is considered as a parameter. The concentrated pressure drop versus the superficial water velocity for single-phase water flow is also presented for VFM. For constant oil volumetric flux, increasing concentrated pressure drop by increasing the water superficial velocity is highlighted. As expected introducing the second phase (oil) results in increasing the concentrated pressure drop.
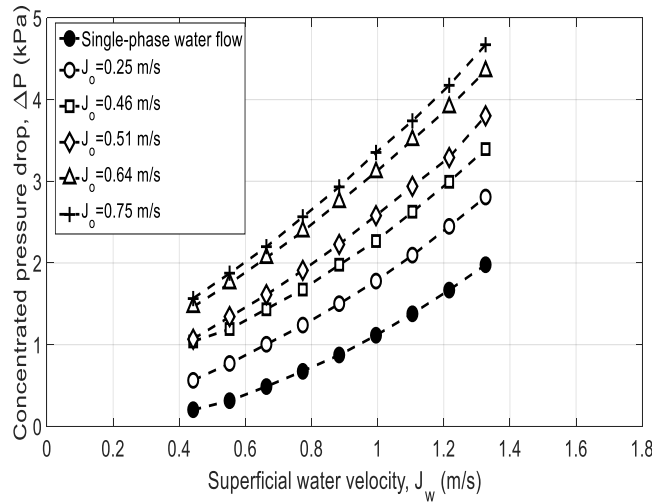
(a)
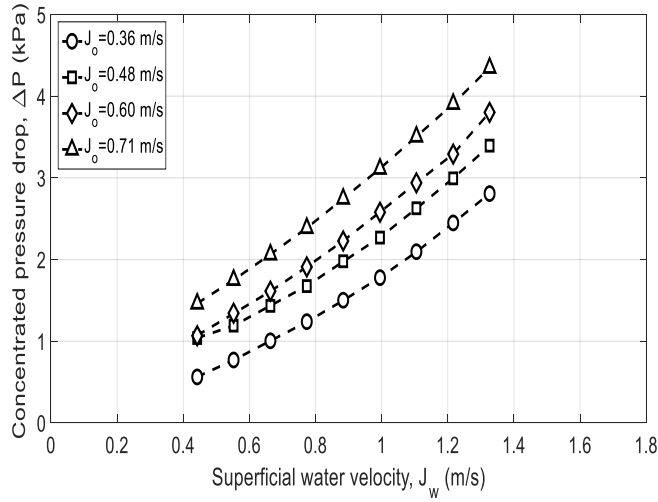
(b)

Figure 6-4 Concentrated pressure drop as a function of superficial water velocity for a) VFM and b) NFM

In Figure 6-5, two-phase concentrated pressure drop, normalized with respect to the single phase water concentrated pressure drop for VFM is shown. For fixed amount of oil, increasing water superficial velocity causes the decrease of this parameter.
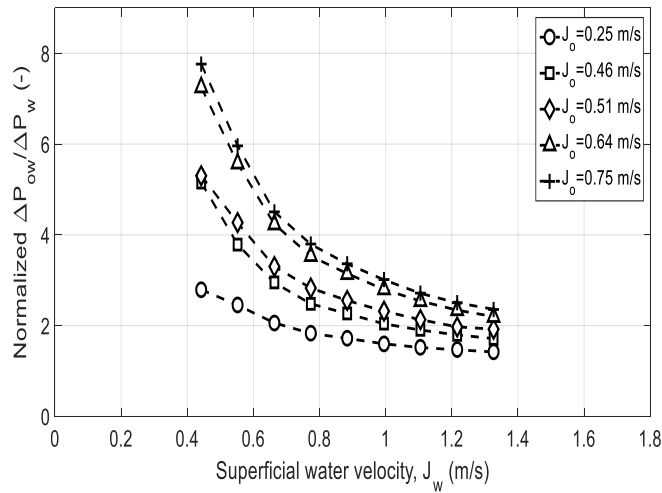
Figure 6-5 Two-phase concentrated pressure drop, normalized by single-phase pressure drop versus water superficial velocity for VFM

It is evident that for higher superficial velocity, normalized two-phase concentrated pressure drop remains almost constant by increasing the water volumetric flux. However, for constant water flow, increasing oil superficial velocity considerably affects the normalized two-phase concentrated pressure drop, particularly at low water flow rate. Increase of the concentrated pressure drop by introducing the oil-phase is caused by the interaction between the water and oil phases: The oil is accelerated from the inlet section to the throat, resulting in increasing the interfacial shear stresses between two phases. The same comment holds for water phase, i.e, water, adjoining to the pipe wall in core-annular and dispersed flow, is accelerated, which, in turn, increases the frictional wall losses and magnitude of the concentrated pressure drop. A deep CFD analysis of the oil-water flow is presented in Chapter 7.

In order to use the theoretical approach to estimate the total volumetric flow rate in liquid-liquid flow, see equation 6-1, experimental calibration of the two-phase flow discharge coefficient C_d is required. For single phase flow, the behavior of the discharge coefficient with the Reynolds number has been reported in section 6.4 and complies with standards, ISO, 5167-4 (2003) for VFMs and NFMs. However, there is no specific standard for oil-water two-phase flow. Hence, the two phase discharge coefficient is calculated from the two-phase concentrated pressure drop and correlated with the two phase flow Reynolds number developed by Arney et al. (1993), equation 5-3, as the flow regime under investigation is mostly core-annular flow. It appears that C_d is practically independent of the Reynolds number and that there is minor difference between the VFM and the NFM. The results of the single-phase and two-phase discharge coefficient are listed in Table 6-4.
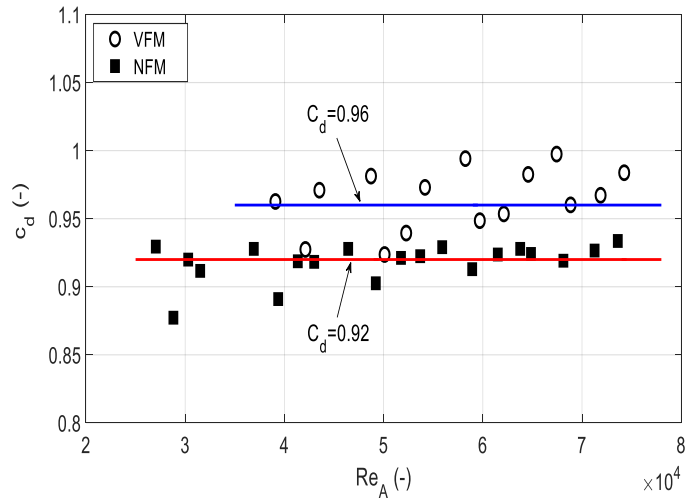
Figure 6-6 Two-phase flow discharge coefficient as a function of the characteristic Reynolds number defined by Arney et al. (1993) for VFM and NFM

Table 6-4 Comparison of mean values of discharge coefficient for single and two-phase flow

Measuring devices	Measured discharge coefficient (single -phase water flow)	Measured two-phase discharge coefficient
VFM	0.99	0.96
NFM	0.92	0.92

By knowing the experimental mixture volumetric flow rate, discharge coefficient from calibration curve, geometrical parameters, and estimation of the mixture density based on equation (6-4), the concentrated pressure drop is computed according to equation 6-1. The parity plot of comparison between predicted concentrated pressure drop from homogeneous model and experimental data is depicted in Figure 6-7 (a-b) for VFM and NFM, respectively. The solid line indicates where the experimental values are equal to the prediction. Different symbols represent different superficial oil velocity. A satisfactory agreement is observed. By comparison of the two devices, it is evident that NFM performs better than VFM (all data fall within ±10 % of relative error for NFM, while 94 % of all data fall within ±10 %). Table 6-5 lists error analysis.

129

Table 6-5 Prediction performance for NFM and VFM

Measuring devices	MAPE %	Average relative error (%)	Maximum relative error (%)	Minimum relative error (%)
VFM	4.5	0.97	7.1	-16.1
NFM	2.0	-1.2	2.0	-9.9
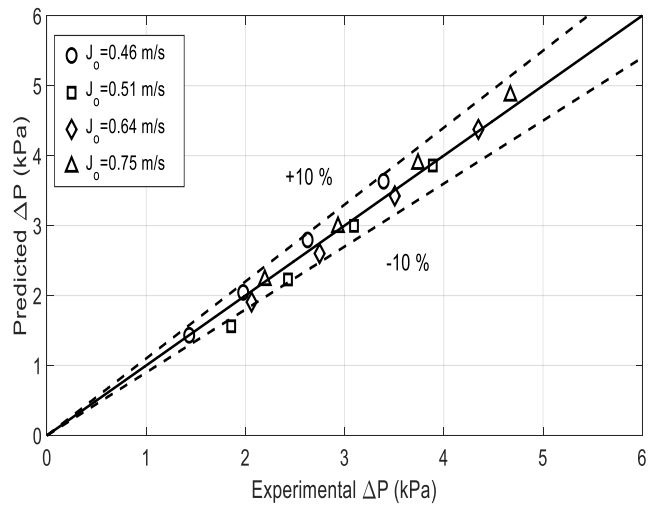
(a)
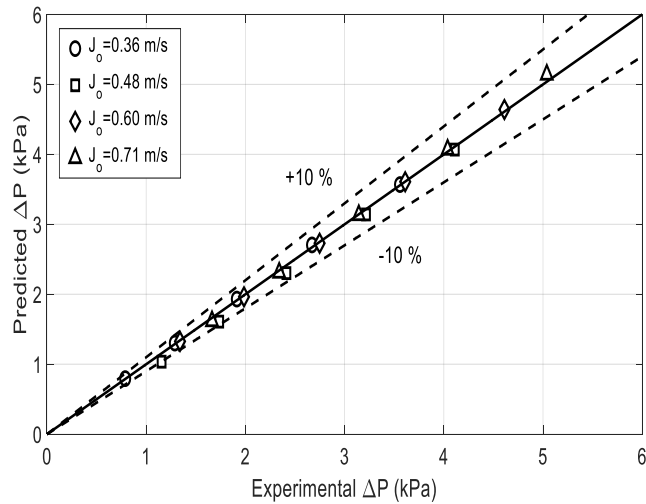
(b)

Figure 6-7 Parity plot of comparison between the concentrated pressure drop (defined by homogeneous mixture density) and experimental concentrated pressure drop for a) VFM, and b) NFM

Conversely, by knowing the experimental concentrated pressure drop and homogeneous density as equation (6-4) the total mixture velocity can be predicted from theoretical approach. The Figure 6-8 (a-b) shows the results of predicted mixture velocity and the experimental data. The mean absolute percentage error (MAPE) for VFM and NFM was found to be 2.3 % and 1.0 %, respectively. These findings were qualitatively approved by analyzing the images of oil-water flowing through VFM. Figures 6-9 (a-b) and 6-10 (a-b) represent oil-water flow patterns for VFM in upstream pipe and throat section, respectively. Two cases of CAF are shown, which included J_o=0.25 m/s and J_w=0.44 m/s (Wavy core-annular flow in upstream pipe) as well as J_o=0.39 m/s and J_w=0.88 m/s (CAF with oil droplet entrainment in upstream pipe). For the case of wavy core-annular flow, it is experimentally observed that the interfacial waves disappear when the mixture flows through the throat section, likely due to the acceleration that induces a transition to core annular flow. For the case of CAF with oil entrainment, it is shown that the number of oil droplets at the oil-water interface is significantly reduced. Hence, it can be concluded that the interfacial waves is disappeared from upstream pipe to the throat section and the entrainment process is damped by the presence of VFM. In the end, it can be inferred that the acceleration of the flow towards the throat section provides "Homogenization", i.e. a tendency to

131

increase the slip ratio so that a model based on the homogeneous flow assumption is able to predict satisfactorily the experimental data. The CFD analysis presented in Chapter 7 confirms this assumption.
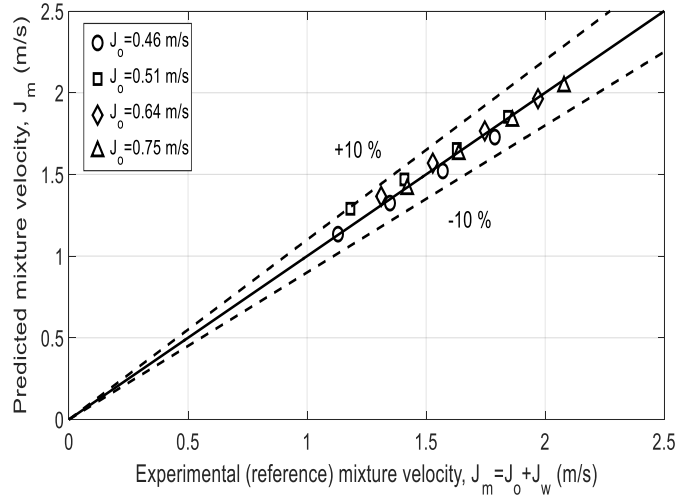
(a)
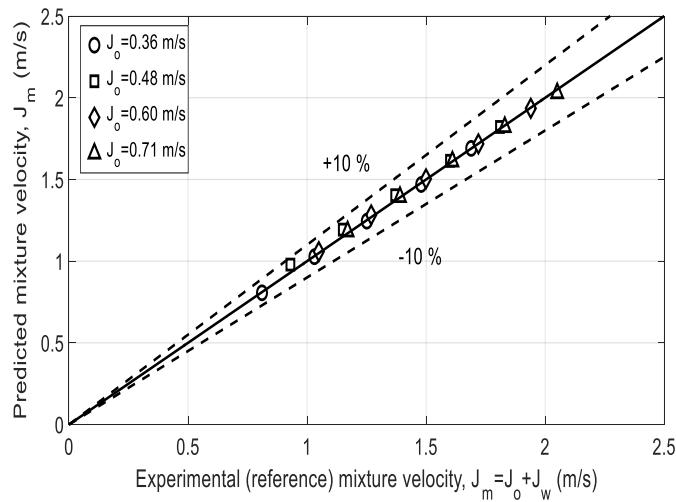
(b)

Figure 6-8 Comparison between reference mixture velocity and predicted counterpart for a) VFM, and b) NFM
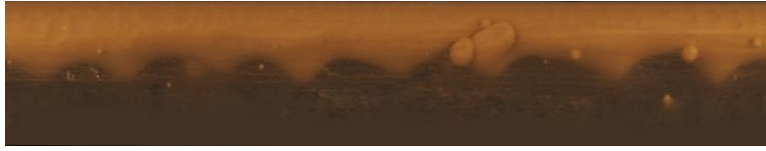
(a)

(b)

Figure 6-9 Experimental observation of core-annular flow in (a) Upstream pipe of VFM, and (b) Throat section for J_o=0.25 m/s, J_w=0.44 m/s
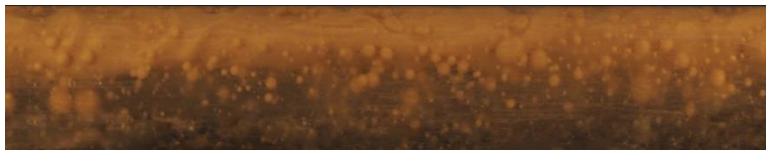
(c)

(d)

Figure 6-10 Experimental observation of core-annular flow with oil droplet entrainment in (a) Upstream pipe of VFM, and (b) Throat section for J_o=0.39 m/s, J_w=0.88 m/s

6.7 New approach to VFM and NFM in very-viscous oil-water flow

Many researchers including He and Bai (2014), Oliveira et al (2009), Steven (2002), Zhang et al (2004) and Tan and Dong (2010), developed their models according to Bernoulli's law (model based on definition of discharge coefficient). However, this approach cannot be used to predict both the total volume flow rate and the individual flow rates of each phase. A new approach based on the simplified two-fluid model described in Chapter 5 is presented in the following. The experimental concentrated pressure drop measured by VFM and NFM have been analysed to evaluate the dependency on the mixture superficial velocity. The calibration curves of mixture superficial velocity as a function of concentrated pressure drop for VFM and NFM are shown in Figures 6-11-a and 6-11-b, respectively. A regular trend is observed for both cases, suggesting the increasing dependency of mixture superficial velocity on the concentrated pressure drop. The experimental mixture superficial velocity as a function of the measured concentrated pressure drop are expressed by the polynomial curve fitting, with the regression coefficients, R=0.99 for VFM and NFM.

The plot shows:
- Legend: ● Experimental data; - - Polynomial curve fitting, R=0.99
- Equation: $y = -2.31 \times 10^{-8} x^2 + 0.000435 x + 0.531$
- Y-axis: Mixture superficial velocity, J_m (m/s)
- X-axis: Concentrated pressure drop, Δp (Pa)
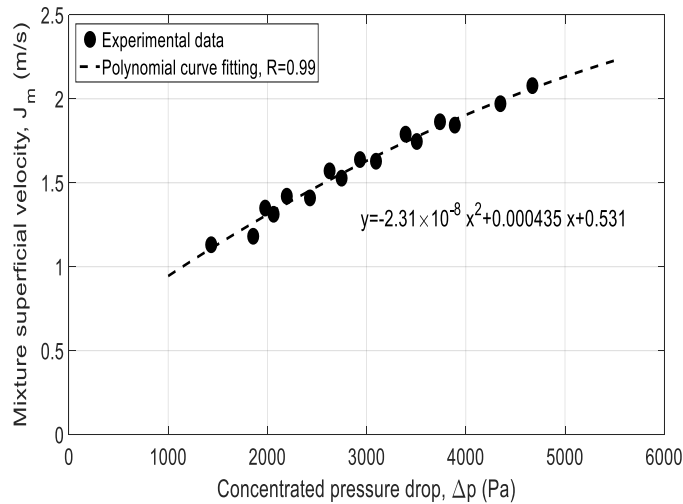
(a) VFM
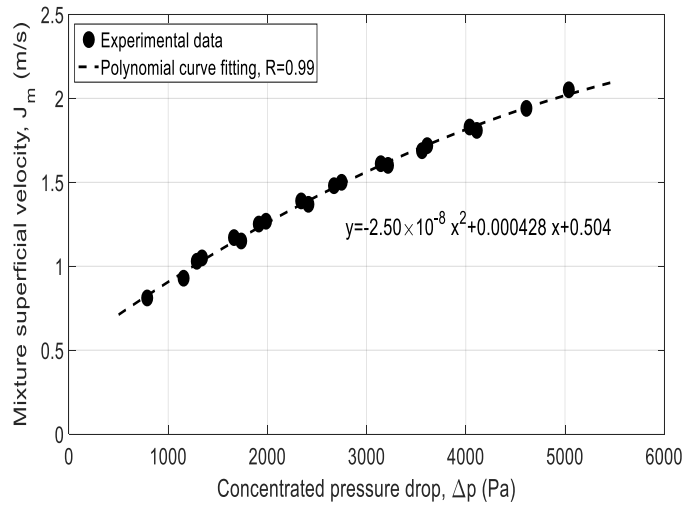
(b) NFM

Figure 6-11 Experimental mixture superficial velocity versus the measured concentrated pressure drop

An iterative process is then adopted to estimate the velocity and volume flow rate of each phases. The model inputs are pipe diameter, water density and viscosity, the concentrated pressure drop measured by VFM and NFM, and distributed pressure gradient upstream of the flow meter. An initial guess value for water superficial velocity is introduced. Using the calibration curve, the mixture superficial velocity, J_m, is computed based on the measured concentrated pressure drop. The holdup value is estimated by means of the proposed SFM in Chapter 5:

$$H_w = \left[\frac{C_w \left(\frac{\rho_w J_w D}{\mu_w} \right)^{-n_w} \rho_w J_w^2}{\left(-\frac{dp}{dx} \right) \frac{D}{2}} \right]^{0.5} \tag{6-5}$$

The value of input water volume fraction is estimated by means of computed water holdup as:

$$H_w = \varepsilon_w [1 + 0.36 \, (1 - \varepsilon_w)] \tag{6-6}$$

The water superficial velocity is calculated as:

135

$$J_w = J_m \cdot \varepsilon_w \qquad\qquad (6\text{-}7)$$

The water superficial velocity is iterated until the error between the calculated water superficial velocity and measured superficial velocity by magnetic pump is less than a threshold value (error $< 10^{-4}$). When the required accuracy is achieved, the value of superficial oil velocity is simply estimated by:

$$J_o = J_m \cdot (1 - \varepsilon_w) \qquad\qquad (6\text{-}8)$$

Figure 6-12 shows the flow chart for calculation of water and oil superficial velocity.

6.8 Prediction of volumetric flux

For practical application, reduced number of instruments in the field is important due to economic reasons and space requirements. The current model is able to predict the velocity of water and oil, without using additional installment of any device to measure the phase holdup. The application of this model only requires the measurements of the concentrated and distributed pressure drop from upstream to throat section and along the pipe, respectively. The VFM has a smoother flow profile than NFM and both of them are characterized by the absence of moving parts. They are used in a wide range of industrial applications. The use of discharge coefficient-based models requires the knowledge of holdup to evaluate the mixture density and, eventually, volumetric flow rate. Generally, this information is extracted by means of QCV that measure the mean volumetric holdup. It is worth noting that mean volumetric holdup differs from the local value of holdup. Instead of measuring the mean volumetric holdup, a simple correlation, based on the measurement of pressure gradient, is proposed which enable us to predict the phase holdup in an accurate way.
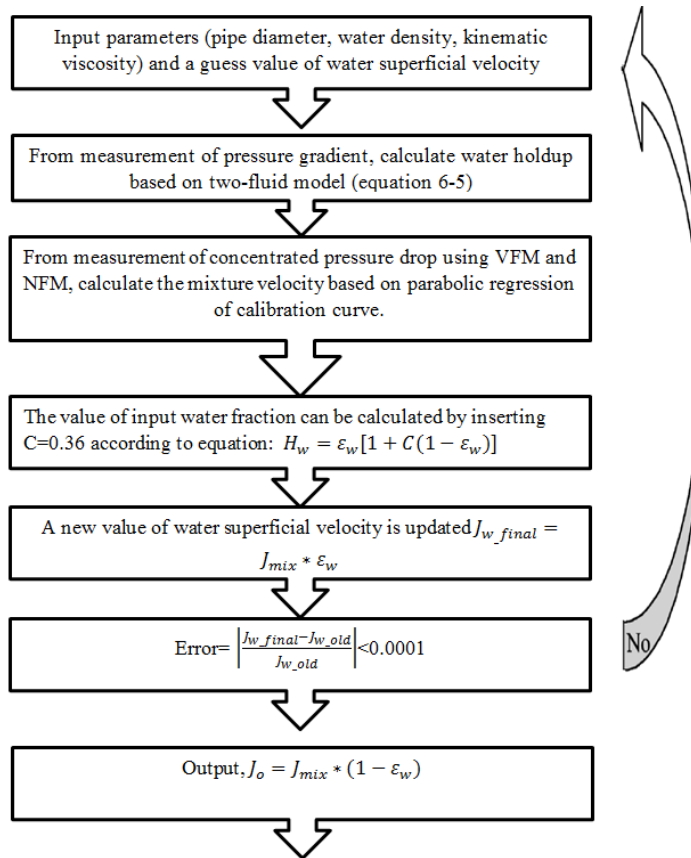
Figure 6-12 Flowchart of calculation of water and oil superficial velocity

Comparison between predicted water, oil velocity and experimental data is shown in Figures 6-13 and 6-14, respectively. The flow regimes under investigation are core-annular and dispersed flow. It is evident from Figures 6-13 and 6-14, the water and oil velocity is well predicted by the proposed model, particularly, for estimation of water phase with MAPE= 7 % and 5.9 % for VFM and NFM, respectively. Regarding estimation of water velocity, the whole data is predicted within ±15 % of relative error for NFM, while 94 % of all data fall within ±15 % for VFM. In Figure 6-15, the input water volume fraction estimated from the proposed model is compared with the experimental values (obtained from the superficial velocity of phases, i.e, $\varepsilon_w=J_w/J_m$. Similarly, the accuracy of the model has been evaluated, considering the relative error between the predicted and experimental values. For VFM and NFM, the input water volume fraction is predicted within relative error less than ±10 %, showing a good agreement with the experimental data. Table 6-6 shows the comparison of performance of the proposed model for phase superficial velocities.

Table 6-6 Comparison of water, oil, mixture velocity and input water volume fraction from proposed model and experimental counterpart for VFM

Investigated parameters	Average relative error (%)	Maximum relative error (%)	Minimum relative error (%)	MAPE (%)
J_o (m/s)	-12.6	4.8	-27.7	13.2
J_w (m/s)	7.0	15.5	2.5	7.0
J_m (m/s)	-0.075	6.5	-3.7	2.3
ε_w (-)	4.8	8.1	-16.0	5.0

Table 6-7 Comparison of water, oil, mixture velocity and input water volume fraction from proposed model and experimental counterpart for NFM

Investigated parameters	Average relative error (%)	Maximum relative error (%)	Minimum relative error (%)	MAPE (%)
J_o (m/s)	-11.8	3.8	-24.2	12.7
J_w (m/s)	5.5	14.8	-13.2	5.9
J_m (m/s)	0.08	3.7	-2.0	1.2
ε_w (-)	1.9	4.4	-1.5	2.0
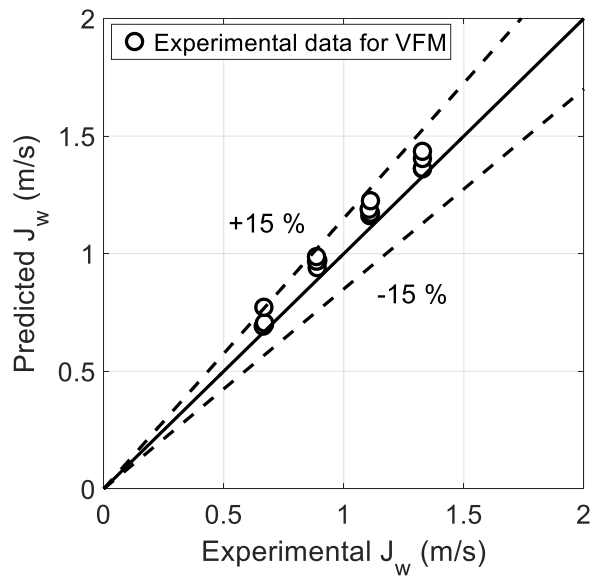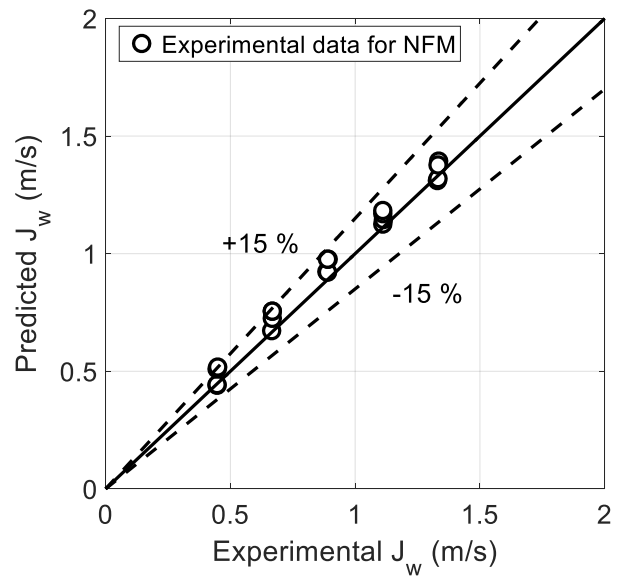
Figure 6-13 Parity plot of predicted water velocity versus experimental value for a) VFM, and b) NFM
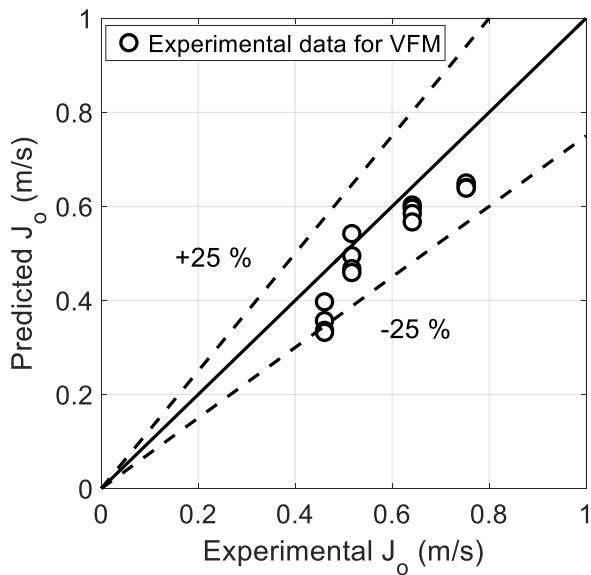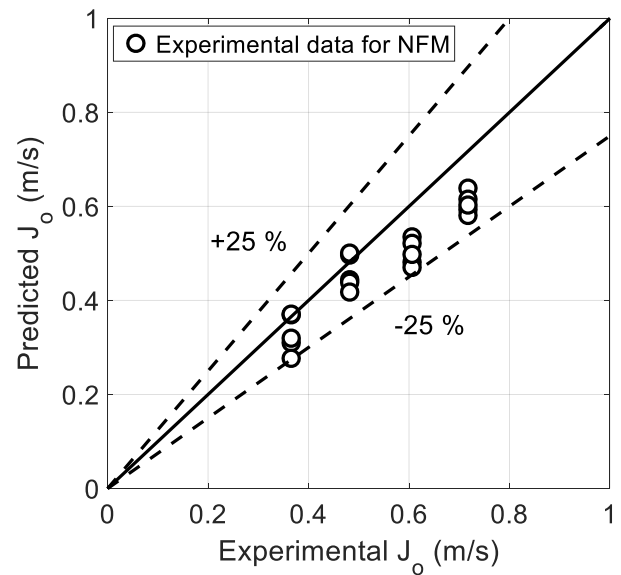
Figure 6-14 Parity plot of predicted oil velocity versus experimental value for a) VFM, and b) NFM
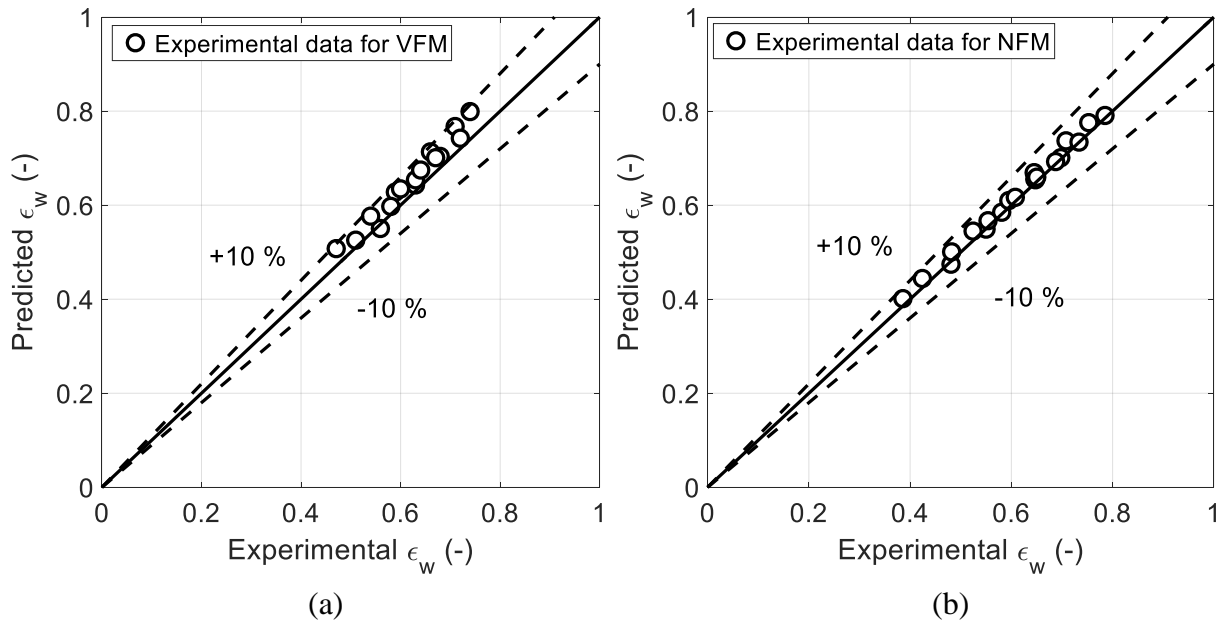
Figure 6-15 Parity plot of predicted input water volume fraction versus experimental counterpart for a) VFM, and b) NFM

7 CFD simulation setup

7.1 Introduction

During the multiphase flow through pipelines, the effects of operation parameters on pressure gradient, phase holdup, and flow pattern have to be studied. In most cases, full experimental campaigns are not available and one may need to improve the design of equipment and pipelines. Three-dimensional CFD (Computational Fluid Dynamic) simulation is an effective alternative to one-dimensional mechanistic models. It is time consuming but provides detailed information regarding flow field.

A number of CFD simulation runs on very viscous oil-water flows have been carried out by means of ANSYS FLUENT 16.2. Concerning core annular flow, CFD simulations have been conducted with VOF (Volume of Fluid) model for different pipe configurations. For instance, one may refer to the works performed by Ghosh et al (2010) for downward pipe, Ghosh et al (2011) for U bend flow, Kaushik et al (2012) for flow through expansions and contractions, and Shi (2015) for flow in a horizontal pipe.

The above literature reveals that detailed information about core annular flow of very viscous oil-water flows undergoing cross-section area variations is still lacking. The objective of present chapter is thus double. In parallel with experimental study (Chapter 4, 5, and 6), the first aim is to investigate if two-phase CFD analysis can be reliable tool and offer significant insight about the behavior of highly viscous oil-water flow through these pipe configurations. The second objective is to evaluate the performance of VFMs and NFMs in the prediction of the two-phase flow rate of very viscous oil-water mixtures in core-annular flow.

The numerical multiphase model is presented in section 7.2. Computational geometry, simulation setup and runs are explained in sections 7.3, 7.4 and 7.5, respectively. Some sensitivity analyses on simulation parameters are reported in section 7.6. Eventually, the simulation results are discussed in section 7.7 and 7.8. Part of this Chapter has been published in Babakhani Dehkordi et al. (2017).

7.2 Numerical multiphase model

7.2.1 VOF model

In the CAF flow pattern, the two-phases are immiscible and separated by an interface having a length scale comparable to the pipe diameter (especially for the oil core, but also for the larger oil drops). Such interface is continuously varying in terms of shape and extension, due to the constant evolution of the flow structures. From CFD simulation point of view, these are conditions for which numerical techniques based on the Volume of Fluid (VOF) (Hirt, 1981) are among the most suitable (Ranade, 2002). The latter were originally developed and used in other two-phase fields (drop impacts, sloshing tanks), but examples of their use for two-phase flow are already reported in the literature (Ghosh et al., 2010; Kaushik et al., 2012; Desamala et al., 2016). Combined methods (e.g. Menard, 2007) would also be very well-suited, but they are also much more complex and no ready-to-use solver is available, so that their use is at present restricted to academic studies. Euler-Euler models (e.g. Vallee et al., 2008) may give good results too, but they lack the interface capturing offered by the VOF approach. Therefore, VOF was selected for this study and simulations were performed on 3D domains using the VOF method implemented in the CFD code ANSYS Fluent 16.2. The software was used with no modification or addition by user defined functions, as one of the aims was to evaluate its performances as it is.

7.2.2 Mathematical equations

According to VOF model, a single set of conservation equations is shared between two phases. By assumption of no mass exchange between phases for incompressible flow, the partial differential equations for mass and momentum equations is discretized and solved throughout the domain:

Continuity equation:

$$\vec{\nabla} \cdot \left(\vec{U} \right) = 0 \qquad\qquad\qquad (7\text{-}1)$$

Momentum equation:

$$\frac{\partial}{\partial t}\left(\rho \vec{U}\right) + \nabla.\left(\overrightarrow{\rho U}\vec{U}\right) = -\nabla P + \nabla.\left[\mu\left(\nabla \vec{U} + \nabla \vec{U}^T\right)\right] + \rho \vec{g} + \vec{F} \qquad (7\text{-}2)$$

Where ρ, $\vec{U}$, μ , P , $\vec{g}$ and $\vec{F}$ are density, velocity field, viscosity, pressure, gravity vector and the contribution to the body force related to surface tension force, as it will be detailed in the following. Unlike Eulerian-Eulerian two-fluid methods that solve a momentum equation for each of the phases, in VOF a unique momentum equation is shared for both phases, with density and viscosity calculated on the basis of the volume fractions of the phases. The amount of the secondary phase (in the present case, oil) in each computational cell is in fact calculated by capturing the state density function (α_o) for such phase (that is why VOF belongs to the family of volume tracking techniques). As the phase density is constant, this is equivalent to solving the continuity equation for the single phase:

$$\frac{\partial(\rho_o \alpha_o)}{\partial t} + \nabla.\left(\rho_o \alpha_o \vec{U}\right) = 0 \qquad (7\text{-}3)$$

In presence of only two phases, the volume fraction of the primary phase is obviously the complement to unity of the previous, exactly as in the physical world. Once the volume fractions of the phases are calculated in each computational cell, average properties in the cell are estimated as:

$$\begin{aligned} \rho &= \rho_o \alpha_o + (1 - \alpha_o)\,\rho_w \\ \mu &= \mu_o \alpha_o + (1 - \alpha_o)\mu_w \end{aligned} \qquad (7\text{-}4)$$

7.2.3 Interface capturing

Within the computational domain, cells were oil holdup α_o is 0 are cell filled with water, while the value $\alpha_o = 1$ is associated with the cells fully filled with oil. A value between 0 and 1 occurs at interface cells. From the set of interface cells, the interface shape has to be reconstructed using a suitable algorithm, as with all volume tracking – interface capturing methods. There are two schemes for interface treatments, which include Geometric reconstruction and CICSAM (Compressive Interface Capturing Scheme for Arbitrary Scheme) techniques. Shi (2015) proved

that the wavy interface can be captured by Geo-Reconstruct scheme, while the CICSAM scheme would result in a smooth interface for very viscous oil-water core annular flow in a horizontal pipe. Therefore, the geometric reconstruction piecewise-linear scheme is used due to its high accuracy. It assumes that the interface between the two phases is planar within each cell and, based on this linear interface representation the normal and tangential velocity distributions, the derivatives of the phase volume fractions and the advection of fluids through each cell are calculated. Finally, phase volume fraction is updated using balances of fluxes calculated in the previous step.

7.2.4 Surface Tension

In the VOF method, addition of the surface tension results in an extra source term in the momentum equation. The Continuum Surface Force (CSF) model by Brackbill et al. (1992) was used.

By assumption of constant surface tension along the interface, the well-known Laplace-Young equation holds, and the source term can be defined as:

$$\vec{F} = \sigma k \frac{\rho \, \nabla \alpha_o}{0.5 \, (\rho_o + \rho_w)} \qquad (7\text{-}5)$$

where σ, k, and $\nabla \alpha_o$ are surface tension, interface curvature and the oil phase volume fraction gradient, respectively. In the CSF model the surface curvature is calculated based on the local gradient of the vector normal to the interface, defined as the gradient of the volume fraction of oil α_o:

$$n = \nabla \alpha_o \, , \; \hat{n} = \frac{n}{|n|} \; \text{ and } \; k = \nabla . \hat{n} \qquad (7\text{-}6)$$

The effect of wall adhesion is directly linked to the contact angle the fluid is made with the wall, and used to adopt the surface normal in those cells close to the wall. This is so-called dynamic boundary condition which, in turn, results in the adjustment of the curvature of surface near the wall:

$$\hat{n} = \hat{n}_w \cos \Theta_w + \hat{t}_w \sin \Theta_w \qquad (7\text{-}7)$$

Where $\hat{n}_w$ and $\hat{t}_w$ are the unit vectors normal and tangential to the pipe wall, respectively. The contact angle, Θ_w, is the angle between the pipe wall and tangent to the interface at the wall.

7.2.5 Realizable k-ε turbulence model

There are three k-ε models programed in the commercial code ANSYS FLUENT 16.2, which include Standard, RNG, and Realizable k-ε. The latter is proposed by Shih et al. (1994), proven to have outstanding performance and superior over former models, particularly for flows in a (1) channel flow, (2) backward facing step, (3) rotating homogeneous shear flow. The difference between Realizable and standard k-ε model is that the former contains a new formulation for the turbulent viscosity. More importantly, a new transport equation for the dissipation rate, ε, has been proposed for the transport of mean-square vorticity fluctuation. The term Realizable means that the model satisfies certain mathematical constraints on the Reynolds stresses, compatible with the physics of turbulent flows. A benefit of Realizable k-ε model is that it provides better performance for flows coping with rotation, boundary layer, separation, and recirculation.

The governing equations of the Realizable k-ε model are:

Turbulent kinetic energy:

$$\frac{\partial}{\partial t}(\rho k) + \frac{\partial}{\partial x_j}(\rho k u_j) = \frac{\partial}{\partial x_j}\left[\left(\mu + \frac{\mu_t}{\sigma_k}\right)\frac{\partial k}{\partial x_j}\right] + G_k + G_b - \rho\varepsilon - Y_M + S_k \qquad (7\text{-}8)$$

Turbulent dissipation rate:

$$\frac{\partial}{\partial t}(\rho\varepsilon) + \frac{\partial}{\partial x_j}(\rho\varepsilon u_j) = \frac{\partial}{\partial x_j}\left[\left(\mu + \frac{\mu_t}{\sigma_\varepsilon}\right)\frac{\partial \varepsilon}{\partial x_j}\right] + \rho C_1 S_\varepsilon - \rho C_2 \frac{\varepsilon^2}{k + \sqrt{\nu\varepsilon}} + C_{1\varepsilon}\frac{\varepsilon}{k}C_{3\varepsilon}G_b + S_\varepsilon \qquad (7\text{-}9)$$

Where

$$C_1 = max\left[0.43, \frac{\eta}{\eta+5}\right], \qquad \eta = S\frac{k}{\varepsilon}, \qquad S = \sqrt{2S_{ij}S_{ij}} \qquad (7\text{-}10)$$

In these equations, G_k and G_b represent the generation of turbulence kinetic energy due to the mean velocity gradient and buoyancy, respectively. The latter can be neglected from transport equations in the case of non-zero gravity field. Y_M represents the contribution of the fluctuating dilation in compressible turbulence to the overall dissipation rate. C_2 and $C_{1\varepsilon}$ are constants, σ_k and σ_ε are the turbulent Prandtl numbers for turbulent kinetic energy and dissipation rate, respectively. The model constants are:

$$C_{1\varepsilon} = 1.44, C_2 = 1.9, \sigma_k = 1.0, \sigma_\varepsilon = 1.2$$

S_k and S_ε are user-defined source terms. Similar to other k-ε models, the eddy viscosity can be computed from:

$$\mu_t = \rho C_\mu \frac{k^2}{\varepsilon} \tag{7-11}$$

Contrary to Standard k-ε model, the coefficient C_μ is no longer constant and calculated as:

$$C_\mu = \frac{1}{A_o + A_s \frac{kU^*}{\varepsilon}} \tag{7-12}$$

Where A_o and A_s are the model constants:

$$A_o = 4.04, \quad A_s = \sqrt{6} \cos \varphi$$

$$U^* = \sqrt{S_{ij}S_{ij} + \tilde{\Omega}_{ij}\tilde{\Omega}_{ij}} \tag{7-13}$$

$$\tilde{\Omega}_{ij} = \Omega_{ij} - 2\varepsilon_{ijk}\omega_k \tag{7-14}$$

$$\Omega_{ij} = \bar{\Omega}_{ij} - \varepsilon_{ijk}\omega_k \tag{7-15}$$

Where $\bar{\Omega}_{ij}$ is the mean rate of rotation tensor with the angular velocity of ω_k. The parameter φ is computed based on the velocity gradients as:

$$\varphi = \frac{1}{3}\cos^{-1}\left(\sqrt{6}W\right), \qquad W = \frac{S_{ij}S_{jk}S_{ki}}{\tilde{S}^3}, \tag{7-16}$$

$$\tilde{S} = \sqrt{S_{ij}S_{ij}}, \qquad S_{ij} = \frac{1}{2}\left(\frac{\partial u_j}{\partial x_i} + \frac{\partial u_i}{\partial x_j}\right)$$

More information on derivations of equations can be found in Shih et al (1994) and Ansys Fluent Theory Guide 16.2 (2012). For the sake of comparison, the SST k-ω model is also tested to investigate the influence of turbulence model.

7.3 Computational geometry

7.3.1 Physical model for VFMs and NFMs

A 3D shaded rendering of the flow domains is shown in Figure 7-1 (a-b) for NFM and VFM, respectively. The simulation domain for NFM denotes as A_1, while VFM geometry is represented as A_2. They reproduce the geometries that have been experimentally tested. The diameter ratio (β) of the VFM and NFM is 0.75, with upstream and downstream pipe diameters of 40 mm and a divergent angle of 7.5° for both devices. Unlike the VFM, the NFM encounters a sudden change of cross section after throat section. Upstream and downstream pipes were modeled with a length of 500 mm and 400 mm as a compromise between the need to allow flow development and the computational expense. Computational domain was meshed using hexahedral elements as they grant both a reduction in the volume element count and superior accuracy and convergence to solution.
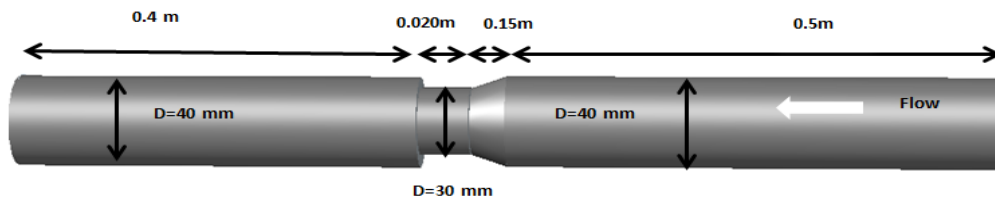
(a) Geometry A-1
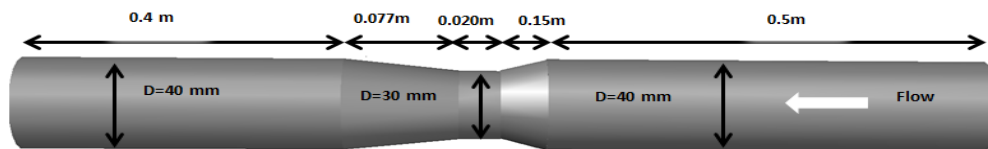
(b) Geometry A-2

Figure 7-1 3D sketch of geometries of (a) NFM (Geometry A-1), and (b) VFM (Geometry A-2)

7.3.2 Physical model for sudden expansion

Figure 7-2 (a-c) shows the geometries of the two-phase flow in horizontal pipes with sudden expansion. Geometries B-1, B-2, and B-3 represent sudden expansion from 21 mm to 30 mm, 30 mm to 40 mm, and 30 mm to 50 mm, respectively. In all cases, the total length of computational domains is 1.3 m, with upstream and downstream pipe length of 0.5 m and 0.8 m, respectively.

Flow direction
D=21 mm
d=30 mm
0.5 m
0.8 m

(a) Geometry B-1

Flow direction
D=30 mm
d=40 mm
0.5 m
0.8 m

(b) Geometry B-2

Flow direction
D=30 mm
d=50 mm
0.5 m
0.8 m
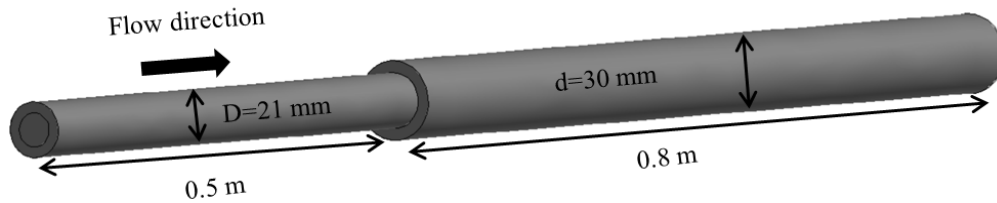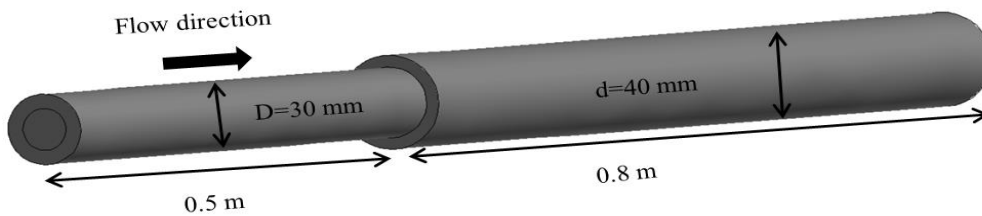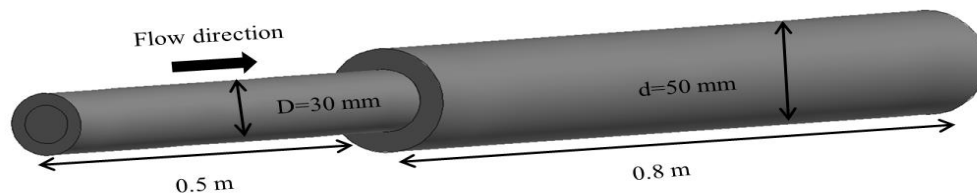
(c) Geometry B-3

Figure 7-2 Schematic of horizontal pipes with sudden expansion, (a) 21-30 mm (Geometry B-1), (b) 30-40 mm (Geometry B-2), (c) 30-50 mm (Geometry B-3)

7.4 Simulation setup

7.4.1 Initial and boundary conditions

Computational domain is initially filled with water as in the experimental conditions, then the two fluids are separately injected into the domain. An example of computational domain for sudden expansion meshed by means of hexahedral cooper mesh is depicted in Figure 7-3. As it is evident from Figure 7-3, oil is injected from the core of the inlet cross-section (part of the mesh colored in red), while water is injected circumferentially (part of the mesh colored in blue). The benefits of defining a surface over a cylinder to introduce oil core from the center is to (1) reduce the total number of mesh elements, and (2) avoid high pressure gradient caused by the contact of oil at the inlet. The mesh is finer near to the wall to enhance accuracy of flow field calculation in the boundary regions. It is worth noting that a hybrid mesh for inlet surfaces is considered, i.e. paving and mapped quadrilateral mesh for oil and water regions, respectively, and all the mesh types on the inlet surfaces were swept to the computational domain. To ensure that the velocities imposed at the inlet surfaces for oil and water are the same as in the experiments, constant and uniform velocity is obtained as

$$U_{o,inlet} = \frac{J_o}{H_o} \qquad (7\text{-}17)$$

$$U_{w,inlet} = \frac{J_w}{H_w} \qquad (7\text{-}18)$$

where H_w is calculated according to the Arney et al. (1993) correlation

$$H_w = \varepsilon_w[1+0.35(1 - \varepsilon_w)] \qquad (7\text{-}19)$$

The latter was checked in previous works as providing a very good agreement with the experimental data, see for instance Arney et al. (1993) and Colombo et al. (2015). No-slip conditions and zero gauge pressure are considered for the duct wall and the duct outlet, respectively.
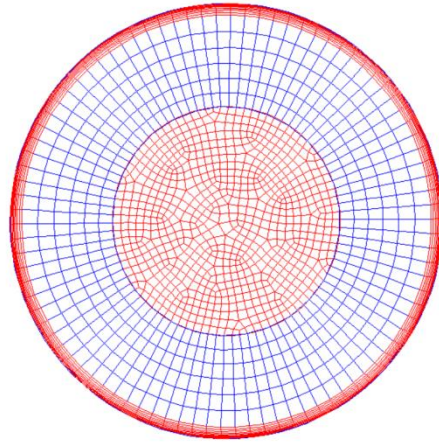
(a)
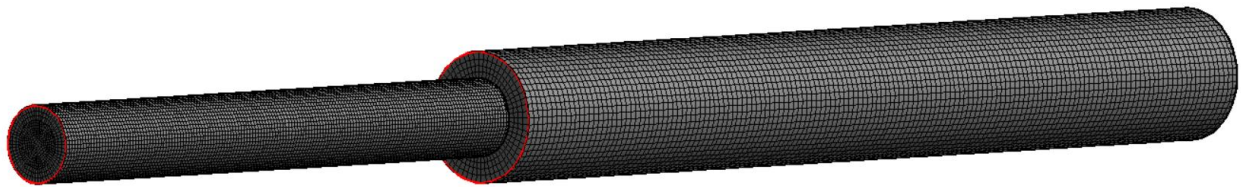
(b)

Figure 7-3 Example of schematic of meshed geometry, (a) cross-sectional area at the inlet (oil is injected from the core, while water is injected circumferentially. Red and blue colors indicate oil and water regions, respectively), (b) cooper hexahedral mesh for sudden expansion

The wall contact angle is the wall adhesion modeling (see equation 7-7) is set 20°. Considering a solid surface in contact with a primary fluid surrounded by a secondary fluid, the following cases for estimation of wall contact angle exists, see Santos et al (2006) and Shi et al (2017):

- $\Theta = 0$: strongly water wetting
- $\Theta = 90$: neutral wettability
- $\Theta > 90$: oil tends to cover the inner surface of the pipe
- $\Theta < 90$: water tends to stick to the pipe wall
- $\Theta = 180$: strongly oil wetting

Two cases with different contact angles were tested and discussed in section 7.6.2.

7.4.2 Numerical procedure

The governing transport equations were discretized using the finite volume method. Three-dimensional transient simulations were carried out because of the natural variation in time and space of the multiphase flow phenomena. Concerning continuity equation and pressure-velocity coupling, the PRESTO and PISO algorithms, originally developed by Patankar (1980) and Issa (1986), were used. The second order upwind method was used for momentum, turbulent kinetic energy and dissipation rate. Geo-reconstruction method was adopted for the volume fraction equation and interface reconstruction. Time step is selected as 0.0001 to respect to Courant number criterion, based on the mesh size and an estimated maximum velocity in the domain. Numerical convergence was assumed when the residuals of continuity are lowered by three orders of magnitude, while for momentum, turbulence and volume fraction equations four order of magnitudes were considered. When turbulence model is active, the turbulence intensity and hydraulic diameter are specified at the inlet. According to the Fluent user's guide 16.2 (2015), the turbulence intensity is correlated to the characteristic Reynolds number based on the following equation:

$$I = 0.16 \cdot Re^{-1/8} \qquad (7\text{-}20)$$

From the superficial Reynolds number provided in Table 6-1 and 6-2 for VFM and NFM, it can be concluded that oil is always laminar, while water remains turbulent. Thus, the water flow rate determines if the turbulence model is activated or not during core-annular flow. The Reynolds number of water annulus is calculated as:

$$Re_w = \frac{\rho_w U_w D_w}{\mu_w} \qquad (7\text{-}21)$$

Where D_w is the hydraulic diameter and defined as:

$$D_w = \frac{4A_w}{\pi D} = H_w D \qquad\qquad (7\text{-}22)$$

$$U_w = \frac{J_w}{H_w} \qquad\qquad (7\text{-}23)$$

By substitution of equations (7-22) and (7-23) in equation (7-21):

$$Re_{sw} = Re_w = \frac{\rho_w J_w D}{\mu_w} \qquad\qquad (7\text{-}24)$$

Equation 7-24 can be used to estimate turbulent intensity. As suggested by Ghosh et al. (2010), monitoring cross sectional contour of turbulent viscosity at different axial location reveals that in the core the viscosity is close to molecular viscosity of oil, while in the annulus the viscosity is significantly larger than the molecular viscosity of water. This indicates that the model is able to maintain oil in laminar conditions and water in turbulent regime in the corresponding regions.

7.5 Simulation runs

The geometries A (A-1 for NFM and A-2 for VFM) and B (B-1, B-2, and B-3 for expansion cases) were used to simulate flow of oil-water mixtures in horizontal pipe with co-axial injectors for oil and water at inlet sections. It is worth remarking that oil viscosity set for each simulation run based on its experimental counterpart changes a little bit, depending highly on mixture temperature. All the simulation Runs performed is reported in Table 7-1 (for measuring devices NFM and VFM) and Table 7-2 (for sudden expansion cases). In each Table, the flow conditions (superficial velocity of each phase with respect to upstream pipe), and the determined parameters are summarized. It should be noted that only core-annular flow regime is considered for CFD analysis, due to the lack of information in the literature regarding this type of spatial distribution for high viscous oil-water flow.

Each simulation run were performed by means of 8 processors of 2 nodes (each node has two four-core, model Intel ® core TM i7 with 3.5 GHz, and 8GB-RAM). The computational time for all cases lasts less than one week. Some sensitivity analyses were performed to evaluate the effect of setup parameters on simulation results, namely the turbulence scheme, the initialization method, and contact angle to ensure the best selected parameters for the next runs.

Table 7-1 Summary of simulation runs for NFM (Geometry A-1) and VFM (Geometry A-2)

Geometry	Notation of CFD runs	J_o (m/s)	J_w (m/s)	μ_o (Pa·s)	Re_{so} (-)	Re_{sw} (-)	determined parameters
A-1	R-1	0.36	0.44	0.92	14	17825	ΔP_s, H_w, flow pattern
	R-2	0.48	0.66	0.96	18	26693	
	R-3	0.60	0.66	0.93	23	26649	
	R-4	0.60	0.89	0.93	23	35562	
	R-5	0.60	1.10	0.94	23	44298	
	R-6	0.71	0.66	0.90	28	26693	
	R-7	0.71	0.88	0.91	28	35518	
A-2	R-8	0.25	0.44	0.85	10	17648	ΔP_s, H_w, flow pattern
	R-9	0.46	0.44	0.85	19	17648	
	R-10	0.51	0.66	0.85	21	26737	
	R-11	0.64	0.66	0.84	27	26737	
	R-12	0.64	0.88	0.84	27	35336	
	R-13	0.64	1.10	0.87	27	44088	
	R-14	0.75	0.66	0.85	31	26649	
	R-15	0.75	0.88	0.87	31	35336	

Table 7-2 Summary of simulation runs for sudden expansion cases (B-1, B-2, and B-3)

Geometry	Notation of CFD runs	J_o (m/s)	J_w (m/s)	μ_o (Pa·s)	D (mm)	d (mm)	determined parameters
B-1	S-1	1.67	3.21	1.01	21	30	$-\left(\frac{dp}{dx}\right)$, H_w, flow pattern
	S-2	2.23	3.23	1.02	21	30	
	S-3	2.79	3.21	1.0	21	30	
	S-4	3.35	3.24	0.98	21	30	
B-2	S-5	0.81	1.58	0.72	30	40	$-\left(\frac{dp}{dx}\right)$, H_w, flow pattern
	S-6	1.09	1.58	0.72	30	40	
	S-7	1.36	1.58	0.72	30	40	
	S-8	1.64	1.57	0.72	30	40	
B-3	S-9	0.81	1.57	0.77	30	50	$-\left(\frac{dp}{dx}\right)$, H_w, flow pattern
	S-10	1.09	1.58	0.80	30	50	
	S-11	1.36	1.58	0.78	30	50	
	S-12	1.64	1.57	0.81	30	50	

7.6 Sensitivity analyses on simulation parameters

7.6.1 Grid independence analysis

In order to verify grid independence of the results, two-phase concentrated pressure drop for the finest used mesh (500,871 elements) is considered as a reference for case R-6 and percentage deviation from such reference is plotted in Figure 7-4. The results presented in the following are all from the simulations with 500,871 elements. Such a mesh can be considered as still quite

coarse and it was selected to keep the simulation time reasonably short (indicatively less than one week) also on common hardware (desktop or laptop PC). One of the aims of the study is in fact to verify if numerical simulation can be a suitable tool for analyzing multiphase flow also from an industrial point of view, in situations where time is often a very scarce resource. Table 7-3 listed predicted two-phase pressure gradient for different meshes. As it is evident from Figure 7-4 and Table 7-3, a considerable improvement has been achieved to calculate two-phase concentrated pressure drop by increasing the number of mesh elements, with total cell of 500,871. Thus, this number of mesh elements is used for future analysis.
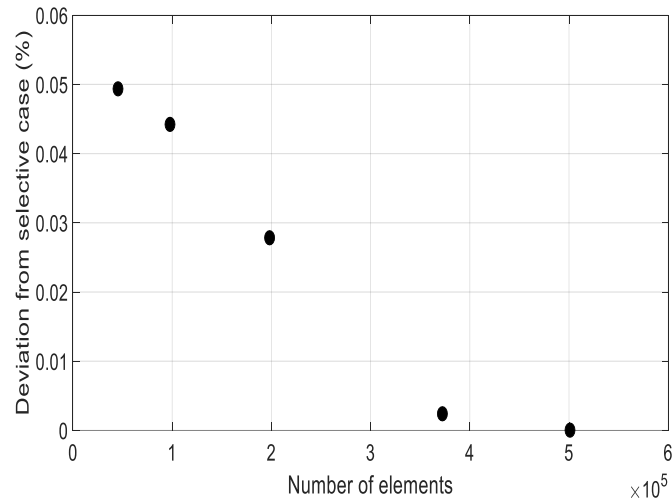
Figure 7-4 Grid independence analysis on the two-phase concentrated pressure drop for case R-6

Table 7-3 Predicted two-phase concentrated pressure gradient for different number of meshes

Number of cells	Experimental concentrated pressure drop, ΔP_c (exp)	Calculated concentrated pressure drop, ΔP_c (CFD)	Relative error (%)
45460	2.386	2.636	10.4
97693		2.623	9.9
198320		2.582	8.2
372450		2.518	5.5
500871		2.512	5.2

7.6.2 Sensitivity analysis on contact wall angle

According to Ansys Fluent User guide 16.2 (2012), it is possible to define either static or dynamic contact angle between the solid wall and water liquid, surrounded by oil. Since the experimental observation shows that there is no oil fouling occurred during core-annular flow (with or without oil droplet at the interface) and water is always present at the wall, acute angle must be adopted for wall adhesion modeling. Some researchers studied the influence of the wall contact on characteristic flow behavior of oil-water mixture both experimentally and numerically. Van Mourik et al (2005) and Shi et al (2017) have shown that the wall contact angle has the most influence on the low viscous oil-water flow, where dimensionless capillary number is low ($Ca = \frac{\mu U}{\sigma} < 0.03$) and surface tension becomes significant. However, for high viscous oil-water flow, where capillary number is high and viscous forces overcomes surface tension, the contact angle has less effect on the characteristic flow behavior.

Santos et al (2006) have investigated the influence of oil polar components on wetting of inner surface of pipes by means of contact angle measurements in core-annular flow. Static contact angles were measured by putting an oil droplet (μ_o=0.511 Pa.s at 40 °C) on the metallic surface

in the presence of water phase. It was concluded that removing the asphaltenes and naphthenic acid on the metallic surfaces would result is changing the contact angle from oil-wet (angles above 145°) to water-wet (less than 60°) behavior. Furthermore, it was revealed that the glass surfaces are more prone to display water-wet behavior. Ghosh et al (2010) provided the contact angle of 27° during CFD simulation of core-annular flow in downward flow based on drop image Goniometer measurement. Since the experimental values of wall contact angle are not experimentally available in the current study and modeling of the wall contact angle is beyond the scope of this study, two different acute contact angles for the case of S-9 have been tested. It is worth remarking that $SST\ k - \omega$ turbulence model is activated to check the effect of turbulence scheme as well. More complete comparison between different turbulent schemes would be discussed in the next section. Figure 7-5 (a) and 7-5 (b) shows the predicted flow patterns for wall contact angles of 90° and 20°, respectively, for downstream pipe of sudden expansion S-9. The cross-sectional spatial phase distribution for each case is also represented, considering L=0.4 m (upstream position) and L=1 m (downstream position) from inlet. Figure 7-5 (c) indicates the experimental counterpart downstream of sudden expansion for simulation run S-9. From numerical CFD simulation, it is observed that core-annular flow is the calculated flow regime, without oil contact at the wall. This is consistent with experimental observation. However, CFD simulation was not able to capture the oil droplets at the interface, probably due to the use of Reynolds Average Navier Stokes (RANS) approach.
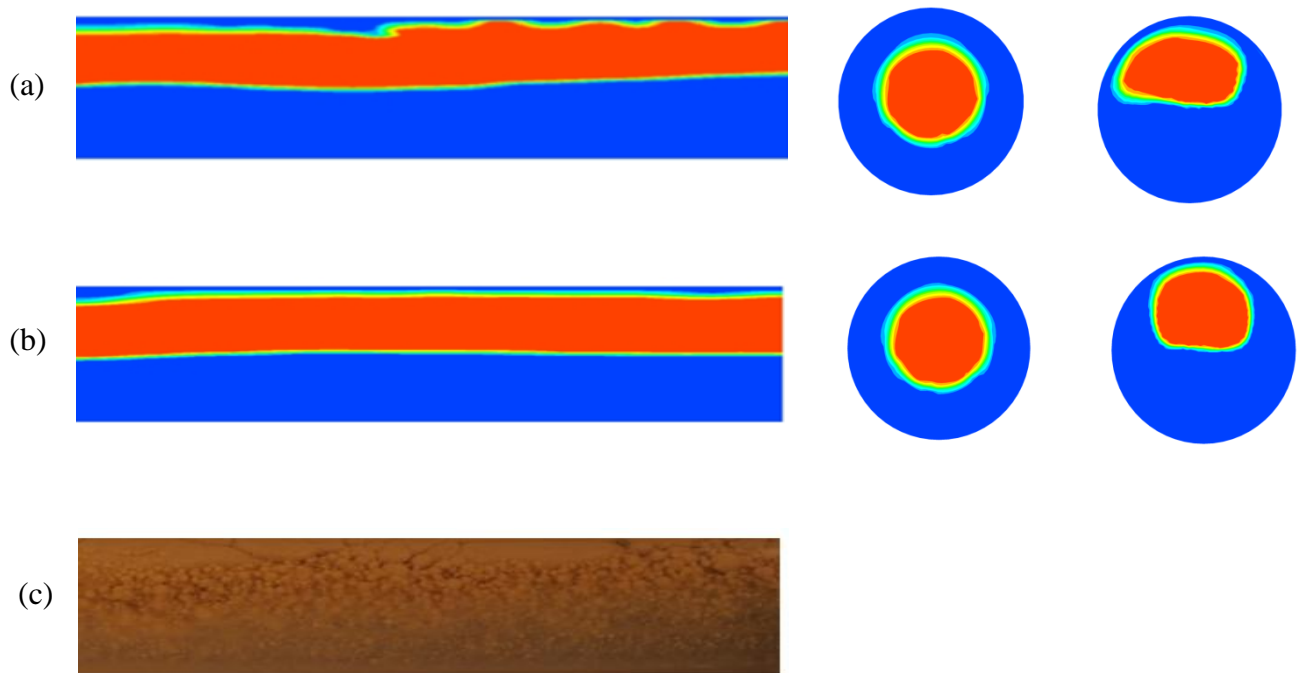
Figure 7-5 Predicted flow patterns (red and blue colors represent the presence of oil and water, respectively) for simulation run S-9 with wall contact angles of (a) 90°, and (b) 20° and comparison with experimental counterpart captured by video camera (c).

There is no significant difference between flow patterns using two different wall contact angles. Since increase of the wall contact angle would enhance the risk of oil fouling phenomenon (the condition that must be avoided), the contact angle of 20° has been selected for other simulation runs. In order to quantitatively investigate the influence of the wall contact angles, the distributed pressure gradients predicted by CFD for simulation run S-9 is compared with experimental value both upstream and downstream of sudden expansion, and results are presented in Table 7-4.

Table 7-4 Calculated pressure gradient upstream and downstream of sudden expansion for simulation run S-9 for different wall contact angles
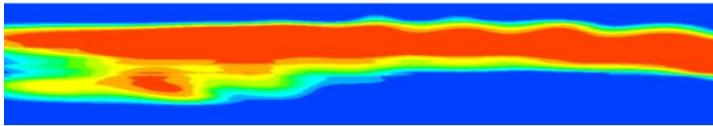
From experiment		From CFD simulation		
$-\left(\dfrac{dp}{dx}\right)_{up}$ (kPa/m)	$-\left(\dfrac{dp}{dx}\right)_{down}$ (kPa/m)	Wall contact angle θ (°)	$-\left(\dfrac{dp}{dx}\right)_{up}$ (kPa/m)	$-\left(\dfrac{dp}{dx}\right)_{down}$ (kPa/m)
1.67	0.20	20	0.81	0.13
		90	0.80	0.10

7.6.3 Sensitivity analysis on turbulence scheme

The standard k-ε model is a powerful model and computationally cheap for fully turbulent flow inside the pipe without separation and adverse pressure gradient. Therefore, it can poorly perform for flow with complex situation, particularly, for regions near to viscous sub-layer. If the cells close to the pipe wall are not properly fine, this would result in numerical stiffness and stability issues, see Menter (1993). Two different turbulence scheme which included Realizable k-ε (RKE) and SST k-ω have been tested to evaluate the influence of different modeling on characteristic behavior of two phase flow of high viscous oil-water mixture in the presence of singularities. The fine mesh is considered in the region close to the pipe wall, with $y^+ \cong 5$. Predicted flow patterns and pressure gradients for simulation run S-9 with different turbulence scheme is compared with experimental counterpart and presented in Table 7-5. It is shown that the Realizable k-ε turbulence scheme gives the better result in terms of pressure gradient, with underprediction of 11% relative error. It is worth noting that both pressure gradients predicted from CFD simulation with different turbulence scheme underpredicted the experimental counterpart. The snapshot of recorded flow pattern for 50 mm downstream of singularity (the optical box is used to reduce light distortion) shows that the degree of dispersion for case S-9 is dramatic and many oil droplets occupy the oil-water interface. This is reproduced by Realizable k-ε scheme, where the interface is shown by green color. On the other hand, the predicted flow pattern by SST k-ω scheme has a sharp and smooth interface. Although some Authors (Vallée et

al, 2008; and Lo and Tomasello, 2010) obtained that turbulence damping at interface (by the $SST\ k-\omega$ model) results in a better prediction of the pressure drop, in the present simulations it is the RKE turbulence model to show the best agreement with the experimental data. Hence, the RKE model is used for other simulation runs.

Table 7-5 Predicted flow patterns and pressure drop downstream of sudden expansion for simulation run S-9, with different turbulence scheme

	Flow pattern	$-\dfrac{dp}{dx}$ (kPa/m)	Relative deviation (%)
Realizable $k-\varepsilon$		0.17	-15%
$SST\ k-\omega$		0.13	-35%
Experiment		0.20	

Cross-sectional turbulence characteristics of flow behavior together with void fraction at axial location of L=1 m from inlet is shown in Figure 7-6 (a) and (b) for SST k-ω and Realizable k-ε turbulence schemes, respectively. Turbulence parameters estimated by CFD simulation using two schemes have the same order of magnitude. Generally, turbulence properties calculated by

k-ε models have the higher magnitude than that using SST k-ω turbulence scheme. It is observed that turbulence viscosity is higher in the regions near to centerline than to the pipe walls.
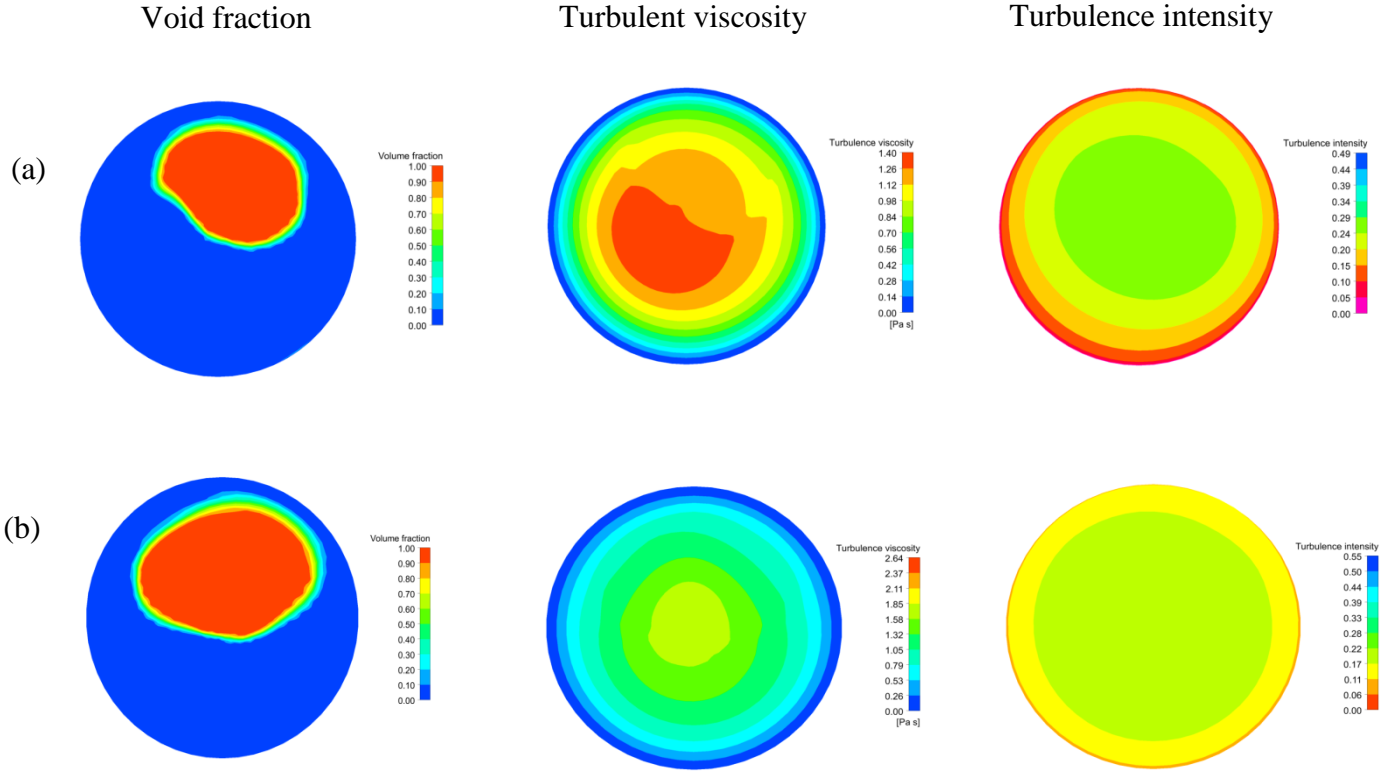
Figure 7-6 Cross-sectional turbulence characteristics of oil-water mixture at axial position L=1 m from inlet (downstream of sudden expansion) for (a) SST k-ω, and (b) Realizable k-ε schemes.

7.6.4 Sensitivity analysis on initialization methods

Two simulation cases have been run to check the influence of the initialization methods on the flow pattern and pressure gradients for case S-9. The computational domains were filled with water and then oil was injected to the system. The inverse procedure has been repeated for higher viscous fluid, where oil is first injected followed by water flow. In order to avoid repeating the predicted flow pattern for the case, where the domain is first filled with water, the calculated flow pattern for system only initialized with oil is presented and shown in Figure 7-7 for different time steps. The red and blue colors represent oil and water, respectively. The presence of oil at the pipe wall is clearly visible from the predicted flow pattern. This is inconsistent with

the experimental observation shown in Table 7-5 and it violates the definition of core-annular flow. This situation must be avoided because it may cause increase the pressure gradient along the pipe axis. However, wavy interface is obviously identified downstream of singularity. The calculated pressure gradients upstream and downstream of singularity for system initialized with oil is 1.28 and 0.33 kPa/m, respectively, while the predicted values for the inverse procedure were found to be 1.21 and 0.17 kPa/m. The overprediction of pressure gradient downstream of cross-sectional area change for the system initialized with oil is due to the oil fouling phenomenon. To reproduce the same situation as experimental procedure, the water initialization method is used in the reset of simulation runs.
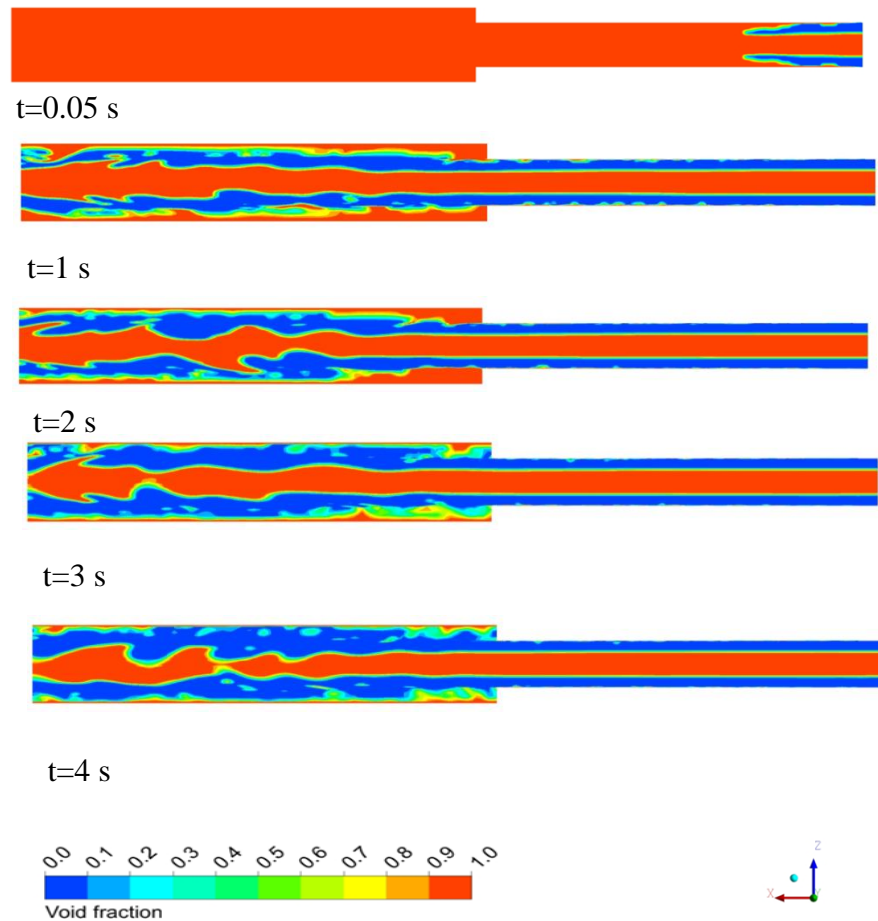
Figure 7-7 Predicted flow pattern for a system initialized with oil in different time step for simulation run S-9. Red and blue colors represent oil and water, respectively.

7.7 Simulation results
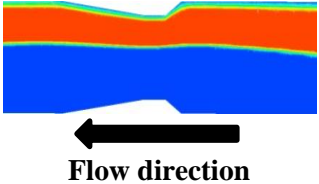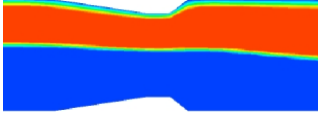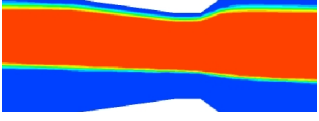
Analysis of CFD simulation results is presented in this section and validation with experimental data (Chapter 4 and 6 for sudden expansion and measurement devices, respectively) are performed. In addition to the most important parameters of oil-water flow (pressure gradient, phase holdup and flow patterns), cross-sectional flow field from CFD simulation is extracted and discussed. First, the results of CFD simulation for VFM and NFM are presented in section 7.7.1, followed by discussion about the CFD modeling of high-viscous oil-water through sudden expansion, with different cross-sectional area ratio (section 7.7.2).

7.7.1 VFM and NFM

7.7.1.1 Qualitative analysis

Table 7-6 reports a qualitative comparison between three experimentally and numerically predicted flow patterns in the VFM. The color scale is from blue (representing water) to red (representing oil), with intermediate colors evidencing the evolution of the VOF color function in the interface region. For the flow conditions under investigation, VOF model is able to capture the macroscopic behavior of the oil core, the presence of a very thin layer of water over the core (also in the throat section of the VFM), the core eccentricity and the shape of its cross-section, the difference between thin and thick oil cores that was already observed by Kaushik et al. (2012). For the cases of wavy core-annular flow, it is experimentally observed that the interfacial waves disappear when the mixture flows through the throat section, likely due to the acceleration that induces a transition to core annular flow. Thus the flow behavior at the throat section is well reproduced by the CFD simulation.

Table 7-6 Flow pattern experimentally observed and predicted by CFD simulation for VFM

Experimental observation (upstream of throat section)	Experimental observation (throat section)	CFD prediction (Throat section)	J_o (m/s)	J_w (m/s)	Flow regime
		Flow direction	0.25	0.44	Core-annular wavy
			0.46	0.44	Core-annular wavy
			0.75	0.66	Perfect core-annular

The velocity contours of the fluid stream in the vertical axial plane of the NFM and the VFM for J_0=0.46 m·s^{-1}, J_W=0.44 m·s^{-1} are shown in Figure 7-8 (a) and (b), respectively. The velocity magnitude is also mentioned beside each figure. Obviously, maximum velocity is reached in the throat section in both cases, however, it lasts for a longer distance for the NFM than the VFM. This might be due to the mixing zone and turbulence effect after the sharp expansion in the case of the NFM. Figure 7-9 reports the transient relative to the development of the oil core in the VFM for a typical core-annular flow pattern ($J_o = 0.46 \, \text{ms}^{-1}, J_w = 0.44 \, \text{ms}^{-1}$). At the early time of simulation, fouling phenomenon occurs downstream of the VFM. However, a thin layer of water is observed at the time higher than 2.5 s showing that the situation rapidly evolves towards a fully core annular, though strongly eccentric, flow pattern.

a) NFM; $J_o = 0.46\ ms^{-1}, J_w = 0.44\ ms^{-1}$

Velocity [m/s]   [m s^-1]
0.0 0.2 0.3 0.5 0.6 0.8 1.0 1.1 1.3 1.4 1.6

Flow Direction   NFM

b) VFM; $J_o = 0.46\ ms^{-1}, J_w = 0.44\ ms^{-1}$

Velocity   [m s^-1]
0.00 0.18 0.36 0.55 0.73 0.91 1.09 1.27 1.46 1.64 1.82

Flow Direction   VFM

Throat
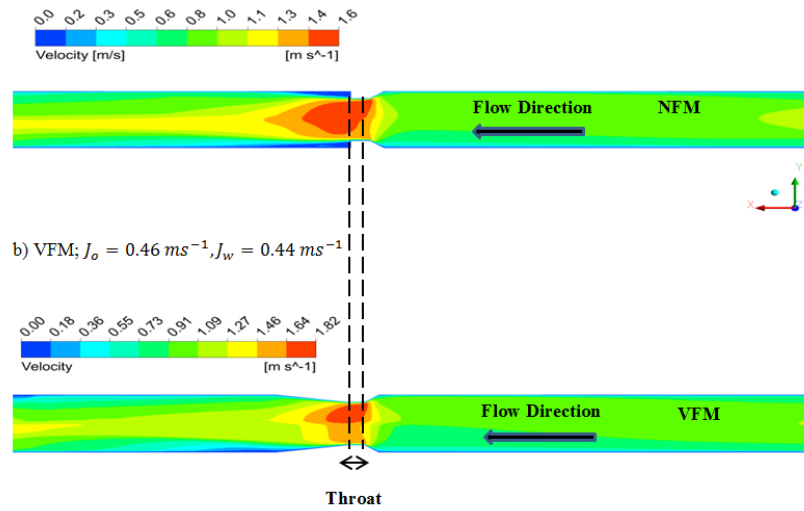
Figure 7-8 Velocity contour in the vertical axial plane for a) NFM and b) VFM

t =0.1 sec

t =0.5 sec

t =1 sec

t =1.5 sec

t =2 sec

t =2.5 sec
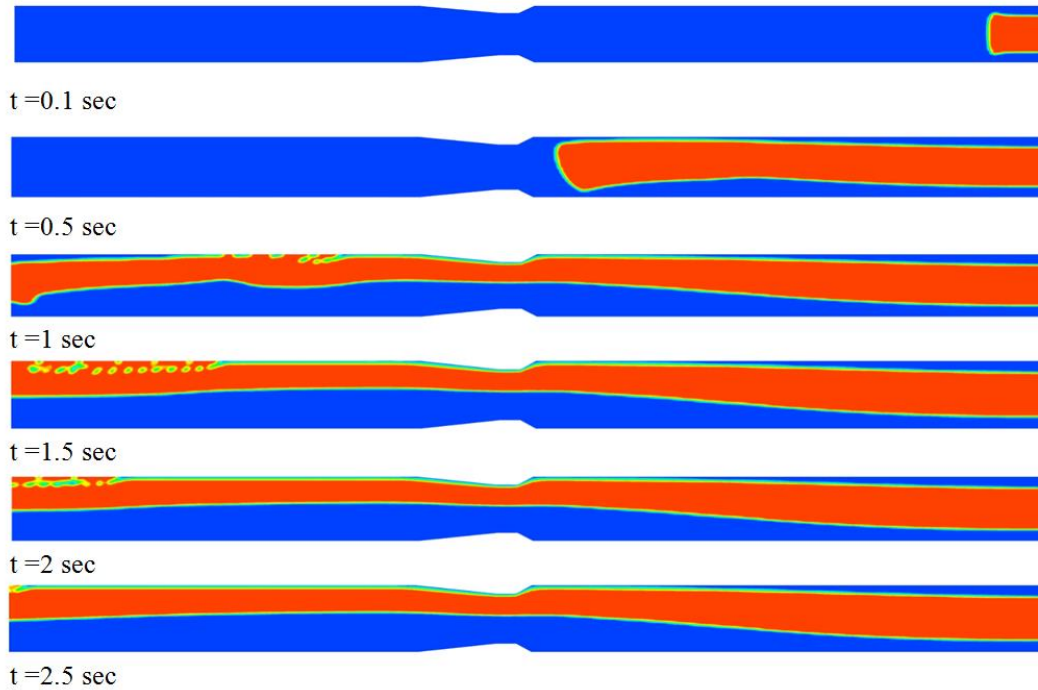
Figure 7-9 Development of the oil core phase through the VFM at different time steps, for the flow pattern corresponding to $J_o = 0.46\ \text{ms}^{-1}, J_w = 0.44\ \text{ms}^{-1}$

7.7.1.2 Concentrated pressure drop

The experimental concentrated pressure drop for VFM and NFM for different flow conditions have been presented in Chapter 6. Results of two-phase concentrated pressure drop predicted by (RKE) and $SST\ k-\omega$ for NFM are reported in Table 7-7. Figure 7-10 reports the comparison between the concentrated pressure drop from simulations and experiments simulated for both the VFM and NFM in terms of a parity plot. Dashed lines represent ±15% deviation from bisector because apart from one point, all data fall within ±15% relative error for both VFM and NFM. Only results using the RKE model are included in this comparison. The results show a good agreement in both cases, with in general a better agreement for the VFM: maximum relative errors are 11.6 % and 16.4 % for the VFM and NFM, respectively. It is worth noticing how the simulated two phase pressure drop generally underestimates the actual two phase pressure drop. The higher deviation for the NFM might be due to a poor representation of the more complex flow downstream the sudden expansion: according to visual observations, very often it presents some degree of dispersion.

Table 7-7 Comparison of two-phase concentrated pressure drop for the NFM

J_o (ms^{-1})	J_w (ms^{-1})	Numerical ΔP RKE (kpa)	Numerical ΔP $SST\ (k-\omega)$ (kPa)	Experimental ΔP (kpa)	Relative deviation (%) for RKE	Relative deviation (%) for $SST\ (k-\omega)$
0.46	0.44	0.78	0.79	0.79	0.91	1.1
0.51	0.66	1.45	1.39	1.735	16.4	19.4
0.64	0.66	1.72	1.64	1.985	12.8	17.3
0.64	0.88	2.41	2.29	2.75	12.0	16.7
0.64	1.10	3.17	3.01	3.61	12.1	16.3
0.75	0.66	2.07	1.95	2.34	11.2	16.5
0.75	0.88	2.72	2.57	3.14	13.3	18.0
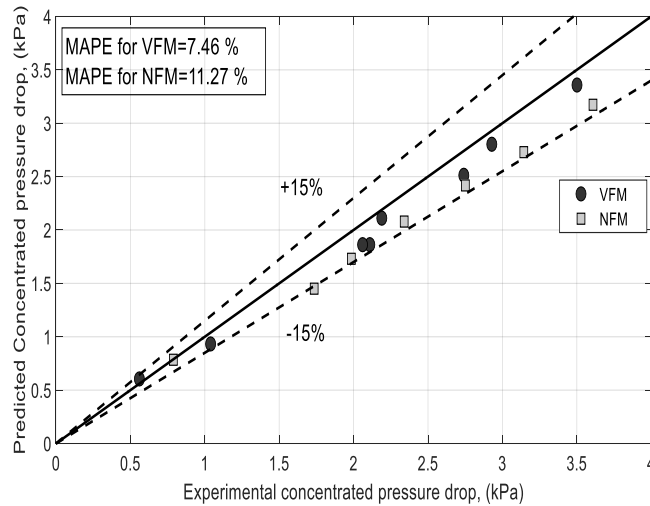
Figure 7-10 Comparison between CFD prediction and experimental two-phase concentrated pressure drop. Dotted lines represent ±15% from the bisector

7.7.1.3 Local Radial Velocity and Oil Phase Holdup

To understand the hydrodynamic behavior of the flow, time-averaged velocity and oil in situ volume fraction (holdup) profiles are evaluated, with reference to VFM cases, along the vertical diameter of a cross section of the upstream pipe at L=0.4 m. Such a distance was selected to ensure that the flow is developed and at the same time that the flow fields are still not affected by the contraction. The results are taken based on time averaging between a period of 4 s and 8 s to ensure that flow fluctuations are removed and steady state conditions are achieved. One core-annular wavy flow and three core-annular flow cases with fixed $J_o = 0.64\ \text{m} \cdot \text{s}^{-1}$ and variable water superficial velocity are considered. The results for the NFM are not shown here since they practically coincide with the VFM results. The red solid line and the black dotted lines in Figure 7-11 display phase local velocity and oil holdup, respectively. It is evident that the oil core moves with higher velocity than the water adjoining the pipe wall for annular flows. Asymmetric nature of phase and velocity profiles, due to oil buoyancy, is clearly evident, particularly for heavily eccentric cores (Figure. 7-11-a). The velocity profile in the core region shows a piston flow with practically uniform velocity, as expected. Regarding to phase holdup profile, there is an abrupt change of values at the interface, evidencing how the numerical interface is satisfactorily. By increasing water superficial velocity, no significant change in the shape of the velocity profile is observed.

167
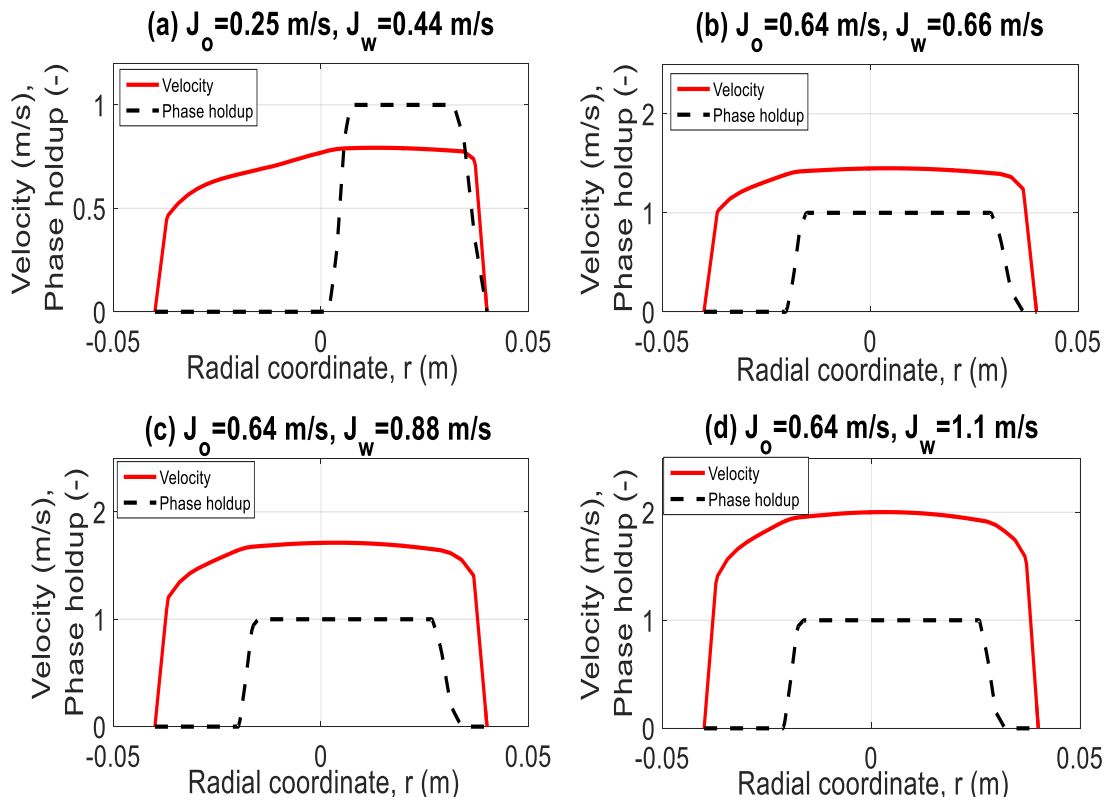
Figure 7-11 Vertical velocity and local oil fraction (holdup) profiles versus radial coordinate, at L = 0.4 m from the inlet.

7.7.1.4 Cross-sectional average holdup

The already cited Arney correlation (eq. 5-2) was found to predict with very good agreement the water holdup both in ducts having uniform diameter and after sudden changes in the duct section, see e.g. Arney et al. (1993), Colombo et al. (2015). Thus, time-averaged cross sectional water holdup predicted by CFD is plotted versus value obtained using Arney correlation in a parity plot for the VFM and NFM at L=0.4 m from pipe inlet (Figure 7-12). The simulated holdup underestimates predictions from the Arney correlation in all cases, with maximum deviation of 16.1 % for the VFM and 12.5% for the NFM. Dashed lines of ±15% are selected; 87% of whole data lies in ±15%, while all data falls within ±20% deviation from bisector. For both devices, regular trends of water holdup are observed as a function of increasing water cut.
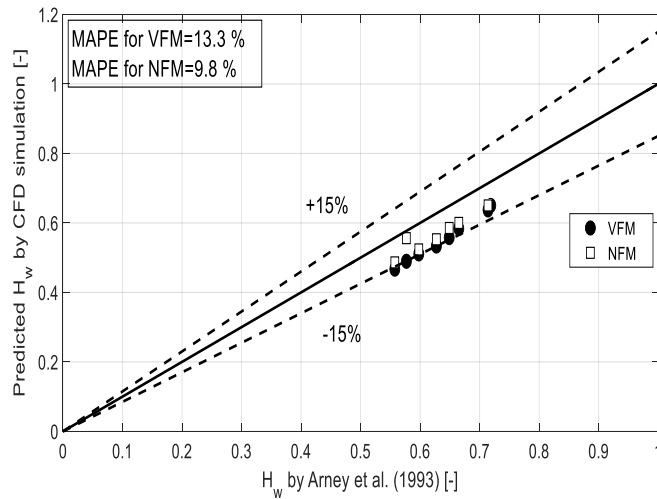
Figure 7-12 Parity plot of cross-sectional and time-averaged water holdup from CFD simulation, versus prediction of the Arney et al. (1993) correlation. Dotted lines represent ±15% from the bisector.

Figures 7-13 and 7-14 present cross sectional contour of phase fraction fields at different axial location: upstream pipe (L=0.4 m), throat section (L=0.515 m) and downstream pipe (L=0.612 m) for the VFM and NFM corresponding to $J_o = 0.51$ ms^{-1}, $J_w = 0.66$ ms^{-1} at time instant t=8 s. Due to the fact that gradual and sudden expansion exist after diffuser for the VFM and NFM, respectively, the axial location at L=0.612 m from the inlet is considered for both devices in CFD model to evaluate the shape of oil core. In both devices, the presence of water layer in the annulus adjacent to the pipe wall is evident. The shape of the oil core evolves from the inlet circular section first towards an elliptic shape and then the lower surface flattens more and more from upstream to downstream of measuring devices. Disturbances and minor deformations of the interface can be observed, as a result of the coarseness of the mesh.
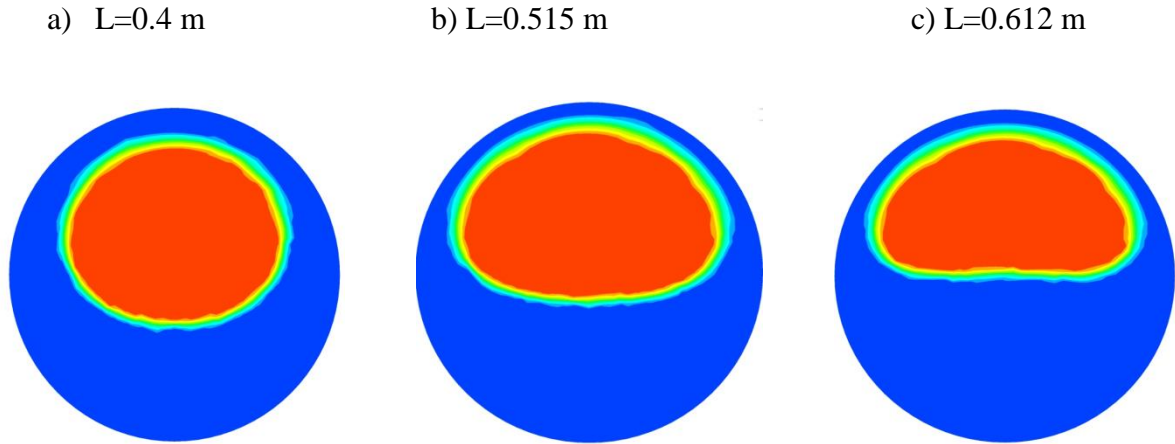
Figure 7-13 Cross-sectional oil holdup fields at different axial location for the VFM at time instant t=8 s (color scale is from blue for water to red for oil).
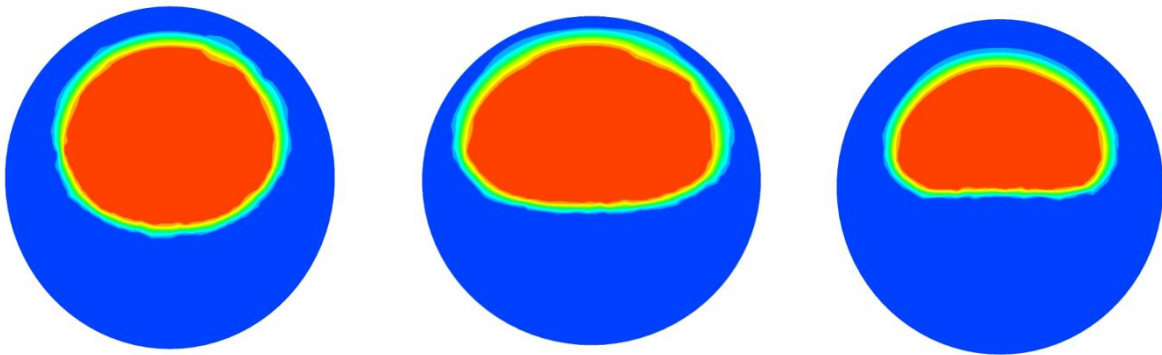
Figure 7-14 Cross-sectional oil holdup fields at different axial location for the NFM at time instant t=8 s (color scale is from blue for water to red for oil).

7.7.1.5 Slip ratio and two phase mixture velocity

To further investigate the effect of the VFM and NFM on the mixture hydrodynamics, the slip ratio was calculated both in the upstream pipe and at the throat section. Figure 7-15 shows the slip ratio as a function of the water holdup at upstream pipe L=0.5 m and throat section L=0.515 m for the VFM case. The average value of slip ratio in the upstream pipe is 0.85 while at throat section it becomes 1.02. It is worth noting that the inverse definition of slip ratio is applied. Table 7-8 compares the mean value of slip ratio for both the VFM and NFM, demonstrating the same behavior for the two devices: within them the mixture accelerates, but the acceleration is not uniform between the two fluids. Water accelerates more than oil (as it seems correct, given

the higher viscosity of oil) so that the mixture flow becomes practically homogeneous, as it is also found from the experiments. Thus simulations confirm their consistency with the experiments.
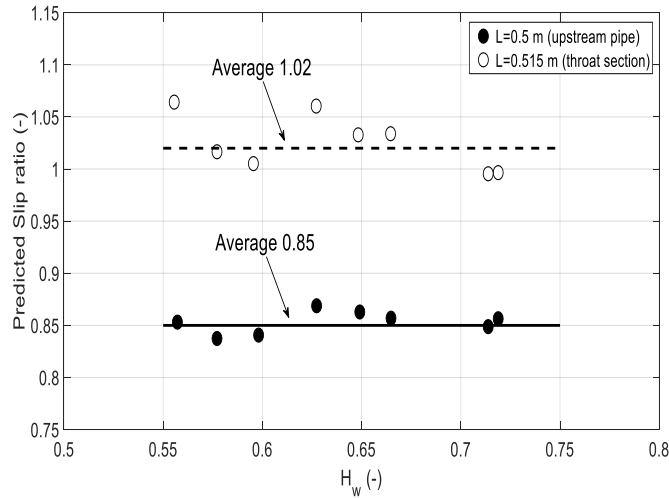
Figure 7-15 Slip ratio predicted from CFD simulation versus average water holdup for axial positions of 0.5 m (upstream) and 0.515 m (throat section) from inlet

Table 7-8 Simulated mean value of slip ratio (S=$\frac{U_w}{U_o}$) upstream pipe and at throat section

Device	Mean Slip Ratio at Upstream pipe (L=0.5 m)	Mean Slip Ratio at Throat Section (L=0.515 m)
VFM	0.85	1.02
NFM	0.86	1.03

In order to calculate the mass flow rate, the value of the discharge coefficient must be provided. The numerical values of the discharge coefficients for core annular flow by means of definition of characteristic Reynolds number provided by Arney et al (1993) are obtained in Chapter 6. Thanks to the homogeneous behavior of the flow within the devices, a further attempt can be made to obtain the mass flow rate by means of the homogeneous model. After calculation of the

discharge coefficient, mass flow rate can be simply obtained by knowing the concentrated pressure drop and the averaged density (computed by Eq. 6-4). For the simulated cases, the actual flow rates of oil and water are known from experiments, as they were measured by calibrated metering pump and magnetic flow meters, respectively. Figure 7-16 reports the comparison between the mass flow rate computed by homogeneous model with concentrated pressure drop from CFD and the experimental mass flow rate taken as reference. The mean relative error and standard deviation are given in Table 7-9. In both the VFM and NFM cases simulation results are in good agreement with reference values. This is especially true for the VFM, while the NFM presents a slightly larger relative error. The dashed lines represent ±15% deviation from the bisector.
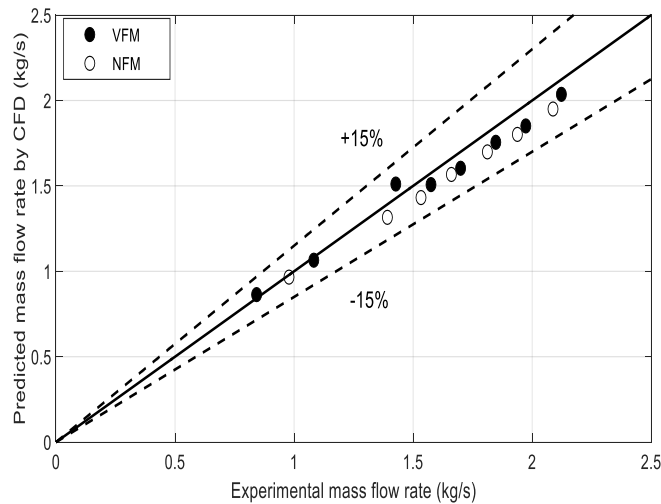
Figure 7-16 Parity plot of the comparison between the computed mass flow rate by CFD simulation and reference experimental flow rate. Continuous line evidence the bisector, dashed lines limit ±15% deviation

Table 7-9 Statistical performance of predicted mass flow rate by CFD
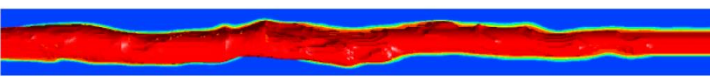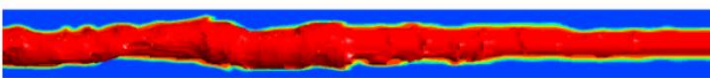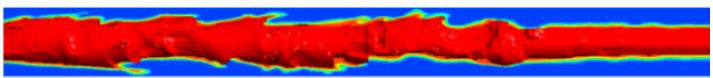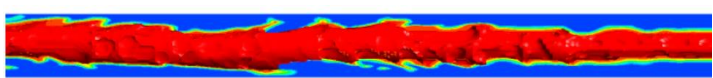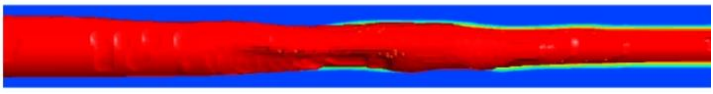
Device	MAPE (%)	Mean Standard Deviation (%)
VFM	4.4	1.5
NFM	5.5	1.7
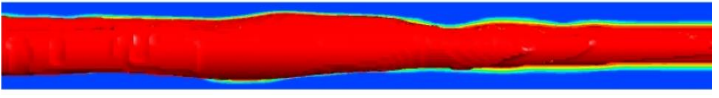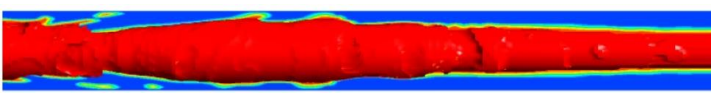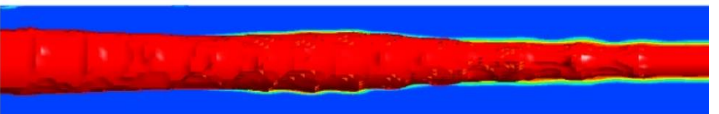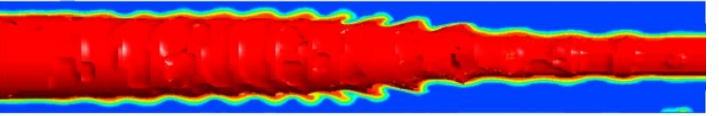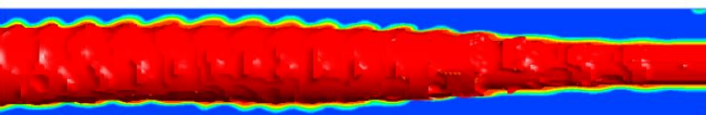
7.8 Numerical results for sudden expansion

7.8.1 Flow patterns

A comparison between the simulated flow patterns and experimental visualizations for sudden expansion cases are reported in Table 7-10. Two flow patterns are experimentally observed, which included transition from core-annular to dispersed (Tr. CAF-D) flow and eccentric core annular flow with oil entrainment (ECAF-E). The transition from CAF to D flow regimes for flow conditions under investigation were observed experimentally for pipe configuration undergoing sudden expansion from 21 mm to 30 mm. On the other hand, core annular flow with oil entrainment is only detected in sudden expansion cases from 30 mm to 40 mm and 30 mm to 50 mm. It is worth remarking that images from experimental data and simulations are concerned with the flow patterns downstream of singularities. The simulated flow patterns for core annular flow are in fairly good agreement with experimental counterparts: thick core downstream of sudden expansion for 40 mm and 50 mm is well reproduced by CFD simulations. The wavy interface caused by interfacial shear stresses between oil and water is observed. It should be remarked that fully dispersed flow is not experimentally observed. Shi (2015) proved that if the interface length is small compared to the computational grid, VOF model is not able to capture the flow pattern of dispersed oil in continuous water flow. Hence, it is necessary to have much finer grid to simulate the oil droplet. Generally, it is suggested to model dispersed flow with the mixture, Euler-Euler models. In the present Chapter, since the interface length scale of core annular flow is comparable to computational grid, VOF model is able to capture the interface with even coarser grid cells. During core-annular flow of high viscous oil-water mixture, both experimental and numerical analysis show that oil is surrounded by the water phase which remains adjacent to the pipe wall.

Table 7-10 Comparison between predicted flow patterns and experimental counterpart in downstream pipes

Simulation runs	Flow pattern	Experiment	Simulation
S-1	Tr. CAF-D		
S-2	Tr CAF-D		
S-3	Tr. CAF-D		
S-4	Tr. CAF-D		
S-6	ECA-E		

S-7	ECA-E		
S-8	ECA-E		
S-9	ECA-E		
S-10	ECA-E		
S-11	ECA-E		
S-12	ECA-E		

7.8.2 Oil fouling phenomenon

Table 7-11 shows the sequences of oil core propagation through computational domains at various time steps for simulation runs of S-3, and S-11. The prediction of core annular flow with oil core at the center and water film around the inner pipe is clearly observed.

Table 7-11 Development of core-annular flow with time for simulation runs of S-3 and S-11
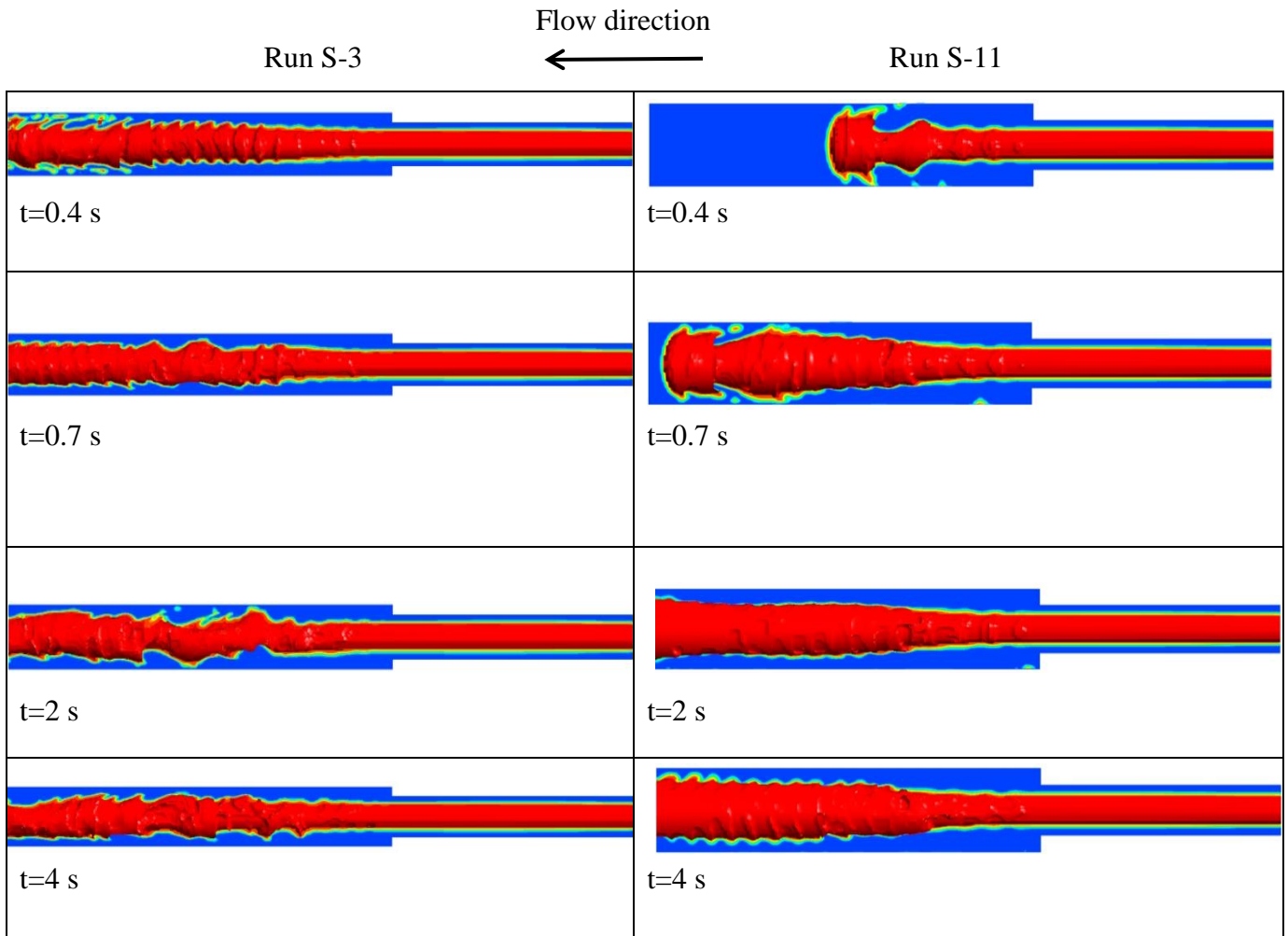
CFD simulation results are consistent with experimental observation in sense that oil never sticks to the wall. To deeply investigate oil fouling phenomenon and the influence of eccentricity on predicted flow pattern, the phase configurations at various cross-sections (axial position of 0.25 m, 0.5 m (singularity plane), 0.75 m, and 1 m from inlet) for three cases of sudden expansion, i.e.

S-2, S-6, and S-10 at t=5 s are displayed in Figure 7-17. It has been observed that oil is concentric upstream of singularity plane, becoming thinner at the cross-sectional area change. The oil core is eccentric far downstream of singularity plane at L=1 m due to the effect of gravity. Since the average velocity is lower downstream than upstream, gravity would significantly affect the predicted flow patterns. The degree of oil core eccentricity concerning simulation runs of S-6 and S-10 (stronger area ratio) is more dramatic than S-2. However, there is no considerable discrepancy between the simulation runs S-6 and S-10. The simulation findings in this section are in agreement with experimental observations presented in Chapter 4. It should be remarked that increasing the downstream pipe diameters may enhance the risk of oil fouling.
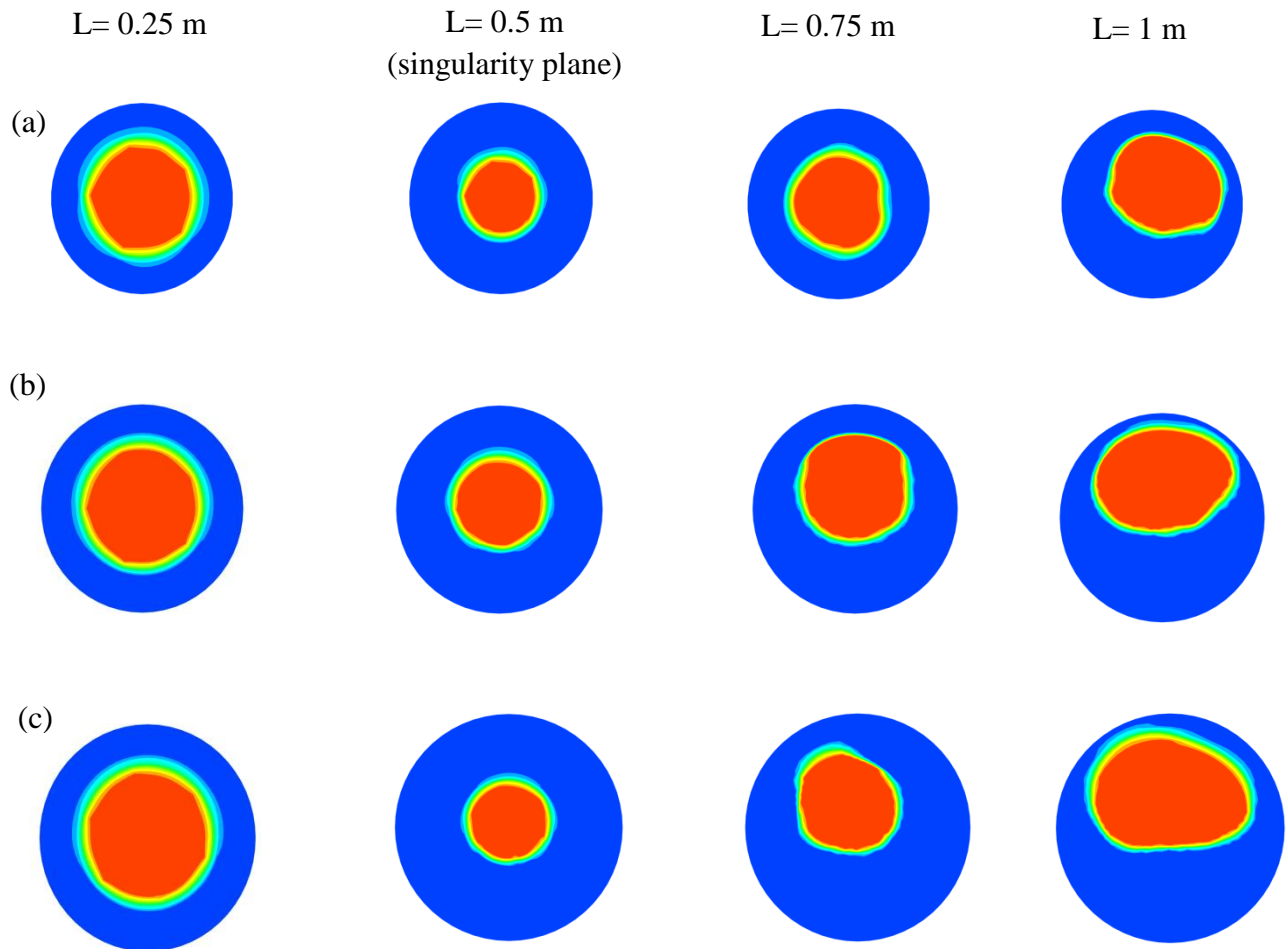
Figure 7-17 Cross-sectional phase configuration at various axial position from inlet for Simulation runs (a) S-2, (b) S-6, and (c) S-10

7.8.3 Prediction of oil holdup

The measured water holdup by means of QCV technique collected from Colombo et al. (2015) work was compared with Arney et al. (1993) correlation in Chapter 5, showing that the Mean Absolute Percentage Error (MAPE) was found to be 3.3% downstream of sudden contraction 50-40 mm and 50-30 mm. Since the experimental measurements of oil holdup for sudden expansion cases are not available, the oil holdup predicted by CFD has been compared against Arney et al. (1993) correlation. The comparison is reported in Figure 7-18, where oil holdup is extracted at downstream of singularity plane (L=1.1 m from inlet section). The dashed lines represent deviation of ±15% from bisector. It is worth noting that the same flow rates are considered for pipe configuration differing in area ratios.
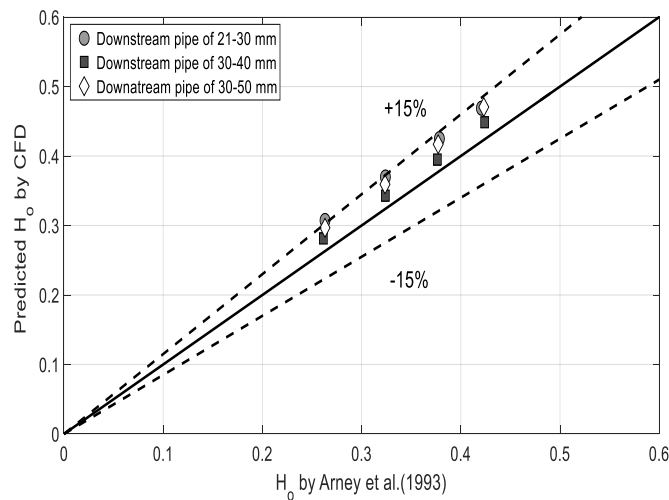
Figure 7-18 Prediction of oil holdup (H_o) by CFD versus estimated oil holdup by Arney et al. (1993). Dashed lines represent ±15% deviation from bisector.

Table 7-12 lists the values of predicted oil holdup and estimation from Arney et al. (1993) correlation for constant superficial water velocities while varying oil superficial velocities. In each sudden expansion case, the values of oil input volume fraction are also presented. From Table 7-12, it is evident that the CFD-predicted H_o always overestimated the values from Arney et al. (1993) correlation. Furthermore, prediction of oil holdup form both Arney et al. (1993) and CFD simulation underestimated input oil volume fraction (ε_o), meaning that oil moves faster than water. These findings are consistent with experimental measurements of oil holdup shown in the

previous Chapters (Chapter 4 and 5).The mean absolute percentage error (MAPE) of 10.3% was found between prediction of holdup by CFD and that from Arney et al. (1993) correlation, with maximum deviation of 16.7%.

Table 7-12 Comparison between predicted oil holdup by CFD and estimation by Arney et al. (1993)

Simulation run	J_o (m/s)	J_w (m/s)	ε_o (-)	H_o by Arney et al. (1993)	H_o (CFD)	Relative error (%)
S-1	1.67	3.21	0.34	0.263	0.307	16.7
S-2	2.23	3.23	0.40	0.323	0.369	14.1
S-3	2.79	3.21	0.46	0.378	0.425	12.3
S-4	3.35	3.24	0.50	0.420	0.469	11.4
S-5	0.81	1.58	0.33	0.261	0.281	7.7
S-6	1.09	1.58	0.40	0.323	0.342	5.8
S-7	1.36	1.58	0.46	0.376	0.395	4.9
S-8	1.64	1.57	0.51	0.423	0.448	5.8
S-9	0.81	1.57	0.34	0.263	0.296	12.7
S-10	1.09	1.58	0.40	0.323	0.359	11.0
S-11	1.36	1.58	0.46	0.377	0.416	10.5
S-12	1.64	1.57	0.51	0.423	0.470	11.1

7.8.4 Cross-sectional time-average mean oil holdup

In order to understand the hydrodynamic behavior of high viscous oil-water flow through sudden expansion, cross-sectional time-average mean oil holdup along pipe axis is shown in Figure 7-19 a-c. The oil holdup gradually increases at axial position close to the inlet section, followed by constant trend up to the singularity planes. After singularity, oil holdup increases sharply due to the influence of changing cross-sectional area, and then remains constant at fully developed region downstream of singularity. It is evident that water phase is considerably affected by the presence of singularity and slows down more significantly than oil phase, resulting in an increase in water holdup. It has been experimentally shown in Chapter 4 that the degree of oil dispersion increases by the presence of sudden expansion, so that oil drops are observed near the oil-water interface in core-annular flows. The oil drops tend to follow the main streamline flow direction. This phenomenon is more dominant in proximity of the sudden expansion, resulting in a sudden reduction in oil holdup just after singularity. The observed trends are in agreement with the results obtained by Kaushik et al. (2012), with lower oil viscosity. At different oil superficial velocity, the fully developed downstream oil holdup can either reduce or remain constant with respect to the oil holdup values upstream of singularity. However, reduction has been observed only for sudden expansion with area ratio 0.56. The fully developed oil holdup values can be estimated in the upstream and downstream regions where the cross-sectional time-average mean oil holdup remained almost constant. The average slip ratio ($S=U_o/U_w$) along pipe axis is shown in Figure 7-20 a-c for sudden expansion cases with different area ratios. In each plot, solid lines represent the homogeneous lines, meaning that oil and water move with the same velocity. It is clearly recognizable that the slip ratio is higher than unity both upstream and downstream of singularity. However, a sharp increase of slip ratio is observed in a region downstream pipe very close to the pipe fitting where magnitude of average slip ratio with respect to upstream pipe increases by factors about 3.5, 3 and 5 fold for area ratios of 0.49, 0.56, and 0.36, respectively. Higher increase of the average slip ratio after singularity in the latter might be associated with the stronger area ratio between upstream and downstream pipe. It is worth remarking that the average slip ratio remained constant, irrespective of oil superficial velocity, in fully developed regions upstream and downstream pipes.

Figure 7-19 Cross-sectional time-average oil holdups along pipe axis for area ratios of (a) 0.49, (b) 0.56 and (c) 0.36
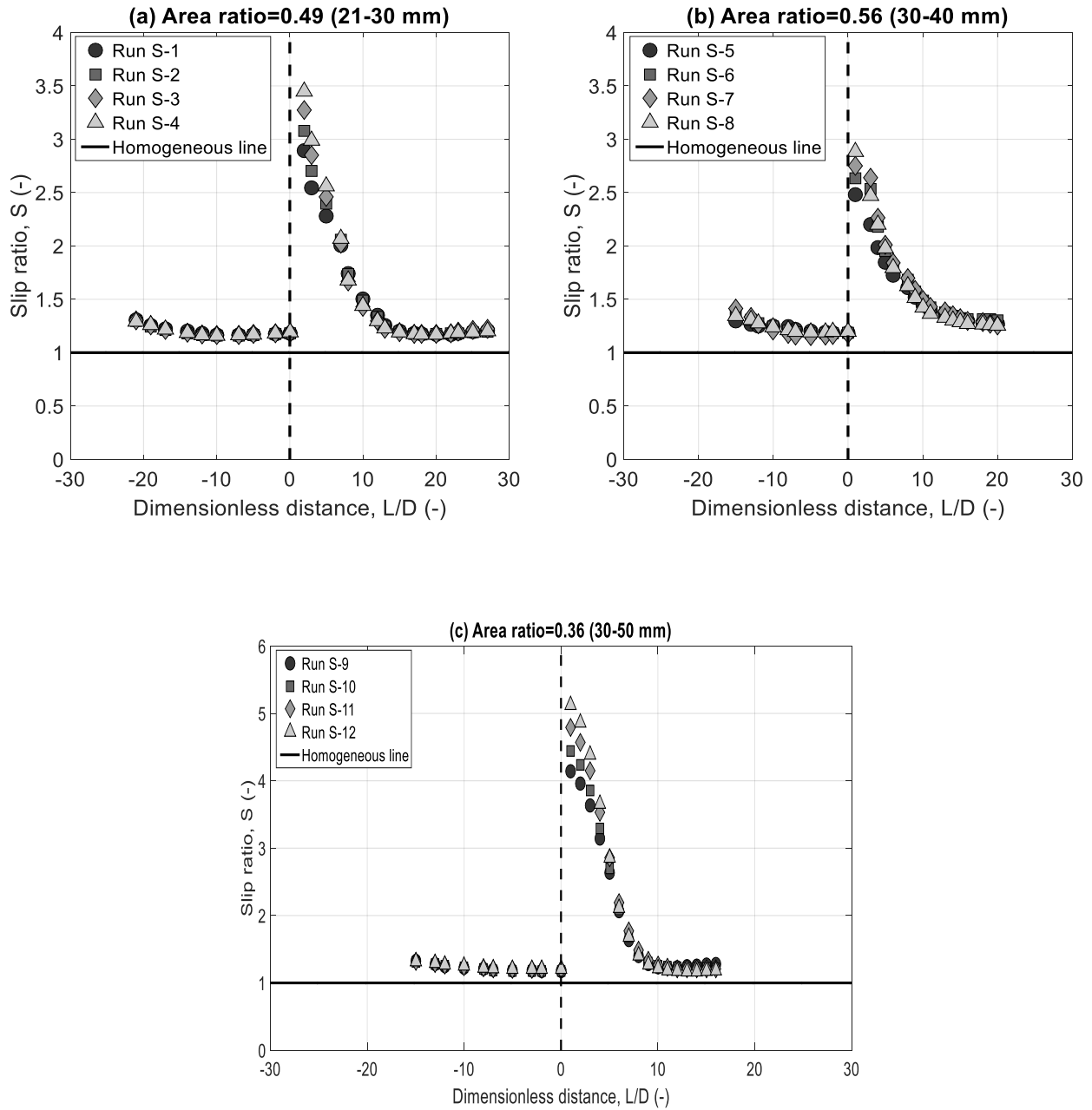
Figure 7-20 The average slip ratio along pipe axis for area ratios of (a) 0.49, (b) 0.56, and (c) 0.36

7.8.5 Time-average local oil holdup and velocity

To understand how oil holdup and velocity change downstream of the singularity, it is important to study the development of high viscous oil-water flow by quantifying the time-average local oil holdup and velocity profiles. Three simulation runs (Run S-1, Run S-5 and Run S-9) for the same oil input volume fraction but different area ratios are considered for the sake of comparison. A summary of flow conditions are reported in Table 7-2. The results are depicted in Figure 7-21 a-c, where r/R represents the dimensionless distance along the vertical axis from the centerline. Hence, the values of r/R=-1 and r/R=1 represent the positions of bottom and top of the pipes, respectively. The local oil holdup profile is more concentric in the upstream pipe up to the singularity plane (L=0.25 m and L=0.5 m, respectively) and becomes more eccentric in the fully developed region downstream of the singularity. This is consistent with flow visualization reported in Table 7-10, where the oil core tends to migrate to the upper part of the tube downstream of the singularity. The profiles are fully developed at axial position of approximately L=1 m from inlet.

(a)

183
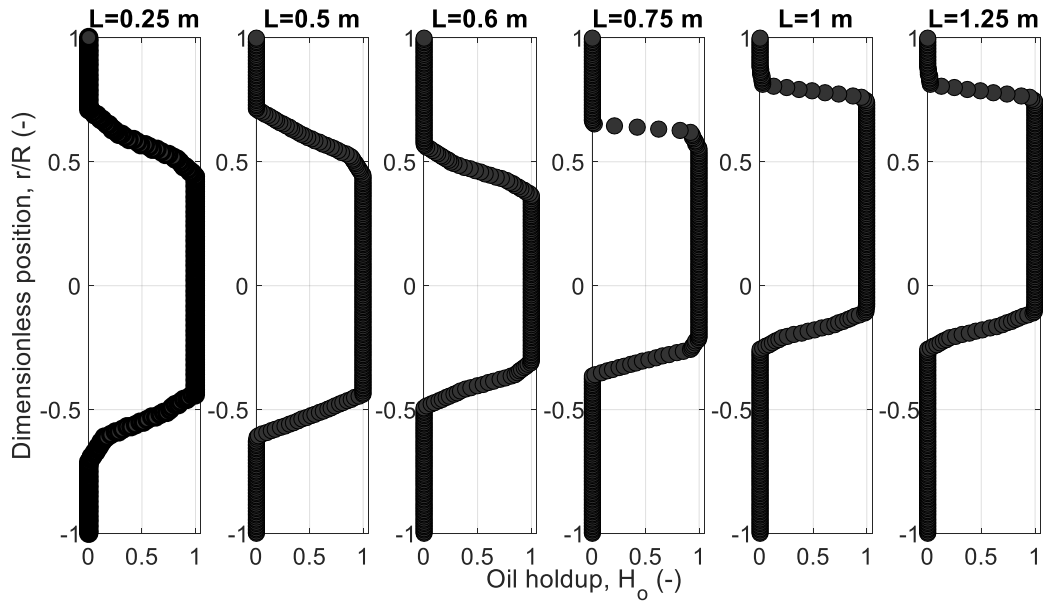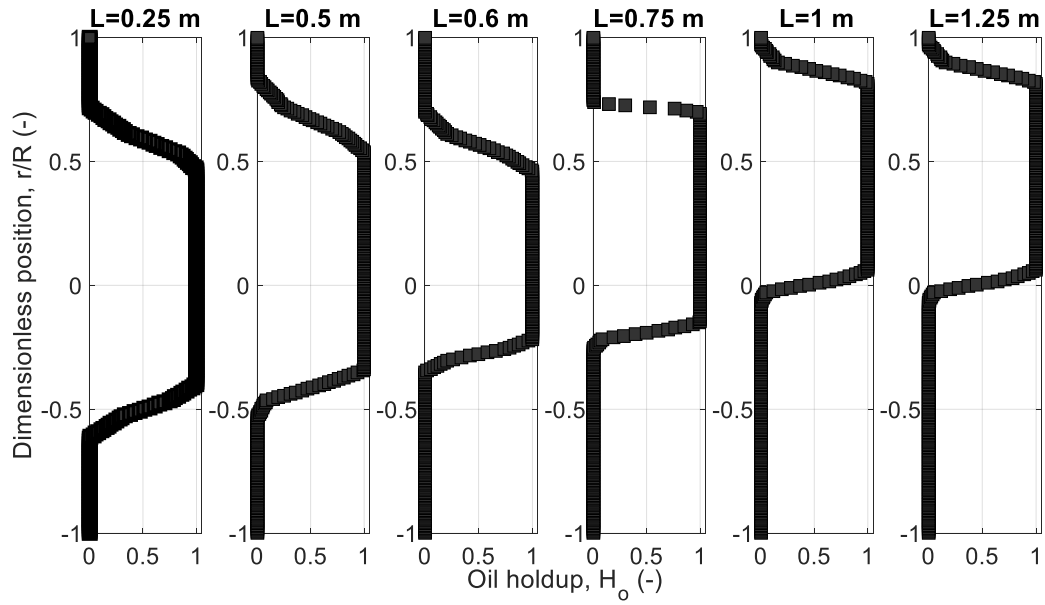
(b)
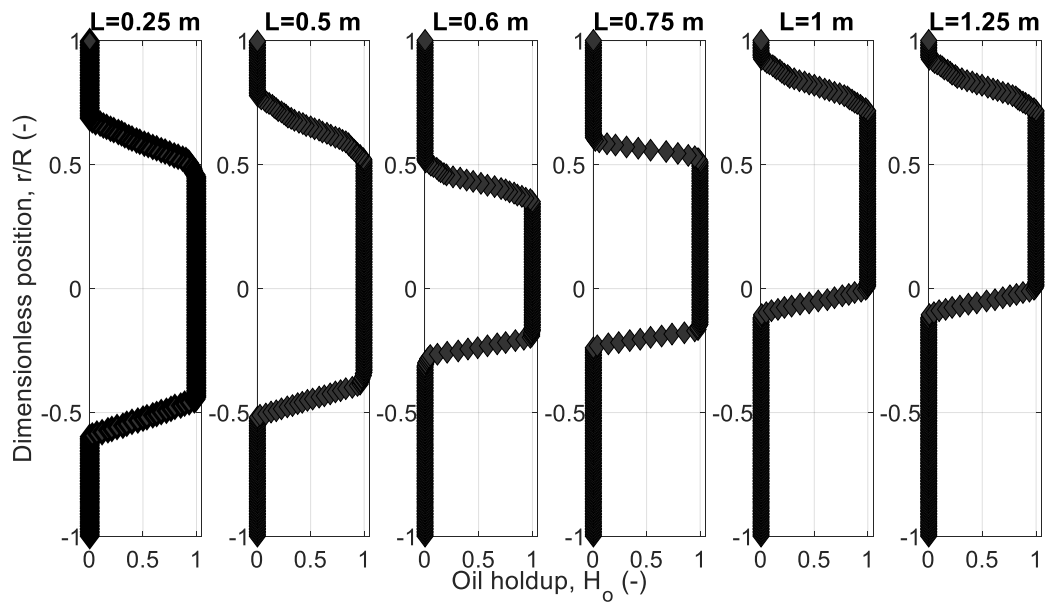
(c)

Figure 7-21 Time-average local oil holdup for simulation runs of (a) S-1, (b) S-5, and (c) S-9

Figure 7-22 illustrates the time-average local velocity profiles downstream of sudden expansion for three simulations runs, i.e, Run S-1, Run S-5, and Run S-9. The axial distance of L=0.5 m from inlet is exactly the position of singularity and L=1.25 m from the inlet is the farthest axial position from singularity. It is evident from Figure 7-22 a-c that the shapes of velocity profile in fully developed regions, i.e, far downstream (L=1.25 m) and at the singularity (L=0.5 m) differ from that in developing regions (L=0.6 m and L=0.75 m). Flatter velocity profiles are observed in fully developed regions. The gradients of velocity are greater in water annular layers, where the velocity reduces sharply towards the pipe wall. Comparing Figure 7-22 (a) to Figure 7-22 (b) and 7-22 (c), it is shown that far from singularity the velocity profile is more symmetric for area ratio of 0.49, while it becomes off-symmetric in cases with area ratio of 0.56 and 0.36 where the influence of oil core eccentricity plays an important role. In all figures, the oil core average velocity is higher than average water velocity. As previously mentioned, the two-phase flow can be considered as fully developed beyond L=1 m from inlet section, where velocity profile is very flattened. For the cases under considerations, the ratio of maximum velocity to mixture velocity (U_{max}/J_t) in fully developed region downstream of singularity becomes 1.13, 1.21, and 1.19 for area ratio of 0.49, 0.56, and 0.36, respectively. These values show that the velocity distribution of high viscous oil-water core annular flow is almost similar to that of single phase turbulent single phase flow, suggesting the positive effect of water-lubricated flow for oil transportation.
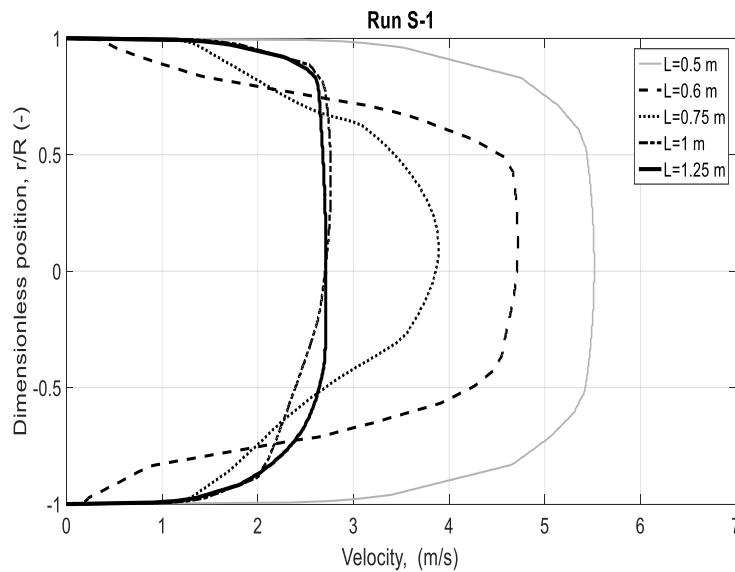
(a)
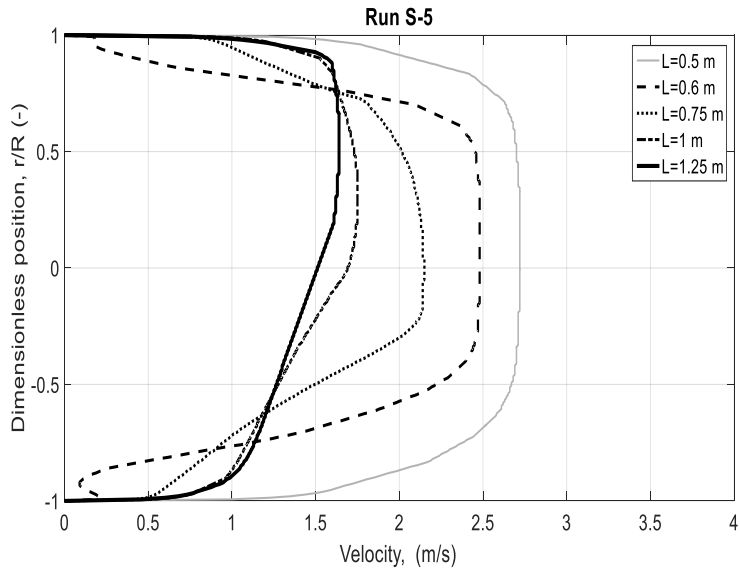
(b)
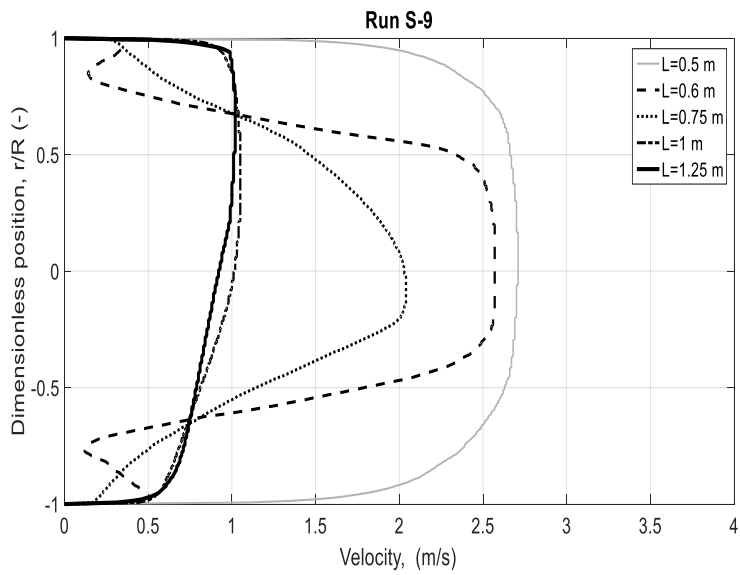
(c)

Figure 7-22 Variation of the velocity profiles upstream and downstream from sudden expansion for simulation runs of (a) S-1, (b) S-5, and (c) S-9

7.8.6 Prediction of pressure gradient

Table 7-13 reports the predicted pressure gradients from CFD simulation both upstream and downstream of the singularity, compared to the experimental data. The relative error between prediction and experimental data is fairly good, with the average relative errors of 21.7% (upstream) and 13.5% (downstream). In all cases, pressure gradients predicted by CFD simulation underestimated experimental data, with larger deviation in the upstream pipe. This might be associated with flow patterns, since it is observed from flow visualization that transition from CAF to Dispersed flow occurs while simulated flow patterns show CAF with wavy interface. Hence, as already mentioned in section 7.8.1 further efforts are valuable to capture properly the dispersed oil droplets within water continuous phase. Nevertheless, the CFD results are acceptable for design purposes.

In Figure 7-23, a comparison between predicted pressure reduction factor (ϕ) by CFD simulations and measurements for area ratios of (a) 0.49, and (b) 0.36 are presented as a function of input water volume fraction. The presence of sudden expansion reduces the pressure reduction factor at the same volume flow rates of phases from upstream to downstream pipes. The pressure reduction factor decreases by reduction of input water volume fraction. The experimental trends of pressure reduction factor are suitably reproduced by CFD simulations, with very high accuracy downstream of singularity. However, reasonable agreement is also observed between measured and prediction of ϕ upstream of singular plane.

Table 7-13 Comparison between predicted pressure gradient from CFD simulation and experimental counterpart

Simulation run	Measured $-(\frac{dp}{dx})$ upstream pipe (kPa/m)	Measured $-(\frac{dp}{dx})$ downstream pipe (kPa/m)	Predicted $-(\frac{dp}{dx})$ upstream pipe (kPa/m)	Predicted $-(\frac{dp}{dx})$ downstream pipe (kPa/m)	Relative error (%) upstream pipe	Relative error (%) downstream pipe
S-1	9.29	1.54	6.30	1.45	-32.2	-6.0
S-2	10.64	1.89	8.00	1.74	-24.8	-7.9
S-3	12.12	2.26	9.31	2.09	-23.2	-7.5
S-4	13.80	2.60	10.57	2.41	-23.4	-7.3
S-5	1.67	0.39	1.19	0.32	-28.6	-16.7
S-6	1.90	0.47	1.58	0.38	-17.1	-19.2
S-7	2.11	0.60	2.03	0.42	-3.8	-28.8
S-8	2.56	0.67	2.17	0.55	-15.3	-16.8
S-9	1.67	0.20	1.20	0.16	-27.8	-17.5
S-10	1.90	0.21	1.50	0.18	-21.0	-12.1
S-11	2.11	0.25	1.62	0.22	-22.9	-9.7
S-12	2.56	0.29	2.02	0.25	-21.0	-13.6
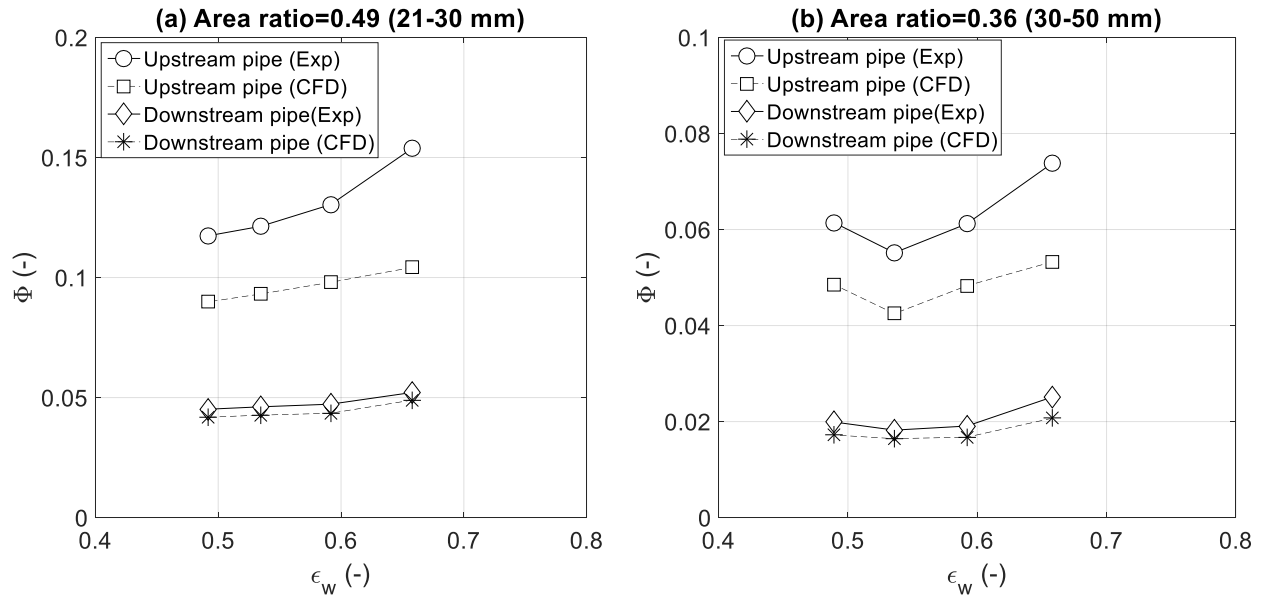
Figure 7-23 Pressure reduction factor (ϕ) as a function of input water volume fraction for area ratios of (a) 0.49, and (b) 0.36

Axial cross-sectional time average pressure distributions through sudden expansion for simulation runs of S-4, S-8, and S-12 are represented in Figure 7-24 a-c. The maximum pressure gradient occurs at the plane of singularity, followed by sharp rise of pressure as a result of pressure recovery and area increase. The pressure gradients in the downstream regions are smaller than in the upstream section because of larger cross-sectional area. Hence, three regions can be detected according to Figure 7-24 a-c, which included (1) fully developed inlet flow, followed by (2) transitional region, and (3) fully developed outlet region.

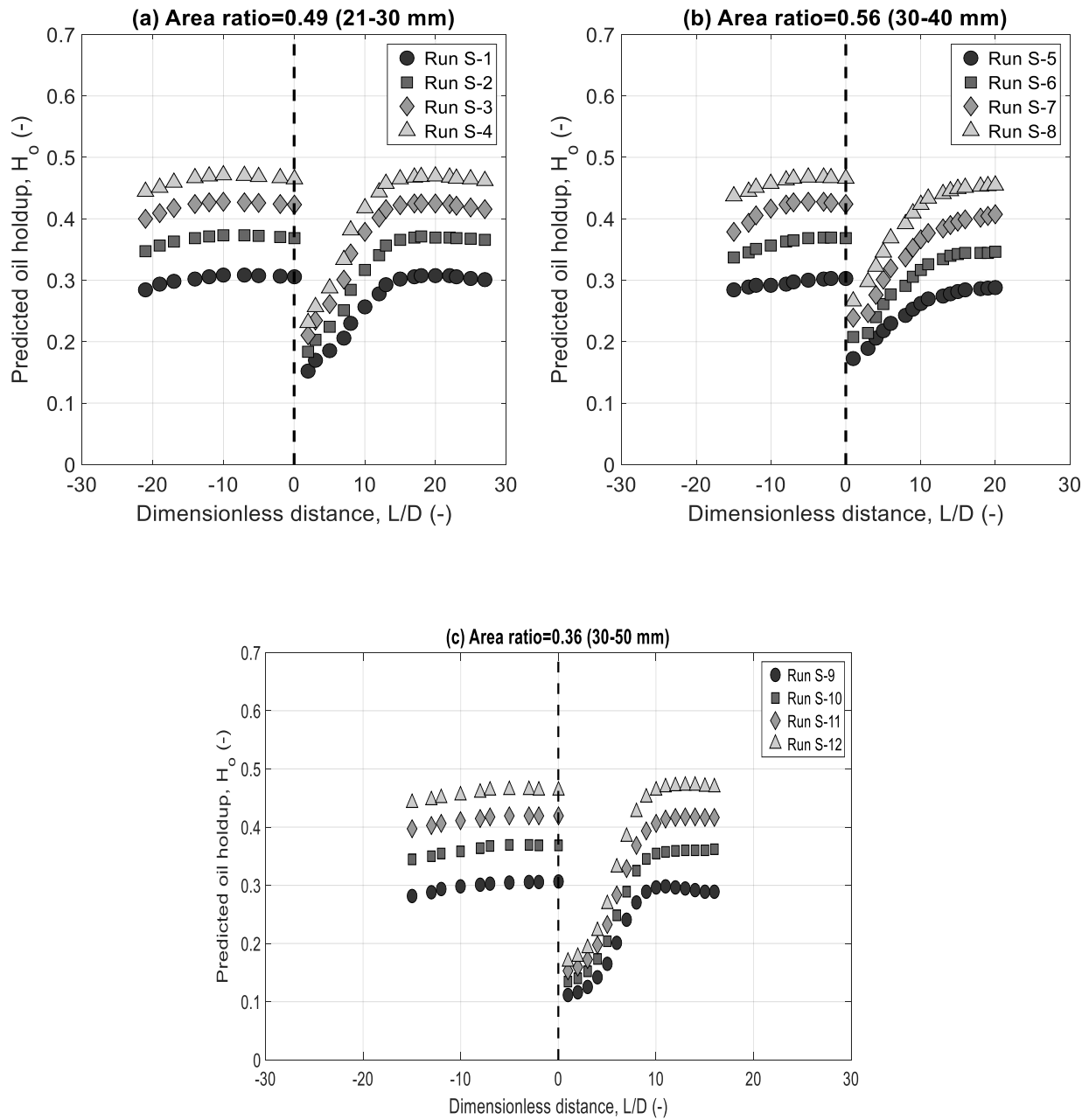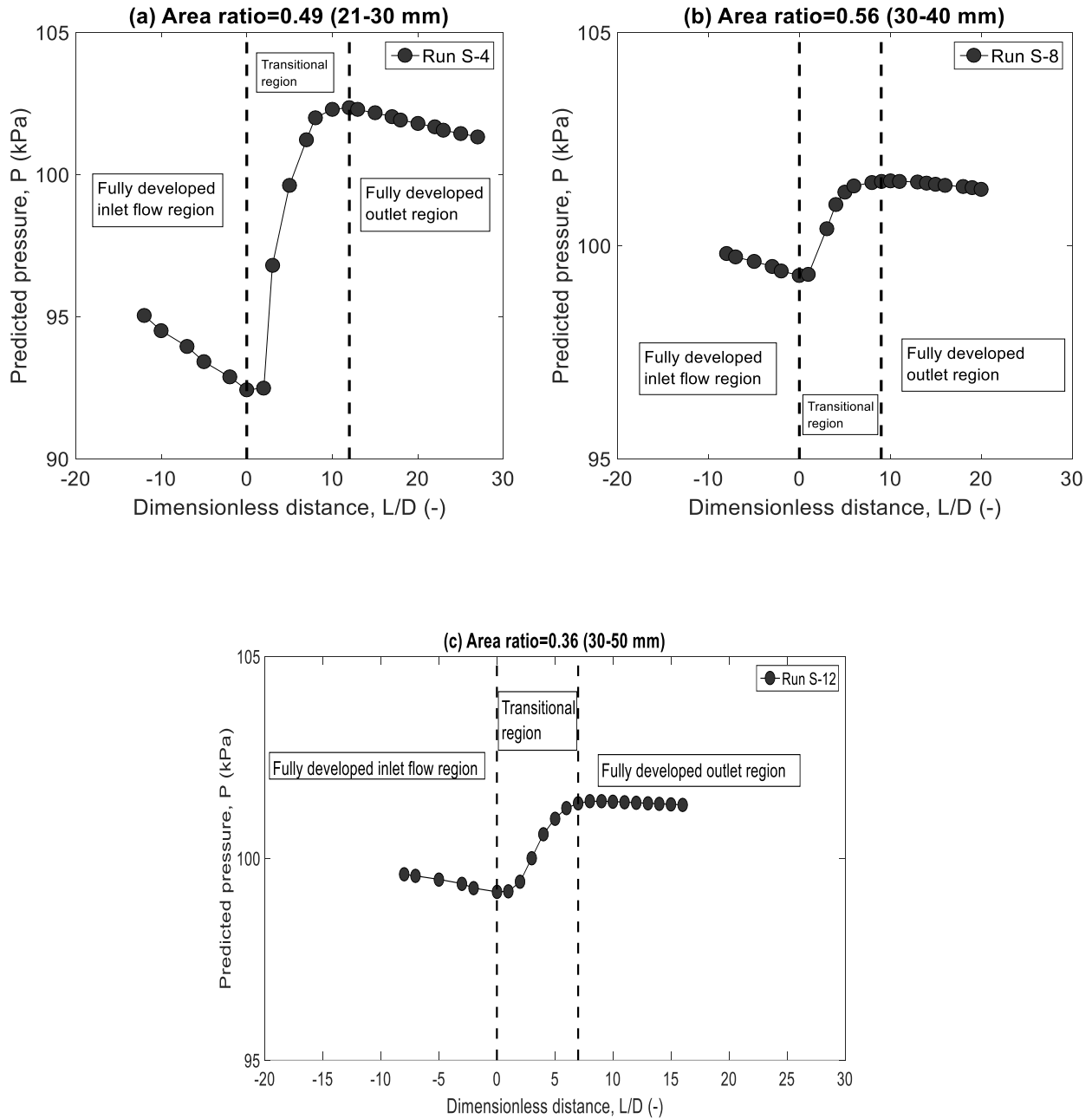Figure 7-24 Predicted cross-sectional time-average pressure along pipe axis for area ratios of (a) 0.49, (b) 0.56, and (c) 0.36

The slope of lines in regions (1) and (3) represent the pressure gradient. The pressure change at the sudden expansion plane is determined from the predicted pressure profiles upstream and downstream of the pipe expansion in the fully developed region extrapolating the pressure

profiles to the expansion plane. The experimental concentrated (singular) pressure drop across abrupt expansion has been presented in Chapter 4. Figure 7-25 compares the singular pressure drop predicted by CFD simulation and measurements for area ratios of 0.49 and 0.36 as a function of water input volume fraction. It is clearly recognizable that increase of input water volume fraction for constant J_w (i.e. reduction of J_o) results in decreased concentrated pressure drop across expansion plane. Similar trends are predicted by numerical simulations. Table 7-14 lists predicted concentrated pressure drop from CFD simulation and experimental data. The average relative errors of 33.9% and -12.7% are obtained for area ratios of 0.49 and 0.36, respectively. The higher deviation in the former might be due to improper prediction of flow pattern (Transition from CAF to D) by numerical simulations, while core-annular flow is adequately predicted by CFD analysis.
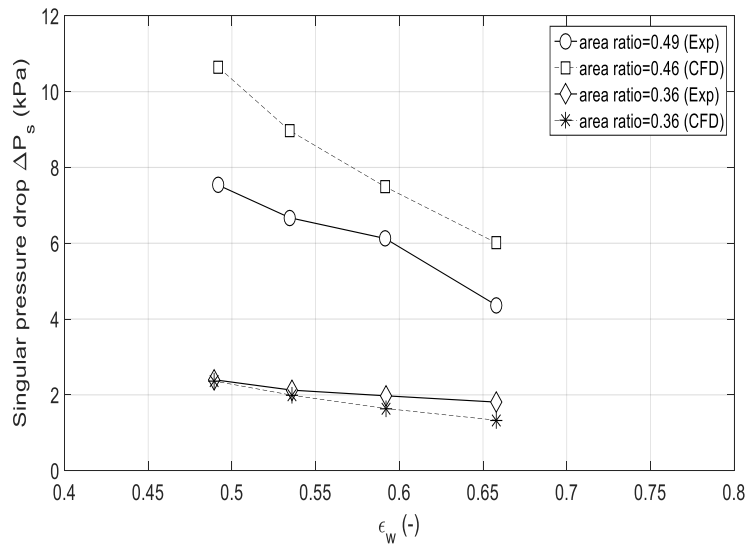
Figure 7-25 Comparison between singular pressure drop predicted by numerical simulation and measurements across expansion plane versus input water volume fraction

Table 7-14 Comparison of predicted concentrated pressure drop with experimental data for different simulation runs

Simulation run	Flow pattern	Measured ΔP_s (kPa)	Predicted ΔP_s (kPa)	Relative error (%)
S-1	Tr. CAF-D	4.36	6.01	37.7
S-2	Tr. CAF-D	6.12	7.49	22.2
S-3	Tr. CAF-D	6.67	8.97	34.4
S-4	Tr. CAF-D	7.53	10.65	41.3
S-9	ECA-E	1.80	1.33	-26.4
S-10	ECA-E	1.97	1.64	-16.9
S-11	ECA-E	2.12	1.99	-6.3
S-12	ECA-E	2.39	2.36	-1.4

8. Experimental characterization and theoretical modelling of very viscous oil-water-air flow slug flow characteristics in horizontal straight pipe

8.1 Introduction

Characteristic behavior of three phase flow in a horizontal straight pipe is evaluated in this Chapter. Firstly, the results of experimental pressure drop for 40 mm i.d. pipe are presented. Elongated bubble velocity is measured by means of two techniques: optical sensor and video analysis. Geometrical characteristics of slug units are measured by using the optical sensor. Secondly, a new correlation to compute the slug unit length as a function gas and liquid superficial velocity as well as pipe diameter is suggested. A mechanistic model based on "the slug unit cell model" is presented and validated with the experimental results.

8.2 Experimental facilities

The experimental tests have been conducted at the laboratory of Multiphase Thermo-Dynamic fluid in Politecnico di Milano, with the same test section used for two-phase flow through VFM and NFM. Thus, the Plexiglass pipe with total length of 12 m and internal pipe diameter of 40 mm is used for measurements. The pressure drop measurement was performed, considering five pressure taps. More details about the experimental facilities are presented in Chapter 3.

8.3 Experimental procedures

Oil, water, and air superficial velocities are in the ranges of J_o=0.36-0.71 m/s, J_w=0.44-1.32 m/s, and J_g=0.22-2.10 m/s, respectively. The following procedures were used to inject the test fluids to the test section:

- Water is drawn first to the test section.
- Oil is then supplied with the selected flow rate.
- Water flow rate is checked and its value is adjusted to the set point, if needed.
- Once the two-phase flow is well established, the pressure drop is measured.
- Air is then supplied with the desired flow rate.
- Once the three-phase flow is well established, the pressure drop is measured.

A total number of 235 pressure drop data points were acquired. The facility is equipped with an optical probe and a video camera (see section 8.5), positioned 7 and 7.5 m from the inlet, to investigate both quantitative and qualitative aspects of three-phase flow.

8.4 Governing parameters

In this section, the main governing parameters are reported. As for two-phase flow, superficial velocity of each phase (phase volumetric flux) is defined as a ratio between volumetric flow rate and total cross-sectional area. Therefore, the mixture volumetric flux in three-phase flow is defined as summation of individual superficial velocity of each phase as:

$$J_t = J_o + J_w + J_g \qquad\qquad (8-1)$$

The same definition is adopted for the mixture liquid superficial velocity as:

$$J_L = J_o + J_w \qquad\qquad (8-2)$$

The ratio between gas superficial velocity and mixture superficial liquid velocity is defined as:

$$\varepsilon_{Lg} = \frac{J_g}{J_L} \qquad \varepsilon_{Lo} = \frac{J_o}{J_L} \qquad\qquad (8-3)$$

The phase holdup of each phase is defined as ratio between actual velocity and superficial velocity of each phase as follows:

$$H_o = \frac{J_o}{U_o} \qquad H_w = \frac{J_w}{U_w} \qquad\qquad H_g = \frac{J_g}{U_g} \qquad\qquad (8-4)$$

The liquid holdup is simply represented by $H_L = H_o + H_w$ and gas holdup is given by $H_g = 1 - H_L$.

The pressure reduction factor defined as the ratio between liquid-liquid and three phase pressure drop, considering the same oil and water flow rates, that is;

$$R_{LG} = \frac{\Delta p_{oil-water}}{\Delta p_{oil-water-gas}} \qquad\qquad (8-5)$$

8.5 Optical analysis

8.5.1 Optical sensor and data analysis

In the present study, a non-intrusive optical sensor has been designed and used to measure the elongated bubble velocity. The results of measured bubble velocity by optical sensor are then compared with the measured bubble velocity by means of video recording technique through image processing. Depending on flow conditions, different configurations of phases can be formed in three phase flows of oil-water-gas. The phases in contact may have either smooth or wavy interface. The developed optical sensor must be able to detect difference between optical properties of phases in medium. Furthermore, it has to be capable of distinguishing between elongated bubble zone and liquid slug zone. The new optical sensor is able to be adjusted to different pipe diameters and the distance between sensible areas can be also changed in an easy way. This new optical probe has been created from a 3D printer, composed by parallelepipeds of dimensions 10x7x1 cm. There is a hole at the center of these elements, with the same diameter as internal pipe diameter and four perpendicular cubic holes through hole. Each parallelepiped is composed of two pieces that can be reconnected and fitted together. Each piece can be removed to mount the Photoresistors and Leds. Due to symmetrical shape of parts, both the Photoresistors and Leds can be hold in a proper manner. Figure 8-1 shows the parallelepiped, with the Photoresistor and Leds which is suitable to attach to the outer external diameter of pipe.

Figure 8-1 Image of 3D printed elements of optical sensor

The 3D printed design of optical sensors allows us to position the Photoresistors and LEDs in the fixed positions attached to the pipe. The length of the pipe inside the sensible areas and outside of where elements are positioned must be well covered to increase the absorption of lights on photoresistors. Figure 8-2 shows the optical sensors places on the pipelines.
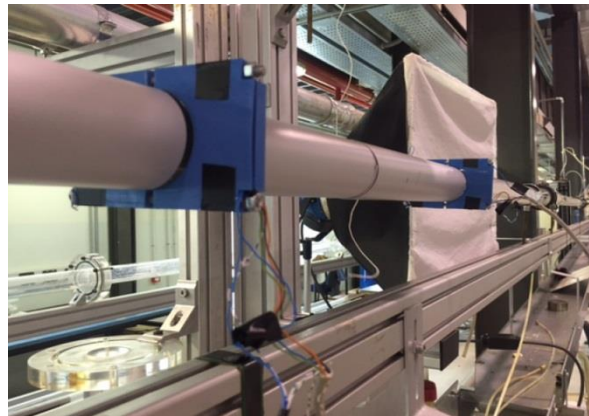
Figure 8-2 Optical sensor with the covered paperboards positioned 7.5 m from inlet

A detailed diagram of optical sensor is shown in Figure 8-3. It is composed of four LEDs (light sources), four photoresistors, and a processing unit. The photoresistor sensors are placed at the diametrically opposite side of LEDs to capture light path transmitted by the source after its passage through the medium. The narrow light beams pass through the three-phase flow medium and reach in the detectors. The amount of light captured by detectors depends mainly upon phase content which is, in turn, related to the spatial distributions of phases. The presence of droplets and wavy interface would result in more light scatterings. As it has been already mentioned, the distance between two sensible areas is adjustable in an axial location and selected to be 30 cm. The LEDs and Photoresistors are placed such a way that it covers the whole height of the tube, with spacing interval of 4 mm. The electric signals of the optical sensor are acquired at 1000 Hz sampling frequency and stored in a PC for post-processing.
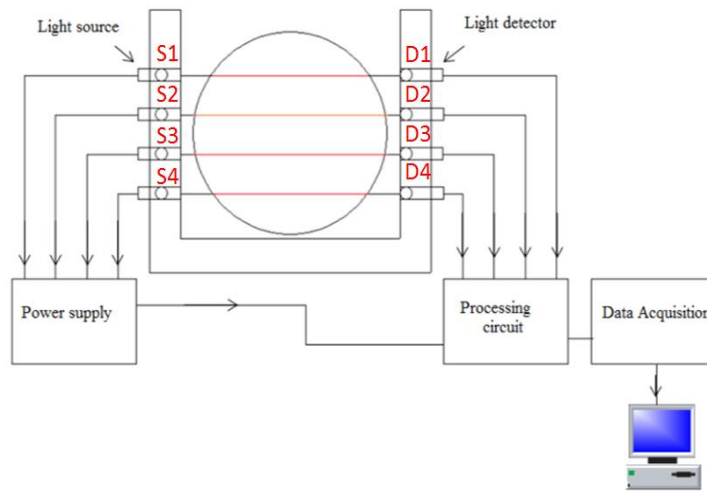
Figure 8-3 Schematic representation of optical sensor

The data saved by acquisition board is composed of 9 columns, one column for time and eight columns for acquired raw signals. All the data acquired from optical sensors and video recording are analyzed by means of MATLAB R15b program. An example of raw output signal for the case of J_o=0.71 m/s, J_w=1.32 m/s, and J_g=2.10 m/s is shown in Figure 8-4 where the black and green signals imply the uppermost and lowest LED signals, respectively.
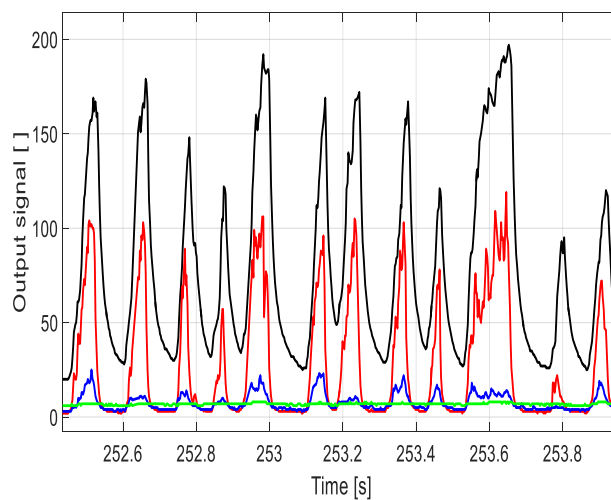
Figure 8-4 Example of raw output signal for case of J_o=0.71 m/s, J_w=1.32 m/s, and J_g=2.0 m/s

197

8.5.2 Bubble velocity measurement

During three-phase flow of oil-water-gas, different flow regimes occur depending mainly on flow conditions at the inlet. The elongated bubble is a type of slug/plug flow regime which has significant dimension. The passage of flows is easily detectable based on signal response. For instance, the presence of gas would result in augmentation of light that passes through bubble in optical sensors, see Arnone (2017). A fully developed slug is characterized by constant liquid pickup (elongated bubble moving along stratified layer pickups liquid at their head) and shedding rates. At axial positions near inlet, slugs are not fully developed because it has a developing velocity profile at its tail and trailing bubble velocity would be accelerated to overtake the leading elongated bubble, see Alsafran et al. (2013). Slug flow regime can be studied in three-phase flow by measurement of elongated bubble velocity, frequency, and elongated bubble length. By considering two similar signals, shifted in time, it is feasible to measure elongated bubble velocity. In the present study, two techniques are adopted. The first method is to use cross-correlation, which is fast but only gives average bubble velocity. The second method is so-called single bubble identification method, which gives velocity of each bubble and its length. In the following sections, two techniques are described in more details.

8.5.2.1 Cross-correlation technique

It is possible to cross-correlated two similar signals and extracted the time lag between two signals by looking at the maximum peak of the cross-correlation. The bubble translational velocity can be calculated from the distance (L) between two probes and the associated time lag (τ):

$$U_t = \frac{L}{\tau} \qquad\qquad (8\text{-}6)$$

First, the raw signal is normalized with power 2, in order to amplify the difference between bubble and liquid passage as:

$$S = \left(\frac{S - \min(S)}{\max(S) - \min(S)}\right)^2 \qquad\qquad (8\text{-}7)$$

Figure 8-5 shows two similar normalized signals shifted in time, while Figure 8-6 illustrates an example of cross-correlation technique by plotting correlation function (R_τ) versus time lag (τ).
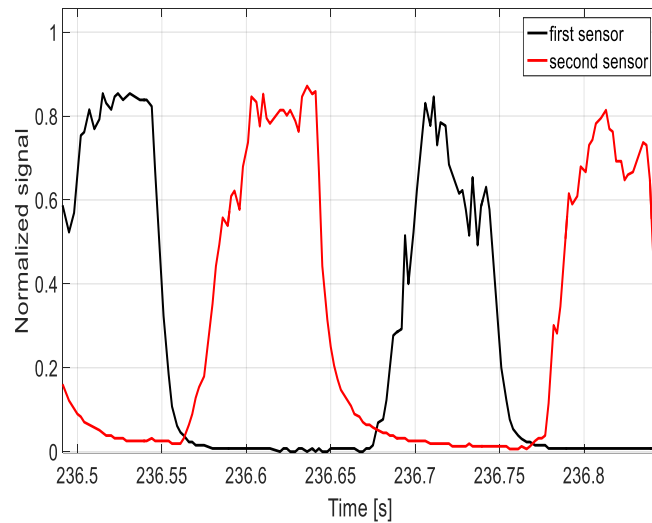
Figure 8-5 An example of two similar signals shifted in time
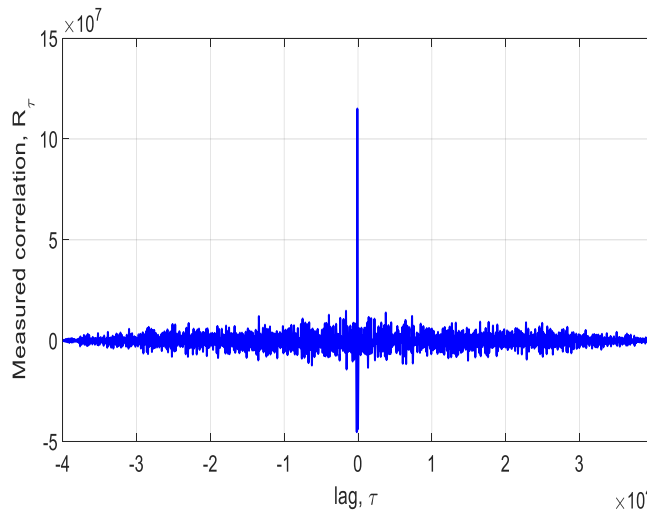
Figure 8-6 An example of cross-correlation technique

It is worth noting that distance between two sensible areas (two sensors) needs to be properly selected because it depends on flow conditions. If bubble are too fast and short, longer distance is required. On the other hand, if distance is too long, it is difficult to identify the bubble because during the passage of elongated bubbles it may happen that elongated bubbles collides each other

and two sensors see different elements of bubbles. In this case it is so difficult to obtain a time lag between two similar signals.

8.5.2.2 Single bubble identification method

Geometrical characteristics of slug flow, such as bubble length cannot be detected by cross-correlation technique. The second approach is based on so-called "single bubble identification method". Figure 8-7 shows the schematic representation of slug flow. As it is evident from Figure 8-7, the slug flow pattern is characterized by liquid slugs alternating with elongated air bubbles. Characteristic parameters of slug unit are defined as:
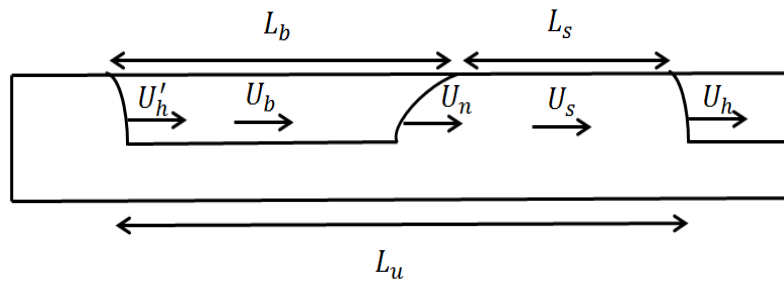
Figure 8-7 Schematic representation of slug flow

U_h: velocity of head of leading liquid slug

U_n: velocity of tail of leading liquid slug or head of bubble

$U_h^{'}$: velocity of tail of trailing liquid slug

L_s: liquid slug length

L_b: bubble length

L_u: total slug unit length

The single bubble identification method is complicated but effective to measure the velocity of head, tail of liquid slug and bubble, and geometrical parameter of slug unit. It is worth noting that velocity of tail of liquid slug, U_n is equal to the velocity of head of bubble. After normalization of signal, it is necessary to convert the normalized signal to a binarized rectangular

wave signal, by means of a threshold value, suitably selected according to the operating conditions to extract some information about geometrical parameters of slug flow. In the binarized signal, the value 1 and 0 relate to the liquid and gas phase, respectively. Figure 8-8 shows typical example of binarization process with threshold value set as 0.3, where transition from 0 to 1 indicates the front of a slug while transition from 1 to 0 indicates the tail of slug. The effect of threshold value on capturing slug unit must be always checked. The threshold value of 0.3 seems to be a good approximation because it captures all slug units.
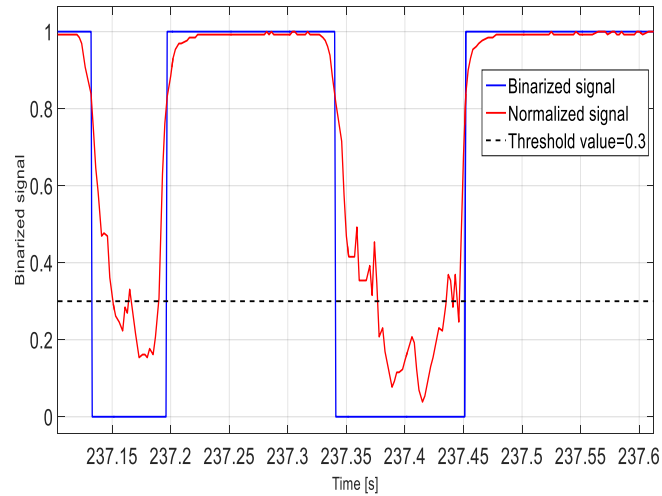
Figure 8-8 typical example of binarization process using threshold technique

After binarization of signals, derivative is calculated based on finite difference as:

$$D(t) = S(t + \Delta(t)) - S(t) \qquad\qquad (8\text{-}8)$$

The head and tails of each of bubble can be obtained by studying derivative D of each signal. Thus, the head of bubble is identified as D=-1, whereas the tail of bubble is detected where D=1. For each signal, it is feasible to provide a list of unit slug, with slug body part and the following bubble. After calculating derivative of each signal, the algorithm is able to extract time residence

of slug and bubble. To measure the bubble (U_{eb}) and liquid slug velocity (U_s), first, the characteristic times of slug unit must be suitably identified. Table 8-1 shows time residence of slug unit characteristic.

Table 8-1. Characteristic time residence of slug unit between two sensible areas

t_{h2}-t_{h1}	Time residence of liquid slug head between two sensible area
t_{n2}-t_{n1}	Time residence of liquid slug tail between two sensible area
t_s	Time passage of liquid slug from first to second sensor
t_b	Time passage of elongated bubble from first to second sensor

Since the time residence of head and tail of slug can be detected from binarized signal, the velocity of head and tail of slug is measured by knowing the distance between two sensors as:

$$U_h = \frac{L}{t_{h2}-t_{h1}} \qquad\qquad (8\text{-}9)$$

$$U_n = \frac{L}{t_{n2}-t_{n1}} \qquad\qquad (8\text{-}10)$$

Slug (U_s) and elongated bubble velocities (U_{eb}) are measured, simply, by averaging velocity of slug head and tail:

$$U_s = \frac{U_h+U_n}{2} \qquad\qquad U_{eb} = \frac{U_n+U_h'}{2} \qquad\qquad (8\text{-}11)$$

The bubble and slug length can be obtained by multiplication of time residence of bubble and slug between two sensible areas and respective velocities.

$$L_b = t_b U_{eb} \qquad\qquad L_s = t_s U_s \qquad\qquad (8\text{-}12)$$

The slug unit cell is the summation of slug body length (L_s) and bubble length (L_b), that is, $L_u = L_s + L_b$.

The slug frequency has been calculated by dividing the number of slug captured between two sensible areas to the total time of slug unit.

$$f_s = \frac{N_s}{\sum_{i=1}^{N_s}(t_s + t_b)_i} \tag{8-13}$$

8.5.3 Image processing

The objective of image processing was to measure the translational velocity of slugs by means of cross-correlation technique. Other geometrical characteristics of slugs can be directly evaluated from image processing of video cameras. To extract quantitative information regarding hydrodynamic behavior of slug flow, a series of images (250×1579 px^2) were taken by video camera (NIKON D3300) at frequency 50 fps (frames per second). The visualization section is exposed by two yellow lamps. An example of the typical flow pattern is depicted in Figure 8-9. It is seen that the oil is mainly opaque, whereas air and water are transparent. Hence, to distinguish air-oil and water-oil interfaces, a threshold technique is required. The image post-processing is carried out using Image Toolbox of Matlab$^{©}$. Bubble translational velocity is computed by means of cross-correlation, using two virtual probes (probe #1 and 2 in Figure 8-9), positioned at the beginning and end of pipe (with known distance Δx) to ensure that even very long elongated bubbles can be captured. Therefore, translational velocity is given by:

$$U_t = \frac{|\Delta x|}{N_{frames}} \cdot pixel\ size \cdot F_s \tag{8-14}$$

Where N_{frames} and F_s (50 fps) are the number of frames passed between two probes and sampling frequency, respectively.
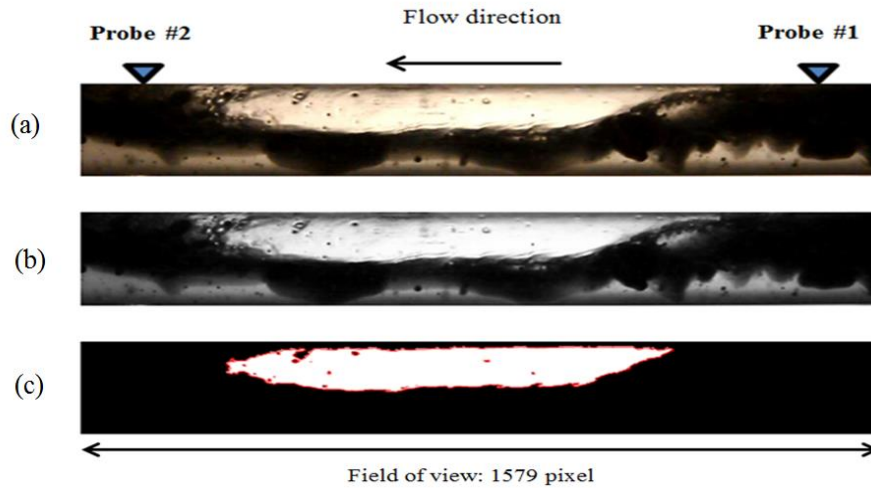
Figure 8-9 Example of image post-processing to detect translational velocity, (a) original image; (b) grey scale image; (c) binarized image. The triangles indicates position of virtual probes

Measurement of bubble translational velocity by image processing is a powerful technique but it is so slow and requires much space for recording time. It cannot give us velocity of bubble in real time.
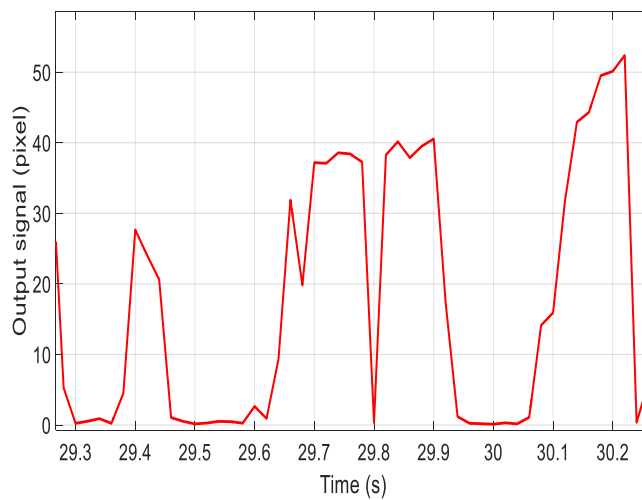
Figure 8-10 An example of output signal acquired from image processing

In the present study, bubble translational velocity is measured by means of cross-correlation techniques, using two virtual probes. An example of output signal taken from image processing is depicted in Figure 8-10.

8.6 Experimental results

8.6.1 Pressure drop

As mentioned earlier, one of the objectives of current Chapter is to collect experimental data related to flows of high viscosity oil-water-gas. Thus, more than 200 experimental data were collected to measure three-phase pressure drop. Figure 8-11 depicts the results of pressure gradients plotted as a function of ratio of gas to liquid superficial velocity, with superficial gas velocity as parameter. Regular trends are observed, that is, for fixed amount of gas, increasing liquid superficial velocity (reducing gas to liquid ratio) would result in increasing in pressure gradient. At low gas values, this increase in pressure drop is more dramatic due to the fact that we observed a transition from slug to plug flow regimes. Therefore, the pipe cross-sectional area has a wider contact with liquid, resulting in increasing frictional shear stresses.
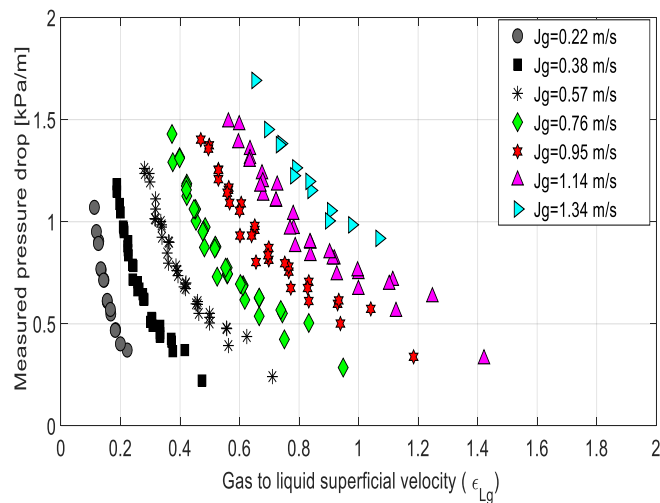
Figure 8-11 Measured pressure drop (ΔP/L) as a function of gas to liquid superficial velocities (ε_{Lg}) for constant gas superficial velocity

Analysis of pressure drop supports the assumption that liquid phases can be treated as equivalent liquid because no scattered data of pressure drop observed for fixed gas flow rate.

8.6.2 Pressure reduction factor

As investigated by other researcher, see for instance Oliemans and Ooms (1986), Colombo et al. (2015), oil-water core-annular flow regime is of practical interest for heavy oil transportation because of high stability and ability to reduce pressure drop. However, as pressure is reduced the amount of dissolved gas in oil is released, so the presence of gas to liquid-liquid flow needs to be evaluated. It would be suitable to calculate pressure reduction factor for three phase flow to evaluate influence of air addition to liquid-liquid flow, as performed by Bannwart et al. (2009). Figure 8-12 depicts the results of pressure reduction factor versus the ratio of gas to liquid superficial velocity (ε_{LG}). Two different oil superficial velocities are considered (J_o=0.24 $m·s^{-1}$ and J_o=0.59 $m·s^{-1}$). Pressure reduction factor has a physical meaning in a sense that if $R_{LG} < 1$ addition of gas has a positive effect and total frictional pressure drop is reduced.
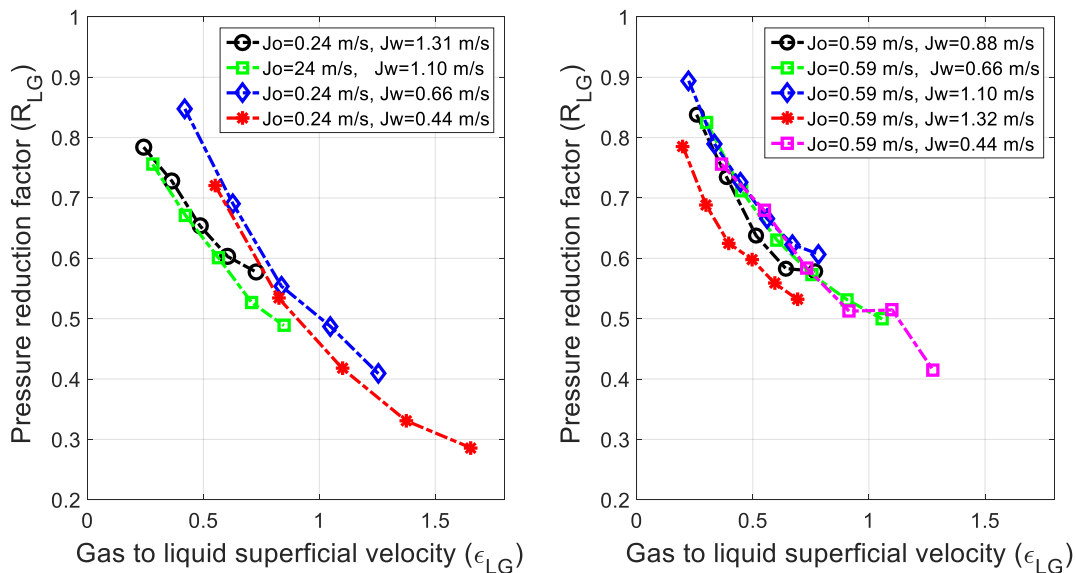
Figure 8-12 Pressure reduction factor versus gas to liquid superficial velocity for two different oil superficial velocities (J_o=0.24 $m·s^{-1}$ and J_o=0.59 $m·s^{-1}$)

These results can be justified by the fact that gas has lower viscosity than oil and water. Therefore, the increasing gas flow rate would result in reducing wall shear stresses and pressure gradient.

8.6.3 Slug body length

Since slug flow regime is a stochastic process, different slug body length can be observed along the pipe varied around its average. So, it is generally accepted that the log normal distribution can properly represent the slug body length as proposed by Losi et al (2016b), Fabre and Line (1992), and shown in Figure 8-13, 8-14. The results of slug body length distribution for two different oil superficial velocities (J_o=0.48 $m·s^{-1}$ and J_o=0.71 $m·s^{-1}$ are considered. On abscissa the slug body length normalized by pipe diameter and on ordinate the number of slugs captured by optical probe was plotted. In each plot, superficial gas velocity increases from left to right while water superficial velocity increases from top to bottom. Moreover, mean, median, mode and standard deviation values are presented. For fixed oil and water superficial velocity, as superficial gas velocity increases from 0.57 $m·s^{-1}$ to 2.1 $m·s^{-1}$, slug body length increases. The shape of distribution is shifted from highly right-skewed to normal like one. The number of slugs is considerably reduced due to longer elongated bubble. As oil superficial velocity increases of constant gas and water superficial velocity, shorter slug length with higher frequency were observed. However, the shape of log-normal distribution remains unchanged. The effect of gas superficial velocity is much more dramatic than liquid superficial velocity, probably because of pickup rate of slug by bubble (Bubble moving along stratified layer pickups liquid at their head), which finally depends on gas superficial velocity.
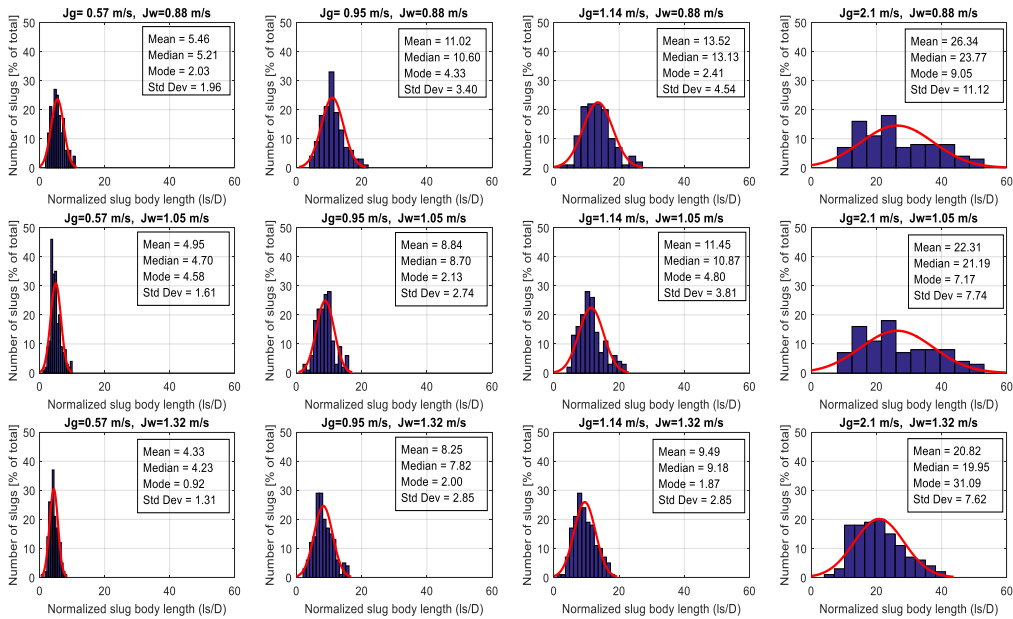
Figure 8-13. Slug body length PDFs for $J_o = 0.48\ m/s$
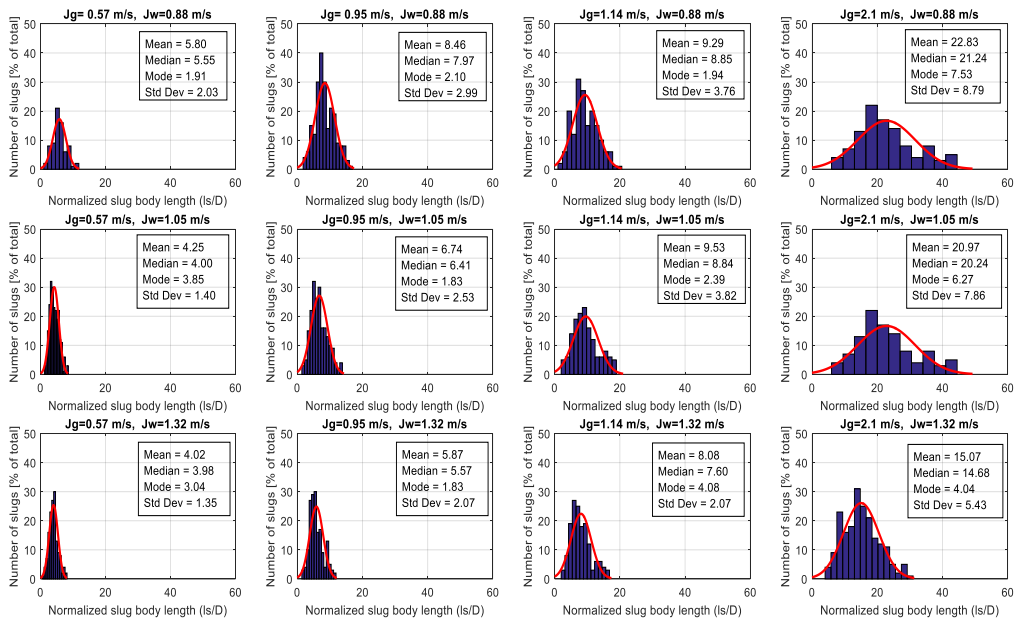
Figure 8-14. Slug body length PDFs for $J_o = 0.71\ m/s$

8.6.4 Bubble and slug unit length

The results of bubble length distribution measured by single bubble identification technique for oil superficial velocity J_o=0.48 m/s is depicted in Figure 8-15. As expected, at constant liquid superficial velocity, increase of gas superficial velocity causes increase in bubble length. The bubble length is measured by multiplication of bubble velocity (U_{eb}) and time passage of bubble (t_b) between two sensors. It is evident from Figure 8-15, the number of bubbles captured by two sensors are different, which is highly dependent on flow conditions.
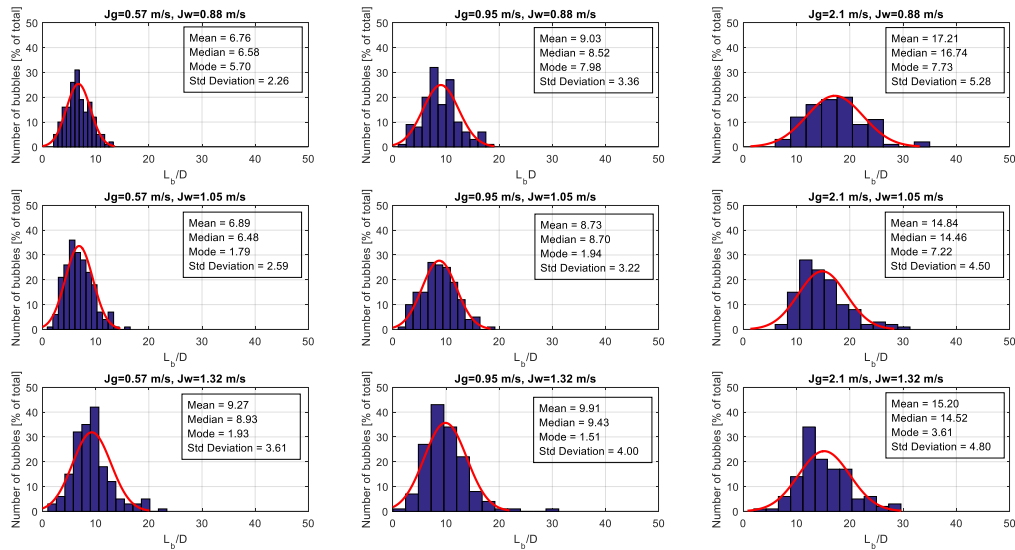
Figure 8-15 PDFs for bubble length, J_o=0.48 m/s

The average value of bubble length is extracted from histograms, and results of elongated bubble length as a function of gas superficial velocity for constant total liquid superficial velocity (J_L) are presented in Figure 8-16. Not surprisingly, increases in gas flow rates would result in longer bubbles. The results regarding to total slug unit ($L_u=L_s+L_b$) measured by optical sensors versus gas superficial velocity are shown in Figure 8-17. Liquid superficial velocity is considered as a parameter. In Figure 8-16 and 8-17, different symbols denote different liquid superficial velocity. Apart from liquid superficial velocity, a regular trend is observed, suggesting significant influence of gas superficial velocity on total slug unit length.
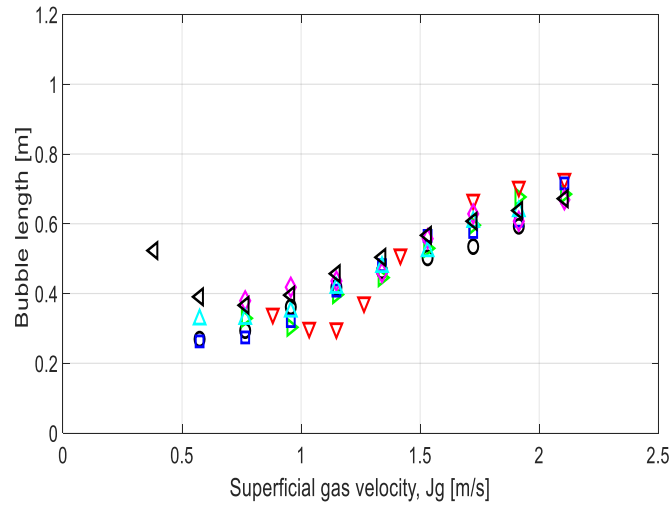
Figure 8-16 Measured bubble length by optical probe versus superficial gas velocity for fixed liquid velocity; o:J_L =1.36 m/s, ◊:J_L =1.48 m/s , △:J_L =1.59 m/s, ▽:J_L =1.7 m/s, ▷ :J_L =1.80 m/s, □:J_L =1.92 m/s, ◁:J_L =2.03 m/s.
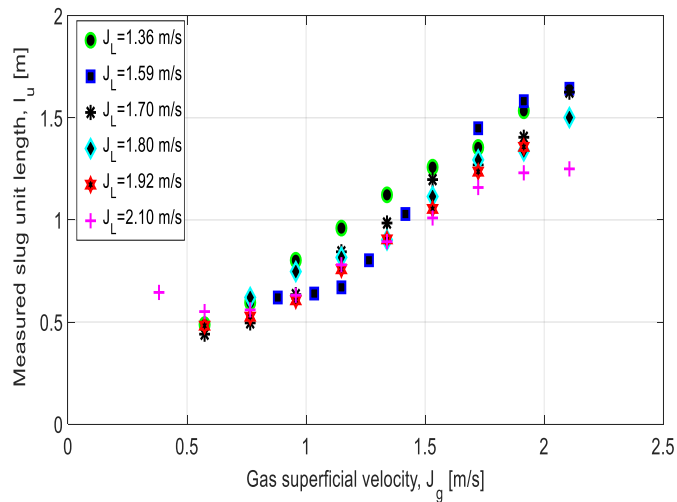
Figure 8-17 Experimental slug unit length, measured by optical probe as a function of gas superficial velocity. o:J_L =1.36 m/s, □:J_L =1.59 m/s, *:J_L =1.70 m/s, ◊:J_L =1.80 m/s, ★:J_L =1.92 m/s, +:J_L = 2.10 m/s

8.6.5 Slug frequency

The result of slug frequency measured by optical sensors is plotted against gas superficial velocity in Figure 8-18. As superficial gas velocity increases, decreased slug frequency was observed, showing the presence of larger elongated bubbles and longer distance between liquid slugs. At fixed gas flow rate, it can be seen that slug frequency increases and shorter slugs form by increasing liquid superficial velocity.
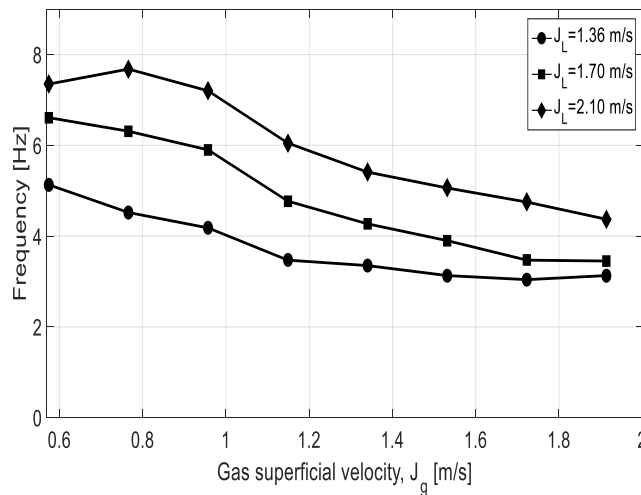
Figure 8-18 Slug frequency for different liquid superficial velocity plotted against gas superficial velocity

8.6.6 Bubble translational velocity

Understanding the bubble translational velocity is crucially important because almost all mechanistic models require the information of this parameter. Bubble translational velocity has been measured by means of optical probe, using cross-correlation and single bubble identification techniques. Furthermore, bubble translational velocity measured by video camera using cross-correlation technique is also presented. The results are presented in the sections 8.6.6.1 and 8.6.6.2.

8.6.6.1 Cross-correlation technique

It is customary to correlate bubble translational velocity to mixture superficial velocity. Figure 8-19 a-b shows the results of bubble translational velocity, measured by optical probe and video camera, respectively. A linear dependency of bubble translational velocity on mixture superficial velocity is marked for both cases. Larger dispersion of data is observed for measurement of bubble translational velocity using video camera, probably due to lower sampling frequency of video as compared to optical sensor. The experimental data are fitted with the regression line of $U_t=C_0 \cdot J_t+C_1$, where intercept (C_1) of line denotes the drift velocity. It is observed that drift velocity of three-phase flow, measured by optical sensor ($C_1=-0.30$) and video camera ($C_1=-0.34$) gives the negative values, particularly at higher mixture superficial velocities. This negative value does not have physical meaning, but, in some ranges of mixture superficial velocity, the drift velocity becomes positive and close to zero. The wider ranges of mixture superficial velocities are needed to evaluate the bubble translational velocity. However, in the present study, this was not possible due to limitation in experimental measurements.

(a)   (b)
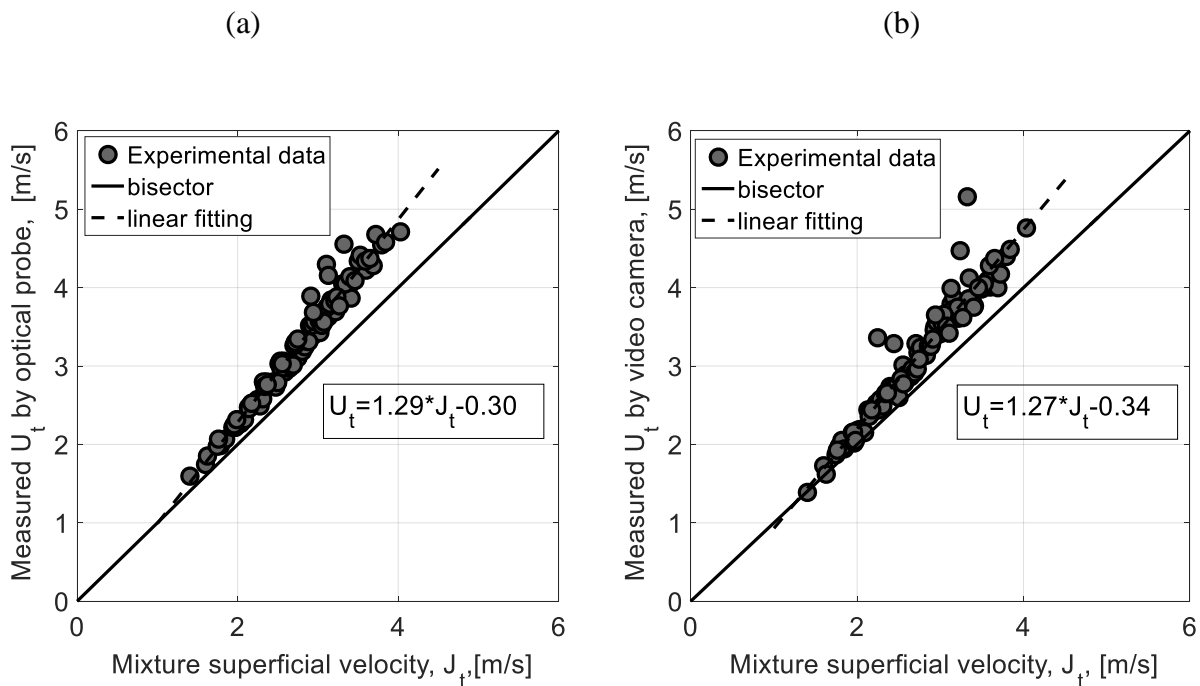
Figure 8-19 Measured bubble translational velocity (U_t) versus mixture superficial velocity (J_t) by means of cross-correlation technique using (a) optical sensor, (b) video camera

8.6.6.2 Single bubble identification technique

Another attempt is made to obtain bubble translational velocity measured by optical sensors, using single bubble identification technique (equation 8-11). Figures 8-20 (a-d) shows the results of bubble velocity as a function of mixture superficial velocity for different J_o, as performed in the previous section. According to single bubble identification method, as perceived from its name, velocity of each bubble is detected. During our tests, hundreds of bubbles are captured by optical sensors, depending on inlet flow conditions. Thus, the mean value of bubble translational velocity is depicted in Figures 8-20 (a-d). The error bars are also presented, showing standard deviation of each bubble velocity around its average value. Linear trends show the best fit of experimental data, which confirms the validity of cross-correlation method in the previous section. It is observed that the negative drift velocities are obtained. The standard deviation of bubble translational velocity is increased by increasing the oil superficial velocity at the inlet. The quantitative values of C_1 and C_0 for different oil superficial velocity using single bubble identification technique are listed in Tables 8-2, whereas Table 8-3 shows comparison between C_1 and C_0 obtained from cross-correlation and single bubble identification methods, considering all data together. It is worth noting that C_1 obtained from single bubble identification method for $J_o=0.36$ m/s shows lower value as compared to other cases. This is due to the lack of experimental data regarding to wider ranges of water superficial velocities. It is shown that bubble translational velocity is highly dependent on gas volume flow rate, but not so sensitive to the liquid volume flow rate.
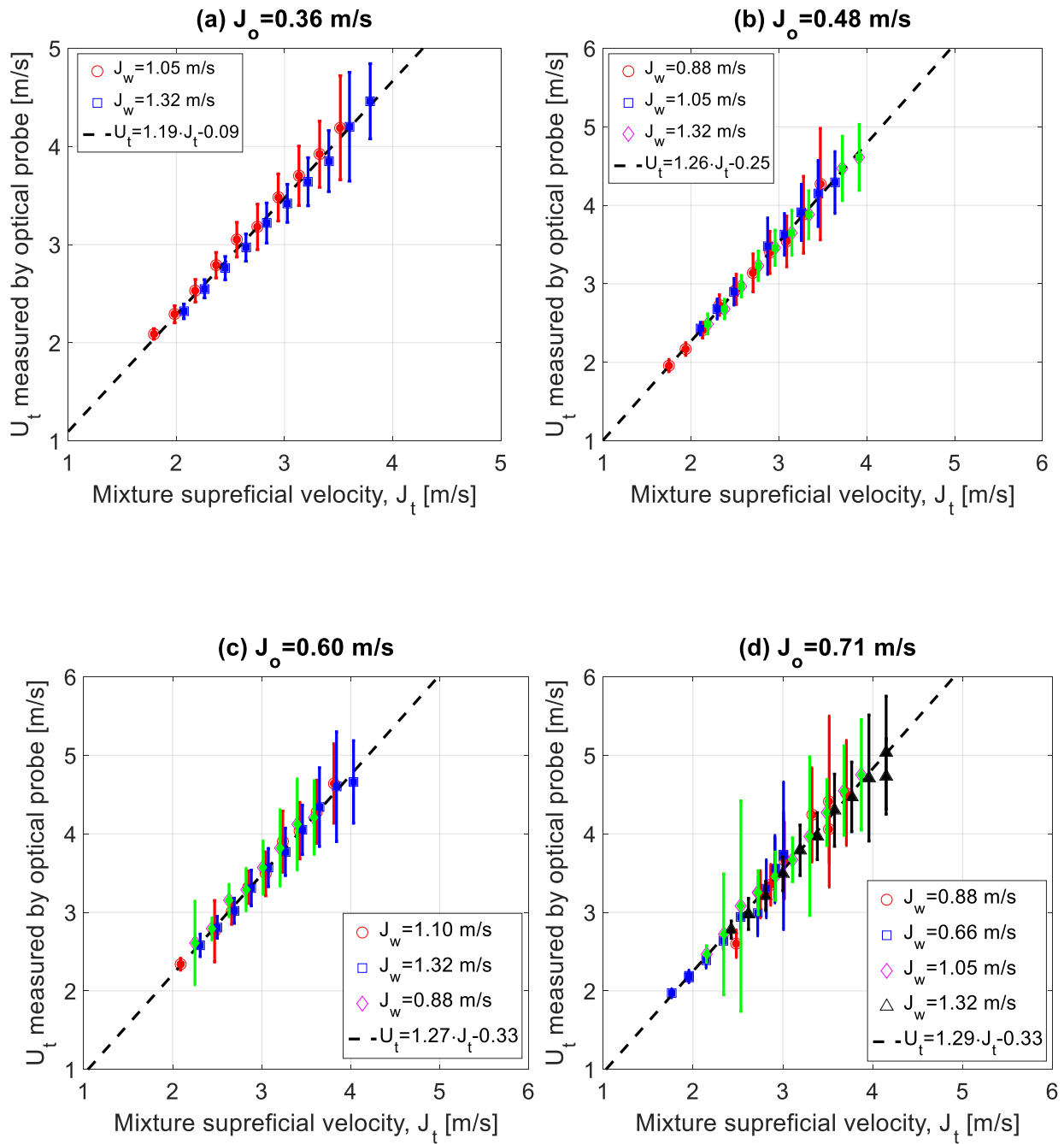
Figure 8-20 Bubble translational velocity measured by optical sensors using single bubble identification technique versus mixture superficial velocity for (a) J_o=0.36 m/s, (b) J_o=0.48 m/s, (c) J_o=0.60 m/s, and (d) J_o=0.71 m/s

Table 8-2 Coefficients of regression lines, C_1 and C_0, for single bubble identification technique

J_o (m/s)	C_0 (-)	C_1 (m/s)
0.36	1.19	-0.09
0.48	1.26	-0.25
0.60	1.27	-0.33
0.71	1.29	0.33

Table 8-3 coefficients of regression lines, C_1 and C_0, for cross-correlation and single bubble identification methods

Measurement technique	C_0 (-)	C_1 (m/s)
Cross-correlation by optical sensor	1.29	-0.30
Cross-correlation by video camera	1.27	-0.34
Single bubble identification using optical sensor	1.26	-0.27

The algorithms developed in the present study to measure bubble translational velocity enable us to compare bubble velocities obtained from different approaches. Thus, it is possible to define a relative error, which takes into account the bubble translational velocity measured by optical sensor (OS) using cross-correlation as a reference. Figure 8-21 reported the relative error between U_t measured by video camera (VC) and that measured by optical sensor. Dashed line indicates the relative error, where bubble translational velocity measured from both techniques is equal. Apart from few points, U_t measured by video camera underestimated bubble velocity obtained from optical sensor. It is worth noting that both techniques in Figure 8-21 made use of cross-correlation approach, which is an averaged-base technique. The maximum and minimum

relative errors were found to be 17.5% and -14.1%, respectively. The relative error between U_t measured by single bubble identification method (SBIM) and that obtained from optical sensor (OS) using cross-correlation technique is computed and presented in Figure 8-22. Again, most of data measured by SBIM underestimated measured bubble velocity by optical sensor.
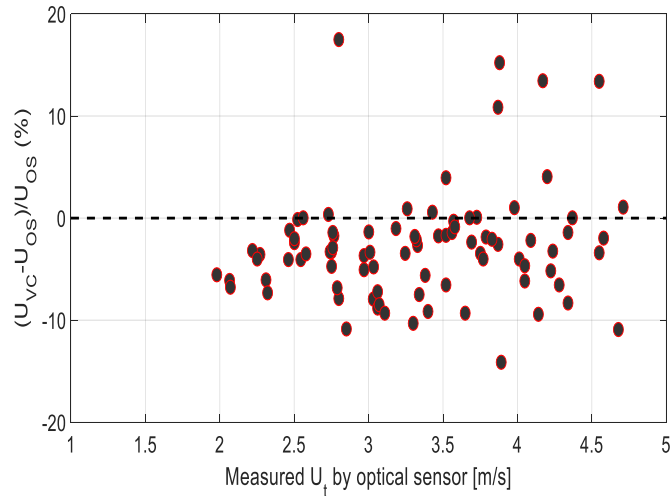
Figure 8-21. Relative error (%) between measured U_t by Video Camera (VC) and Optical Sensor (OS)
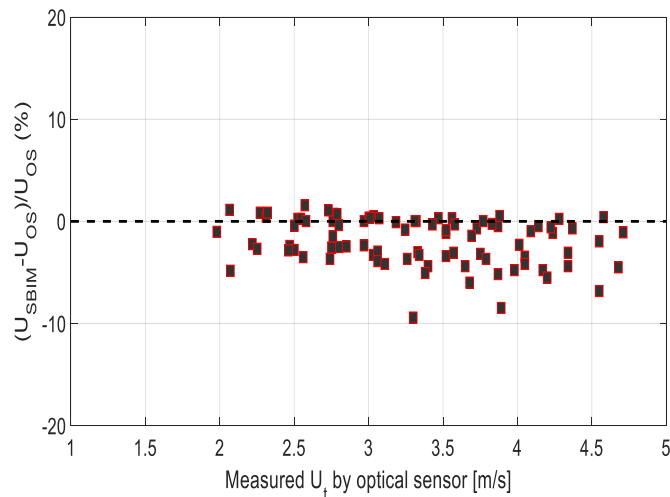
Figure 8-22. Relative error (%) between measured U_t by Single Bubble Identification Method (SBIM) and Optical Sensor (OS)

8.7 Hydrodynamic model

8.7.1 Mass conservation equations

The mathematical model presented here is based on the slug unit cell propagating with the translational velocity, U_t in horizontal pipe. The schematic geometry of slug is depicted in Figure 8-23. As previously mentioned, the slug unit cell is divided into two sections: a liquid slug body with a length of L_s and a film section with elongated bubble length of L_b where gas and liquid are stratified. The slug body contains gas entrainment in the form of dispersed bubbles. Thus, the current hybrid model is a combination of a two-fluid model for the segregated flow part and a drift-flux model for the dispersed component. The model is a steady state model in which liquid and gas are treated as incompressible flows. This assumption is still valid even for long pipelines where the density is not constant, see Taitel and Barnea (1990). In order to make use of two-fluid model in the film section with characteristic length of L_b, a homogeneous distribution of liquid phases is assumed and the effective viscosity of liquid is calculated according the Einstein's equation:

$$\mu_{eff} = \mu_{cont}(1 + 2.5\ \varepsilon_{Lo}) \qquad\qquad (8\text{-}15)$$

Where μ_{cont} and ε_o are viscosity of continuous phase (water) and input volume oil fraction $(\varepsilon_{Lo} = \frac{J_o}{J_L})$, respectively. The application of eq. 8-15 requires that spherically dispersed bubbles are distributed evenly in a radial direction. The combined continuity and momentum equations for gas/two phase liquid are adopted. If a reference frame with the same velocity as U_t is considered, the mass balance for both liquid and gas phases can be written by considering the liquid and gas mass flow rates entering and exiting control volume:

$$H_{ls}(U_t - U_l) = H_{lf}\ (U_t - U_f) \tag{8-16.a}$$

$$(1 - H_{ls})(U_t - U_b) = (1 - H_{lf})\ (U_t - U_g) \tag{8-17.b}$$

Where U_l, U_b are liquid and bubble velocities in slug body and U_f, U_g are velocities of liquid and gas in gas pocket (film section). The dispersed bubble velocity in slug body can be estimated by model of Wallis (1969) which is a drift-flux based approximation as $U_b = 1.2 \cdot J_t$.
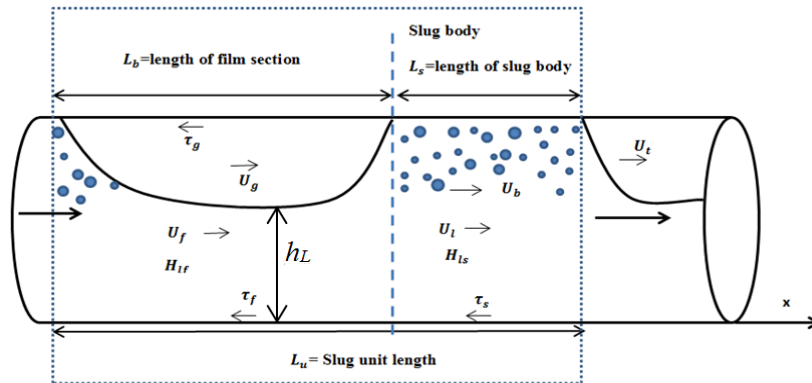
Figure 8-23 Schematic of slug flow structure

When a slug unit cell passes, the following equations can be written for gas and liquid:

$$L_u J_l = L_s H_{ls} J_t + L_b H_{lf} U_f \tag{8-18}$$
$$L_u J_g = L_s (1 - H_{ls})\, J_t + L_b (1 - H_{lf}) U_g \tag{8-19}$$
$$L_u = L_s + L_b \tag{8-20}$$

The mean average gas holdup can be calculated based on following equation:

$$H_g = 1 - \frac{(U_t H_{ls} + U_b (1 - H_{ls}) - J_g)}{U_t} \tag{8-21}$$

8.7.2 Momentum equations

For the sake of simplicity, the liquid height and its shape (h_L) along the liquid film is considered to be uniform. The shape of liquid film requires a special attention, because, at the bubble front the liquid holdup gradient differs from that at the bubble tail. Refering to Figure 8-23, momentum equations can be derived according to the analysis of forces exerted at the inlet and out of control volume containing important information such as pressure loss. The entire film section as control volume is considered and momentum equations solved, see for instance, Zhang et al. (2003a). The momentum equation for liquid and gas pocket in horizontal pipe is given by:

$$\frac{\rho_l(U_t-U_f)(U_l-U_f)}{L_b} = \frac{\Delta p}{L_b} + \frac{\tau_f S_f}{A_f} - \frac{\tau_i S_i}{A_f} - \rho_l\, g\,\cos\beta\,\frac{\partial h_L}{\partial x} \qquad (8\text{-}22)$$

$$\frac{\rho_g(U_t-U_g)(U_b-U_g)}{L_b} = \frac{\Delta p}{L_b} + \frac{\tau_g S_g}{A_g} - \frac{\tau_i S_i}{A_g} - \rho_g\, g\,\cos\beta\,\frac{\partial h_L}{\partial x} \qquad (8\text{-}23)$$

The pressure drop terms and the last term in RHS of eq. 8-22 and 8-23 are eliminated from above equations. Thus, the combined momentum equation may be given by:

$$\frac{\rho_l(U_t-U_f)(U_l-U_f)-\rho_g(U_t-U_g)(U_b-U_g)}{L_b} - \frac{\tau_f S_f}{A_f} + \frac{\tau_g S_g}{A_g} + \tau_i S_i\left(\frac{1}{A_f}+\frac{1}{A_g}\right) = 0 \qquad (8\text{-}24)$$

The first term at LHS of equation (8-24) is the force due to momentum exchange between slug body and film section of unit. Zhao and Yeung (2015) reported that If there is low liquid film height (h_L in Figure 8-23), there is no considerable difference between gas pocket velocity (U_g) and liquid velocity in the film region (U_f) beneath it. Zhang and Sarica (2006) developed a unified model, taking into account the stratified gas-oil-water in both liquid slug body and film sections. They stated that L_b tends to be infinitely long in stratified flow of gas-oil-water. Thus, the momentum exchange term is neglected from equation (8-24), the original form of momentum equation, developed by Taitel and Barnea (1990) can be obtained. It is worth noting that liquid height calculated in this way is the one in its equilibrium level and can be iteratively computed according to equation 8-24.

Gas-wall (τ_g), liquid-wall (τ_f) and interfacial shear stresses between gas pocket and liquid in film region are defined as:

$$\tau_f = f_l \frac{\rho_l U_f^2}{2} \qquad (8\text{-}25)$$

$$\tau_g = f_g \frac{\rho_g U_g^2}{2} \qquad (8\text{-}26)$$

$$\tau_i = f_i \frac{\rho_g (U_g - U_f)|U_g - U_f|}{2} \qquad (8\text{-}27)$$

To calculate shear stresses in film region, some geometrical parameters are required. The geometrical parameters, $A_f, A_g, S_f, S_g, S_i, H_{lf}$ are presented by Aziz and Govier (1972), assuming that interface between gas-liquid is flat. They are all functions of liquid film height (h_L) given by:

$$\alpha = 2cos^{-1}[1 - \frac{2h_L}{D}] \qquad (8\text{-}28)$$

$$A_f = \frac{A}{2\pi}(\alpha - \sin\alpha) \qquad (8\text{-}29)$$

$$A_g = A - A_f \qquad (8\text{-}30)$$

$$H_{lf} = \frac{A_f}{A} \qquad (8\text{-}31)$$

$$S_f = \frac{D\,\alpha}{2} \qquad (8\text{-}32)$$

$$S_g = \pi D - S_f \qquad (8\text{-}33)$$

$$S_i = 2D\sqrt{[\frac{h_L}{D} - (\frac{h_L}{D})^2]} \qquad (8\text{-}34)$$

The friction factors in equations 8-25-8-27 can be directly linked to the phase Reynolds number for liquid film and gas pocket:

$$Re_l = \frac{4\,A_f U_f \rho_L}{S_f \mu_L}, \qquad\qquad Re_g = \frac{4\,A_g U_g \rho_g}{(S_g + S_i)\mu_g} \qquad (8\text{-}35)$$

In definition of gas Reynolds number, the cord length at the interface, S_i is used as suggested by Taitel and Dukler (1976).

8.7.3 Pressure gradient prediction

The total pressure drop for slug unit length can be computed using three contributions as frictional, gravitational and acceleration pressure gradients:

$$-\frac{dP}{dx} = -\left(\frac{dP}{dx}\right)_F - \left(\frac{dP}{dx}\right)_G - \left(\frac{dP}{dx}\right)_A \qquad (8\text{-}36)$$

We assumed that gas expansion would not occur from the entrance to downstream of pipeline (flow is incompressible) and acceleration contribution is negligible. Thus, the only contribution that remains is frictional term in horizontal pipe and computed as:

$$-\left(\frac{dP}{dx}\right)_F = \frac{\tau_s \pi D}{A}\frac{L_s}{L_u} + \frac{\tau_f S_f + \tau_g S_g}{A}\frac{L_b}{L_u} \qquad (8\text{-}37)$$

The first term in equation above corresponds to frictional pressure drop in slug body and the second is frictional contribution to the pressure drop in the film zone. Rheological properties of mixture in slug zone are calculated based on weighted average of liquid and gas holdup, as proposed by Taitel and Barnea (1990) and Zhao and Yeung (2015)

$$\rho_s = H_{ls}\rho_l + (1 - H_{ls})\rho_g$$
$$\qquad (8\text{-}38)$$
$$\mu_s = H_{ls}\mu_l + (1 - H_{ls})\mu_g$$

The shear stress in slug body caused by interaction between homogeneous mixture (dispersed bubble entrained to slug body zone and liquid) and pipe wall in slug region, τ_s, is calculated considering total mixture superficial velocity for Reynolds number:

$$Re_s = \frac{\rho_s J_t D}{\mu_s} \qquad (8\text{-}39)$$

$$\tau_s = f_s \frac{\rho_s J_t^2}{2} \qquad (8\text{-}40)$$

To compute pressure drop and phase holdup in high viscous oil-water-gas flow based on hydrodynamic model presented in sections 8.7.1 to 8.7.3, some information are required, including slug body holdup (H_{ls}) and length (L_s), and closure relation for two-phase friction factor and bubble translational velocity. All information is obtained from available models in the literature for gas-liquid flow due to the lack of suitable models

for three-phase flow in horizontal pipes, discussed in sections 8.7.4 to 8.7.6. In addition to aforementioned parameters, an appropriate model for slug unit length is necessary to calculate actual velocity of phases and avoid iterative procedure in continuity equations. In the present Chapter, a new formulation for computing the total unit length as a function of pipe diameter, and flow conditions are presented, explained in section 8.7.7.

8.7.4 Slug body holdup

The developed model requires the information of slug body holdup. Some researchers have studied liquid body holdup for gas-liquid flow in the case of low viscosity oil, see for instance, Andreussi et al. (1993) and Nadler and Mewes (1995). The slug body region can be divided into two sub-regions, namely, developed body region and developing mixing region. When liquid moves from the layer beneath gas pocket to slug region, a sudden expansion occurs which in turn helps to form a jet and create a mixing region at the head of slug. As a result of mixing developing region and liquid loss, the generated liquid re-circulate from slug body and move toward the leading Taylor bubble tail. The rest of liquid is transported to the developed slug region, see Figure 8-24. This phenomenon has significant effect on the developing mixing length and its intensity as well as slug body liquid holdup.
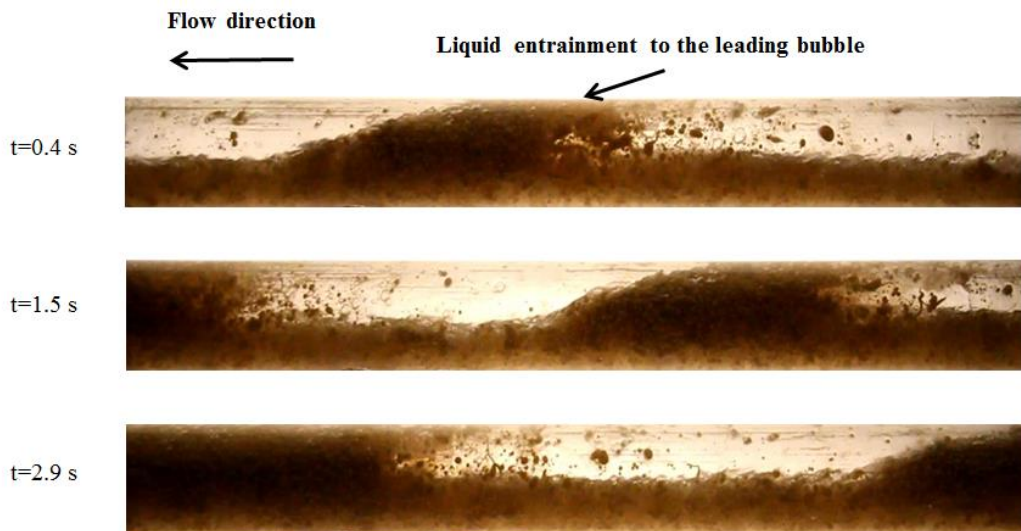
Figure 8-24 Frames of subsequent images to show the liquid entrainment mechanism

222

Al-Safran et al. (2015) experimentally examined the influence of high liquid viscosity on slug liquid holdup in horizontal pipe. They concluded that viscous and inertia forces are responsible for bubble loss, fragmentation (changing the size of larger bubbles to dispersed bubbles) in slug body. According their work, increase in liquid viscosity would result in increasing slug body liquid holdup. A new formulation for slug body liquid holdup was presented as:

$$H_{ls} = 0.85 - 0.075\,\varphi + 0.057\,\sqrt{\varphi^2 + 2.27} \qquad\qquad (8\text{-}41)$$

$$\varphi = N_{Fr}N_\mu^{0.2} - 0.89 \qquad\qquad (8\text{-}42)$$

$$N_{Fr} = \frac{J_t}{(gD)^{0.5}}\sqrt{\frac{\rho_L}{(\rho_L - \rho_g)}} \qquad\qquad (8\text{-}43)$$

$$N_\mu = \frac{J_t\,\mu_L}{g\,D^2(\rho_L - \rho_g)} \qquad\qquad (8\text{-}44)$$

8.7.5 Slug body length

In two phase flow of air and water, slug body length ranged between 12-30 D (Dukler and Hubbard, 1975). For two phase flow with low viscosity of liquid, Barnea and Brauner (1985) proved that length of slug is 32D. Al-Safran et al. (2011) measured liquid slug by means of laser and capacitance sensors in high viscosity oil-water. They conclude that average slug length of 10D is a reasonable approximation for high viscosity liquid-gas flow. According to the experimental measurements obtained from optical sensor, the mean slug body length ranged between 3D and 27D. Losi et al. (2016b) experimentally investigated two-phase flow of high viscous oil/water in horizontal a pipe. They proposed a correlation to compute slug body length, considering the effect of both gas superficial velocity and pipe diameter.

$$\frac{L_s}{D} = K \cdot \left(J_g + \frac{J_{go}^2}{J_g}\right) \qquad\qquad (8\text{-}45)$$

Where, K is a constant which depends on liquid properties and J_{go} is the gas superficial velocity corresponding to the shortest slug body length. The numerical values of K and

J_{go} were found to be 5.3 and 0.3 from data fitting regression. Slug length data is compared with model developed by Losi et al. (2016b) in Figure 8-25, while Table 8-4 shows comparison between experimental slug length data and models for gas-liquid flow in the literatures. It is observed in Figure 8-25 that at low gas superficial velocity, transition from slug to plug and finally dispersed flow regime occurs and slug body length tends to become infinite. It is evident from Figure 8-25 and Table 8-4 that Barnea and Brauner (1985), and Al-Safran et al. (2011) models are unable to describe the behaviors of our data, whereas the approach by Losi et al. (2016b) seems to be consistent, though affected by rather large deviation. Average relative error between experimental data and model by Losi et al. (2016b) is found to be 20.8%, while maximum relative error is 34%. As compared to other correlations in Table 8-4, the lower average relative error and standard deviation of Losi et al. (2016b) model suggests the strong influence of gas superficial velocity on slug body length. Therefore, the model by Losi et al. (2016b) is used to compute the slug body length.
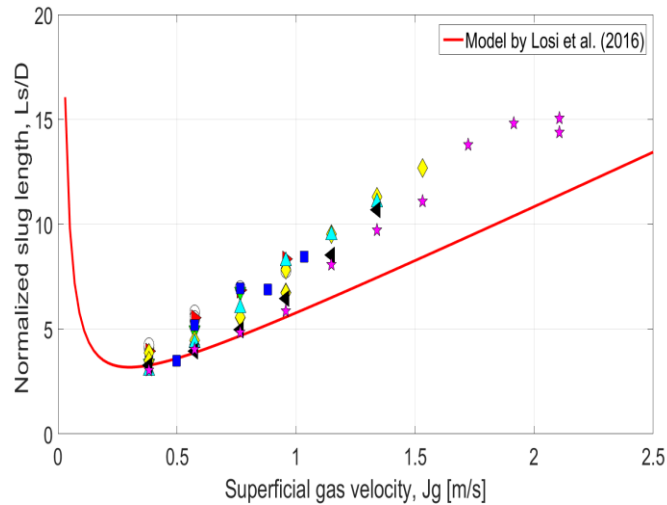
Figure 8-25 Slug unit length measured by optical probe as a function of gas superficial velocity for different total liquid superficial velocity: $o:J_L = 1.36$ m/s, $\triangleright:J_L = 1.41$ m/s, $\nabla:J_L = 1.53$ m/s , $\square:J_L = 1.68$ m/s, $\lozenge:J_L = 1.7$ m/s, $\triangle:J_L = 1.8$ m/s, $\triangleleft:J_L = 1.92$ m/s, $\star:J_L = 2.04$ m/s

Table 8-4 Comparison of slug length for different correlations of gas-liquid flow

Correlation	Average Relative Error (%)	Maximum Relative Error (%)	Standard Deviation (%)
Barnea and Brauner (1985)	454.2	963.1	228.5
Al-Safran et al.(2011)	79.7	232.2	64
Losi et al. (2016b)	20.8	34	10.4

8.7.6 closure relation

8.7.6.1 Two phase friction factor

Some empirical correlations to express two phase friction factors as a function of phase Reynolds number is required. For gas-wall friction factor, Blasius formulation is often used as described by Taitel and Dukler (1976). The validity of gas-liquid friction factors estimated by Blasius is assessed by Khor et al. (1997) for three phase stratified flow. These are:

$$f_g = \frac{16}{Re_g} \qquad \text{for} \quad Re_g \leq 2100 \qquad (8\text{-}46)$$

$$f_g = \frac{0.046}{Re_g^{0.2}} \qquad Re_g > 2100 \qquad (8\text{-}47)$$

Zhao et al. (2013b) developed a new expression for liquid-wall friction factor in the case of laminar liquid for gas-liquid flow over the large range of liquid viscosity

$$f_l = \frac{20.76}{Re_l} \qquad \text{for} \quad Re_l \leq 2100 \qquad (8\text{-}48)$$

Kowalski (1987) measured wall-to-liquid shear stresses and proposed a new correlation for turbulent liquid-wall friction factor as a function of liquid superficial Reynolds number and local liquid holdup for the large range of phase superficial velocity.

$$f_l = \frac{0.0262}{(H_{lf}Re_{sl})^{0.139}} \qquad\qquad \text{for} \qquad Re_l > 2100 \qquad\qquad\qquad (8\text{-}49)$$

Regarding interfacial friction factor, no dependence of gas-wall shear stresses on interfacial characteristic of gas-liquid in film region was observed, see for instance Taitel and Dukler, 1976 and Kowalski (1987).

Andritsos and Hanratty (1987) studied the effect of large-amplitude wave on interfacial conditions of gas-liquid flows and concluded that interfacial shear stresses increases as a result of higher large-amplitude wave. They defined a critical superficial velocity at which large amplitude wave appears and proposed a new correlation as a function of non-dimensional liquid height and superficial gas velocity.

$$\frac{f_i}{f_g} = 1 \qquad\qquad \text{for} \qquad J_g \le J_{g,c}$$

$$\qquad\qquad\qquad\qquad\qquad\qquad\qquad\qquad\qquad\qquad\qquad (8\text{-}50)$$

$$\frac{f_i}{f_g} = 1 + 15(\frac{h_L}{D})^{0.5} (\frac{J_g}{J_{g,c}} - 1) \quad \text{for} \qquad J_g > J_{g,c}$$

$$J_{g,c} = 5 \, (\frac{\rho_{go}}{\rho_g})^{0.5} \qquad\qquad\qquad\qquad\qquad\qquad\qquad (8\text{-}51)$$

Where ρ_{go} is the gas density at atmospheric pressure.

8.7.6.2 Translational velocity of elongated bubble

Nicklin (1962) proposed a model for calculating slug unit translational velocity (U_t) in gas-liquid flow which is a function of mixture superficial velocity (J_t) and drift velocity (U_d).

$$U_t = \zeta \cdot J_t + U_d \qquad\qquad\qquad\qquad\qquad\qquad\qquad (8\text{-}52)$$

The distribution parameter, ζ was found to be 1.2 when flow is turbulent and 2 in the case of laminar flow. Benjamin (1968) suggested that drift velocity can be correlated to Froude number, diameter and gravitational acceleration in horizontal pipe.

$$Fr = \frac{U_d}{\sqrt{g\,D}} = 0.54 \qquad\qquad\qquad\qquad\qquad\qquad\qquad (8\text{-}53)$$

However, this correlation does not take into account viscous effect. Losi and Poesio (2016) evaluated the influence of oil viscosity on drift velocity of a gas bubble in liquids for different axial positions in both horizontal and inclined pipes. They concluded that drift velocity for very viscous oil-gas flow (μ_o=0.804 *Pa·s*) is ranged between 0.0025-0.0065 *m·s^{-1}* for different axial positions in a horizontal pipe, which can be approximated equal to zero. Thus, it seems that bubble translational velocity of U_t=1.2· J_t is a reasonable approximation to predict the experimental data. Figure 8-26 shows bubble translational velocity measured by optical sensor as a function of mixture superficial velocity. The square symbols denote the experimental data, while solid line shows the homogenous line. It is observed that experimental data is underestimated by Nicklin (1962) correlation, due to improper drift velocity expression introduced in this correlation which does not take into account the viscous and surface tension effects. The proposed model for bubble translational velocity gives a satisfactory agreement, which is exactly equivalent to the model proposed by Wallis (1969).
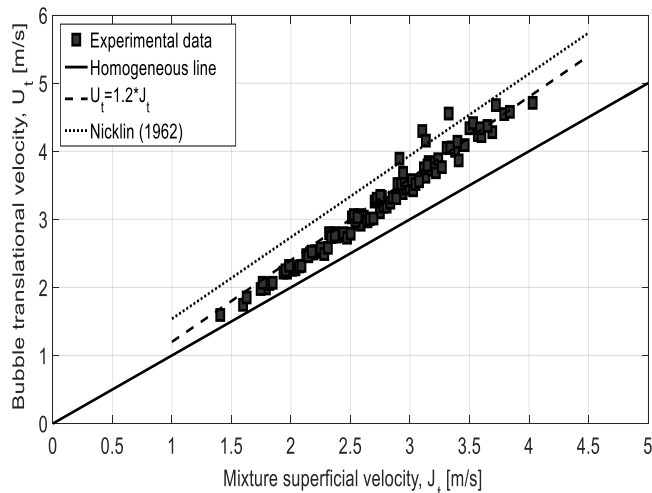
Figure 8-26 Bubble translational velocity (U_t) versus mixture superficial velocity (J_t)

8.7.7 Model development for slug unit length

The slug unit length measured by optical probe is plotted against dimensionless parameter ($1+\varepsilon_{LG}$) in Figure 8-27 to evaluate the effect of liquid and gas superficial velocity on slug unit length. At fixed liquid superficial velocity, increases gas flow rate

causes increasing in slug unit length. All data collapse on a common line, so it is customary to express slug unit length normalized by pipe diameter with a power law functional form as function of operating conditions, that is:

$$\frac{l_u}{D} = C \cdot (1 + \varepsilon_{LG})^n \qquad (8\text{-}54)$$

From experimental measurements of total unit length measured by optical sensor, coefficients C and n are found to be 7.3 and 2, respectively.
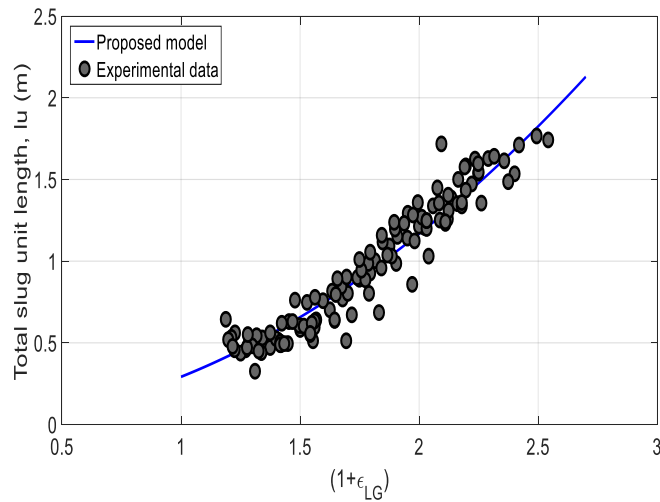
Figure 8-27 Experimental total slug unit length measured by optical probe as a function of dimensionless parameter $(\frac{J_t}{J_L})$.

Cook and Behnia (2000b) developed a model to compute total slug unit length for water-air flows as a function of bubble length (L_b), gas superficial velocity, and liquid holdup in slug body.

$$l_u = \frac{L_b[(1-H_{lf}).U_t - J_g]}{J_g} \qquad (8\text{-}55)$$

Where H_{lf} is the mean liquid holdup in film section. They concluded that the liquid hold up at bubble head ($H_{lfe} \sim \frac{U_t - J_t}{U_t}$) is different from mean value and suggested that

228

H_{lf} can be calculated as $H_{lf} \sim 1.4\, H_{lfe}$. To make use of equation 45, information of bubble length is required, which can be obtained from experimental data. Figure 8-28 illustrates the parity plot of predicted slug unit length against measured slug units using 106 data points. As it is evident, the total slug unit length predicted by proposed model is consistent with experimental data (87% of all data fall within ±20% relative error), with the mean absolute relative error of 10.7%. However, the model by Cook and Behnia (2000b) shows a strong under-prediction, due to the fact that it is originally developed for gas-liquid flow and the effect of the third phase (oil) is not considered for model development.
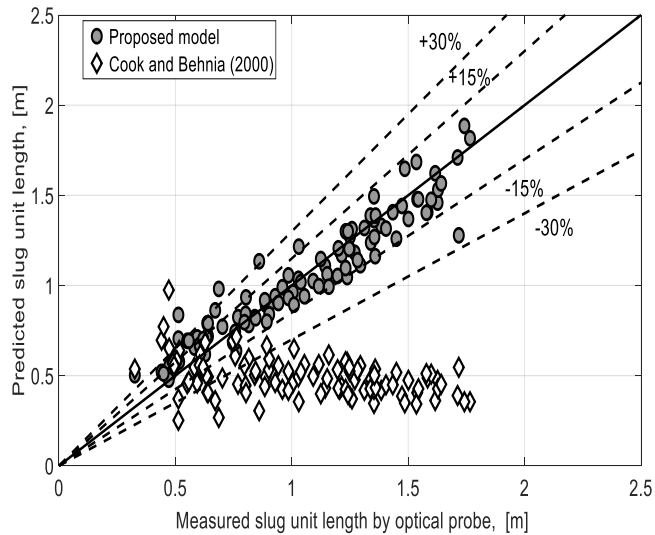
Figure 8-28 Parity plot of comparison between experimental data and predicted slug unit length; dashed lines represent ±15% and ±30% deviation from bisector

8.8 Validation of hydrodynamic model

The hydrodynamic model presented in sections 8.7.1 to 8.7.3 is used to compute pressure gradient and gas holdup. The hydrodynamic model requires some input quantities such as slug body holdup and length, total slug unit length and closure relationship which is presented in sections 8.7.4 to 8.7.7. The solutions of continuity

and momentum equations only require rheological properties of phases, pipe diameter, and flow conditions. In the following sections, the results of three-phase pressure drop and gas holdup predicted by hydrodynamic model are compared with experimental counterpart and other data source in the literature.

8.8.1 Pressure drop prediction

Unfortunately, due to the lack of experimental data for very viscous oil-water-gas flow in horizontal pipe, only two sets of experimental data are available to evaluate the model performance. One source is data bank in the work of Poesio et al. (2009) who performed tests with higher viscosity than current campaign in a 21 mm i.d. horizontal pipe. Another comparison is made with the current experimental data. The details of data bank are reported in Table 8-5.

Table 8-5 Details of data sources used to evaluate model performance

Data source	Diameter [m]	Oil viscosity [Pa.s]	Gas velocity [m/s]	Liquid velocity [m/s]	Data points
Our data bank	0.040	0.83 @ room temp	0.22-1.91	1.02-2.05	131
Poesio et al. (2009)	0.021	1.2	0.29	0.13-3.4	30

As it is evident from Figure 8-29, there is a fairly good agreement between predicted and measured pressure drop data of Poesio et al. (2009), considering the average relative error of -14.8% and standard deviation 14.7%. Almost all data predicted by hydrodynamic model are underestimated measurements. Considering acceleration pressure drop contribution in equation 8-36 might result in a better prediction of measured data by model and can be a topic of further investigation. About 87% of all data predicted by the model falls within ±30% of relative error. Larger deviation occurs at low oil superficial velocity. At low oil superficial velocity, oil and water tends to form core-annular flow and degree of stratification increases. Since the present model assumes an equivalent liquid for oil and water, which oil and water treated as a fully-

mixed liquid, it is possible that the pressure drop predicted by the model shows larger deviation.
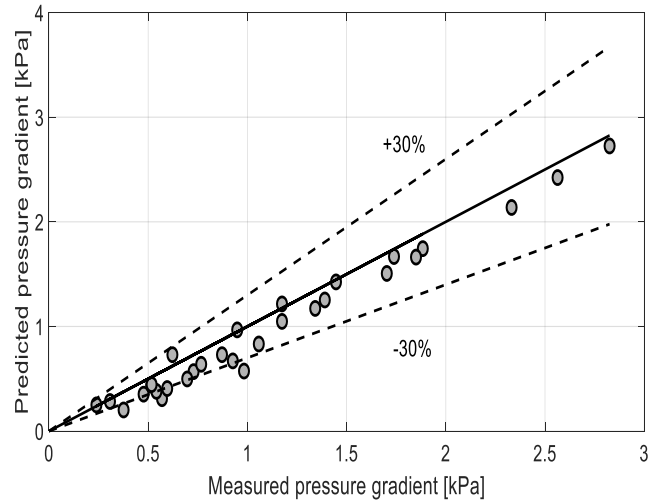
Figure 8-29 Pressure drop comparison between prediction and data of Poesio et al (2009) for D=21mm

The comparison of pressure gradient computed by model and present data is depicted in Figure 8-30 showing a good agreement with an average relative error of -15.4%, while standard deviation was found to be 10.2%. The wide range of operating conditions was considered for this comparison. To evaluate the performance of current mechanistic model, hybrid model developed by Poesio et al. (2009) is also compared in Figure 8-30. They used Lockhart-Martinelli parameter (χ) modified by Chisholm (1973) to predict three-phase pressure drop. The hybrid model is based on solution of two-fluid model for liquid-liquid developed by Brauner (1991), which is eventually substituted in Lockhart-Martinelli parameter to compute overall pressure drop. Table 8-6 lists the equations required for the hybrid model proposed by Poesio et al. (2009).

Table 8-6 Hybrid model proposed by Poesio et al. (2009)

Hybrid model	Additional information

$$\Delta P_{o-w-g} = \phi_g^2 \cdot \Delta P_g$$

$$\chi = \sqrt{\frac{\Delta P_{liq}}{\Delta P_g}}$$

$$\phi_g^2 = 1 + C \cdot \chi + \chi^2$$

(Lockhart-Martinelli parameter)

$$C = 15$$
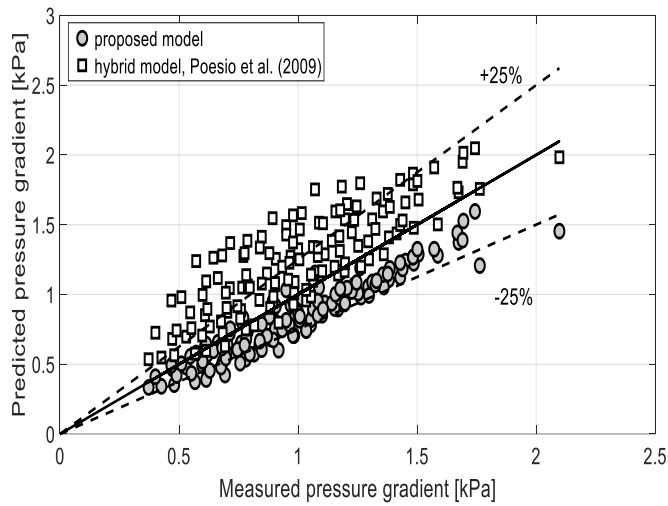
Figure 8-30 Predicted pressure drop versus measured data for present data and comparison with hybrid model developed by Poesio et al. (2009)

The proposed mechanistic model is able to predict pressure drop better than hybrid model over entire range of operating conditions. Almost 84% of all data fall within 25% of relative error for proposed model while 54% of all data falls into 25% of relative error predicted by hybrid model. Table 8-7 shows statistical analysis of proposed model and comparison with hybrid model.

Table 8-7 Comparison of pressure drop for proposed mechanistic model with hybrid model

Models	e (%)	Max e_{ri} (%)	Min e_{ri} (%)	Std. deviation (%)

Hybrid, Poesio et al. (2009)	27.9	116	-13.1	26.4
Proposed mechanistic model	-15.4	8.7	-39.1	10.2

The results of pressure drop prediction shows that in spite of complexity of three phase flow of high viscous oil-water-gas, the developed mechanistic model is able to predict pressure gradients with a reasonable average relative error. Hence, it can be used as an operative engineering tool to compute pressure drop.

8.8.2 Gas holdup prediction

The results of mean gas holdup predicted by proposed model (equation 8-21) is compared with the experimental holdup measured by optical probe and shown in a parity plot, see Figure 8-31. The effect of liquid viscosity is implicitly considered in slug body holdup (H_{ls}). The average experimental gas holdup can be computed as $H_g = \frac{J_g}{U_g}$ where $U_g = 1.29 \cdot J_t$. A very good agreement was observed between prediction and average measurement, considering 7.5% average absolute relative error. Further comparison has been made between prediction of gas holdup and models available in literature for two phase flow of gas-liquid to check the possibility to use in three phase flow. The 68 void fraction correlations according to large data set have been reported by Woldesemayat and Ghajar (2007). Among all correlations presented in their work, only three correlations in the families of slip ratio (Lockhart and Martinelli, 1949, and Chen, 1986) and Kε_H (Armand, 1946) models are selected. The apparent viscosity of liquid calculated from eq. 8-15 is simply replaced in the correlation for mixture of oil-water. The results are reported in Table 8-8 showing the average relative error less than 20%.
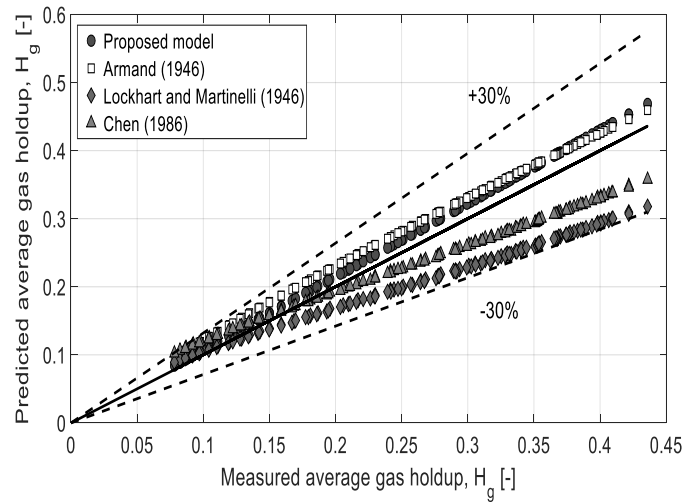
Figure 8-31 Comparison between prediction and measurement for mean gas holdup, lines represent ±30 deviation from bisector

Table 8-8 Performance of available correlation for mean gas holdup

Correlation	Avg absolute error (%)	Max absolute error (%)	Std. deviation (%)
Armand (1946)	12.3	22.9	4.8
Lockhart and Martinelli (1946)	19.3	27.1	7.7
Chen (1986)	12.7	31.4	5.9

9. Conclusions and recommendations for future work

9.1 Conclusions

The main objective of the present study was to investigate high viscous oil-water flow in horizontal pipe undergoing changes in cross-sectional area. Variable cross-sectional area includes the sudden expansions and contractions or the adoption of Venturi flow meter (VFM) and Nozzle flow meter (NFM). Accordingly, experimental investigation, theoretical modeling, and CFD analysis were conducted. The last part of the current thesis is devoted to three-phase flow of high viscous oil-water-air mixture in a straight horizontal pipe due to its importance in petroleum industry. The conclusions regarding the above aspects are summarized as follows.

(1) Experimental investigation of high viscous oil-water flow in horizontal pipe with variable cross-sectional area

Experimental results on very viscous oil-water flow in the presence of sudden contractions and expansions were reported regarding flow patterns, distributed pressure gradient, concentrated pressure drop, and phase holdup. At first, Information extracted from the experimental investigation is discussed. Secondly, conclusions regarding the same flows through VFM and NFM are summarized. The most significant achievements are briefly highlighted in the following:

- The main flow patterns observed in very viscous oil-water flow included dispersed oil-in -water (D), Core-annular flow (CAF), Corrugated Core-annular flow (CCA), eccentric Core-annular with and without drop entrainment (ECA-E and ECA), and transition from CAF to D flow.

- Flow pattern maps were developed for downstream pipes of sudden expansions TS2 (21-30 mm), and TS3 (30-40 mm), and TS4 (30-50 mm) to evaluate the influence of different area ratio on flow patterns. It was concluded that for the largest cross-sectional area change (TS4), the dominant flow pattern resulted dispersed flow, whereas CAF was the major flow pattern in the other configurations (TS2 and TS3). Comparisons of flow regime maps with literature data bank were reported and the major parameters affecting flow regime maps were addressed. In addition to phase velocity, oil viscosity, pipe

diameter and oil density were shown to be the most influential factors on flow regime maps.

- The results of pressure gradient reduction factor for sudden contraction and expansion in upstream and downstream pipes were investigated. It was concluded that the pressure reduction factor is lower downstream of the sudden expansion as compared to the upstream pipe due to the influence of singularity, which causes the oil-water flow to be more eccentric. The proper choice of the area ratio is crucial for sudden expansions due to the fact that a very strong area ratio would determine contact of oil with the wall (oil fouling) in the downstream pipe and, hence increased pressure gradient. On the other hand, it was observed that pressure reduction factor is lower for upstream pipe than for downstream pipe in the case of sudden contraction.

- Concentrated pressure drop was evaluated by means of the pressure gradient technique. This information is needed to calculate the total localized loss coefficients in the case of expansion and contraction. Analysis of localized loss coefficient as a function of mixture superficial velocity showed that the values of loss coefficient are almost constant, irrespective of the oil superficial velocity for sudden contraction TS1 and sudden expansion TS2. Thus, it is possible to provide a best-fit line in these cases. However, in the case of stronger area ratio change (TS4), a decreasing trend was observed.

In Chapter 6, the experimental results of very viscous oil-water flow through Venturi Flow Meter (VFM) and Nozzle Flow Meter (NFM) in a horizontal pipe (40 mm i.d.) are presented. The conclusions regarding modeling aspect of high viscous oil-water flow through VFM and NFM to compute the total and individual volume flow rate will be presented in the next section. As far as the experimental results are concerned with:

- The concentrated pressure drop between the device inlet and throat section has been measured and the dependence on the flow parameters (flow velocities) was analyzed and discussed. The concentrated pressure drop has been analyzed as a function of the water volumetric flux for different superficial oil velocity, showing the increase of the pressure drop by increasing the water and oil superficial velocity.

- The mixture superficial velocity has been computed by adoption of the theoretical approach of Bernoulli's equation and introducing the definition of discharge coefficient

from calibration curve. The calculation of mixture velocity requires the proper definition of two-phase density, which was assumed to be computed from the homogeneous model. The mixture superficial velocity was well predicted within ±10% of relative error, as compared to the experimental data for both VFM and NFM.

(2)   Theoretical modeling of high viscous oil-water flow within horizontal pipe

In Chapter 5, the modeling aspects of high viscous oil-water flow in a straight horizontal pipe regarding the prediction of water holdup, pressure gradient, and pressure reduction factor are summarized.

- A complete review on the models available in the literature concerning water-lubricated very-viscous oil-water flow was given. A mechanistic model based on the Two-Fluid Model (TFM) for fully-developed Core-Annular flow of oil-water mixtures was developed. The interfacial stress terms were eliminated from two-fluid model and replaced by an empirical formulation of the water holdup as a function of measured pressure gradient, superficial water velocity, rheological properties of water.

- Among the available models in the literature for prediction of the water holdup, the correlation by Arney et al. (1993) predicted the water holdup with very high accuracy (MAPE=3.3 %). The models by Oliemans (1986), Ullman and Brauner (2004) can also give the reasonable predictions of the water holdup, with the mean absolute percentage error of 16% and 8.4%, respectively.

- Based on Arney et al. (1993) approach, an empirical correlation based on a very large experimental database (Charles et al. (1961), Sinclair (1970), Oliemans (1986), and Bai et al., 1992) was developed showing a very satisfactory agreement.

- Regarding the prediction of pressure gradient, it was demonstrated that models of Arney et al. (1993) and Brauner (1998) generally overestimate the measured pressure gradient for D=21 mm, D=30 mm, and D=40 mm. Both models gave satisfactory prediction of pressure gradients, with 80 % and 87 % of all data fall within ±30 % of relative error for Brauner (1998) and Arney et al. (1993), respectively.

- The model developed in the current study to calculate pressure gradient significantly improved the prediction of pressure drop with MAPE=9.3%.

Part of Chapter 6 is associated with the modeling aspect of high viscous oil-water flow through VFM and NFM. The proposed model is based on the developed TFM in Chapter 5, which analytically gives the estimation of water holdup as a function of the distributed pressure gradient for fully-developed flow.

- Generally, information of volumetric flow rate of phases is not available in advance to calculate the two-phase flow density and mixture volumetric flow rate. Hence, the measurement of phase holdup (for instance, by QCV technique) or using the available correlations in the literature is essential to provide such information. A new model was developed to calculate the mixture, oil, and water velocity, without direct measurement of phase holdup. The superficial velocity was correlated to the measurement of concentrated pressure drop through calibration curve. The input parameters of the developed model are concentrated and distributed pressure drop (from measurement), rheological properties of water, and pipe diameter, whereas output of the model are mixture, oil, water velocities. The flow regimes under investigation were core-annular and dispersed flow.

- The developed model allowed the evaluation of the input water volume fraction with MAPE=5% and MAPE=2% for VFM and NFM, respectively. Furthermore, good agreement between the predicted value of water velocity and experimental data was observed, with average relative error of 7% and 5.5% for VFM and NFM, respectively. Slightly, higher deviation for estimation of oil superficial velocity is observed, with average relative error of -12.6% and -11.8% for VFM and NFM, respectively.

(3) CFD modeling of high viscous oil-water flow through horizontal pipe with variable cross-sectional area

In Chapter 7, CFD simulation of very viscous oil-water flow through measurement devices (VFM and NFM) as well as sudden expansion was studied, most important aspects of flow such as oil holdup, pressure gradients and flow patterns were predicted. The main results obtained from numerical simulation are summarized as follows:

- Numerical simulation results were validated by experimental data presented in Chapters 4 and 6. Volume of Fluid (VOF) multiphase flow model combined with Realizable k-ε turbulent model resulted to predict phase configurations of very viscous oil-water in core-

annular flow regime. However, it was shown that dispersion of oil droplets in water continuous flow could not be captured due to the fact that interface length scale is not comparable to the pipe diameter. Hence, to properly capture the dispersed flow regime by numerical scheme, finer mesh resolution is required. During core-annular flow, CFD simulation was able to predict the core eccentricity without oil contact at the pipe wall. This is consistent with flow visualization observed experimentally.

- The concentrated pressure drop through the convergent section of the VFM and NFM calculated by CFD showed a very good agreement with experimental data. This information is crucially important because it would be directly correlated to prediction of volumetric flux. Although core-annular flow is a separated flow regime, the analysis of slip ratio highlighted that the presence of the VFM and NFM shift hydrodynamics towards homogeneous flow. The two phase mixture velocity and the mass flow rate were predicted with satisfactory accuracy (particularly for the VFM) by means of CFD simulation.

- Regarding oil-water flow through sudden expansions, the simulated time-averaged oil holdup and pressure gradients both upstream and downstream of expansion plane are also found to be in reasonable agreement with experimental data. The average oil holdup predicted from CFD is compared to Arney et al. (1993) correlation due to the lack of experimental data for sudden expansion, showing the maximum relative error of 16.7%. The experimental trend of pressure reduction factor as a function of input water volume fraction was reproduced by the numerical analysis.

- Time-average velocity and oil holdup along pipe axis were extracted from numerical simulation for sudden expansion pipe configuration. Three regions were detected for flow of oil-water mixtures, which included fully developed inlet flow, transitional region, and fully developed outlet flow.

- The results of the present study thus confirm that CFD is able to offer valuable insight about the flow of oil-water mixtures for different pipe configurations. By offering good predictions of the main flow characteristics, even with limited computational requests, it confirms its role as a promising engineering tool in this field. Different design solutions could be tested using CFD, avoiding operational and capital expenditures and reducing the time needed for the development.

(4) **Experimental investigation of high viscous oil-water-air flow within straight horizontal pipe**

In Chapter 8, the results of an experimental campaign devoted to three-phase flow of very viscous oil-water-air mixtures in a straight horizontal pipe (40 mm i.d.) were reported. Furthermore, a mechanistic model based on solution of the continuity and momentum equations was developed to compute phase holdup and pressure drop. The flow regime under investigation was slug flow. The main conclusions are summarized as follows:

- Slug body, elongated bubble and total slug unit lengths were experimentally measured by optical probes. Statistical analysis of slug body length was performed, enabling the characterization of slug flow based on probability density function (PDFs). It was found that superficial gas velocity has a significant influence on slug body and bubble length, that is, the higher the superficial gas velocity, the higher the slug body and bubble length.

- A new correlation for slug unit length was developed based on experimental data obtained by optical probes. Acceptable agreement between predicted slug unit length and measurements was observed.

- Translation velocity of slug unit was measured by both optical probes and image processing technique. A modified version of translational velocity developed by Nicklin (1962) was used as a closure relation for the model because it showed a satisfying agreement with actual data.

- The mechanistic model requires as input superficial velocity of phases and their rheological properties. The mixture density for oil-water phases was linearly interpolated, whereas oil-water mixture viscosity was calculated according to Einstein's equation. The output of the mechanistic model was pressure drop and average phase holdup for gas and liquid across slug unit cell. The results of predicted pressure drop were compared with measurements, showing that the method is promising. In particular, average gas holdup computed from mechanistic model shows average relative error of 7.5%, which is better than the available correlations.

9.2 Recommendations for future work

Since the most important aspects of very viscous oil-water flows such as pressure drop, phase holdup, and flow pattern are highly affected by the oil fouling phenomenon and eccentricity of oil core, it is highly recommended that further experimental and computational works are conducted. In particular, within the areas of liquid-liquid flows:

- It is important to theoretically investigate the influence of eccentricity on characteristic behavior of very viscous oil-water flow because it was shown that it has a significant effect.

- The experimental tests on high viscous oil-water flow through sudden expansion with stronger area ratio showed a peculiar behavior that is still to be understood in light of the theory. Thus, new tests providing a larger data bank are highly recommended.

- Regarding CFD analysis, much more refined mesh must be adopted to capture the onset of dispersion at the oil-water interface.

- Regarding three phase flow of oil-water-air mixtures, this work has put in evidence that both experimental and theoretical approaches are viable at least until the liquid-liquid system behaves like an "equivalent" liquid phase. This is certainly valid if the air flow rate is not too high. However, hard work has to be made to understand the limitations of the presented approach as well as the very complicated phenomenology of the three-phase flow.

References

Abdelall, F.F., Hahn, G., Ghiaasiaan, S.M., Abdel-Khalik, S.I., Jeter, S.S., Yoda, M., Sadowski, D.L. (2005). Pressure drop caused by abrupt flow area changes in small channels. Experimental Thermal and Fluid Science, 425-434.

Acikgoz, M., Franca, F., Lahey JR, R.T. (1992). An experimental study of three-phase flow regimes. International Journal of Multiphase Flow, 18, 327-336.

Ahmed, W.H., Chan, Y.C., Shoukri, M. (2008). Development of two-phase flow downstream of a horizontal sudden expansion. International Journal of Heat Fluid Flow, 29, 194-206.

Ahmed, W.H., Ching, C.Y., Shoukri, M. (2007). Pressure recovery of two-phase flow across sudden expansions. International Journal of Multiphase Flow, 33, 575-594.

Alboundwarej, H., Felix, J., Taylor, S., Badry, R., Bremner, C., Brough, B., Skeates, C., Baker, A., Palmer, D., Pattison, K., Beshry, M., Krawchuk, P., Brown, G., Calvo, R., Triana, J.A.C., Hathcock, R., Koerner, K., Hughes, T., Kundu, D., West, C. (2006). Highlighting Heavy Oil. Oilfield review, 18(2), pp. 34-53.

Al-Safran, E., Gokcal, B., Sarica. C. (2011). High viscosity liquid effect on two-phase slug length in horizontal pipes. Presented at the 15th International Conference on Multiphase Production technology. Cannes, France, Jun 15-17.

Al-Safran, E., Kora, C., Sarica C. (2015). Prediction of slug liquid holdup in high viscosity liquid and gas two-phase flow in horizontal pipes. Petroleum Science and Engineering, 133, 566-575.

Andreussi, P., Minervini, A., Paglianti, A. (1993). Mechanistic model of slug flow in near-horizontalpipes. AICHE, 39.

Andritsos, N., Hanratty, T.J. (1987). Influence of interfacial waves in stratified gas-liquid flows. AICHE, 33, 444-454.

ANSYS Fluent Theory Guide. (2012). USA: ANSYS, Inc.

ANSYS Fluent User's Guide. (2012). USA: ANSYS, Inc.

Armand, A. (1946). The resistance during the movement of a two-phase system in horizontal pipes. Izv Vse Tepl Inst, 1, 16-23.

Arney, M.S., Bai, R., Guevara, E., Joseph, D.D., Liu, K. (1993). Friction factor and holdup studies for lubricated pipelining- I experiments and correlations. Internation Journal of Multiphase Flow, 19, 1061-1076.

Arnone, D. (2017). Experimental study of two-phase flow air-oil in water emulsion in horizontal pipes. Ph.D thesis. Universita degli studi di Brescia.

ASTM, D445. (1965). Standard test method for kinematic and dynamic viscosities of transparent and opaque liquids.

Atkinson, I., Berard, M., Conort, G., Groves, J., Lowe, T., McDiarmid, A., Mehdizade, P., Perciot, P., Pinguet, B., Smith, G., Williamson, K.J. (Winter 2004/2005). A New Horizon in Multiphase Flow Measurement. Retrieved from www: http://www.slb.com/resources/publications

Attou, A., Bolle, L. (1997). A new correlation for the two-phase pressure recovery downstream from a sudden enlargement. Chemical Engineering Technology, 419-423.

Aziz, K., Govier, G.W. (1972). The flow of complex mixtures in pipes. New York: Van Nostrand Reinhold.

Babakhani Dehkordi, P., Colombo, L.P.M., Guilizzoni, M., Sotgia, G. (2017). CFD simulation with experimental validation of oil-water core-annular flows through Venturi and Nozzle flow meters. Journal of Petroleum Science and Engineering, 149, 540-552.

Bai, B., He, D. (2014). A new correlation for wet gas flow rate measurement with Venturi meter based on two-phase mass flow coefficient. Journal of Measurement, 58, 61-67.

Bai, R., Chen, K., Joseph, D.D. (1992). Lubricated pipelining stability core-annular flow, Part 5. Experiments and comparison with theory. Journal of Fluid Mechanics, 240, 97-142.

Baker, C. (2000). Flow Measurement Handbook. Cambridge University Press.

Balakhrisna, T. G. (2010). Oil-water flows through sudden contraction and expansion in a horizontal pipe- Phase distribution and pressure drop. Internation Journal of Multiphase Flow, 13-24.

Bannwart, A. (2001). Modeling aspects of oil-water core-annular flows. Journal of Petroleum Science and Engineering, 32, 127-143.

Bannwart, A.C., Rodriguez, O.M.H., De Carvalho, C.H.M., Vara, Rosa M.O. (2004). Flow patterns in heavy crude oil-water flow. Journal of Energy Resources Technology, 126, 184-189.

Bannwart, A.C., Rodriguez, O.M.H., Trevisan, F.E. (2009). Experimental investigation on liquid-liquid-gas flow: Flow patterns and pressure gradient. Journal of Petroleum Science and Engineering, 65, 1-13.

Barnea, D., Brauner, N. (1985). Holdup of the liquid slug in two phase intermittent flow. International Journal of Multiphase Flow, 11, 43-49.

Beggs, H.D., Brill, J.P. (1973). A study of two-phase flow in inclined pipes. J.Pet.Technol.Trans, 607-617.

Benjamin, T. (1968). Gravity currents and related phenomena. Journal of Fluid Mechanics, 31, 209-248.

Bertani, C., De Salve, M., Malandrone, M., Monni, G., Panella, B. (2010). State-of-the-art and selection of techniques in multiphase flow measurement. Politecnico di Torino.

Brackbill, J.U., Kothe, D.B., Zemach, C. (1992). A continuum method for modeling surface tension. Journal of Computational Physics, 100, 335-354.

Brauner, N. (1991). Two-phase liquid-liquid annular flow. International Journal of Multiphase Flow, 17, 59-76.

Brauner, N. (1998). Liquid-liquid two-phase flow. HEDU-Heat Exchanger Design Handbook. Begelll House, New York (Chapter 2.3.5).

Brauner, N. (2002). Liquid-liquid two-phase flow systems. In: Bertola, V. (Ed.). Modeling and Control of Two-phase Flow Phenomena. CISM Center. Udine, Italy.

Charles, M.E., Govier, G.T., Hodgson, G. (1961). The horizontal pipeline flow of equal density oil-water mixtures. The Canadian Journal of Chemical Engineering, 1, 27-36.

Charles, M.E., Redberger, P.J. (1962). The reduction of pressure gradients in oil pipelines by the addition of water: Numerical analysis of stratified flow. The Canadian Journal of Chemical Engineering, 40, 70-75.

Chen, I.Y., Liu, C.C., Chien, K.H., Wang, C.C. (2007). Two-phase flow characteristics across sudden expansion in small rectangular channels. Experimental Thermal and Fluid Science, 32, 696-706.

Chen, I.Y., Tseng, C.Y., Lin, Y.T., Wang, C.C. (2009). Two-phase flow pressure change subject to sudden contraction in small rectangular channels. International Journal of Multiphase Flow, 35, 297-306.

Chen, J.J.J. (1986). A further examination of void-fraction in annular two-phase flow. International Journal of Heat Mass Transfer, 29, 1760-1763.

Chisholm, D. (1967). Pressure gradients during the flow of incompressible two-phase mixtures through pipes, venturis and orifice plates. British Chemical Engineering, 12, 454-457.

Chisholm, D. (1973). Pressure gradients due to friction during the flow of evaporating two-phase flow mixtures in smooth pipes and channels. International Journal of Heat Mass Transfer, 16, 347-358.

Chisholm, D. (1983). Two-phase flow in pipelines and heat exchangers. Godwin, London. pp. 175-192.

Clark, A., & Shapiro, A. (1950). Patent No. 2,533,878. US Patent.

Colombo, L.P.M., Guilizzoni, M., Sotgia, G., Marzorati, D. (2015). Infulence of sudden contarctions on in-situ volume fractions for oil-water flows in horizontal pipes. International Journal of Heat and Fluid Flow, 53, 91-97.

Colombo, L.P.M., Guilizzoni, M., Sotgia, G.M. (2012). Characterization of the critical transition from annular to wavy-stratified flow for oil-water mixtures in horizontal pipes. 53, 1617-1625.

Cook, M., Behnia, M. (2000b). Slug length prediction in near horizontal gas-liquid intermittent flow. Chemical Engineering Science, 55, 2009-2018.

Delhaye, J. (1981). Singular pressure drops, in: A.E. Bergles (Ed.). In Two-Phase and Heat Transfer in the Power and Process Industries (pp. 124-149). Hemisphere, Washington, DC.

Desamala, A.B., Vijayan, V., Desari, A., Desmahapatra, A.K., Mandal, T.K. (2016). Prediction of oil-water flow patterns, radial distribution of volume fraction, pressure and velocity during separated flows in horizontal pipe. Journal of Hydrodynamics Serie B, 4, 658-668.

Dos Santos, R.G., Rahoma, S.M., Bannwart, A.C., Loh, Watson. (2006). Contact angle measurements and wetting behavior of inner surfaces of pipelines exposed to heavy crude oil and water. Journal of Petroleum Science and Engineering, 51, 9-16.

Dukler, A.E., Hubbard, M.G. (1975). A model for gas-liquid slug flow in horizontal and near horizontal tubes. Industrial and Engineering Chemistry Fundamentals, 14.

Fabre, J., Line, A. (1992). Modeling of two-phase slug flow. Journal of Fluid Mechanic, 24, 21-46.

Falcone, G., Hewitt, G.F., Alimonti, C. (2009). Multiphase Flow Metering: Principles and Applications. Oxford, UK: Elsevier.

Gateau, P., Henaut, I., Barre, L., Argillier, JF. (2004). Heavy oil dilution. Journal of Oil & Gas Science and Technology, 59 (5), 503-509.

Ghosh, S., Das, G., Das, P.K. (2010). Simulation of core-annular downward flow through CFD - A comprehensive study. Chemical Engineering Process, 49, 1222-1228.

Ghosh, S., Das, G., Das, P.K. (2011). Simulation of core annular in return bends- A comprehensive CFD study. Chemical Engineering Research and Design, 89, 2244-2253.

Ghosh, S., Mandal, T.K., Das, G., Das, P.K. (2009). Review of oil water core annular flow. Renewble and Sustainable Energy Reviews, 13, 1957-1965.

Grassi, B., Poesio, P., Piana, E., Lezzi, A.M., Beretta, G.P. (2006). Influence of inlet conditions on flow patterns in oil-water flows in horizontal tubes at intermediate Eötvös number. In: 6th Euromech Fluid Mechanics Conference. Stockholm, Sweden.

Grassi, B., Strazza, P., Poesio, P. (2008). Experimental validation of theoretical models in two-phase high-viscosity ratio liquid-liquid flows in horizontal and slightly inclined pipes. International Journal of Multiphase Flow, 34, 950-965.

Guglielmini, G., Muzzio, A., Sotgia, G. (1997). The structure of two-phase in ducts with sudden contractions and its effects on the pressure drop. Experimental Heat Transfer, Fluid Mechanics and Thermodynamics.

Hall, A. (1992). Multiphase flow of oil, water and gas in horizontal pipes. Ph.D thesis. Impreial college. London, UK.

Hart, A. (2014). A Review of Technologies for Transporting Heavy Crude Oil and Bitumen via Pipelines. Journal of Petroleum Exploration and Production Technology, 4, 327-336.

Hewitt, G. (1997). From gas-liquid to liquid-liquid two-phase flow: a difficult journey. International Symposium on Liquid-Liquid Two-Phase Flow Transport Phenomena. Antalya, Turkey. Nov. 3rd-7th .

Hewitt, G. (2005). Three-phase gas-liquid-liquid flows in the steady and transient states. Nuclear Engineering and Design, 235, 1303-1316.

Hirt, C.W., Nichols, B.D. (1981). Volume of fluid (VOF) method for the dynamics of free boundries. Journal of Computational Physics, 39, 201-225.

Hwang, C-Y. J., Pal, R. (1997). Flow of two-phase oil/water mixtures through sudden expansions and contractions. Chemical Engineering, 157-163.

ISO 5167-4. (2003). Measurement of fluid flow by means of pressure differential devices inserted in circular cross-section conduits running full -- Part 4: Venturi tubes.

Issa, R. (1986). Solution of the implicitly discritized fluid flow equations by operator splitting. Journal of Computational Physics, 62, 40-65.

Jana, A.K., Das, G., Das, P.K. (2008). The hydrodynamics of liquid-liquid upflow through a venturimeter. International Journal of Multiphase Flow, 34, 1119-1129.

Kaushik, V.V.R., Ghosh, S., Das. G,. Das. P.K. (2012). CFD simulation of core annular flow through sudden contraction and expansion. Petroleum Science and Engineering, 86, 153-164.

Keskin, C., Zhang, H.Q., Sarica, C. (2007). Identification and classification of new three-phase gas/oil/water flow patterns. Presented at the SPE annual technical conference and exhibition. Abaheim, California, USA, 11-14 November. SPE-110221-MS.

Kowalski, J.E. (1987). Wall and interfacial shear stress in stratified flow in a horizontal pipe. AICHE, 33, 274-281.

Leeuw, D. (1997). Liquid correction of Venturimeter reading in wet gas flow. North Sea Flow Measurement Workshop. Kristiansand, Norway.

Li, X., Huang, Z., Meng, Z., Wang, B., Li, H. (2009). Oil-water two phase flow measurement using a venturi meter and an oval gear flow meter. Chemical Engineering Communications, 223-231.

Lo, S., Tomasello, A. (2010). Recent progress in CFD modelling of multiphase flow in horizontal and near-horizontal pipes. 7th North American Conference on Multiphase Technology. Banff, Canada.

Lockhart, R.W., Martinelli, R.C. (1949). Proposed correlation of data for isothermal two-phase, two component flow in pipe. Chemical Engineering Progress, 45, 39-48.

Loh, W.L., Premanadhan, V.K. (2016). Experimental investigation of viscous oil-water flows in pipeline. Journal of Petroleum Science and Engineering, 147, 87-97.

Losi, G., Arnone, D., Correra, S., Poesio, P. (2016b). Modelling and statistical analysis of high viscosity oil/air slug flow characteristics in a small diameter horizontal pipe. Chemical Engineering Science, 148, 190-202.

Losi, G., Poesio, P. (2016). An experimental investigation on the effect of viscosity on bubbles moving in horizontal and slightly inclined pipes. Experimental Thermal and Fluid Science, 75, 77-88.

Malinowsky, M. (1975). An experimental study of oil-water and air-oil-water flowing mixtures in horizontal pipes. MS thesis. University of Tulsa, US.

Massey, B. (2001). Mechanics of Fluids. Nelson Thrones Ltd.,UK.

McCabe, W.L., Smith, J.C., Harriott, P. (1993). Unit Operations of Chemical Engineering. New York: McGraw-Hill.

Menard, T., Tanguy, S., Berlemont, A. (2007). Coupling level set/VOF/ghost fluid methods: Validation and application to 3D simulation of the primary break-up of a liquid jet. International Journal of Multiphase Flow, 33, 510-524.

Menter, F. (1993). Zonal two equation k-w turbulence models for aerodynamic flows. 24th Fluid Dynamics Conference. Orlando, Florida.

Monni, G. (2013). Special instrumentation for two-phase flow. Ph.D thesis. Politecnico di Torino.

Nadler, M., Mewes, D. (1995). Effect of the liquid viscosity on the phase distribution in horizontal gas-liquid slug flow. International Journal of Multiphase Flow, 21, 253-266.

NFOGM. (2005). Handbook of Multiphase Flow Metering. The Norwegian Society for Oil and Gas Measurement and The Norwegian Society of Chartered Technical and Scientific Professionals.

Nicklin, D. (1962). Two-phase bubble flow. Chemical Engineering Science, 17, 693-702.

Oddie, G., Anthony Pearson, J.R. (2004). Flow Rate Meaasurement in Two-Phase Flow. Schlumberger Cambridge Research.

Odozi, U. (2000). Three-phase gas/liquid/liquid slug flow. Ph.D thesis. Imperial college. London, UK.

Oliemans, R. (1986). The lubricating-film Model for Core-annular flow. Ph.D. Thesis. The Netherlands: Technische Hogeschool Delft. Delft University Press.

Oliemans, R.V.A., Ooms, G. (1986). Core-annular flow of oil and water through a pipeline. In G. Hewitt, Multiphase Science and Technology (pp. 427-476).

Oliemans, R.V.A., Ooms.G., Wu, H., Duijvestjn, A. (1987). Core-annular oil/water flow:The turbulent-lubricatinf-film model and measurements in a 5cm pipe loop. International Jurnal of Multiphase Flow, 13, 23-31.

Oliveira, J.L.G., Passos, J.C., Verschaeren, R., Van der Geld, C. (2009). Mass flow rate measurements in gas-liquid flows by means of a venturi or orifice plate coupled to a void fraction sensor. Experimental Thermal and Fluid Science, 33(2), 253-260.

Ooms, G., Segal, A., Van Der Wees, A.J., Meerhoff, R., Oliemans, R.V.A. (1984). A theoretical model for core-annular flow of a very viscous oil core and water annulus through a horizontal pipe. International Journal of Multiphase Flow, 10, 41-60.

Pal, R. (1993). Flow of oil-in-water Emulsions through Orifice and Venturi meters. Industrial and Engineering Chemistry Research, 32, 1212-1217.

Pan, L., Jayanti, S., Hewitt, G.F. (1995). Flow patterns, phase inversion and pressure gradient in air-oil-water flow in a horizontal pipe. presented at the 2nd International conference on multiphase flow. Kyoto, Japan.

Patankar, S. (1980). Numerical heat transfer and fluid flow. Washington DC.

Perry, R.H., Green, D.W., Maloney, J.O. (1984). Perry's Cheical Engineers' Handbook. New York: McGraw-Hill.

Poesio, P., Strazza, D., Sotgia, G. (2009). Very viscous oil/water/air flow through horizontal pipes:Pressure drop measurement and prediction. Chemical Engineering Science, 64, 1136-1142.

Ranade, V. (2002). Computational flow modeling for chemical reactor. Engineering Bath:Academic Press.

Russell, T.W.F., Charles, M.E. (1959). The effect of the less viscous liquid in the laminar flow of two immiscible liquids. The Canadian Journal of Chemical Engineering, 37, 18-24.

Santos, R.G., Loh, A.C., Bannwart, A.C., Trevisan, O.V. (2014). An Overview of Heavy Oil Properties and Its Recovery and Transportation Methods. Brazilian Journal of Chemical Engineering, 31, 571-590.

Shi, J. (2015). A study on high-viscosity oil-water two-phase flow in horizontal pipes. Ph.D thesis. Cranfield University.

Shi, J., Gourma, M., Yeung, H. (2017). CFD simulation of horizontal oil-water flow with matched density and medium viscosity ratio in different flow regimes. Journal of Petroleum Science and Engineering, 151, 373-383.

Shih, T.H., Liou, W.W., Shabbir, A., Yang, Z., Zhu, J. (1994). A new k-ε eddy viscosity model for high Reynolds number turbulent flows-model development and validation. Institute for Computational Mechanics in Propulsion and Center for Modeling of Turbulence and Transition Lewis Research Center. Cleveland, Ohio.

Sinclair, A. (1970). Rheology of viscous fracturing fluids. Journal of Petroleum Technology, 711-719.

Skea, A.F., Hall, A.W.R. (1999). Effects of water in oil and oil in water on single-phase flowmeter. Flow Measurement and Instrumentation, 10, 151-157.

Sotgia, G., Tartarini, P., Stalio, E. (2008). Experimental analysis of flow regimes and pressure drop reduction in oil-water. International Journal of Multiphase Flow, 1161-1174.

Stapelberg, H.H., Mewes, D. (1994). The pressure loss and slug frequency of liquid-liquid-gas slug flow in horizontal pipes. International Journal of Multiphase Flow, 20, 285-303.

Steven, R. (2002). Wet gas metering with a horizontally mounted Venturi meter. Journal of Flow Measurement and Instrumentation, 361-372.

Taitel, Y., Dukler, A.E. (1976). A model for predicting flow regime transitions in horizontal and near horizontal gas-liquid flow. AICHE, 22, 47-55.

Tan, C., Dong, F. (2010). Modification to mass flow rate correlation in oil-water two phase flow by a V-cone flow meter in consideration of the oil-water viscosity ratio. Measurement Science and Technology, 21.

Toms, B. (1948). Some observations on the flow of linear polymer solutions through straight tubes at large Reynolds numbers. in Proceedings of the First International Congress on Rheology, 2, pp. 135-141. North-Holland, Amsterdam, Netherlands.

Ullmann, A., Brauner, N. (2004). Closure relations for the shear stress in two-fluid models for core-annular flow. Multiphase Science and Technology, 16, 355-387.

Vallee, C., Hohne, T., Prasser, H-M., Suhnel, T. (2008). Experimental investigation and CFD simulation of horizontal stratified two-phase flow phenomena. Nuclear Engineering and Design, 238 (3), 637-646.

Van Mourik, S., Veldman, A., Dreyer, M. (2005). Simulation of capillary flow with a dynamic contact angle. Microgravity-Science and Technology, 17, 87-93.

Wadle, M. (1989). A new formula for the pressure recovery in an abrupt dissusor. International Journal of Multiphase Flow, 241-256.

Wallis, G.B. (1969). One-dimensional two-phase flow. New York: McGraw-Hill.

Wang, S., Zhang, Q., Sarica, C., Pereyra, E. (2013). Experimental study of high-viscosity oil/water/gas three-phase flow in horizontal and upward vertical pipes. Society of Petroleum Engineers, 28(3).

Woldesemayat, M.A., Ghajar, A.J. (2007). Comparison of void fraction correlations for different flow patterns in horizontal and upward inclined pipes. International Journal of Multiphase Flow, 33, 347-370.

Zhang, H., Yue, W., Huang, Z. (2004). Investigation of oil-air two phase mass flow rate measurement using Venturi and void fraction sensor. Journal of Zhejiang university science.

Zhang, H.Q., Sarica. C. (2006). Unified Modeling of Gas/Oil/Water Pipe Flow - Basic Approaches and Preliminary Validation. Society of Petroleum Engineers, 1(02), 1-7.

Zhang, H.Q., Wang, Q., Sarica, C., Brill, J.P. (2003a). Unified model for gas-liquid pipe flow via slug dynamics- part 1: Model development. Journal of Energy Resources and Technology, 125.

Zhao, Y., Lao, L., Yeung, H. (2015). Investigation and prediction of slug flow characteristics in highly viscous liquid and gas flows in horizontal pipes. Chemical Engineering Research and Design, I02, 124-137.

Zhao. Y., Yeung. H., Lao. L. (2013b). High liquid viscosity effects on wall and interfacial shear stresses in horizontal liquid-gas flows. Proceedings of 8th International Conference on Multiphase Flow, ICMF, (pp. 26-31). Jeju, Korea.